Photoexcitation and Photoionization Dynamics of Doped Liquid Helium-4 Nanodroplets

THÈSE N^{O} 4207 (2008)

PRÉSENTÉE LE 4 DÉCEMBRE 2008

À LA FACULTÉ SCIENCES DE BASE

LABORATOIRE DE CHIMIE PHYSIQUE MOLÉCULAIRE

PROGRAMME DOCTORAL EN CHIMIE ET GÉNIE CHIMIQUE

ÉCOLE POLYTECHNIQUE FÉDÉRALE DE LAUSANNE

POUR L'OBTENTION DU GRADE DE DOCTEUR ÈS SCIENCES

PAR

Evgeniy LOGINOV

M.Sc. in applied mathematics and physics, Moscow institute of physics and technology, Russie
et de nationalité russe

acceptée sur proposition du jury:

Prof. P. Vogel, président du jury
Dr M. Drabbels, directeur de thèse
Prof. F. Stienkemeier, rapporteur
Prof. J. Vanicek, rapporteur
Prof. A. Vilesov, rapporteur

ÉCOLE POLYTECHNIQUE
FÉDÉRALE DE LAUSANNE

Suisse
2008

Abstract

The photoexcitation and photoionization dynamics of sodium atoms deposited on the surface of helium nanodroplets and aromatic molecules (aniline, phenol and toluene) embedded in the interior of droplets have been investigated by a variety of spectroscopic techniques. The mean droplet sizes varied in the range of ≈ 2 000 - 20 000 atoms.

For the first time, the excitation spectra of Na-doped helium droplets corresponding to Rydberg states of Na atoms have been measured from the lowest excited 3p state up to the ionization threshold. All lines in the excitation spectra are shifted and broadened with respect to atomic lines. The desorption of bare excited Na atoms and $NaHe_n$, n=1-4, exciplexes was observed upon excitation. The experiments revealed that the relative abundance of desorbed species, their internal energy states, their speed and angular distributions are specific to the state of sodium atom to which it was excited to on the droplet's surface. In the lowest excited states (3p, 4s, 3d and 4p), we observed rather regular dynamics. The photoelectron spectroscopy of products revealed the desorption of excited sodium atoms in the initially excited state and in lower lying states which were populated by radiative decay of the higher ones. The velocity distributions showed interesting characteristics: the mean kinetic energy of desorbed sodium increased linearly with excitation frequency, while angular anisotropy varied monotonically. In contrast, the recorded velocity distributions of exciplexes did not manifest systematically such regular properties. It was found that the excitation spectra and relative abundances of exciplexes depended on the mean droplet size, while the velocity distributions of desorbed species were, in general, not dependent on size. The tentative explanation of the observed features is based on the approximation that "Na-helium nanodroplet" interaction potentials can be described by a sum of Na-He pair potentials over the helium atoms constituting the nanodroplet. The shapes and shifts of the transitions to low excited states of Na obtained within this model are in a good agreement with experimental observations. The velocity distributions of desorbed Na atoms can be qualitatively interpreted by the overall interaction potentials of sodium with a helium nanodroplet where they act as counterparts in a diatomic system. In contrast, the $NaHe_n$ exciplex formation on the surface of nanodroplets appears to be mainly governed by the Na-He pair potentials. The excitation to higher than 4p states of Na on the droplet's surface revealed complex situations. The experimental spectra correlated poorly to those calculated within the pair-wise interaction model. The velocity distributions of desorbed sodium and exciplexes often consisted of two components compared to one in the lower states. The photoelectron spectra disclosed the presence of species in the states that could not be populated by radiative decay of the higher ones, indicating that relaxation plays an important role during the detachment.

The experiments on the photoionization of Na-doped helium droplets revealed that their ionization threshold is red-shifted with respect to a free sodium atom. The time-of-flight mass spectra showed that the directly created Na^+ ion was solvated in the droplet. The indirect evidence of creating special Na-droplets in high Rydberg states, when the ionic core remains inside the cluster and the weakly bound electron orbits outside, was obtained. The shape of ionization transition and the droplet size dependence of the ionization threshold are in line with the model of a pair-wise additive interaction of the created sodium ion with helium atoms in the nanocluster.

The photoionization of aromatic molecules (aniline, phenol, and toluene) in helium droplets was studied with photoelectron spectroscopy. The photoelectron spectra resemble closely those of gas phase molecules except for the droplet size dependent shift. This shift is caused by the lowering of the ionization threshold upon solvation and can be readily estimated. The individual peaks in photoelectron spectra are broadened, which is thought to partially reflect the rearrangement of helium

upon ion solvation. The droplet size and kinetic energy dependences of the peak broadening towards lower energy may be attributed to the relaxation of the photoelectrons as they pass through a helium droplet.

Keywords: heluim droplets, nanoclusters, velocity map ion imaging, state resolved dynamics, spectroscopy, exciplex, ionization, ZEKE, Rydberg states, aniline, phenol, toluene, electronic spectroscopy, sodium.

Résumé

La dynamique de photoexcitation et de photoionisation des atomes de sodium déposés en surface de gouttelettes d'hélium et de molécules aromatiques (aniline, phénol et toluène) incrustées dans des gouttelettes a été examinée par diverses techniques spectroscopiques. La taille moyenne des gouttelettes utilisées a varié entre ≈ 2 000 et ≈ 20 000 atomes.

Pour la première fois, les spectres d'excitation des gouttelettes dopées au sodium, spectres caractéristiques des états de Rydberg des atomes de sodium, ont été mesurés depuis l'état d'énergie le plus bas (3p) jusqu'au seuil d'ionisation. Toutes les raies des spectres sont décalées et élargies par rapport aux raies atomiques de sodium. La désorption des atomes de sodium excités et des exciplexes $NaHe_n$, n=1-4, a été observée suite à l'excitation. Les expériences ont révélé que l'abondance relative des espèces désorbées, leurs états d'énergie interne ainsi que leurs distributions angulaire et de vitesse sont spécifiques à l'état de l'atome de sodium excité en surface de la gouttelette d'hélium. Pour les états excités de plus basses énergies (3p, 4s, 3d et 4p), nous avons observé une dynamique plutôt conventionnelle. La spectroscopie de photoélectrons montre que la désorption des atomes excités de sodium se fait à la fois dans l'état d'excitation initiale et dans des états de plus basses énergies peuplés par décroissance radiative. Les distributions de vitesse présentent des caractéristiques intéressantes: l'énergie cinétique moyenne des atomes de sodium désorbés augmente linéairement avec l'énergie d'excitation tandis que l'anisotropie angulaire varie de manière monotone. Par contraste, les distributions de vitesse des exciplexes ne manifestent pas systématiquement des propriétés similaires. Il a été trouvé que les spectres d'excitation et l'abondance relative des exciplexes dépendent de la taille moyenne des gouttelettes, contrairement aux distributions de vitesse des espèces désorbées. L'explication proposée des caractéristiques observées est basée sur l'approximation que le potentiel d'interaction « Na-gouttelette d'hélium » peut être décrit par la somme des potentiels de paires Na-He sur l'ensemble des atomes d'hélium constitutifs de la gouttelette. La forme et le décalage des transitions pour les états de basses énergies du Na obtenues avec ce modèle sont en bon accord avec les observations expérimentales. Les distributions de vitesse des Na désorbés peuvent être interprétées qualitativement par les potentiels d'interaction globale du sodium avec la gouttelette d'hélium dans un système diatomique. Par contraste, la formation des exciplexes $NaHe_n$ à la surface des gouttelettes parait être principalement gouvernée par les potentiels de paires Na-He. L'excitation des états d'énergies supérieures aux états 4p du Na sur la surface de la gouttelette révèle une situation plus complexe. Les spectres expérimentaux ne sont pas bien reproduits par le modèle d'interaction de paires précédemment utilisé. Les distributions de vitesse des atomes de sodium désorbés et des exciplexes sont bien souvent constituées de deux composantes quand une seule composante est présente pour les états de plus basses énergies. Les spectres de photoélectrons révèlent la présence d'espèces dans des états ne pouvant pas être peuplés par décroissance radiative, indiquant que la relaxation joue un rôle important pendant le détachement.

Les expériences de photoionisation des gouttelettes dopées au sodium montrent que leur seuil d'ionisation est décalé vers le rouge par rapport à l'atome de sodium libre. Les spectres de temps de vol montrent que les ions Na^+ sont directement solvatés dans la gouttelette. Nous avons obtenu la preuve indirecte de la création de gouttelettes dopées au sodium spéciales dans un état de Rydberg élevé, où l'ion Na^+ demeure dans la gouttelette tandis que l'électron faiblement lié orbite à l'extérieur de la gouttelette. La forme de la transition de photoionisation et la dépendance du seuil d'ionisation à la taille des gouttelettes sont en accord avec le modèle additif d'interaction de paires entre l'ion de sodium et les atomes d'hélium constitutifs de la gouttelette.

La photoionisation de molécules aromatiques (aniline, phénol et toluène) dans des gouttelettes d'hélium a été étudiée par spectroscopie de photoélectrons. Les spectres de photoélectrons ressemblent à ceux des molécules libres, à l'exception d'un décalage en fréquence qui est fonction de la taille des gouttelettes. Ce décalage est causé par l'abaissement du seuil d'ionisation dû à la solvatation et peut être aisément évalué. Les pics individuels dans le spectre de photoélectrons sont élargis, ce qui reflète partiellement le réarrangement des atomes d'hélium lors de la solvatation de l'ion. Les dépendances, à la taille des gouttelettes et à l'énergie cinétique, de l'élargissement du pic vers les basses énergies peuvent être attribuées à la relaxation des photoélectrons lors de leurs trajets à travers la gouttelette d'hélium.

Mots clés: gouttelette d'hélium, nano-agrégats, imagerie de champs de vitesses, dynamique spécifique aux états d'énergie, spectroscopie, ionisation, ZEKE, niveaux énergétiques de Rydberg, aniline, phénol, toluène, spectroscopie électronique, sodium.

Contents

Chapter 1 : Introduction

1.1 Liquid helium

Helium is the most inert known element. This neutral character originates from its filled electronic shell, thus it cannot easily share outer electrons for the formation of chemical bonds with other elements. Helium has two stable isotopes ^{3}He and ^{4}He, each of them having two protons plus one and two neutrons respectively. The resulting nuclear spin of 1/2 defines the ^{3}He as a fermion, while the ^{4}He is a boson with the nuclear spin of zero. Different quantum statistics of these two types of particles, weak van-der-Waals interatomic interaction and light masses result in particular properties of bulk samples of ^{3}He and ^{4}He at low, < 2 K, temperatures.

^{3}He and ^{4}He are the unique noble gases with the lowest boiling points of 3.19 K and 4.21 K[1], respectively. They remain liquid down at the absolute zero temperature under their saturated vapor pressures. Liquid ^{4}He undergoes a second order phase transition from the normal liquid state (He I) to the superfluid state (He II) at 2.18 K. At this point its specific heat capacity passes abruptly through a maximum, the shape of which has given the term of a "λ-transition". Below the λ-point, He II has vanishingly small viscosity, meaning macroscopic objects can move in the liquid without any friction up to the a certain speed limit. The characteristic speed is called the Landau speed after the author of the first phenomenological theory of superfluidity[2]. The abrupt change of liquid helium properties is attributed to the Bose-Einstein condensation of bosonic ^{4}He atoms. As for the ^{3}He isotope, it does not have such a transition at similar temperature due to the different quantum statistics of fermions. It undergoes a superfluid phase transition at much lower temperature of 2.6 mK, which is assigned to the formation of pairs of helium-3 atoms, resulting in a zero spin species.

Bulk He II has a number of unique properties such as the infinitely small viscosity, the exceptionally high heat conductivity and heat propagation in "temperature waves" called ”second sound”. These properties can be largely explained with the two-fluid model of Landau[2, 3]. In this model superfluid helium is the mixture of normal and superfluid components with densities ρ_n and ρ_s, respectively, such that:

$$\rho = \rho_n + \rho_s$$
$$\text{curl}\ \vec{\mathbf{v}}_s = 0 \qquad (1.1)$$

The superfluid component is considered as an inviscid, irrotational ”background fluid”, in the sense that at T = 0 K He II is completely superfluid with thermal excitation moving upon that background. At temperatures above the λ-point, liquid helium is a normal liquid and $\rho = \rho_n$. The two-

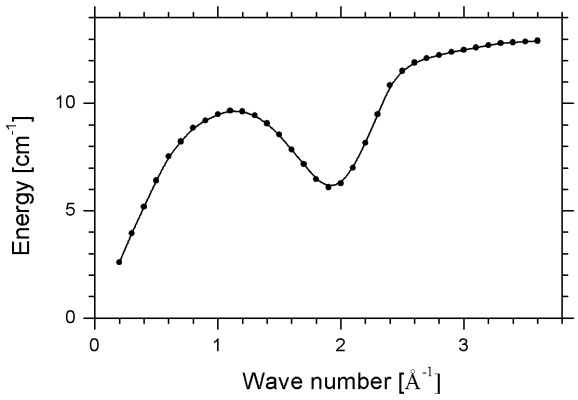

Figure 1.1: Dispersion curve of bulk superfluid helium at 1.1 K under its saturated vapor pressure. The displayed data is from Ref[4]. The line connecting the data points is to guide the eye.

fluid model was elegantly confirmed in the experiment of Andronikashvilli[5]. By monitoring the oscillation of torsional multi-disk pendulum immersed in liquid helium, he discovered the reduction of the moment of inertia of the pendulum below the λ-point. The proposed interpretation of the experiment agreed well with the two-fluid model.

The elementary excitations at low temperatures form the normal viscous fluid and represent all thermal energy of He II. These excitations consist of phonons and rotons, both being density fluctuations. The phonons are quantized sound waves with energies $\varepsilon = cp = c\hbar k$, where c is the velocity of sound, p is the momentum, $\hbar$ is the Planks constant and k is a wave number. The rotons are special excitations at low temperatures with energies $\approx$ 6 cm^{-1}. They do not possess angular momentum as their name might imply[6]. One may consider them as fast moving helium atoms with a backflow. The energy spectrum of elementary excitations obtained with neutron scattering is presented in Figure 1.1. From the graph one sees that the population of the elementary excitation, according to the Boltzmann law, is large near Q$\rightarrow$0 Å^{-1} and Q$\rightarrow$2 Å^{-1}, where the dispersion curve has the minimum. These two regions of phase space are called 'phonon' and 'roton' regions. The peculiar shape of the excitation spectrum leads to the existence of the critical velocity of the superflow. Landau analyzed the energy and momentum conservation conditions under which a single roton can be created[2]. A faster flow would be greatly slowed down by creating multiple rotons. His findings put the upper limit on the superflow's speed determined by the spectrum of elementary excitations:

1.2
$$\frac{d\varepsilon}{dp} \geq \frac{\varepsilon}{p}$$

The same formalism is applicable for the motion of a microscopic body through superfluid helium. The limit is slightly mass-depended and for a particle of infinite mass the critical velocity is v_L $\approx$ 58 m/s. The critical velocity of negative ions moving in superfluid helium was extensively studied by Allum and coworkers[7] and this experiment was further extended by Ellis *et al.*[8]. Allum *et al.* found that the onset of a drag on the ion corresponds well to Landau's prediction. At higher than Landau's velocities the energy of the moving ion is dissipated by creating a pair of rotons. Ellis and coworkers performed measurements of the critical velocity versus pressure of liquid helium and indeed found that the pressure dependence also followed the two-rotons law. An overview of the research was presented by McClintock[9].

In view of the optical transparency of helium in the 0-20 eV region of photon energy[10], the optical methods of probing the superfluid helium environment on the microscopic level were focused on the spectroscopy of impurities in bulk helium[11]. The implanted particles form complex defect structures and act as micro-probes of the surrounding liquid. The well known examples of defect structures are a 'bubble' for an excess electron[12] and a 'snowball' for a positive ion[13] in liquid helium. It is also interesting to use the ultra cold helium environment as a host for matrix isolation spectroscopy[14]. The main handicap of the investigation of neutral impurities in liquid helium is the difficulty of their implantation into the liquid. At low temperatures helium is an extremely pure liquid which contains only $1.37 \cdot 10^{-6}$ of ^{3}He[1]. After the implantation of neutral species, fast coagulation takes place. The formed aggregates are frozen on the walls of a container and are thus removed from the liquid[15]. Only for metals the laser sputtering technique allowed the easy introduction of single atoms into the liquid helium[16]. No similar techniques were developed for implantation of molecular species.

1.2 Helium nanodroplets

The advent of easy production of liquid helium nanodroplets in a jet expansion of cold gas opened a number of possibilities to study the unique quantum superfluid. As in the case of bulk superfluid helium, the nanodroplets can be used for many fundamental and applied purposes. Both fields experience intensive experimental and theoretical developments and are regularly reviewed[17-20], see also the special issue of the Journal of Chemical Physics v.115 No.22[21-25]. On the fundamental side, the helium nanoclusters allow one to study quantum liquid on the nanometer and even angström scales. On the applied side, the "softness" of liquid clusters, its ultralow temperature of 0.4 K[26] and simple embedding of impurity species[27, 28] opened several new research fields: spectroscopy of species that are unstable in the gas phase[18, 20]; the study of chemical reactions between dopants in the droplet[29]; formation of complex impurity clusters inside nanodroplets[30, 31].

The structure of helium clusters remains the subject of extensive theoretical and experimental studies, see the review of Barranco[19] and references therein. Helium clusters ^4He_n, $n \geq 2$, were found to be stable[32-34]. The shape of a cluster in the ground state is expected to be spherical and is often approximated by a sphere of uniform density so that the cluster's radius is expressed as:

1.3 $$R = r_0 N^{1/3}$$

where $r_0 = 2.22$ Å^{-1}[35] is the unit radius for ^{4}He and N is the number of helium atoms in the cluster. According to the above expression, the clusters with $N > 90$ have $R > 10$ Å = 1 nm and are typically called nanodroplets. In the following text, only large clusters with $N > 300$ will be considered, so the terms as nanodroplet, droplet, nanocluster and He_N will be used interchangeably to designate the nanometer-size ^{4}He clusters. The real surface of helium droplets is not sharp and has a smooth profile. In theoretical works the surface thickness is defined as the distance between the radii where the helium density drops from 90% to 10% of the value in the centre of the nanodroplet[35]. The theoretical results correspond well to the experimentally found value 7±1 Å[36].

The spectrum of elementary excitations of pure droplets was derived using the liquid drop model by Brink and Stringari[37]. Based on this model, the energy of the volume and surface excitation modes are of the order of 1 cm^{-1} and 0.1 cm^{-1} for a droplets consisting of 10^3-10^4 ^{4}He atoms, respectively. The volume vibrations are too high in the energy to be populated even at temperatures of several Kelvin, so only the surface modes are expected to be excited. They define the final 0.4 K

temperature of the helium nanodroplets predicted by the evaporation of atoms in vacuum. A more realistic microscopic approach used by Whaley and Krishna[38], Krotscheck and coworkers[32, 39], who explicitly took into account the quantum nature of the fluid helium, showed that the droplets with more than 100 ^{4}He have characteristic dispersion curve with the roton minimum. In this respect, the excitation spectrum of helium nanodroplets resembles that of the bulk He II.

The embedding of impurities in the droplets by collisions with the gas phase species was clearly demonstrated by the group of Toennies in 1990[27, 28]. They found that the introduction of single and multiple species was simple by passing the droplet beam through a vacuum chamber filled with the gas of interest at low pressure, less than 10^{-4} mbar. It was also possible to dope droplets by crossing the helium droplet beam with an auxiliary beam of species. The species with low vapor pressure could be introduced by heating samples in small ovens. Laser ablation close to the expanding beam of cold helium was also successfully applied to dope droplets[40, 41].

A crucial aspect of the doped droplets is the equilibrium location of the impurity and its solvation structure. The solvation is governed by the balance between the energy gain in solvation determined by the "He-impurity" pair interactions and the energy cost by removing fluid to create a void in order to accommodate the defect structure. Based on that balance Ancilotto[42] developed a simple parameter to estimate the location of the spherical impurity:

1.4 $$\lambda = \frac{\rho \varepsilon R_m}{2^{1/6}\sigma}$$

where ρ is the liquid density, σ is the surface tension of the liquid, ε is the well depth and R_m is the equilibrium distance in the helium-impurity pair interaction. The limiting value for liquid helium-4 is $\lambda = 1.9$, so impurities with $\lambda < 1.9$ do not dissolve in the liquid and stay on the surface. In the opposite case, the impurity is solvated inside the droplet. The theoretical works[43, 44] indicate that closed shell atoms and molecules reside inside the droplet, while open shell alkali atoms reside on the surface of nanoclusters.

The helium atoms form a number of shells around solvated impurity, where the helium density is up to 4 times higher than that in the bulk liquid helium[43]. According to microscopic studies of Whaley and coworkers[45], the multiparticle permutation exchange of He atoms in the solvation shells with surrounding atoms in the rest of liquid allows for free rotation of molecular dopants. This exchange in the pure liquid helium is thought to be essential sign of the superfluidity[46]. The degree of the exchange depends on the strength of impurity-helium interaction and for strongly interacting impurities, like ions, this exchange can be completely suppressed for the nearest He atoms.

The impurity solvated inside the droplet experiences the confinement potential due to the long-range interaction with all helium atoms, so the droplet surface acts as box walls[47-49]. Close to the cluster centre, the confining potential is rather flat, which results in the largely delocalized radial position of the impurity well far from the centre and the surface.

Unique molecular clusters and complexes can be formed in helium droplets due to the high mobility of species in ultra-cold neutral superfluid environment that facilitates stabilization by efficient cooling. This was widely exploited by the group of Miller. They created peculiar cyclic water hexamer[50] and linear chains of polar molecules[51]. The consecutive doping also made possible the assembly of exotic layered structures, the HF-Ar_n could be an example[52]. In this work, Nauta and Miller showed that if the HF was doped first then the Ar atoms, which were added afterwards, encapsulated the molecule. The reverse procedure led to surface located HF on Ar_n cluster inside helium droplets.

The helium nanodroplets were used by Toennies and Vilesov as an ultra-cold containers for testing the superfluidity of para-hydrogen clusters[53] and even for enhancing and manipulating of chemical reactions[29]. The group of Vilesov also demonstrated surface deposition of the heterogeneous metal and molecular clusters formed in helium droplets[30].

Like bulk helium, pure helium droplets are transparent up to photon ≈ 20 eV energy[10], so IR and VIS-UV spectroscopic interrogation of an embedded impurity is readily possible. The detection methods of IR spectroscopy in doped helium nanodroplet are based on the detection of cluster size reduction due to the relaxation of the excited dopant in the droplet and the following evaporation of helium atoms[54]. There are two major beam depletion techniques: electron-impact ionization of doped clusters and bolometer measurements of heat flux from a droplet beam. In the first method the depletion of He_n^+, n>2, ions, which are formed exclusively by ionization of nanodroplets, is measured. The ionization cross-section of the cluster depends on its geometrical cross-section and is thus sensitive to the evaporation loss of helium atoms. In the UV-VIS spectroscopy laser induced fluorescence (LIF) is one of the most used detection schemes[55]. Resonance-enhanced multiphoton ionization (REMPI)-based techniques are also applied[18, 20].

The first IR spectrum of a species embedded in helium droplets was the vibrational spectrum of SF_6 recorded by the group of Scoles in 1992[56, 57]. The next milestone achievement was the rotationally resolved IR spectrum of SF_6 by Toennies and coworkers in 1995[26], which made possible the direct measurements of the cluster's temperature of 0.37±0.05 K. The significance of this experiment was also in showing that free rotation of molecules is possible in helium nanoclusters due to their superfluid nature. Additional evidence of superfluidity of ^{4}He droplets was elegantly demonstrated by Grebenev *et al.* in 1998[58]. They carried out a microscopic variant the Andronikashvili experiment[59], embedding OCS in ^{3}He droplets as an atomic-size pendulum and adding gradually ^{4}He atoms to OCS-^3He_N. The rotational structure reappeared in the spectrum after adding, on average, 100 ^{4}He that formed approximately two solvation shells around OCS inside the ^{3}He cluster.

The influence of helium environment on the solute is spectroscopically detectable. The rotational spectra of molecules in helium droplets show that their rotational constants are decreased by a factor of 3 for heavy species and only by a few percent for lighter ones[60]. Two models, which treat the helium-impurity interaction from hydrodynamic and microscopic points of view, were put forward to explain this effect. The hydrodynamic model[61] is based on the adiabatic following of the rotating molecule by the normal fraction of superfluid helium. This leads to the increase of it's effective moment of inertia of the impurity, like a body moving in the viscousless and irrotational fluid. The microscopic model takes into account the molecule-induced reduction of superfluid fraction in the first solvation shell[45, 62], which may be considered as partial "sticking" of helium atoms to the rotating impurity. Both models predict values of rotational constants that are close to the experimental ones for heavy molecules like SF_6 but are not so successful for light molecules such as HF[23]. The vibrational lines of molecules inside clusters containing 10^3-10^4 ^{4}He atoms are mostly red-shifted by less than 2 cm^{-1} with respect to the gas phase values, see the compilation in Ref.[20]. The line shift is thought to be the interplay between the long-range dispersion and attractive induction interactions that lead to the red shift and the stiffening of the vibrational potential by helium solvation shell around the dopant that lead to the blue shift. The experimentally observed width of vibrational lines is expected to originate from both inhomogeneous broadening due to broad cluster size distribution in the helium droplet beam, the impurity location[47, 48] and due to the homogeneous broadening by the vibrational relaxation in the matrix[63].

The electronic spectra of molecules embedded in helium droplets resemble those in gas phase, normally obtained in super-sonic jets, but new features can appear. Hartmann et al.[64] showed on the example of glyoxal that single vibrational line in the electronic spectrum becomes a sharp peak, called a zero phonon line (ZPL), accompanied with a high frequency tail, called phonon wing (PW), separated from the ZPL by a gap. The ZPL corresponds to the pure electronic excitation of the molecules without involvement of droplet-specific modes. The PW reflects the excitation of phonons in the He droplet accompanying photon absorption by the molecule. The characteristic features with a gap could be explained by the superfluid nature of helium droplets with a characteristic excitation spectrum. Indeed, the same molecule in normal liquid ^{3}He droplets did not demonstrate the gap between ZPL and PW[65].

The first electronic p←s excitation spectra of all alkali metal atoms attached to ^{4}He nanodroplets have been measured[66-69]. All alkali systems demonstrated broad transitions which were mainly blue-shifted with respect to correlated atomic resonance lines. These spectra could be reproduced with a pair-wise additive model of alkali-He_N interaction[70]. The spectral analysis of the light emitted after the excitation of alkali-doped droplets revealed the formation and desorption of alkali-helium exciplexes[67, 69, 71, 72]. The dynamics of exciplex formation was studied with time-resolved techniques using Na[72], K[73, 74] and Rb[75] systems. It was concluded that the desorption of excited alkali atoms and exciplex occurred on the picosecond time scale. Two simulations of dynamics of excited alkalis on the surface of helium clusters were performed with quantum molecular dynamics methods by the example of Li(2p)-He_{99}[76] and K(4p)-He_{300}[77] systems. Takayanagi and Shiga found that the excitation of K atoms resulted in its desorbtion from the surface of helium droplets on the time scale of a few picoseconds[77]. They also assessed the KHe exciplex formation in the D2 band of K-He_N excitation spectrum and extracted the formation time of ≈10 ps, which contrasted to 180 fs in the experiment of Shulz *et al.*[73]. Pacheco and coworkers studied the dynamics of excited Li(2p)interacting with the model cluster surface and with the helium droplet. They found that the excited atom is either attracted into the cluster interior or repelled from the surface, which depends on whether the p-orbital is oriented parallel to the surface or perpendicular, respectively.

The photoionization of droplets doped with impurities with ionization threshold below 20 eV was studied with the mass analysis of created ions[78] and photoelectron spectroscopy[79-81]. In the latter cases, the resonance two-photon ionization (R2PI) photoelectron spectra of Ag_8 , Ag_2 and Ag_3 embedded in helium nanodroplets were measured. Droplet induced effects were observed in photoelectron spectra. In the case of Ag_3-He_N[79], the photoelectron peak was broadened with respect to the gas phase and had long a tail on the low energy side. The ionization thresholds of doped silver cluster, within the experimental resolution, were the same as those in the phase. The mass-selective R2PI ionization of NO embedded in helium droplets[78] revealed complex dynamics of intermediate excited states and NO^+-He_n formation. The ionization of NO* and the attachment of helium atoms were thought to happen on the surface after the transport of the excited molecule from the interior of helium droplets.

1.3 Motivation

The short overview of the helium nanodroplets domain presented above shows that many fundamental and applied aspects of use of pure and doped helium clusters have been studied and understood. Especially, the weak interaction of the impurity and helium environment was successfully studied by IR spectroscopy, which probes rotational and vibrational degrees of dopant, and is to a large extent understood. The interaction of electronically excited species and helium clusters is a still

developing area, which is relevant to the study of chemical reactions in the soft ultra-cold environment, since the chemical reactions involve essentially the rearrangement of electronic structures of reactants. The fates of the electronically excited impurity, the created photoion and the photoelectron inside and on the surface of helium cluster are of great interest.

The aim of this work is to gain new insight into photoexcitation and photoionization dynamics of species inside and on the surface of helium droplets. For this purpose, two model systems were chosen: Na-doped and aromatic (aniline, phenol, and toluene) molecules-doped droplets. The Na-doped helium droplets represent a system where the impurity resides on the surface of nanoclusters. Aromatic molecules, in contrast, reside in the interior of nanoclusters. The influence of the helium environment on the electronically excited and ionized impurities is expected to be different. In the experiment presented in this work, photoexcitation products are analyzed with the aid of a velocity map ion imaging setup. From the recorded ion images, both the speed and angular distributions of the ejected excited species can be recovered. Photoelectron imaging allows us to obtain the energy content of the photofragments and information about the ionization of embedded molecules. In addition, product-specific excitation spectra, time-of-flight mass spectra and state-selective detection of products can be carried out with the same setup. In this way, the interaction of electronically excited species, ions and electrons interacting with helium droplets can be assessed.

1.4 Outline

The material in this thesis is ordered as follows. Chapter 2 contains the description of the experimental setup and the spectroscopic techniques used. Chapter 3 is devoted to photoexcitation and photoionization dynamics of Na-doped helium nanodroplets. In the latter chapter we separately show and discuss the excited states of Na-He_N correlated to: a) low excited states of Na, namely 3p, 4s, 3d and 4p; b) medium excited states, which lie in the energy region of atomic states from 5s to 6p; c) excited states which are higher in energy than 6p atomic states. The results on photoionization of Na-doped droplets are included in the end of Chapter 3. In Chapter 4 we present and discuss the photoionization dynamics of nanodroplets doped with aromatic molecules (aniline, phenol and toluene). It is divided in to two parts, the first of which contains the results on dynamics of intermediate electronic excited S_1 states of molecules inside the nanocluster. This information is valuable to our understanding of the photoionization of dopant via these states, which is considered in the second part of Chapter 4. The most important results obtained in this work and suggestions for future experiments are summarized in Chapter 5.

Chapter 2 : Experimental Setup

2.1 Apparatus

2.1.1 Overview

A helium droplet beam machine specially designed to study photodissociation and photoionization events inside and on the surface of helium nanodroplets was at our disposal. The detailed technical description of the machine can be found elsewhere[82]. The modifications to the previously reported setup were following:

- previously used slow-output CCD camera was replaced by high-speed high-sensitivity one. This allowed to implement every-shot image analysis and to use counting integration method instead of normal continuous on-chip integration.
- an additional differential pumping stage was installed between the doping chamber and the detection chamber. This reduced the gas effusion from doping chamber to the detection chamber by a factor of 100. As a consequence, the background from gas phase species, which were not embedded in helium droplets, was also reduced.
- a second room-temperature nozzle was mounted above the helium nozzle. This allowed to perform conventional super-sonic jet molecular spectroscopy in parallel with droplet experiments for reference and alignment purposes.

The last two changes do not alter the overall performance of the setup, so they are not described in detail. The counting method is presented in section 2.2.2.1. The aspects of the machine which are relevant to the experiments presented in Chapter 3 and Chapter 4 will be given below.

The overall scheme of the experimental setup is shown in Figure 2.1. Helium droplets are formed by expanding high-purity ^{4}He gas (99.9999%, Carbagas) into vacuum through a 5 μm nozzle cooled by closed cycle refrigerator to temperatures in the region of 11-22K. After passing a 0.3 mm diameter skimmer, the beam of nanodroplets enters the second vacuum stage, the so called doping chamber, equipped with a leak valve (UDV 235, Balzers) and a home built high-temperature oven. Traversing the doping chamber, droplets pick up impurities by inelastic collisions. The vapor of a highly volatile substance is introduced into the doping chamber through the leak valve. The leak rate is regulated in order to obtain the pressure at which droplets peak up on average less than one atom or molecule as the beam passes through the chamber. The scattering gas can be also generated by heating a low vapor pressure substance over the length of 30 mm in the oven. The temperature of the oven, consequently the scattering gas pressure in the oven, is adjusted to provide a single pick up of foreign species by droplets as well. The temperature is measured by thermocouple connected to temperature

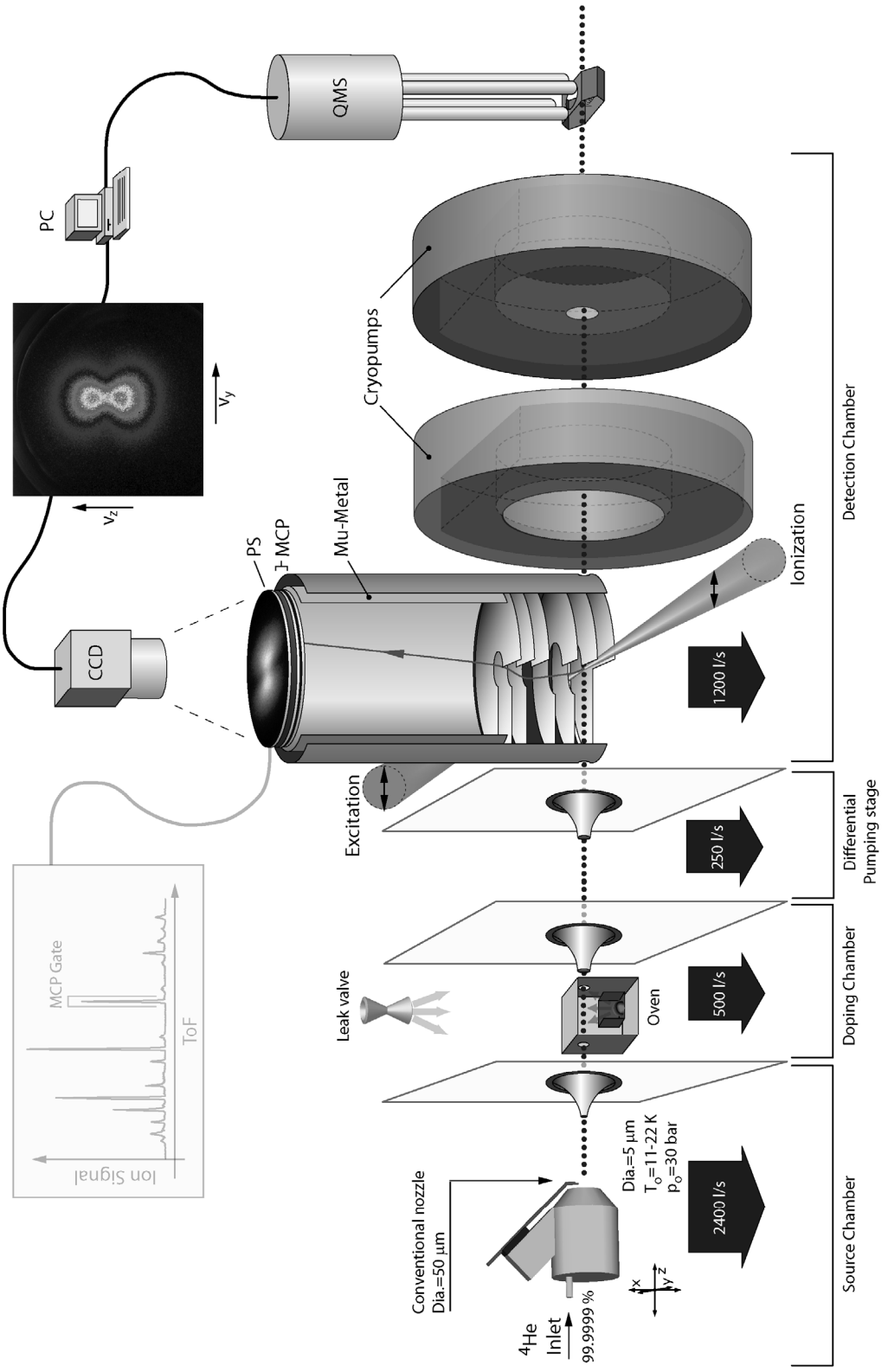

.

Figure 2.1: Overview of the experimental setup

controller that maintains the desired value within ±1 °C by regulating the output of the oven's power supply. The oven can be heated up to 900 °C.

The beam of doped droplets enters the main chamber after an additional differential pumping stage. The main chamber, the so called detection chamber, holds the ion imaging setup, a quadruple mass spectrometer (QMS) and liquid nitrogen containers (Cryopumps) that act as cryogenic pumps to reduce background pressure in the chamber. The QMS is used to control the constitution of the background gas, the oven operation by detecting effused species and the doping of droplets.

The species embedded in nanodroplets are excited and ionized by crossing beams of Nd:YAG pumped dye lasers in the centre of the imaging setup. The created charged particles are projected by an electrostatic asymmetric immersion lens onto a position sensitive detector consisting of two 75 mm in diameter, chevron mounted microchannel plates (MCP) and a phosphor screen (PS). The 40 cm flight path from the lens to the detector is shielded from stray magnetic fields by a high permeability foil (Mu-metal). The electrical signal from the phosphor screen is fed into an oscilloscope and a multichannel scaler (P7886, FAST ComTec GmbH) that allows to record ion time-of-flight mass spectra.

The light emitted by the phosphor screen is captured by a high resolution machine vision CCD camera (A200, Basler AG) interfaced to a PC. The camera captures an image every laser shot at the rate of 20 Hz. The individual images are then analyzed online and the centroids of the ion or electron impacts are determined with single pixel resolution. High resolution ion or electron images are constructed by adding together the centroids of individual images collected during a certain time. Ion images can be recorded for a specific ion mass by gating the voltage applied to the front electrode of the MCP detector. The 3D velocity distributions of ions or electrons are finally derived by performing an inverse Abel inversion on the recorded two-dimensional images. High signal-to-noise excitation spectra can be recorded with this camera setup by counting the number of ions or electrons hitting the detector at a specific wavelength.

In this work, various spectroscopic and imaging techniques were applied using the same imaging setup consisting of a repeller plate (Repeller), an open extractor (Extractor) and an open ground electrode, see Figure 2.2. Each type of measurements requires different set of voltages to be applied to electrodes. The descriptions of techniques used and voltage settings will be given below in appropriate sections.

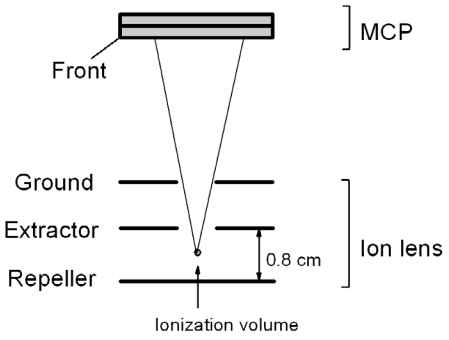

Figure 2.2: Scheme of the velocity map ion imaging setup with the main electrodes. The flight tube is not shown.

2.1.2 Droplet size distribution

The source conditions with the stagnation temperature T = 11 - 22 K and the constant pressure of P = 30 bars used in our experiments correspond to the so-called subcritical regime[83], when droplets are formed by condensation of helium gas. The atom number distribution $f(N)$ in this case is log-normal[84, 85]:

2.1
$$f(N) = \frac{1}{N\delta\sqrt{2\pi}} \exp\left[-\frac{(\ln N - \mu)^2}{2\delta^2} \right]$$

where μ and δ are parameters connected to the mean droplet size $\bar{N}$ and standard deviation of the distribution $f(N)$ as:

2.2
$$\bar{N} = \exp\left(\mu + \delta^2/2\right)$$
$$S = \bar{N}\sqrt{\exp\left(\delta^2\right) - 1}$$

Experimentally[36] it was found that there is practically linear relation between $\bar{N}$ and S:

2.3
$$S/\bar{N} = 0.60 \pm 0.04$$

which translates via equations 2.2 to :

2.4
$$\delta = 0.55 \pm 0.03$$

Based on the scaling law from Knuth et al.[85] the mean droplet sizes $\langle N \rangle$ and the corresponding mean droplet radii $\langle R \rangle$ of droplets from our source were previously estimated[82] and are tabulated in Table 1. The radii were calculated according to expression 1.3 and rounded to units.

Table 1 Experimental droplet size distribution

T [K]	11	12	13	14	15	16	17	18	19	20	21	22
$\langle N \rangle$	20060	14710	10860	8080	6080	4620	3540	2750	2150	1710	1370	1100
$\langle R \rangle$ [Å]	60	54	49	44	41	37	34	31	29	27	25	23

The flux of helium droplets may be estimated by converting the gas flux through the orifice into droplet flux of the mean cluster size from the adopted cluster size distribution. For the typical stagnation conditions for our droplet source at T=15 K and P=30 bars the droplet flux into the detection chamber is around $8 \cdot 10^{10}$ droplets/s[82]. This estimation should be taken with care due to the assumptions of complete condensation of helium atoms into clusters. Furthermore, the real droplet flux is expected to depend on the divergence of the helium jet.

2.1.3 Doping of helium nanodroplets

The foreign atoms and molecules can be deposited inside or on the surface of helium droplets by passing the helium droplet beam through the scattering cell. The much heavier droplets pick-up lighter impurities in inelastic collisions. If the pressure of scattering gas is high enough then multiple collisions can lead to the successive pick-up of several impurities.

In the simplest assumption, the droplet pick-up an impurity in any collision and the pick-up cross-section $\sigma(N)$ of the droplet consisting of *N* helium atoms is equal to the geometrical cross-section of the droplet:

2.5 $$\sigma(N) = \pi R^2$$

where *R* is calculated according to expression 1.3. In the pick-up process the kinetic, the internal and the solvation energies of the particle are deposited into the helium nanocluster. This leads to the evaporative cooling and the reduction of the droplet size. Usually the change in the pick-up cross-section by evaporative cooling is neglected[20] and the probability for the droplet to pick-up *k* impurity species is approximated by a Poisson distribution[86]:

2.6 $$P_k(z) = \frac{z^k}{k!}\exp(-z)$$

where *z* is the average number of collisions leading to the pick-up of species by the droplet. It is related to the pressure P_S of the foreign gas in the scattering cell and the length L of the cell as[86]:

2.7 $$z = n_S \sigma(N) LF = P_S \frac{\sigma(N) LF}{k_B T_S}$$

where n_S is the number density of the scattering gas, k_B is the Boltzmann constant, T_S is the temperature of the scattering gas, $F \geq 1$ is the correction factor that compensates for the relative motion of the droplet beam with respect to species of the scattering gas.

By varying the pressure of the scattering gas, one can control how many impurities, on average, the droplet of size *N* will pick-up. The above expressions does not take into account the broad cluster size distribution in the droplet beam. However, it can be shown[82] that the inclusion of the size distribution does not change much the pick-up probability from the Poisson distribution in expression 2.6.

2.1.3.1 Evaporation loss of He atoms upon capturing foreign species

The energy released into the droplet upon pick-up of an impurity can be written as[82]:

2.8 $$E_{pick-up} = \frac{1}{2}\frac{m_S m_D}{m_S + m_D}\left(\vec{v}_S - \vec{v}_D\right)^2 + E_{\text{int}} + E_{bind}$$

where m_S is the mass of the impurity, m_D is the mass of the droplet; $\vec{v}_S$ is the velocity of the impurity and $\vec{v}_D$ is the velocity of the droplet in the laboratory frame; E_{int} is the internal energy of the impurity, E_{bind} is the binding energy of the impurity to the helium droplet. Following the approach of Lewerenz et al.[86], the first kinetic energy term in the above expression can be significantly simplified due to the geometry involved. First, the droplet mass is normally much larger than that of

the impurity. Second, the velocities of scattering particles have the isotropic Maxwell-Boltzmann distribution. So, after averaging over $\vec{v}_S$ one obtains:

$$\left\langle E_{pick-up} \right\rangle = \frac{m_S}{2}\left\langle \left(\vec{v}_S - \vec{v}_D\right)^2 \right\rangle + \left\langle E_{\text{int}} \right\rangle + E_{bind} =$$

2.9

$$= \frac{m_S}{2}\left(\left\langle {v_S}^2 \right\rangle + \left\langle {v_D}^2 \right\rangle\right) + \left\langle E_{\text{int}} \right\rangle + E_{bind} =$$

$$= \frac{3k_B T_S}{2} + \frac{m_S {v_D}^2}{2} + \left\langle E_{\text{int}} \right\rangle + E_{bind}$$

where $\frac{m_S {v_S}^2}{2}$ is replaced by the mean kinetic energy of the particle in scattering gas with the temperature T_S. The mean speed of droplets is taken to be constant and equal to the upper limit $v_D \approx$ 400 m/s in our source[82] in view of the sharp speed distribution of droplet beams[83, 84]. The average vibrational energy of aromatic molecules $\left\langle E_{\text{int}} \right\rangle$ at room temperature was estimated on the basis of harminc oscilator approximation. The energies of vibrational levels are from ab initio calculations of Tishchenko et al.[87] for phenol, from Wojciechowski et al.[88] for aniline and from Whiteside et al. [89] for toluene. The rotational energy was taken as $\frac{3k_B T_S}{2}$. The binding energy of Na to a helium cluster is taken from the work of Ancilloto and coworkers[44]. The binding energies $\left\langle E_{\text{int}} \right\rangle$ of aromatic molecules to a helium droplet are not known and are thought to be of the same order as the binding energy of SF_6 of 500 cm^{-1} according to calculations of Dalfovo[43]. The mean number of evaporated helium atoms $\left\langle \Delta N_{He} \right\rangle$, see Table 2, is calculated assuming that 5 cm^{-1}[35] of energy is carried by each evaporated atom.

Table 2 Evaporation loss of helium atoms upon capturing of foreign species

Species	T_S [K]	$\frac{3k_B T_S}{2}$ [cm^{-1}]	$\frac{m_S {v_D}^2}{2}$ [cm^{-1}]	$\left\langle E_{\text{int}} \right\rangle$ [cm^{-1}]	$\left\langle E_{bind} \right\rangle$ [cm^{-1}]	$\left\langle E_{pick-up} \right\rangle$ [cm^{-1}]	$\left\langle \Delta N_{He} \right\rangle$
Na	400	400	150	-	10	560	112
Aniline	300	315	600	710	500	2 125	425
Phenol				725		2 140	428
Toluene				730		2 145	429

As one can see from the table, the number of evaporated helium atoms does not exceed 430, which is negligible with the typical mean droplet size of ≈ 6 000 He atoms used in our experiments. In contrast, for the smallest droplets with $\left\langle N_{He} \right\rangle \approx$ 1 000 the evaporation loss will be important. For the simplicity, in the following we will neglect the evaporation losses and will use mean droplet sizes from Table 1.

2.1.4 Lasers

One or two Nd:YAG pumped dye lasers were used in the one- or two-color ionization schemes, respectively. The principal dye laser used over all experiments was a PrecisionScan SL, *Sirah Laser- und Plasmatechnik GmbH,* pumped by the frequency doubled or tripled output of a Nd:YAG laser Quanta-Ray Pro 250, *Spectra-Physics Lasers*. As the second laser in the experiments, the following three dye lasers were successively used: TDL 50, *Quantel International*; ScanMate 2 E, *Lambda Physik Lasertechnik GmbH* and NarrowScan, *Radiant Dyes Lasers & Accessories GmbH*. The second dye laser was pumped by a Nd:YAG laser Quanta-Ray GCR-170, *Spectra-Physics Lasers*. The polarization of the laser light was kept parallel to the droplet beam axis. The repetition rate of all lasers was 20 Hz. Depending on the frequency required, a particular laser dye was used and the output of dye laser was frequency doubled in KDP or BBO crystals. In the experiments, the laser output covered the frequency region from 15 000 cm^{-1} to 42 000 cm^{-1} and had a typical pulse energy of several mJ. The diameter of laser beams was usually around 5 mm.

2.2 Methods

2.2.1 Recording excitation spectra

Excitation spectra are recorded by detecting mass-selected photoions or photoelectrons that impinge onto the MCP detector while varying the excitation frequency. The data acquisition program records the number of counts per laser shot while the energy of excitation and ionization lasers are monitored by photodiodes. The photodiode signals are used to correct the recorded spectra for variations in laser intensity.

2.2.2 Velocity map ion imaging

Discovered in 1997 by Eppnik and Parker[90, 91], the velocity map imaging technique has become a powerful tool in molecular dynamics[92]. Below we summarize the basics of the technique.

Being different from conventional ion optics concepts, where charge particles with different velocities are focused to a small spot, the velocity map imaging technique spatially separates particles with different velocities. The particles with the same velocity vectors are focused in one spot even if they are created at different locations. The trajectories of charged particles in velocity map imaging depend only on the charge and the kinetic energy of a particle, which results in important properties. The first is that the fragments with the same kinetic energy are mapped on the position sensitive detector in shapes of rings with the radius squared being proportional to the kinetic energy:

2.10 $$R^2 = (CT)/(qV_{\mathrm{Repp}})$$

where C is the calibration constant, T stands for the kinetic energy of an ion, q is the ion's charge, V_{Rep} is the Repeller voltage, see Figure 2.2. The behavior of R^2 versus T is almost linear, the deviation being less than 0.5% at typical conditions. The focusing condition, when the width of a ring is the narrowest, is experimentally determined by the voltage ratio of Repeller and Extractor within 1% of accuracy. The second is that the same settings of an electrostatic immersion lens can be used to image ions or electrons, with respective polarities of voltages applied to electrodes. An important advantage is the conservation within 1% of the time-of-flight conditions:

2.11 $$t \propto \sqrt{m/q}$$

where m is the mass of the particle and t is the time of flight. Thus mass separation of fragments is easily performed by gating the position sensitive detector.

2.2.2.1 Event counting

Photoions, which are created during the laser pulse, hit the MCP and produce light flashes on the phosphor screen. A CCD camera records these light flashes every laser shot. The image is integrated over many laser shots by collecting signal on the CCD chip or by the summation of the signal from each laser shot in the computer[93]. In our setup the latter method is combined with centroiding and provides several advantages. A single ion hitting event on the MCP produces a light flash of 100-200 μm radius on the phosphor screen that covers several pixels on the CCD chip. The centroiding algorithm determines a local maximum of surrounding pixels and thus maps the position of the event to a pixel-resolution. The background, which is caused by CCD matrix, is discarded by setting the discriminating threshold in the centroiding algorithm, below which the pixel intensity is considered as noise. Thus, the inhomogeneous sensitivity of the detector is corrected for, since the summation is done over individual events. Care was taken to avoid count losses caused by too high signal level, when overlapping events are recognized as a single event, and too low signal level, when the signal intensity is not high enough to be recognized as the proper event.

2.2.2.2 Calibration and energy resolution

The energy resolution of the imaging setup is largely defined by the voltage settings, which determines the radius of hitting ions with a given kinetic energy, and the spatial resolution of the position sensitive detector. The initial resolution is determined by the pore size and the channel spacing of the microchannel plate. The phosphor screen, the projection optics with CCD camera and the size of the ionization volume define the final resolution achievable in experiments. The ionization volume size was kept less than 1 mm by choosing the focal length of the lens, which focuses the beam of the ionization laser, and its distance from the centre of the imaging setup. In this work the energy resolution estimated with photoelectron imaging is about 3%. It is determined as the full width at half maximum (FWHM) of the peak corresponding to the photoelectrons with a given kinetic energy.

The calibration of the imaging setup was performed according to the procedure described in Ref[82] by 1+1' REMPI of aniline in a seeded He supersonic beam from the second orifice. The photoelectrons produced were imaged at series of fixed voltages applied to the Repeller and to the Extractor with the ratio of 1:0.707. The vertical position of the lens, focusing the beam of the ionization laser, was adjusted for each voltage setting for the sharpest image of the ionic streak of aniline ions from the molecular beam observed on the PC display. The deviation of the calibration constant for a given voltage setting was normally better than 5% along experiments. It is determined by the reproducibility of the lens position, by the voltage reproducibility of the high voltage power supplies and by the laser beam profile.

2.2.2.3 Data analysis

Already raw images in velocity map imaging reveal some important information about the dynamics in photoinduced processes. The outer radius of an image represents the maximum kinetic energy of a fragment created in the process. The presence of several rings in an image indicates several channels in energy release after the photoexcitation. The angular distribution, isotropic or anisotropic, of products can also be inferred qualitatively from the raw image.

For a deeper insight into the dynamics, knowledge about the three-dimensional speed distributions of the photofragments is necessary. The cylindrical symmetry of the imaging setup, where molecular beam axis and polarization of ionization laser are parallel to the plane of the position sensitive detector, allows for a unique reconstruction of 3D speed distribution from the 2D projection.

The Abel inversion software used in this work was described in detail in Ref[82]. Here we present only the most important aspects. Due to the cylindrical symmetry and the inversion procedure used the 3D velocity distribution is presented as the product of the 1D velocity distribution $P_v(v)$ and the 2D speed dependent angular distribution $P_\theta(v,\theta)$. $P_v(v)$ represents the distribution of particles moving into a particular direction of space and the angle θ is the angle between the axis of symmetry and the velocity vector of the particle. The physically relevant speed distribution is expressed as:

2.12 $$P_S(v) = v^2 P_v(v)$$

From the above speed distribution the kinetic energy distribution is derived according to particle conservation $P_S(v)dv = P_e(E)dE$:

2.13 $$P_e(E) = \frac{1}{mv} P_S(v)$$

where $E = mv^2/2$ is the kinetic energy of the particle with the mass *m* and the speed *v*. The mean kinetic energy $\langle E_{kin} \rangle$ and its standard deviation $\langle \Delta E_{kin} \rangle$ from the mean value (root mean squar) are calculated as:

2.14
$$\left\langle \mathrm{E_{kin}} \right\rangle = \int_0^\infty P_e\left(E\right) E dE$$
$$\left\langle \left(\mathrm{E_{kin}}\right)^2 \right\rangle = \int_0^\infty P_e\left(E\right) E^2 dE$$
$$\left\langle \Delta \mathrm{E_{kin}} \right\rangle = \sqrt{\left\langle \left(\mathrm{E_{kin}}\right)^2 \right\rangle - \left\langle \mathrm{E_{kin}} \right\rangle^2}$$

The information about the angular distribution of photofragments created in one-photon photolysis is extracted from the 2D function $P_\theta(v,\theta)$ as the anisotropy parameter $\beta(v)$ by computing a linear regression for each individual speed *v* since:

2.15 $$P_\theta(v,\theta) = \frac{1}{4\pi} + \beta(v) \cdot \frac{1}{8\pi}\left(3\cos^2\theta - 1\right)$$

for all angles θ according to the classical definition of Zare[94], see also section 3.1.5.4.1.2. The mean anisotropy parameter $\langle \beta \rangle$ and its standard deviation $\langle \Delta\beta \rangle$ are calculated as:

$$\langle \beta \rangle = \int_0^\infty P_S(v)\,\beta(v)\,dv$$

2.16 $$\langle \beta^2 \rangle = \int_0^\infty P_S(v)\,\beta^2(v)\,dv$$

$$\langle \Delta\beta \rangle = \sqrt{\langle \beta^2 \rangle - \langle \beta \rangle^2}$$

2.2.3 Time-of-flight mass spectra

As described in section 2.2.2, the velocity map imaging setup provides also time-of-flight conditions, which was used to record the mass content of the species formed in experiments. For the best time-of-flight resolution of 20 ns the ratio of the potentials applied to the Repeller and to the Extractor was found to be 1:0.85. The heavy species with masses of the order of 10^4 amu, corresponding to helium droplets with embedded ion, were detected by applying the highest possible constant voltage of 8 KV to the Repeller. In this regime the geometry of the electrodes and the finite size of the detector limited the mass of the detected species to roughly $5 \cdot 10^4$ amu. At lower Repeller voltages the detection of heavy species is also possible but the upper mass limit and the sensitivity of MCP are reduced. A correction of the TOF spectra for the species-specific sensitivity of MCP was not made.

2.2.4 Photoelectron spectroscopy

Photoelectron spectra are derived from photoelectron images recorded using the velocity map ion imaging setup with negative voltages applied to Repeller and Extractor electrodes. The data analysis of photoelectron images is analogous to that for ion imaging.

Due to features in the design of the imaging setup, when the copper surfaces of the flight tube are exposed to scattered laser light, background-free photoelectron images can be obtained only at frequencies below ≈ 35 000 cm^{-1}. This value is close to the work function of copper of 37 900 cm^{-1} [95]. The scattered laser light can create parasitic photoelectrons which then can be projected together with the photoelectrons of interested onto the detector. At higher frequencies than ≈ 37 000 cm^{-1} the background photoelectrons are dominant. In an attempt to reduce this parasitic background, the two-color ionization scheme was sometimes employed when appropriate. In this scheme the pulse energy of the excitation laser, which had frequency close to the work function, was reduced in order to lower the background. At the same time, the frequency of ionizing laser was kept essentially lower than the copper workfunction. The drawback of using two lasers instead of one is the non-perfect timporal and spacial alignment between two laser beams, which potentially decrease the signal level.

2.2.5 ZEKE spectroscopy

The main principle of zero electron kinetic energy (ZEKE) spectroscopy is to select electrons in high Rydberg (HR) states confined in the potential of the positive charge just below the ionization threshold (IT) instead of analyzing the kinetic energies of photoelectrons that overpass it. First demonstrated by Muller-Dethlefs and coworkers in 1984[96], the technique is now a widely used laboratory tool[97].

To illustrate the principles of ZEKE we will use the simplest model, that of the hydrogen atom. In this case the potential is Coulombic and is written as:

2.17 $$V_C(r) = -\frac{1}{4\pi\varepsilon_0}\frac{q}{r}$$

where ε_0 is dielectric permeability of vacuum, q is the charge and r is the electron-ion distance. The electronic energy levels in the above potential scales as[98]:

2.18 $$E_n = -\frac{Ry}{n^2}$$

where Ry=109 737 cm^{-1} is the Rydberg constant[99] and the positive integer n is the principle quantum number. The Rydberg states, which lie approximately within 10 cm^{-1} (n > 100) below the ionization threshold, possess special characteristics[100].

First, the HR states are very fragile and can be easily ionized by an external electric field with the strength of several V/cm. In the uniform electric field with the strength F , the potential 2.17 becomes:

2.19 $$V(r) = -\frac{1}{4\pi\varepsilon_0}\frac{q}{r} + Fqr$$

The saddle point formed in the potential, see Figure 2.3, lowers the ionization threshold and destroys the HR states down to the energy E_S which is expressed in [cm^{-1}] as:

2.20 $$E_S = 6.1\sqrt{F}$$

where F is in V/cm.

Second, the radiative life time of these HR states, which normally scales as n^3[98], starts to scale as n^5 and attains several tenths of microseconds. This enhancement of the life time was explained by Chupka[101] as state mixing between adjacent HR states due to the stray electric fields.

The standard scheme of ZEKE exploits the long life time of HR states and their field ionization. In short, the procedure is the following. Atoms or molecules are photoexcited to HR states under the field-free conditions. The HR states which survived after typical time delay of several microseconds are ionized by a pulsed electric field. The direct photoelectrons leave the ionization volume during the

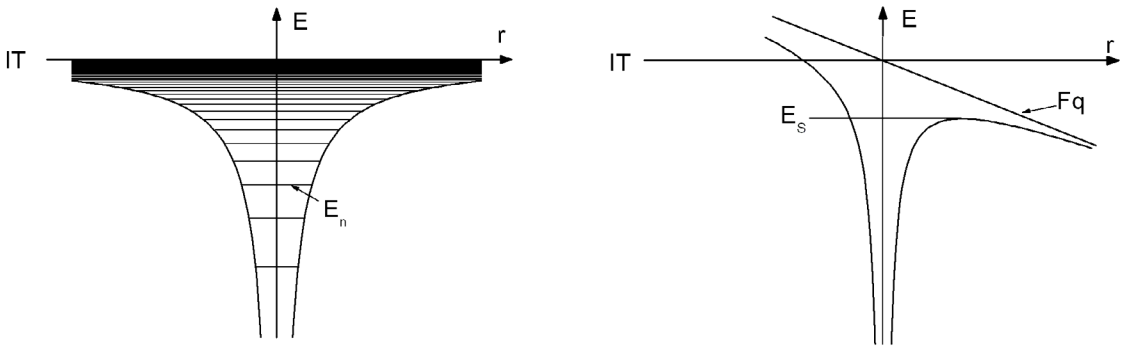

Figure 2.3: Left panel: Coulomb potential with energy levels. Right panel: modification of the Coulomb potential by an external uniform electric field.

time delay and can be easily discriminated from the electrons produced by field ionization. The field strength determines the energy resolution. Classically, the resolution ΔE is defined by the energy of the saddle point in expression 2.20. More realistic considerations, which take into account the tunneling through the potential barrier, yield [102]:

2.21 $$\Delta E = 4.6\sqrt{F}$$

where F as before in V/cm and ΔE is in cm^{-1}. In the following we will use the classical expression 2.20 for the estimation purposes.

Table 3 Resolution in ZEKE experiments

Repeller voltage [V]	Resolution [cm^{-1}]	System studied
0.5	1.5	Na(3p)-He
4	5	Na^+-He_N
30	25	$Aniline^+$-He_N

In our imaging setup, it is possible to perform ZEKE spectroscopy, though the setup was not initially conceived for this. The field ionization is done by applying to the Repeller electrode the output from the Stanford SRS 535 delay generator, which produces voltage pulses with the amplitude in the range of -4÷0 V with 0.01 V precision. The typical time delay is 1 μs. The Extractor electrode is kept grounded. The selection of the direct and ZEKE electrons is effectuated by appropriate gating of the Front MCP electrode. The field strengths used in experiments and achieved resolutions are presented in Table 3.

2.2.5.1 Ion yield spectrum

The ionization threshold can be probed by scanning the excitation frequency and detecting the photoions under the field-free conditions. In principle, this technique will yield a step in the ion outcome versus frequency which marks the ionization threshold. If one takes the derivative of the ion yield versus frequency then the step at the ionization threshold will produce a peak. Thus, a ZEKE spectrum represents a derivative of the ion yield spectrum[97]. The advantage to monitor the ion yield is to get additional mass-specific information, which often helps to disentangle complex ZEKE spectrum. Below we will illustrate this statement.

We consider the ideal case when a specie with closely lying ITs is photoexcited with varying frequency. The total outcome of photoelectrons or ions is measured under the field-free conditions in order to avoid lowering of the IT, see upper graph in Figure 2.4. In the spectrum, there will be a step at the position of each IT and the signal level will be increased every time when the frequency will reach the next threshold. If the same region will be scanned using the ZEKE method then, just below an IT, there will be a peak in the signal. As was explained in the previous section, the width of this peak is determined by the resolution that depends on the strength of the ionizing pulsed electric field. Basically, the resolution in the ZEKE may be considered as delta-function centered on the IT, provided that the pulsed-field is infinitely small. A broad ionization threshold we can represent as a sum of elementary ITs, each of them having its elementary step in the direct photoion yield spectrum and its elementary peak in the ZEKE spectrum. The sum of these elementary steps in the ion spectra and peaks in the ZEKE spectrum will result in the broad feature.

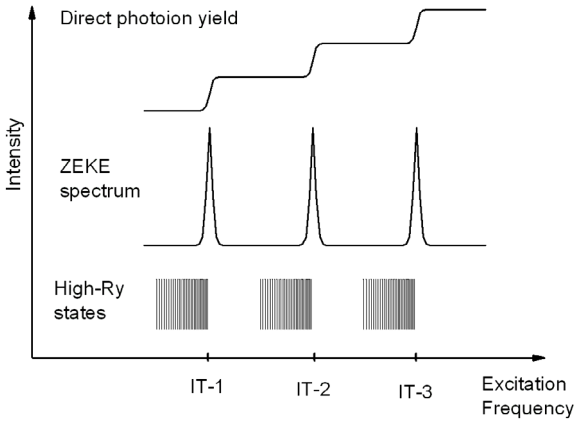

Figure 2.4: Scheme illustrating the equivalence of the integrated ZEKE spectrum to the ion yield spectrum.

In practice, one needs an accelerating electric field in order to efficiently detect ions. Therefore a delayed pulsed electric field is applied immidiately after the photoexcitation. In this case, due to much heavier masses of ions with respect to electrons, both direct photoions and the ions produced by the pulsed field ionization of species in HR states are detected. The implication of such approach is the broadening of the step in the ion yield spectrum that represents the IT. The field strength determines the width of this step via expression 2.20. Thus, the ion yield spectrum allows to detect an IT but with low energy resolution. We used this scheme of pulsed field ionization to record an ion-specific yield spectrum of a particular species, when the mass-selected variant of the ZEKE (MATI) was not efficient due to the presumably short lifetime of created HR states.

In a typical experiment, Repeller and Extractor voltages of +4 000V and +2 812V are applied, with a delay of 200 ns after the laser excitation of species. The voltages correspond approximately to a field strength 1 485 V/cm if the field between the electrodes is uniform. The Front MCP is gated on the species of interest. The short delay time of 200 ns, compared to 2 μs used in MATI-based technique described in the next section, allows us to observe, though at low energy resolution, the IT of species with the life times shorter than 1 μs, see sections 3.1.1.3 and 3.4.2.2.

2.2.6 MATI spectroscopy

The ZEKE method does not provide species-specific information, since the detected ZEKE electrons can originate from different excited atoms or molecules. The mass-resolved variant of ZEKE, mass analyzed threshold ionization or MATI, uses the same philosophy of separating the direct photoions from the species in HR states. It was proposed by Zhu and Johnson in 1991[103] who used a weak constant external field of several V/cm to discriminate photoionized species from neutral in HR states. The last were ionized by pulsed field after the delay of several microsecond. The resolution of MATI is the same as in the case of ZEKE and is determined by the strength of the pulsed field.

In our experiments we used the technique based on MATI to selectively detect species in different intermediate excited states, see section 3.1.1 and Ref[104]. In order to provide the constant field for discriminating the direct ions the Repeller voltage was kept fixed at +500 V and the voltage on the Extractor electrode was set to +370 V during photoexcitation. This was returned to +352 V, which corresponds to normal conditions for ion imaging, after a 2 μs time delay. The ions produced by the pulsed-field ionization were selected by gating the Front MCP electrode. The achieved resolution

was 3 cm^{-1}, which is smaller compared to value obtained with expression 2.20. The observed deviation may be attributed to the non-uniform electric field in the ionization volume.

Chapter 3 : Excited states dynamics of Na-doped helium nanodroplets

3.1 Low excited states

In this section we present the experimental data on the dynamics of sodium atoms attached to helium droplets excited to the lower (3p, 4s 3d and 4p) excited states. Excitation spectra, photoelectron spectra, relative abundance of photoproducts and their velocity distributions obtained in the experiments are rather regular and correlate to a particular excited state of the free Na atom. We interpret the observed features with a number of simple models that allow to explain qualitatively most of the data.

3.1.1 3p-band

3.1.1.1 Excitation spectrum

We start the presentation of the experimental results with the excitation spectrum. The Figure 3.1 presents excitation spectra recorded by detecting the fragments with masses of Na, NaHe, $NaHe_2$ and all possible fragments together. All spectra were recorded by scanning the frequency of the excitation laser within the frequency of 16 900-17 450 cm^{-1} while the frequency of the second ionizing laser was kept fixed at 25 157 cm^{-1}. The $NaHe_3$ and $NaHe_4$ complexes were also detected, but their signal levels were too weak to record excitation spectra with sufficient signal-to-noise (S/N) ratio. We will call the excitation spectrum, corresponding to the detection of all fragments together, a total excitation spectrum. It was recorded by detecting ionized species with 100 μs width of voltage pulse applied to the Front MCP, which comprised the arrival times from Na ion up to arrival times of fragments with masses corresponding to helium nanodroplets with attached sodium ions. The excitation spectra recorded by detecting individual fragments we will call according to a fragment's composition, for example, Na excitation spectrum. They were recorded with the gating of the Front MCP of the detector with a 150 ns voltage pulses with the appropriate time delay.

The energy of the second photon was sufficient to ionize not only sodium atoms in the 3p states but also any Na(3p)-He_N complexes that are formed. At the same time, this frequency was almost not absorbed by single sodium atoms on the nanodroplets. The non-zero background visible in the total and Na spectra is due to the two-photon ionization of sodium dimer by the 25 157 cm^{-1} frequency. This was specially verified in the additional experiment, where the excitation spectrum was recorded by scanning the frequency of the second laser and monitoring Na_2^+ ions.

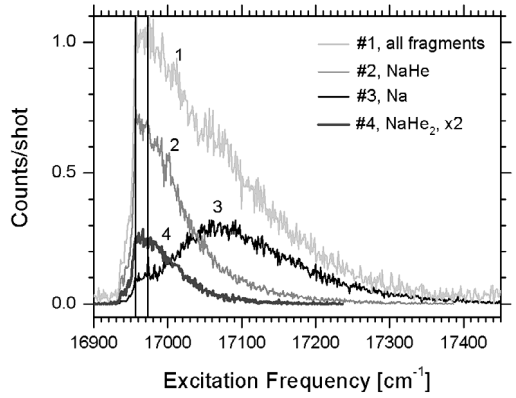

Figure 3.1: Excitation spectrum of Na-He_N with the mean droplet radius <r> = 41 Å recorded by monitoring bare Na atoms, NaHe, $NaHe_2$ and all products. The ionization frequency is 25 157 cm^{-1}. The vertical lines indicate the positions of the atomic $3p\ ^2P_{1/2,3/2} \leftarrow 3s\ ^2S_{1/2}$ transitions.

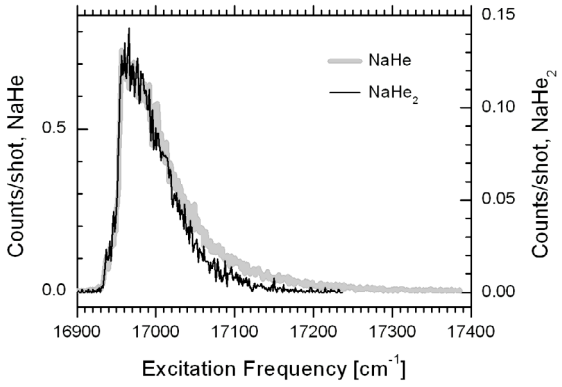

Figure 3.2: Comparison of the excitation spectra recorded by monitoring NaHe and $NaHe_2$ from Figure 3.1.

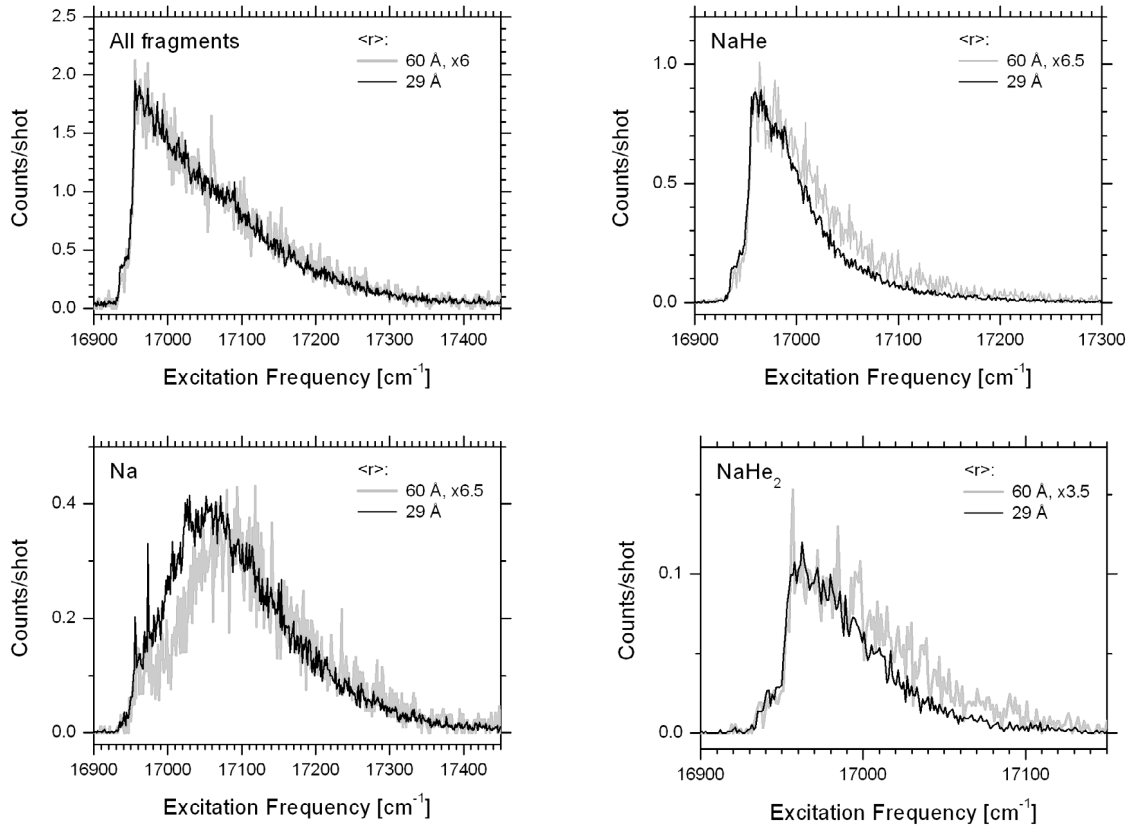

Figure 3.3: Comparison of excitation spectra of Na-He_N with <r> = 29 Å and <r> = 60 Å recorded by monitoring bare Na, NaHe, $NaHe_2$ and all fragments. The ionization frequencies are 25 157 cm^{-1} and 25 641 cm^{-1} for the spectra recorded at <r> = 29 Å and <r> = 60 Å, respectively.

Inspection of the individual spectra in Figure 3.1 reveals two distinct regions in the total excitation spectrum: the maximum in the total spectrum is mainly due to NaHe with a small contribution of $NaHe_2$, while the tail originates exclusively from bare sodium. The comparison of the excitation spectra of NaHe and $NaHe_2$ in Figure 3.2 demonstrates their almost identical shapes. The shape of our total excitation spectrum corresponds to those obtained with laser induced fluorescence[69] and beam depletion[68] techniques. We extended the measurements up to 17 450 cm^{-1} of the excitation frequency, compared to approximately 17 250 cm^{-1} , reported in Ref[69]. The decomposition of the total excitation spectrum in our experiments coincides with previous results obtained with LIF measurements in Ref[69] if one considers the NaHe excitation spectrum to be equivalent to "bound-bound" transition and the Na excitation spectrum to be equivalent to "bound-free" transition. The ratio of peak intensities between NaHe and Na excitation spectra in our measurements is different from that between "bound-bound" and "bound-free" transitions observed with LIF, which might be due to the saturation of the transition with 0.7 mJ/cm^2 of fluence of the excitation laser, see also section 3.1.5.1.6.5. The unresolved peak structure in the region of 3p $^2P_{1/2,3/2}$←3s $^2S_{1/2}$ gas-phase sodium transitions in Figure 3.1 may be the evidence of saturation, since previously Stienkemeier et al.[69] have observed two peaks in LIF experiments using much lower laser fluences.

The ”bump” in the sodium excitation spectrum at ≈ 16 965 cm^{-1}, which corresponds to the maximum of the total excitation spectrum, is caused by the dissociative ionization of NaHe and $NaHe_2$. This “bump” is absent in excitation spectra recorded with the state-selective detection of desorbed bare sodium atoms in 3p $^2P_{1/2}$ and 3p $^2P_{3/2}$ states, see the sub-section 3.1.1.1.1 below.

The shape of the total excitation spectrum in our experiments does not practically depend on the mean droplet sizes in the range of <r> = 27 - 60 Å used in our experiments, see Figure 3.3. This might be due to the saturation of transition, as noted above, and the unsufficient S/N ratio. In contrast to the total excitation spectrum, the Na, NaHe and $NaHe_2$ spectra demonstrate some variations. The Na excitation spectrum shifts by ≈ 20 cm^{-1} to the higher frequencies in going from the smallest droplets with <r> = 29 Å to the biggest with <r> = 60 Å. The NaHe and $NaHe_2$ excitation spectra become wider by 20 cm^{-1} at FWHM, but their maxima do not shift within the signal-to-noise ratio achieved in our experiments.

The excitation spectra of Na-He_N recorded in the group of Scoles using LIF[69], which can be considered as an analogue to the total excitation spectrum in our experiments, showed weak droplet size dependences. At larger droplet sizes they had longer blue-shifted tails. This discrepancy with our findings we explain by saturation effects and unsufficient S/N ratio in the experiments. Scoles and coworkers also recorded the excitation spectrum by detecting only red-shifted emission from NaHe exciplexes, but did not report on its droplet size dependence.

3.1.1.1.1 State-selective excitation spectra of Na

With MATI-based state-selective ion imaging, see Chapter 2, we were able to implement ion imaging of the desorbed Na atoms in 3p $^2P_{1/2}$ or 3p $^2P_{3/2}$ states, see section 3.1.1.4 below. To carry out the state-specific ion imaging of desorbed sodium atoms, we first need the information about excitation frequencies of Na-He_N which result in the desorbtion of Na atoms in a particular spin-orbit (SO) state.

The excitation spectra recorded by detecting Na atoms desorbed from the surface of helium nanodroplets in 3p $^2P_{1/2}$ and 3p $^2P_{3/2}$ states are presented in Figure 3.4. Even though the spectra have different intensities and positions, their shapes are essentially the same. This can be seen in Figure 3.5, where spectra are scaled to the same intensity and shifted in frequency in order to facilitate their

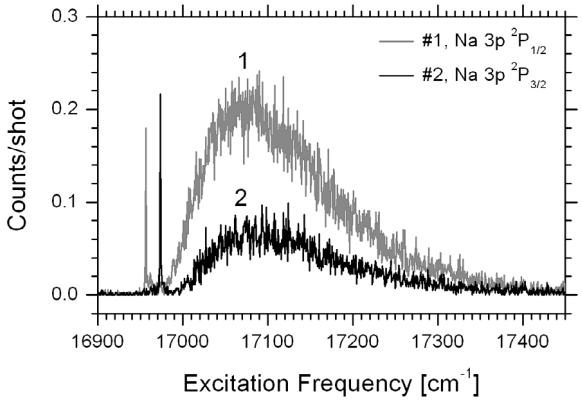

Figure 3.4: Excitation spectrum of Na-He_N with <r> = 41 Å recorded with the state-selective detection of Na atoms in the 3p $^2P_{1/2}$ and 3p $^2P_{3/2}$ states. The fluence of the laser light is 0.7 mJ/cm^2.

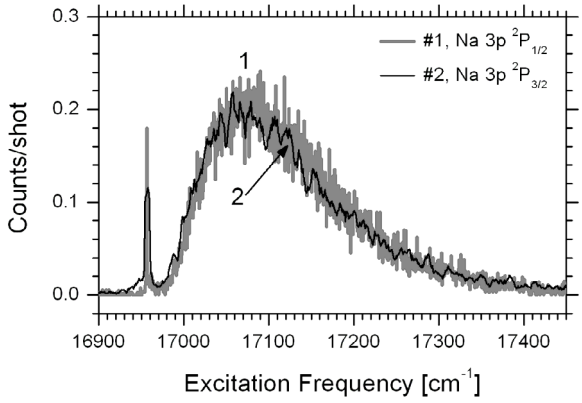

Figure 3.5: Comparison of the shape of two spectra from Figure 3.4. The 3p $^2P_{3/2}$ spectrum was smoothed, multiplied by 3 and shifted by 17 cm^{-1} to the red in order to show that its shape coincides with the 3p $^2P_{1/2}$ spectrum.

comparison. The shift used is ≈ 17 cm^{-1}, which is the same as the SO splitting in 3p state of Na[99]. The droplet size dependences of Na excitation spectra are similar for both atomic spin-orbit states: with the increase in droplet size the spectra shift towards higher frequencies, while keeping essentially the same shapes. The comparison of excitation spectra of Na-He_N with <r> = 27 Å and <r> = 60 Å recorded by detecting Na atoms in the 3p $^2P_{1/2}$ state is presented in Figure 3.5. The overall shift between two spectra is ≈ 20 cm^{-1}. It is interesting to compare the droplet size dependence of the normal, see Figure 3.3, and state-resolved, see Figure 3.6, Na excitation spectra. In the case of normal spectra it is the red part of the spectrum in the region of 16950-17100 cm^{-1} that shifts, while the state-resolved spectra clearly show that it is the whole spectrum that shifts. The possible explanation may be the different relative intensities of the spectra: the Na(3p $^2P_{3/2}$) spectrum is three times weaker that the Na(3p $^2P_{1/2}$). Furthermore, the latter spectrum is constantly shifted by ≈ 17 cm^{-1} towards low frequencies with respect to the Na(3p $^2P_{3/2}$) spectrum. Therefore, in the normal Na spectrum the most pronounced droplet size effect, which is observed as the shift of the red part of the spectrum, originates from the shift of the strongest Na(3p $^2P_{1/2}$) component. This effect is thought to be less visible in the tail of the spectrum due to the less favorable S/N ratio.

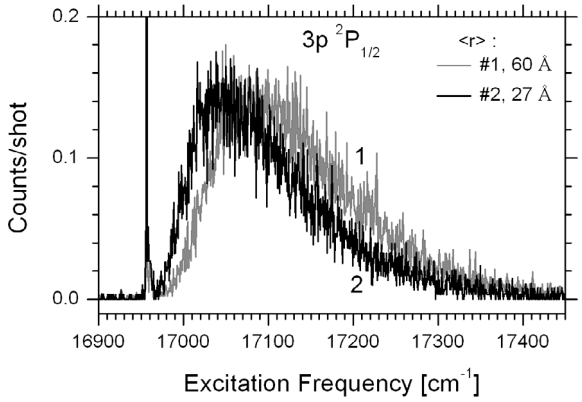

Figure 3.6: Comparison of excitation spectra of Na-He_N with <r> = 27 Å and <r> = 60 Å recorded with the state-selective detection of desorbed Na atoms in the 3p $^2P_{1/2}$ state.

3.1.1.2 Time-of-flight mass spectra

The total excitation spectrum of Na atoms on the surface of helium nanodroplets shows several contributions due to the formation of $NaHe_n$ complexes on the cluster surface. It also reveals the weak dependence of individual exciplex excitation spectra on the mean droplet size. However, a direct comparison of intensities in the excitation spectra in order to obtain the relative abundances of species is not possible, since each spectrum was acquired separately, meaning at different experimental conditions. Furthermore, the voltages on the MCP electrodes used for velocity map ion imaging are not the most optimal in terms of the sensitivity and time-of-flight resolution. In order to obtain relative abundances of the species formed, TOF mass-spectra were recorded using the multi-channel scaler. In this case, the voltages applied to the electrodes were optimized to provided better sensitivity and TOF resolution, see Chapter 2. An example of a TOF mass-spectrum recorded following 17 007 cm^{-1} excitation of Na-He_N with <r> = 41 Å in the range of 20-50 atomic mass units (amu) is presented in Figure 3.7. A second photon of 41 227 cm^{-1} was used to ionize the desorbed species. The assignment of the peaks in the TOF spectrum is straightforward with the separation between peaks of 4 amu, which equals to the mass of helium atom. The first peak corresponds to the mass of 23 amu, which is the mass of the bare Na atom. The second peak with the mass of 27 amu corresponds to NaHe. The following three peaks are $NaHe_2$, $NaHe_3$ and $NaHe_4$, respectively. $NaHe_n$ exciplexes with n>4 were not detected, which is in line with the findings of Enomoto and coworkers[105], who investigated the Na(3p)-He_n, n=1-4, formation in cold He gas by exciting laser ablated Na atoms to the 3p state and analyzing the following light emission from the created exciplexes.

The evolution of the relative abundances of Na-$NaHe_4$ fragments with excitation frequency is presented in Figure 3.8. This variation of relative abundance represents a sort of excitation spectrum with coarse resolution. The overall trend in relative abundances of Na-$NaHe_2$ fragments follows that of the excitation spectrum: close to 17 000 cm^{-1} the main contribution comes from NaHe, while the contributions of Na and $NaHe_2$ are about 10% each. At higher excitation frequencies bare sodium atoms dominate. In the 16 950 - 17 000 cm^{-1} region, the rising relative abundance NaHe arrives at its maximum. The evolution of Na abundance is opposite to that of exciplexes. This depletion of the $NaHe_n$, n = 1 - 4, in favor of Na may be attributed to the dissociative ionization of $NaHe_n$ exciplexes, which was observed in the same frequency region in THE excitation spectra presented in section 3.1.1.1.

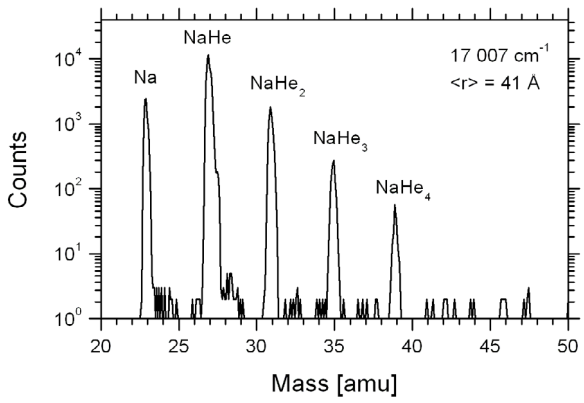

Figure 3.7: Time-of-flight mass spectrum recorded following 17 007 cm^{-1} excitation of Na-He_N with <r> = 41 Å. The ionization frequency is 41 227 cm^{-1}.

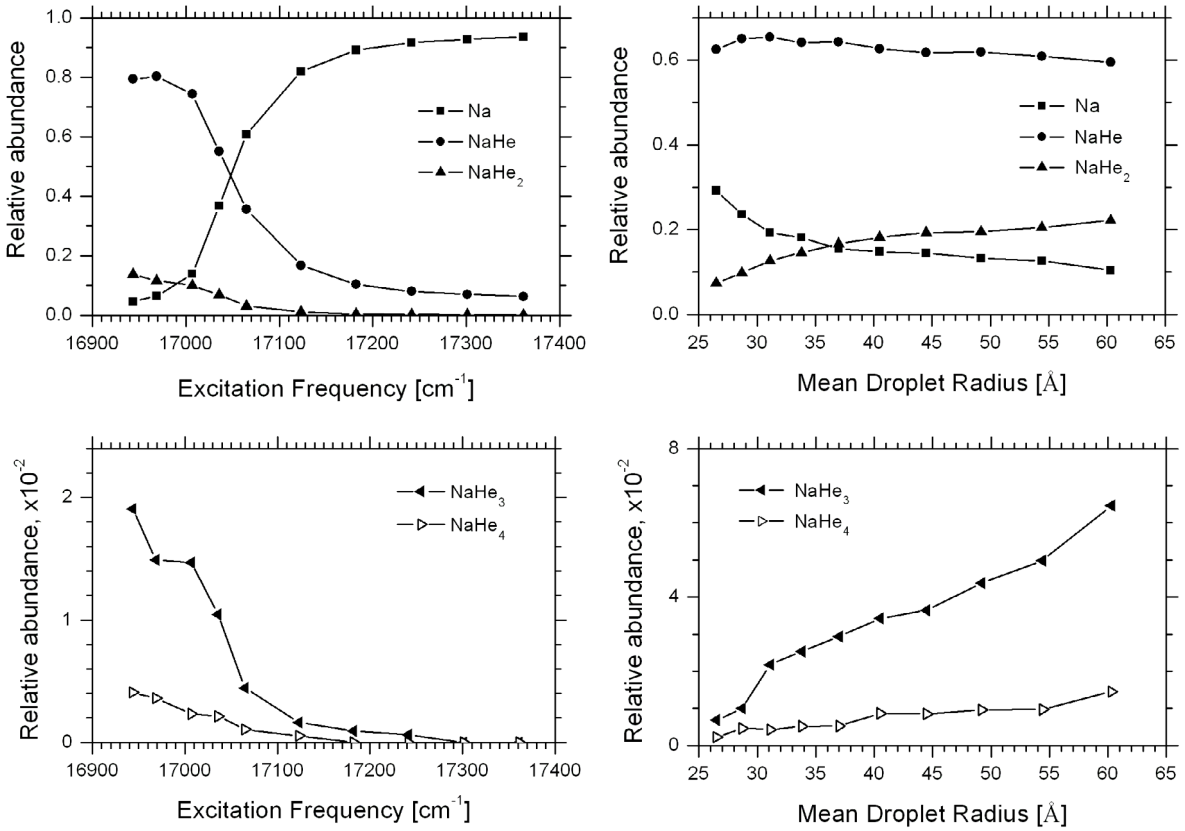

Figure 3.8: Upper panel: relative abundance of desorbed Na, NaHe and $NaHe_2$ after the excitation of Na-He_N at different frequencies. Lower panel: relative abundance of desorbed $NaHe_3$ and $NaHe_4$. The mean droplet radius is 41 Å. The ionization frequency is 41 227 cm^{-1}. The lines through the data points are to guide the eye.

Figure 3.9: Upper panel: relative abundance of desorbed Na, NaHe and $NaHe_2$ after the excitation of Na-He_N at 17 002 cm^{-1} at different mean droplet sizes. Lower panel: relative abundance of desorbed $NaHe_3$ and $NaHe_4$ are shown at enlarged scale. The ionization frequency is 26 846 cm^{-1}. The lines through the data points are to guide the eye.

The $NaHe_3$ and $NaHe_4$ complexes are readily detectable, see lower panel in Figure 3.8. One can see, by comparing the two graphs, that their coarse excitation spectra are similar to those of NaHe and $NaHe_2$. The contributions of $NaHe_3$ and $NaHe_4$ together are inferior to 2% of the total number of desorbed fragments.

To check the droplet size dependence of exciplex formation, TOF mass spectra were recorded at different mean droplet sizes following 17 002 cm^{-1} excitation and 26 846 cm^{-1} ionization steps. The excitation frequency was chosen such that to have all discovered complexes in the largest possible quantity for better counting statistics. The energy of ionization photon was lowered from 41 227 cm^{-1} to 26 846 cm^{-1} in order to reduce the fragmentation upon ionizing the exciplexes. Indeed, the effect of lowering the ionization energy could be observed. Tthe relative abundances of $NaHe_n$, n = 2-4, exciplexes increased by a factor of two while the NaHe abundance decreased by 0.2 from ≈ 0.8 to ≈ 0.6, see Figure 3.8 and Figure 3.9. It could be interesting to note that the contribution of bare Na atom did almost not change, while the decrease in the abundance of NaHe by ≈ 0.2 is approximately equal to the sum of increases in the abundances of $NaHe_n$, n = 2-4. This might mean that NaHe ions are formed by dissociative ionization of largerer $NaHe_n$, n = 2-4, exciplexes.

As can be seen in both panels in Figure 3.9, the bigger the mean droplet radius of helium droplets is the more of $NaHe_2$, $NaHe_3$ and $NaHe_4$ complexes are formed. At the same time, the abundances of bare Na atoms and NaHe complex are reduced.

Large $NaHe_n$, n>4, exciplexes and products with masses of the order of $1 \cdot 10^4$ amu, corresponding to helium nanodroplets with attached Na(3p) atoms, were not detected in our experiments.

3.1.1.3 Photoelectron and ZEKE spectra

The Na state-resolved excitation spectra have provided information on the spin-orbit state distribution of desorbed bare Na atoms. Additional information can be provided by photoelectron spectroscopy (PE), which is used here to probe state distributions of all created species. To achieve good energy resolution, photoelectron images were recorded at an ionization frequency of 25 157 cm^{-1} Figure 3.10 shows photoelectron images recorded following 16 995 cm^{-1} and 17 118 cm^{-1} excitation of Na-He_N with <r> = 41 Å. Already the raw image obtained at 16 995 cm^{-1} excitation frequency reveals two contributions in the photoelectron yield visible as two rings. In contrast, the image corresponding to 17 118 cm^{-1} excitation demonstrates only one ring. By applying inverse Abel transformation, the corresponding photoelectron spectra can be obtained, see Figure 3.11. These two spectra are obviously different and they reflect the composition of the desorbed fragments revealed by excitation spectra and TOF mass spectra. The photoelectron spectrum recorded following 17 118 cm^{-1} excitation is dominated by the peak near 700 cm^{-1} that can be unambiguously assigned to 3p states of bare Na atoms, since the ionization of bare Na atoms in 3p states at this frequency will produce photoelectrons with ≈ 680 cm^{-1} of kinetic energy. Indeed, the excitation spectra recorded by detecting bare Na atoms and NaHe complex have shown that the main outcome at ≈ 17 118 cm^{-1} excitation is bare sodium atoms.

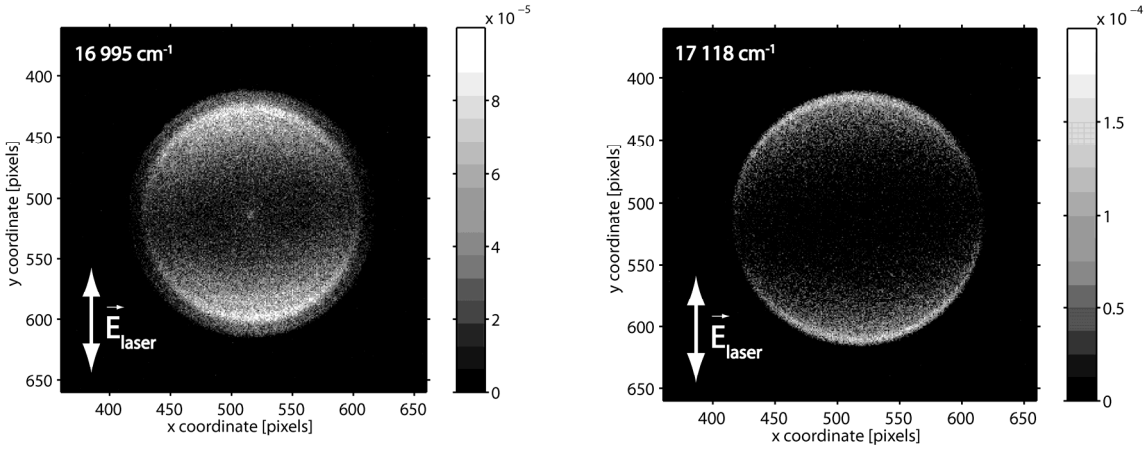

Figure 3.10: Photoelectron images recorded following 16 995 cm^{-1} and 17 118 cm^{-1} excitation of Na-He_N with <r> = 41 Å. The ionization frequency is 25 157 cm^{-1}. The images show the central part of 300x300 pixels of the full frame consisting of 1000x1000 pixels. The images are normalized by the maximum number of counts per pixel. The total numbers of counts are $2.3 \cdot 10^5$ and $9.8 \cdot 10^4$ for the left and the right images respectively. The gradient bars on the right show the corresponding intensity scales.

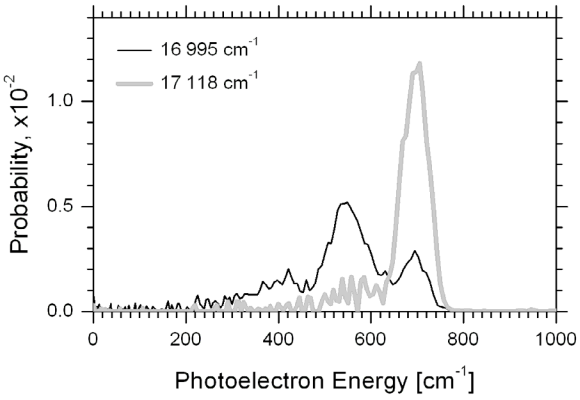

Figure 3.11: Photoelectron spectra derived from photoelectron images in the Figure 3.10 recorded following excitation of Na-He_N with a mean radius of 41 Å at excitation frequencies of 16 995 cm^{-1} and 17 118 cm^{-1}. The ionization frequency is 25 157 cm^{-1}.

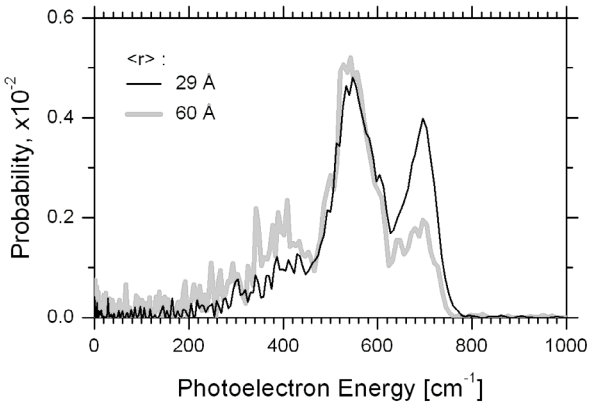

Figure 3.12: Photoelectron spectra derived from photoelectron images recorded following excitation at 16 995 cm^{-1} of Na-He_N with a mean radius of 60 Å and 29 Å. The ionization frequency is 25 157 cm^{-1}.

TOF mass spectra have demonstrated that bare Na atoms constitute more than 60% of the created species at that excitation frequency. The resolution of the PE spectrum does not allow for resolving two possible spin-orbit states of Na(3p) separated by only 17 cm^{-1}[99].

The photoelectron spectrum following 16 995 cm^{-1} excitation reveals another two prominent peaks centered at ≈ 420 cm^{-1} and at ≈ 550 cm^{-1} , the latter being the strongest. As has been previously demonstrated, excitation near 16 995 cm^{-1} leads to the desorption of mainly NaHe with appreciable contributions from bare Na atoms and $NaHe_2$. To confirm the assignment of the peaks at ≈ 550 to NaHe and that of at ≈ 420 cm^{-1} to $NaHe_2$, the photoelectron spectra following 16 995 cm^{-1} excitation were recorded at different droplet sizes, see Figure 3.12. It is clearly visible that at larger droplets the peak at ≈ 700 cm^{-1}, assigned to bare Na atoms, is reduced, while that of $NaHe_2$ at ≈ 420 cm^{-1} is enhanced. At the same time, the NaHe peak at ≈ 550 cm^{-1} stays almost unchanged. This behavior of the assigned photoelectron peaks is in accordance with the relative abundances of exciplexes in the TOF mass spectra presented in Figure 3.9. It is difficult to quantitatively characterize the relative intensities of the photoelectron peaks, since they are not clearly separated from one another. This is why we make only a tentative assignment of the non-zero signal in photoelectron spectra at energies lower than 300 cm^{-1} to $NaHe_3$ and $NaHe_4$ complexes.

The peaks in photoelectron spectra corresponding to NaHe and $NaHe_2$ complexes are broader than the experimental resolution, which might reflect unresolved rovibrational structure of the desorbed exciplexes. Therefore, it was decided to use a ZEKE detection scheme, which allows for recording spectra with much higher resolution, see Chapter 2. The ZEKE spectrum of the desorbed $NaHe_n$, n=1-4, is shown in the middle panel in Figure 3.13, and the corresponding photoelectron spectrum in the upper panel. The extension of the ZEKE spectrum to lower frequencies is demonstrated in Figure 3.14. The ZEKE spectra were recorded by fixing the excitation frequency and scanning the ionization frequency from the second laser. The non-zero background in the spectrum originates from electrons produced by the direct ionization of species by the second laser. The intensities in ZEKE spectra depend on many factors. In the presented ZEKE spectrum the correction for the variations of laser power has not been carried out, so the intensities are convoluted by the

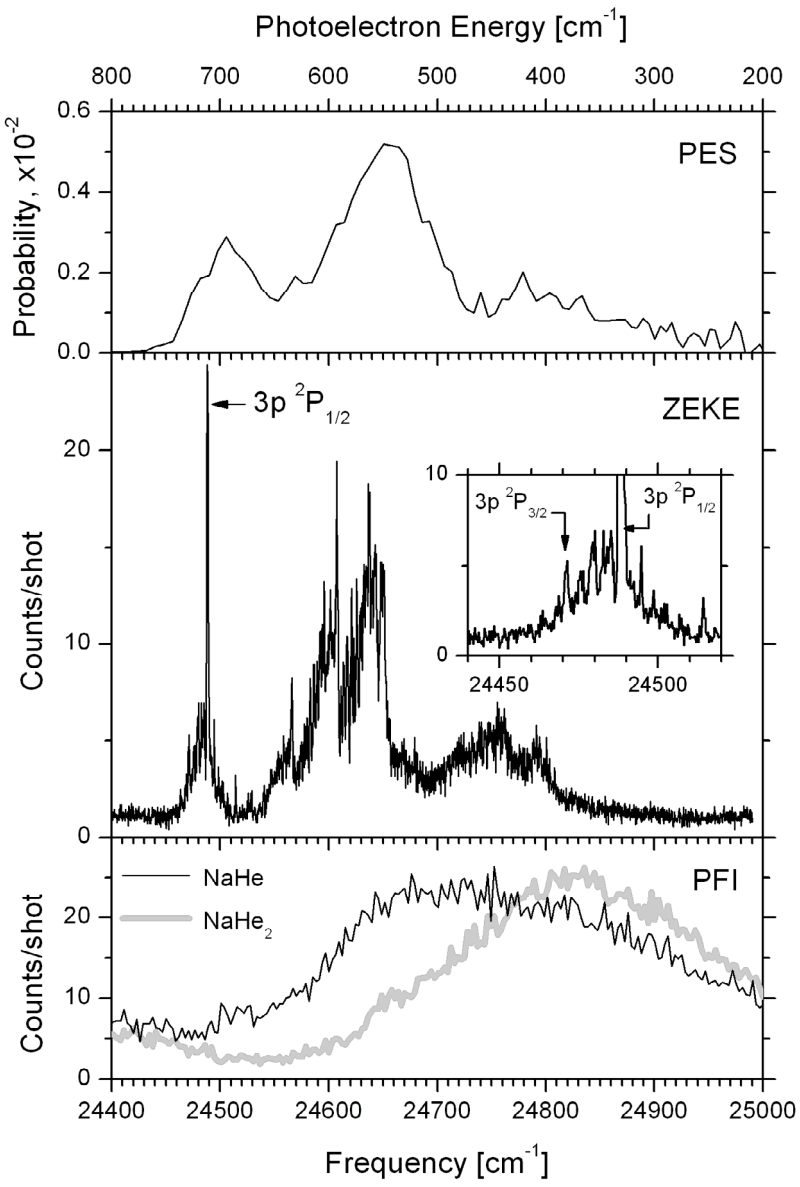

Figure 3.13: ZEKE spectrum of Na-He_N with <r> = 41 Å recorded following excitation at 17 000 cm^{-1} (middle panel) and corresponding photoelectron spectrum recorded following 16 995 cm^{-1} excitation (upper panel). The insert shows the region corresponding to the ionization of Na 3p spin-orbit states at an enlarged scale. The lower panel shows ion yield spectra of NaHe and $NaHe_2$ recorded using a pulsed field of 371 V/cm. The mean droplet sizes are 41 Å for NaHe and 26 Å for $NaHe_2$.

power variations of the second laser. In addition, the intensities in ZEKE spectrum depend on the species being probed since the lifetime of Rydberg states in molecular systems are generally affected by non-radiative processes[102]. This implies that the observed line intensities in the ZEKE spectrum may not reflect the real state distributions.

The high resolution ZEKE spectrum reveals that broad peaks in the photoelectron spectrum consist of several narrower overlapping peaks. The sharp intense line at 24 488 cm^{-1} corresponds to the ionization of bare Na atoms in 3p $^2P_{1/2}$ state. Closer inspection of the spectrum shown in the insert of the middle panel in Figure 3.13 reveals a weak peak at 24 471 cm^{-1} corresponding to the 3p $^2P_{3/2}$ state of Na. The frequency of the ZEKE peak corresponding to 3p $^2P_{1/2}$ and 3p $^2P_{3/2}$ states of Na are 5 cm^{-1}

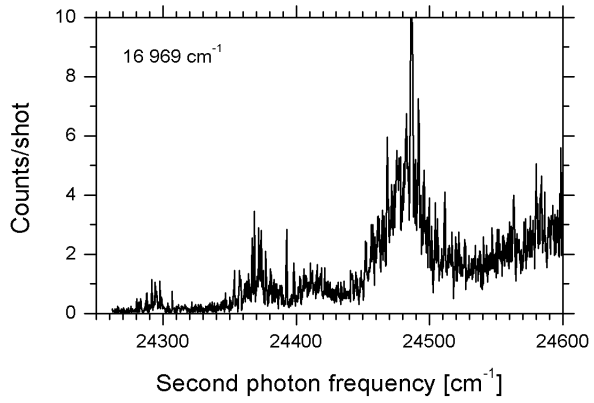

Figure 3.14: Two-color ZEKE spectrum that demonstrates the lowest frequency features and the best resolution of 1.2 cm^{-1} achievable in our setup with the lowest possible strength of 0.25 V/cm of the pulsed electric field. The excitation frequency is 16 969 cm^{-1}.

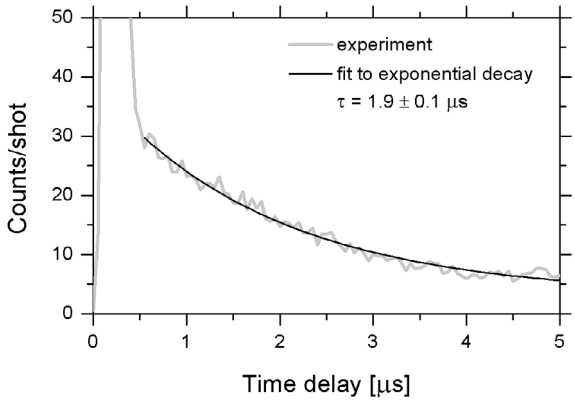

Figure 3.15: The scan of the time delay between the pulsed field ionization and the photoexcitation in the ZEKE of Na-He_N with <r> = 41 Å: the first excitation at 16 964 cm^{-1} is followed by the second excitation at 24 638 cm^{-1}.

below the values of 24 493 cm^{-1} and 24 476 cm^{-1} calculated from the tabulated energies[99] of 3p excited state and the ionization potential of Na atom. This discrepancy can be assigned to the lowering of the ionization threshold by pulsed electric field. This lowering can be estimated with the classical expression 2.20, taking into account the strength of the pulsed field of 0.6 V/cm used to record the spectrum in the middle panel of Figure 3.13. The obtained value of 4.7 cm^{-1} corresponds well to the experimental observations.

In order to disentangle the ZEKE spectrum of Na-He_N into NaHe- and $NaHe_2$-specific features we recorded the corresponding Na^+He and Na^+He_2 ion yield spectra presented at the bottom panel in Figure 3.13. This partially compensates the absence of state-selective exciplex excitation spectra, since the onset in the ion yield spectrum normally correlates to the peak in the corresponding ZEKE spectrum, see section 2.2.5. The choice of different mean droplet sizes, <r> = 41 Å for NaHe and <r> = 29 Å for $NaHe_2$, is based on the relative abundance of $NaHe_2$, see Figure 3.9. The $NaHe_2$ abundance is minimal at smallest droplets, so the Na^+He_2 signal interferes less with that of Na^+He. The signal onset in ion-yield spectra clearly corresponds to the onsets of previously identified NaHe and $NaHe_2$ signals in the ZEKE spectrum at ≈ 24 650 cm^{-1} and at ≈ 24 800 cm^{-1} if one takes into account the ≈ 115 cm^{-1} red-shift of the ionization threshold due to pulsed electric field of 371 V/cm.

The atomic 3p ^2P lines in the ZEKE spectrum in Figure 3.13 originate exclusively from Na atoms desorbed from helium droplets and not from gas phase Na atoms present in the detection region due to effusion from the oven, since the excitation frequency of 17 000 cm^{-1} is out of resonance with the two 3p←3s transitions of free Na. All other sharp lines belong to rovibrational transition between Na*He and Na*He_2 and their corresponding ionic levels. One can see that the main contributions from NaHe and $NaHe_2$ species to ZEKE spectra are still partially overlapped. We have tried unsuccessfully to further separate them with the MATI-based detection scheme also used to record the Na(3p $^2P_{1/2,3/2}$)-specific excitation spectra reported in section 3.1.1.1.1. It is likely that NaHe and $NaHe_2$ in high Rydberg states decay via dissociation within 2 μs, the time delay between excitation and field ionization. The dissociation of molecules in high Rydberg states by their overlap with repulsive states is a well known phenomenon[102]. To check this issue we recorded the level of the ZEKE signal

coming from the pulsed field ionization of exciplexes by varying the time delay between laser excitation and pulsed field ionization, see Figure 3.15. The fitting to the exponential function

3.1 $$f(t) = A\exp(-t/\tau)$$

where t is the time delay, A is the amplitude, yielded a lifetime of $\tau \approx 1.9$ μs. This value is comparable to the time delay used in MATI-based ion detection, see section 2.2.6. It should be also noted that the lifetime of 1.9 μs was measured under essentially field-free conditions, while in the MATI-based technique there is constant static field in the excitation volume. This field is used to separate direct photoions from ions created by pulsed-field ionization, but at the same time the field ionizes otherwise long-living unperturbed high Rydberg states and thus might shorten the experimentally measured lifetimes. So, the lifetime shortening of high Rydberg states of NaHe and $NaHe_2$ by electric field and dissociation may be the cause of the inefficiency of our MATI-based technique to record the state-selective excitation spectra.

3.1.1.3.1 Analysis of ZEKE spectrum

As was shown in the emission analysis[72] of Na(3p)He exciplexes desorbed from the surface of helium clusters, the complexes are mainly residing in the first three vibrational levels v = 0-2 in the electronic 3p $^2\Pi$ molecular states. The population of high vibrational states of NaHe exciplexes indicates a high "rovibrational" temperature. Consequently, the population of rotational levels of each vibrational state should be also considerable. The bands observed in the ZEKE spectrum originate from transitions between these levels and vibrational levels of Na^+-He in the electronic ground state. The rotational constants B for Na(3p)-He and Na^+-He in the vibrational ground states can be estimated from the pair potentials plotted in Figure 3.16 according to the classical expression for rigid rotor:

3.2 $$B = \frac{h^2}{8\pi^2 \mu R_e^2}$$

where $\mu = m_{He}m_{Na}/(m_{He}+m_{Na})$ is the reduced mass of the rotor, R_e is the equilibrium internuclear distance. It is convenient to convert the above formula to have B in cm^{-1} units: $B\left[cm^{-1}\right] = 17.4/\left(\mu R_e^2\right)$, where the reduced mass is in atomic mass units, and the internuclear distance R_e is in Å. The calculated B constants are ≈ 0.97 cm^{-1} for both Na(3p)He and Na^+He, since the equilibrium internuclear distances are practically the same. This leads to a maximal line spacing between rotational transitions of ≈ 2 cm^{-1}. The selection rules are not restricted to $\Delta J = 0, \pm 1$, J stands for the rotational angular momentum, because the electron can also carry angular momentum and only the conservation of the total angular momentum is required. As can be seen from the ZEKE spectrum at the highest resolution of 1.2 cm^{-1} achieved in Figure 3.14, the complex structure of rovibrational transitions is not resolved due to insufficient resolution. In view of all arguments given above and taking into account that Na(3p)-He has two spin-orbit states, we estimate that the resolution of at least 0.1 cm^{-1} is necessary to further unravel the congested ZEKE spectrum we have recorded. Nevertheless, the sharp onsets near 24 565 cm^{-1}, 24 610 cm^{-1}, 24 650 cm^{-1} may mark the transitions between the first three most populated vibrational states of Na(3p)-He and vibrational levels of Na^+-He.

To make qualitative assignment of onsets in the ZEKE spectrum we used pair potentials of Pascale[106] for the Na(3p)He exciplex and the *ab-initio* pair potential of Wright and coworkers[107] for Na^+-He. In Table 4 the relative energies of vibrational levels are presented. They were calculated using the LEVEL 8.0 program of Le Roy[108], which solves the one dimensional radial Schrodinger equation with the Numerov-Cooly algorithm. The potentials are quite similar, having their minima

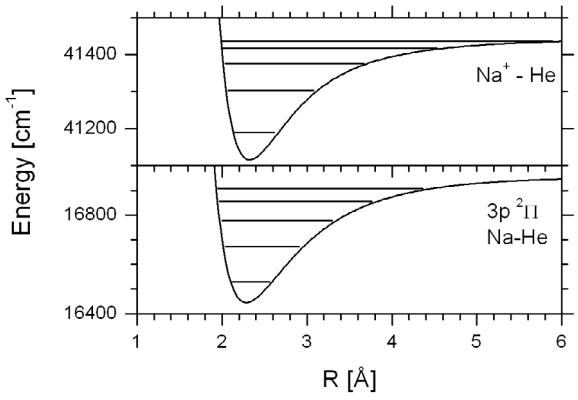

Figure 3.16: Upper panel: Na^+-He pair potential of Wright[107] together with the first five vibrational levels. Lower panel: 3p $^2\Pi$ Na-He pair potential of Pascale[109] together with the first five vibrational levels.

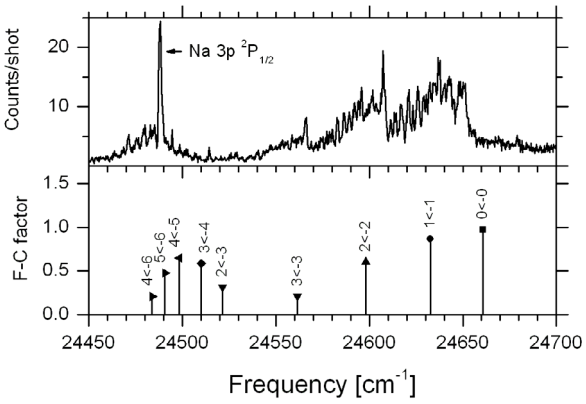

Figure 3.17: Comparison of the ZEKE spectrum from Figure 3.13 and frequencies of the transitions between vibrational levels of Na(3p)-He exciplex in the $^2\Pi$ state and vibrational levels of Na^+-He ion. Franc-Condon factors are shown only if they are lager than 0.2.

near an internuclear distance of R = 2.3 Å. This similarity implies a maximum overlap of vibrational wavefunctions with the same vibrational quantum numbers. As a result, the v'←v" transition probabilities (Franc-Condon factors) are the highest for $\Delta v = 0$ transitions. The Franc-Condon factors larger than 0.2 calculated with LEVEL 8.0 program and the corresponding frequencies of $\Delta v = 0, \pm 1, \pm 2$ transitions with J' = J" = 0 are displayed in the lower panel of Figure 3.17 together with the ZEKE spectrum in the upper panel. The overall agreement between of the calculated transition frequencies with the bands onsets in the ZEKE spectrum is satisfactory.

Table 4 Vibrational levels of Na-He and Na^+-He calculated with LEVEL 8.0

3p $^2\Pi$ Na-He		Na^+-He	
V"	E [cm^{-1}]	V'	E [cm^{-1}]
0	- 426	0	- 255
1	- 284	1	- 141
2	- 177	2	- 69
3	- 10	3	- 28
4	- 49	4	- 9
5	- 18	5	- 2
6	- 3.5	6	- 0.1

3.1.1.3.2 Conclusion

Summarizing the results on ZEKE spectroscopy of $NaHe_n$, n=1-2, exciplexes, we provided an additional evidence, apart from the previous studies with LIF[69], that the exciplexes formed on the surface of helium nanodroplets are desorbed in vibrationally excited states. The insufficient resolution in our experiments did not allow for the separation of single rovibrational lines in the dense spectrum in order to extract parameters of true pair potentials. However, the overall spectrum can be qualitatively modeled with the pair potentials of Na(3p)He[106] and Na^+He[107] available in the

literature. A specially designed experiment which will use both ZEKE and MATI techniques will certainly allow to disentangle the dense rovibrational structure recorded in this work. This will make it possible to reconstruct the Na(3p)He potential curves from the experimental data.

3.1.1.4 Ion Imaging

The excitation spectra, photoelectron spectra and TOF mass spectra presented earlier revieled the presence of not only bare Na atoms and NaHe exciplexes but also the appreciable amount of $NaHe_2$. Below we will discuss the velocity distributions of these photoproducts determined by velocity map imaging. The $NaHe_3$ and $NaHe_4$ exciplexes had much lower abundances, so the ion imaging of these species was not performed because impractically long integration times would be needed to record ion images with sufficient S/N ratio.

The Figure 3.18 displays the experimental velocity map ion images of bare Na atoms in $^2P_{1/2}$ and $^2P_{3/2}$ states desorbed from the surface of helium nanodroplets with a mean droplet radius of 41 Å recorded using state-selective detection after 17 094 cm^{-1} excitation. The velocity map images of NaHe and $NaHe_2$ recorded using normal ion imaging after the excitation at 17 100 cm^{-1} are presented in the same figure. The images of desorbed bare Na atoms demonstrate a prominent angular anisotropy with the maximum intensity in the direction parallel to the laser polarization. This anisotropy is more pronounced in the case of Na atoms desorbed in 3p $^2P_{3/2}$ state than in 3p $^2P_{1/2}$ state. In contrast, the images of recoiled NaHe and $NaHe_2$ complexes are angularly isotropic. By varying the excitation frequency, the size and the anisotropy of the ion images recorded by detecting bare sodium changed, while the exciplexes' detection resulted in the same isotropic patterns.

Velocity distributions of the profucts, which allow for a quantitative analysis, were extracted from velocity map images by applying an inverse Abel transformation. In Figure 3.19 and Figure 3.20, we present the speed, anisotropy parameter and kinetic energy distributions derived from images presented in Figure 3.18. The speed distributions of Na atoms desorbed in the two spin-orbit states are quite similar. Both distributions have a pronounced limit near 250 m/s. However, the speed distribution of Na atoms desorbed in the $^2P_{3/2}$ state is slightly narrower than that of in the $^2P_{1/2}$: FWHM is ≈ 80 m/s for the $^2P_{3/2}$ and ≈ 120 m/s for the $^2P_{1/2}$. The maximum in the speed distribution of Na($^2P_{3/2}$) at ≈ 155 m/s is shifted by ≈ 20 m/s to higher speeds compared to that of Na($^2P_{1/2}$).

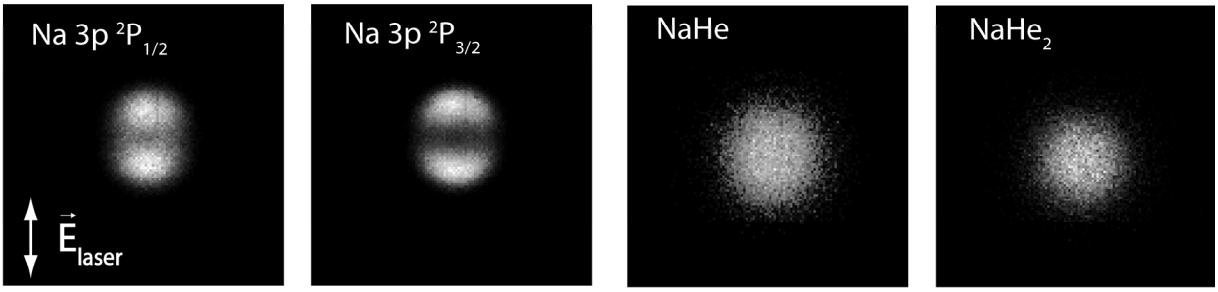

Figure 3.18: Velocity map ion images of desorbed products recorded following 17 094 cm^{-1} (Na 3p $^2P_{1/2}$ and Na 3p $^2P_{3/2}$) and 17 100 cm^{-1} (NaHe and $NaHe_2$) excitation of Na-He_N with <r> = 41 Å. For the imaging of bare Na atoms a state-selective detection technique is used. The ionization frequency for NaHe and $NaHe_2$ is 41 227 cm^{-1}. The polarizations of both lasers are vertical. The images show the central part of 120x120 pixels of the full frame consisting of 1000x1000 pixels. Every image is normalized by the maximum number of counts per pixel.

The angular anisotropy parameter β of desorbed sodium atoms increases with speed. The β-parameter of Na atoms desorbed in $^2P_{3/2}$ state is systematically highly than that of $^2P_{1/2}$ by ≈ 0.3. Contrary to Na atoms, the speed distributions of the two exciplexes are practically identical and the corresponding angular distributions are isotropic. The speed distributions of NaHe and $NaHe_2$ extend upto 300 m/s, which is noticeably higher than in the case of bare Na atoms at comparable excitation frequencies.

The velocity distributions of desorbed Na atoms vary with excitation frequency, but practically do not change at different mean droplet sizes. The evolution of the mean kinetic energies (KE) and angular anisotropy parameters of desorbed Na with excitation frequency is shown in Figure 3.21. The mean kinetic energies and standard deviations, which represent the width of the KE distributions, have an almost linear dependence on the excitation frequency. There seems to be a kind of turning point near 17 200 cm^{-1}, after which the slopes of the lines become less steep. The measurements beyond the 17 200 cm^{-1}, in the tail of the 3p-band excitation spectrum, were done using higher laser power in order to obtain images with sufficient S/N ratio. The fluence of the excitation laser was increased from 0.3 mJ/cm^2 at 17 000 - 17 200 cm^{-1} to 1.7 mJ/cm^2 at 17 400 cm^{-1}, which might cause the observed effect in the mean KE variation. Within the region 17 020 - 17 200 cm^{-1} of excitation frequency, the data points were fitted to linear function:

$$f(x) = a(x - b) \tag{3.3}$$

where x is the excitation frequency in cm^{-1}, a designates the dimensionless slope and b stands for the frequency onset in cm^{-1}. The fitting results for the mean kinetic energy $\langle E_{kin} \rangle$ and the standard deviation $\langle \Delta E_{kin} \rangle$ are collected in Table 5.

The mean anisotropy parameter $\langle \beta \rangle$ of desorbed bare Na depends on the excitation frequency too, but its standard deviation stays practically constant. The evolution of $\langle \beta \rangle$ is shown in the lower panel of Figure 3.21. The $\langle \beta \rangle$ corresponding to desorbed Na 3p $^2P_{1/2}$ atoms starts at slightly negative value $\langle \beta \rangle$ = -0.07 at 17 000 cm^{-1}, while that of Na 3p $^2P_{3/2}$ atoms starts at well positive value $\langle \beta \rangle$ = 0.34. Keeping approximately the same difference of 0.3 within the region of 17 020÷17 200 cm^{-1}, the anisotropy parameters of desorbed Na atoms in both spin-orbit states smoothly increase to the limit of ≈ 1.6 near 17 400 cm^{-1}, where the difference between the two states is reduced to ≈ 0.1.

Table 5 Fitting parameters for $\langle E_{kin} \rangle$ and $\langle \Delta E_{kin} \rangle$ of desorbed Na within the 3p-band

Species	$\langle E_{kin} \rangle$		$\langle \Delta E_{kin} \rangle$	
	a	*b* [cm^{-1}]	*a*	*b* [cm^{-1}]
Na 3p $^2P_{1/2}$	0.195±0.002	16988.5±1.3	0.078±0.001	16955±2
Na 3p $^2P_{3/2}$	0.228±0.002	16993.7±0.7	0.068±0.001	16950±3
$\langle E_{kin} \rangle$ and $\langle \Delta E_{kin} \rangle$ are the mean kinetic energy and its root mean square deviation calculated according to expression 2.14 *a* is the slope and *b* is the onset in the fit of experimental points to linear function 3.3				

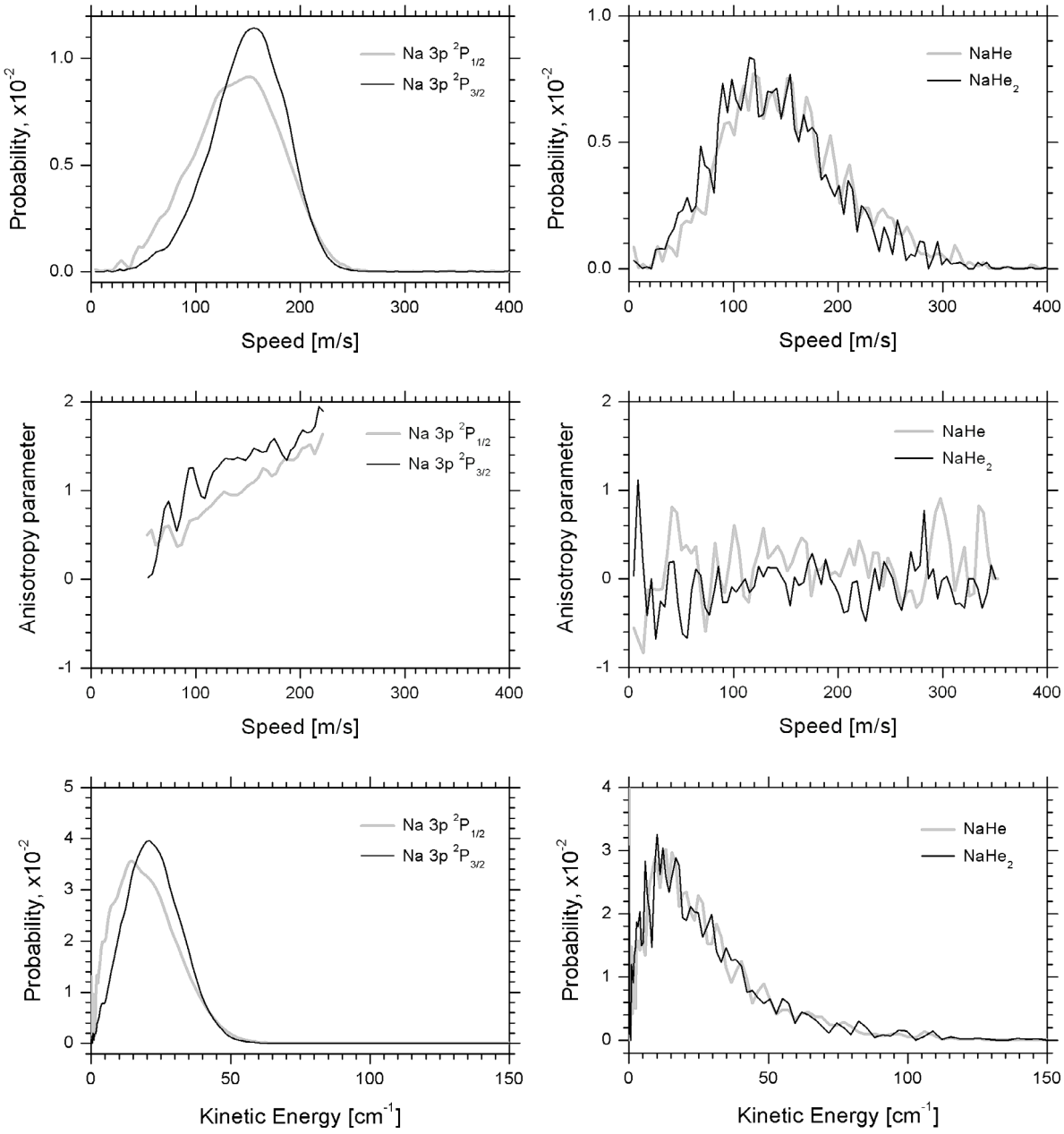

Figure 3.19: Upper panel: speed distributions of desorbed Na atoms in 3p $^2P_{1/2}$ and 3p $^2P_{3/2}$ states. Middle panel: corresponding anisotropy parameters. Lower panel: kinetic energy distributions. The data have been obtained from reconstructed 3D velocity distributions after applying an Abel inversion to the corresponding ion images in Figure 3.18.

Figure 3.20: Upper panel: speed distributions of desorbed NaHe and $NaHe_2$. Middle panel: corresponding anisotropy parameters. Lower panel: kinetic energy distributions. The data have been obtained from reconstructed 3D velocity distributions after applying an Abel inversion to the corresponding ion images in Figure 3.18.

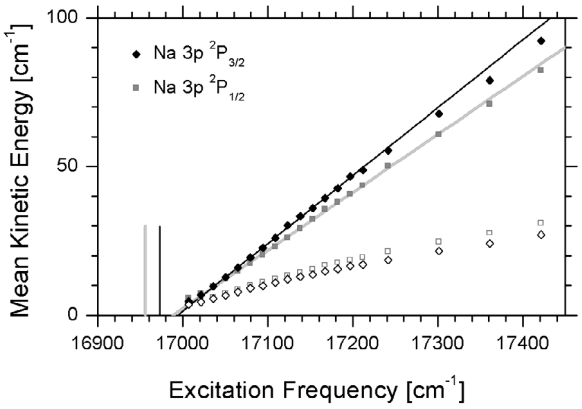

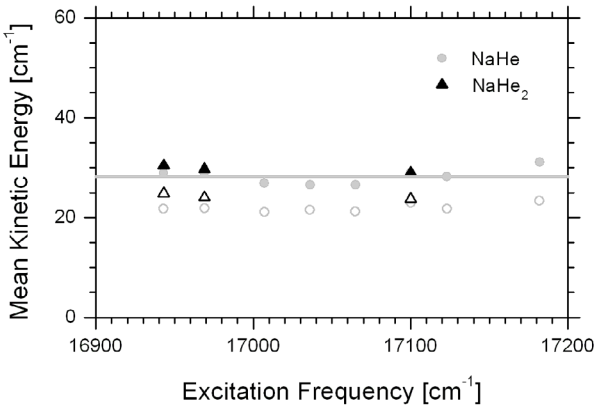

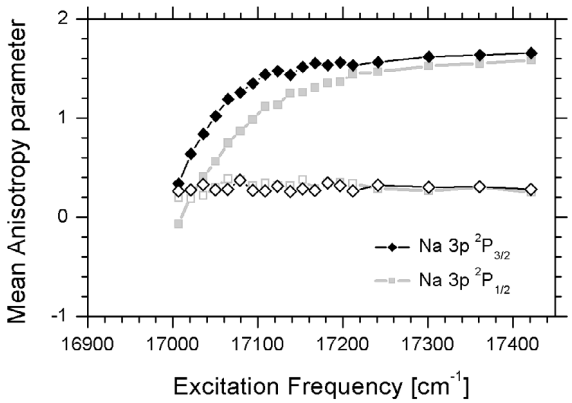

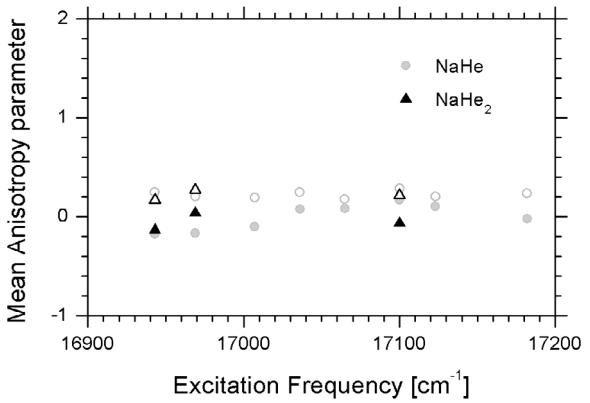

Figure 3.21: Upper panel: mean kinetic energies of desorbed Na atoms in 3p $^2P_{1/2}$ and 3p $^2P_{3/2}$ states after the excitation of Na-He_N with <r> = 41 Å at different frequencies. Open symbols show the standard deviation from the mean kinetic energy. The two short vertical lines in the left part show the frequencies of the D1 and D2 lines. The lines going through experimental points are fits to the linear function 3.3. Lower panel: corresponding mean anisotropy parameters of recoiled Na atoms. Open symbols show the standard deviation from the mean anisotropy parameter. The lines through the data points are to guide the eye.

Figure 3.22: Upper panel: mean kinetic energies of desorbed NaHe and $NaHe_2$ after the excitation of Na-He_N with <r> = 41 Å at different frequencies. Open symbols show the standard deviation from the kinetic energy. The horizontal line marks the averaged value of the mean kinetic energies of NaHe. Lower panel: corresponding mean anisotropy parameters. Open symbols show the standard deviation from the mean anisotropy parameter. The ionization frequency is 41 227 cm^{-1}.

3.1.2 4s-band

3.1.2.1 Excitation spectrum

The excitation spectrum of Na on the surface of helium nanodroplets with <r> = 41 Å corresponding to the 4s level of the free atom is presented in Figure 3.23. Only bare sodium atoms were detected following the excitation,as was explicitly checked by TOF mass-spectrometry. The shape of the spectrum is slightly asymmetric with a FWHM ≈ 400 cm^{-1}, which is remarkably wider

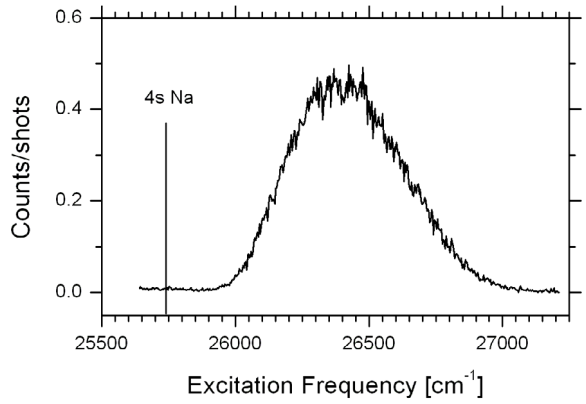

Figure 3.23: Excitation spectrum of the 4s-band of Na-He_N with <r> = 41 Å recorded by detecting bare sodium atoms. The vertical line marks the 4s←3s transition of free sodium.

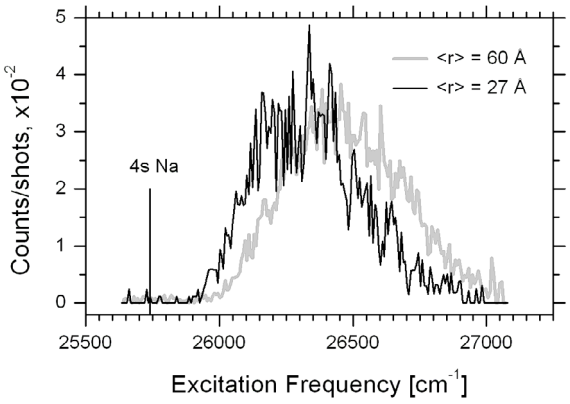

Figure 3.24: Excitation spectrum of 4s-band of Na atoms on the surface of helium nanodroplets with <r> = 60 Å and <r> = 27 Å recorded by detecting bare Na. The vertical line marks the 4s←3s transition of free Na.

than the FWHM ≈ 150 cm^{-1} of the total excitation spectrum in the 3p-band. The maximum of the spectrum is blue-shifted by ≈ 650 cm^{-1} with respect to the 4s←3s atomic transition at 25 740 cm^{-1}[99]. The shift depends on the droplet size, see Figure 3.24, but it is difficult to characterize the variation of shape due to the much lower S/N ratio in the excitation spectra recorded with mean droplet sizes <r> = 27 Å and <r> = 60 Å. In spite of the noise, a shift of ≈ 200 cm^{-1} between the spectra can be easily estimated.

3.1.2.2 Photoelectron spectrum

The photoelectron spectrum obtained following 26 316 cm^{-1} excitation at the maximum of the 4s-band is shown in Figure 3.25. The two peaks in the photoelectron spectrum originate from the ionization of Na in 3p and 4s states. Both these levels can be ionizaed in a one-color laser scheme, where a photon of the same energy used for excitation ionizes the desorbed excited Na atoms. The relative peak intensities, determined from the peak area, are 0.956±0.002 and 0.0434±0.0004 for 3p and 4s, respectively. No droplet size effects on the relative intensities of the peaks were observed. There are two major factors that define the relative intensity of the photoelectrons from 3p and 4s states in the photoionization of free Na using nanosecond laser pulses: a) the radiative decay of 4s level to 3p level and subsequent radiative decay of the 3p level to the 3s ground state level, because the radiative lifetime of the Na(4s) of ≈ 40 ns[99] is comparable to the typical duration of the laser pulse of 11 ns in our experiments; b) the ionization cross-sections of the Na atoms in 3p and 4s states at the photon energy of 26 316 cm^{-1}. This issue will be addressed later in more detail in section 3.1.5.3.

3.1.2.3 Ion Imaging

An example of the speed and anisotropy parameter distribution of recoiled sodium derived from an ion image recorded by exciting Na-He_N in the centre of the 4s-band is presented in Figure 3.26. The variation of the mean KE and anisotropy parameters of desorbed Na atoms versus excitation frequency are plotted in the left and right panels of Figure 3.27, respectively. As in the 3p-band, the mean KE of the desorbed sodium depends on the excitation energy, while the $<\beta>$ ≈ 1.8 is practically constant. The fit of the $<E_{kin}>$ and $<\Delta E_{kin}>$ to the expression 3.3 yields the values listed in Table 6.

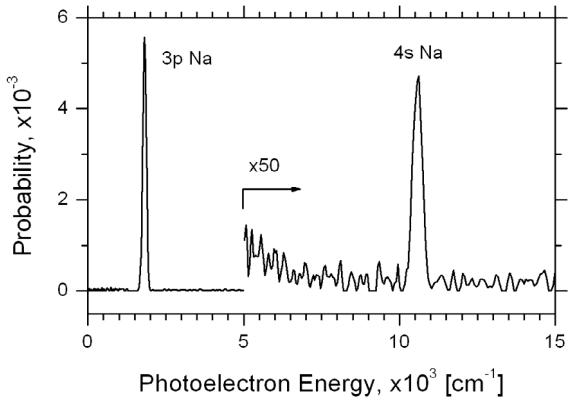

Figure 3.25: One-color photoelectron spectrum derived by photoelectron imaging following excitation at 26 316 cm^{-1} of Na atoms on the surface of helium nanodroplets <r> = 41 Å.

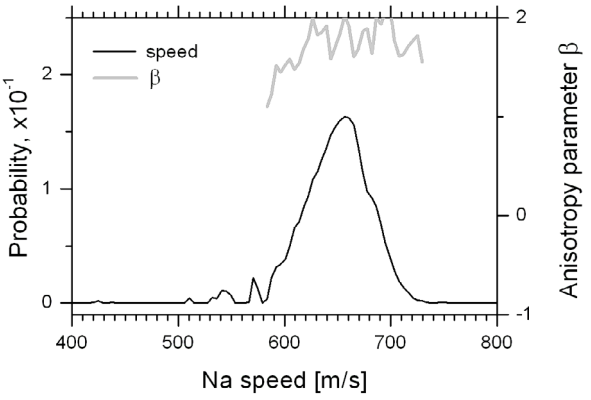

Figure 3.26: Speed and anisotropy parameter distribution of desorbed Na derived from velocity map ion image recorded following 26 500 cm^{-1} excitation of Na-He_N with <r> = 41 Å.

The parameters of linear dependence of $<E_{kin}>$ versus the excitation frequency in the 4s-band are different from those in the 3p-band: the onset of the fitted line starts at the atomic transition value within the fitting error, while in the 3p-band the onset is blue-shifted by ≈ 15 cm^{-1}; the slope of 0.515 ± 0.002 is a factor of two larger than that of ≈ 0.2 in the 3p-band. The variation of $<\Delta E_{kin}>$ with frequency can be also fitted to linear function 3.3, though data points are more scattered, which results in large fitting errors than for $<E_{kin}>$. The slope of 0.07 ± 0.01 is very close to those in the 3p-band of 0.078 ± 0.001 and 0.068 ± 0.001 for Na desorbed in the 3p $^2P_{1/2}$ and 3p $^2P_{3/2}$ states, see Table 5. No influence of the droplet size on the velocity distribution of desorbed Na at an excitation frequency of 26 300 cm^{-1} was observed. The speed and anisotropy parameter distributions recorded at two droplet sizes <r> = 29 Å and <r> = 60 Å were identical within the experimental S/N ratio.

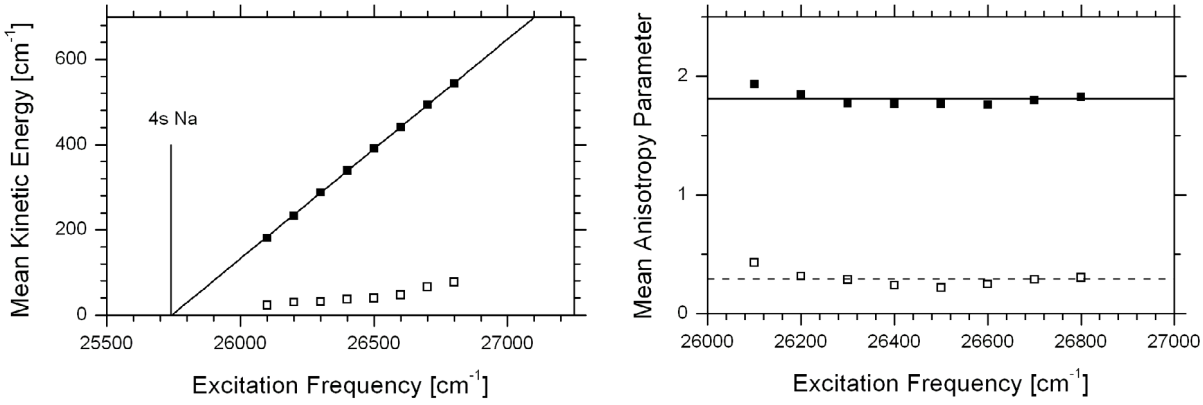

Figure 3.27: Left panel: The mean kinetic energy of desorbed Na atoms derived from velocity map ion images recorded following excitation of Na-He_N with <r> = 41 Å within the excitation spectrum in Figure 3.23. The vertical line marks the 4s←3s transition of free sodium. The open symbols are the standard deviations from the mean KE. The line going through experimental points is the fit to the expression 3.3. Right panel: Corresponding mean anisotropy parameters. The open symbols are standard deviations from $<\beta>$. The solid horizontal line marks averaged value of $<\beta>$ = 1.81±0.06. The dashed horizontal line marks the averaged value of standard deviation $<\Delta\beta>$ = 0.29±0.07 from $<\beta>$.

Table 6 Fitting parameters for $<E_{kin}>$ and $<\Delta E_{kin}>$ of desorbed Na in the 4s excitation band

Species	$<E_{kin}>$		$<\Delta E_{kin}>$	
	a	b [cm^{-1}]	a	b [cm^{-1}]
Na	0.515 ± 0.002	25 743 ± 3	0.07 ± 0.01	25 840 ± 92

3.1.3 3d-band

3.1.3.1 Excitation spectra

In contrast to excitation via the 4ws band, the excitation via the band corresponding to the 3d excited state of free Na leads to the formation of $NaHe_n$, n=1-4, exciplexes. The spectra recorded by detecting Na, NaHe, $NaHe_2$ and all these fragments together following the excitation of Na-He_N with <r> = 41 Å are presented in Figure 3.28. All excitation spectra are slightly asymmetric with the tails on the high frequency side. The maxima of spectra are blue-shifted with respect to the atomic 3d←3s transition. The shifts increase from $NaHe_2$ to NaHe and Na: 200 cm^{-1}, 300 cm^{-1} and 450 cm^{-1}, respectively. The signal decreases to zero near atomic 4p line at 30 267 cm^{-1} and increases again after ≈ 100 cm^{-1} at the beginning of the 4p-band. At the obtained signal-to-noise ratio, the spectra do not shift by more than 30 cm^{-1} to the blue between droplet sizes with <r> = 27 Å and <r> = 60 Å, retaining essentially the same shapes.

3.1.3.2 Time-of-flight mass spectra

The relative abundance of fragments desorbed after the excitation of Na-He_N within 3d-excitation band is shown in Figure 3.29. $NaHe_3$ and $NaHe_4$ exciplexes were also detected, but their relative abundances were inferior to $2 \cdot 10^{-3}$, so they are not considered in the following presentation. The variation of exciplex relative abundances is similar to the case of 3p-excitation band. NaHe and $NaHe_2$ complexes are most abundant in the low frequency part of the band close to 3d←3s atomic

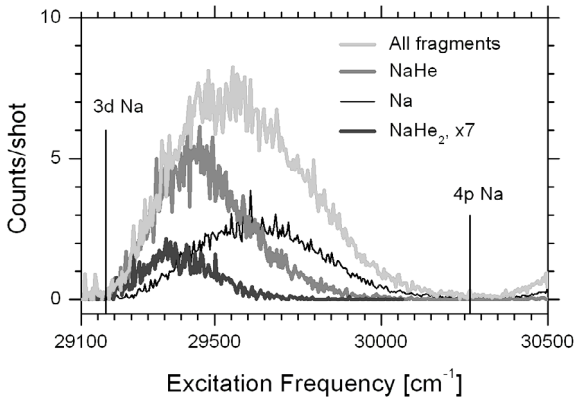

Figure 3.28: Excitation spectrum of 3d-band of Na-He_N with <r> = 41 Å recorded by monitoring bare Na atoms, NaHe, $NaHe_2$ and all these products together. The spectra, except for $NaHe_2$, are scaled to reflect the relative abundances found in time-of-flight mass spectra. $NaHe_2$ excitation spectrum is specially multiplied by a factor of 7 for the visibility. The vertical lines indicate positions of free atomic 3d←3s and 4p←3s transitions.

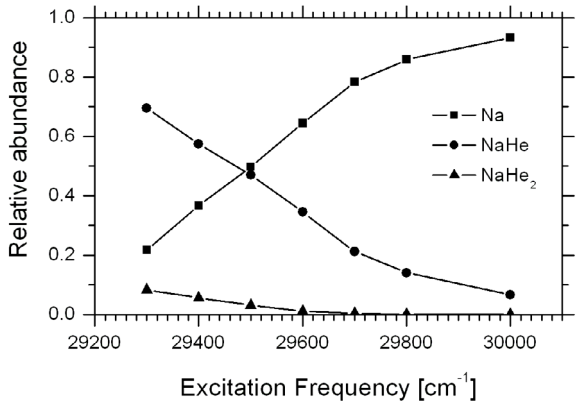

Figure 3.29: Relative abundance of desorbed Na, NaHe and $NaHe_2$ after excitation of Na-He_N with <r> = 41 Å at different frequencies. The lines through the data points are to guide the eye.

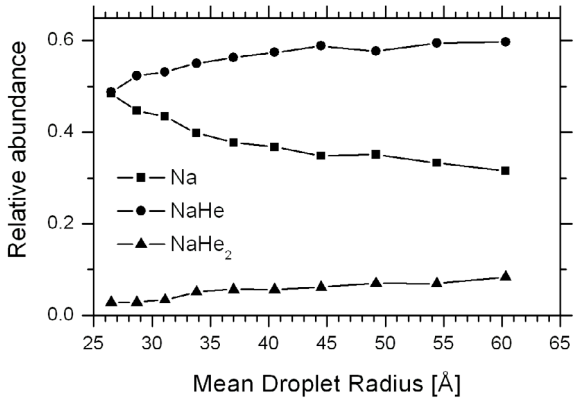

Figure 3.30: Relative abundance of desorbed Na, NaHe and $NaHe_2$ after 29 400 cm^{-1} excitation of Na-He_N at different droplet sizes. The lines through the data points are to guide the eye.

transition. The dependence of relative abundance on droplet size has been also observed and is presented in Figure 3.30. The excitation frequency of 29 400 cm^{-1} was chosen in order to have significant signal levels for all observed complexes. As in the case of 3p-band, the abundances of NaHe and $NaHe_2$ increase at the expense of bare Na with increasing mean droplet radius.

3.1.3.3 Photoelectron spectra

An example of the photoelectron spectrum obtained at an excitation frequency of 29 400 cm^{-1} is shown in Figure 3.31. Only peaks corresponding to the 3p and 3d excited states of sodium are seen in the spectrum. The 4s level can be also ionized at the photon energy used but is absent in the spectrum. The resolution of the photoelectron spectrum is not sufficient to resolve Na, NaHe and $NaHe_2$ peaks. The relative intensities of the 3d and 3p peaks are 0.80±0.05 and 0.20±0.05 respectively. No dependences of relative intensities of 3p and 3d photoelectron peaks on the droplet sizes and on the excitation frequency was observed.

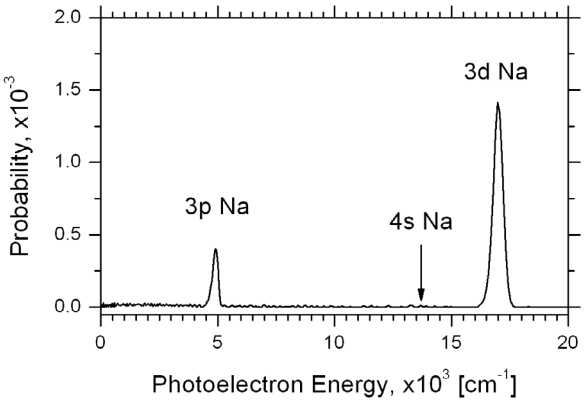

Figure 3.31: Photoelectron spectrum derived from photoelectron images recorded following 29 400 cm^{-1} excitation of Na-He_N with <r> = 41 Å.

3.1.3.4 Ion imaging

An example of the speed and anisotropy parameter distributions of desorbed products after the ≈ 29 400 cm^{-1} excitation of Na-He_N at the maximum of the 3d-band is presented in Figure 3.32. All species have similar speed profiles, but the exciplexes demonstrate somewhat higher speeds and broader distributions than bare sodium atoms. The angular distributions do not show a pronounced anisotropy: Na has small positive value of the anisotropy parameter β, while for the NaHe and $NaHe_2$ exciplexes β oscillates around zero. The mean KE of the desorbed Na and NaHe fragments demonstrate a linear dependence on the excitation energy within the excitation band, see the upper panel in Figure 3.33. As can be seen on the graph, the $<E_{kin}>$ of desorbed NaHe is systematically higher that of Na. The standard deviations of the $<E_{kin}>$ for both fragments vary almost linearly with

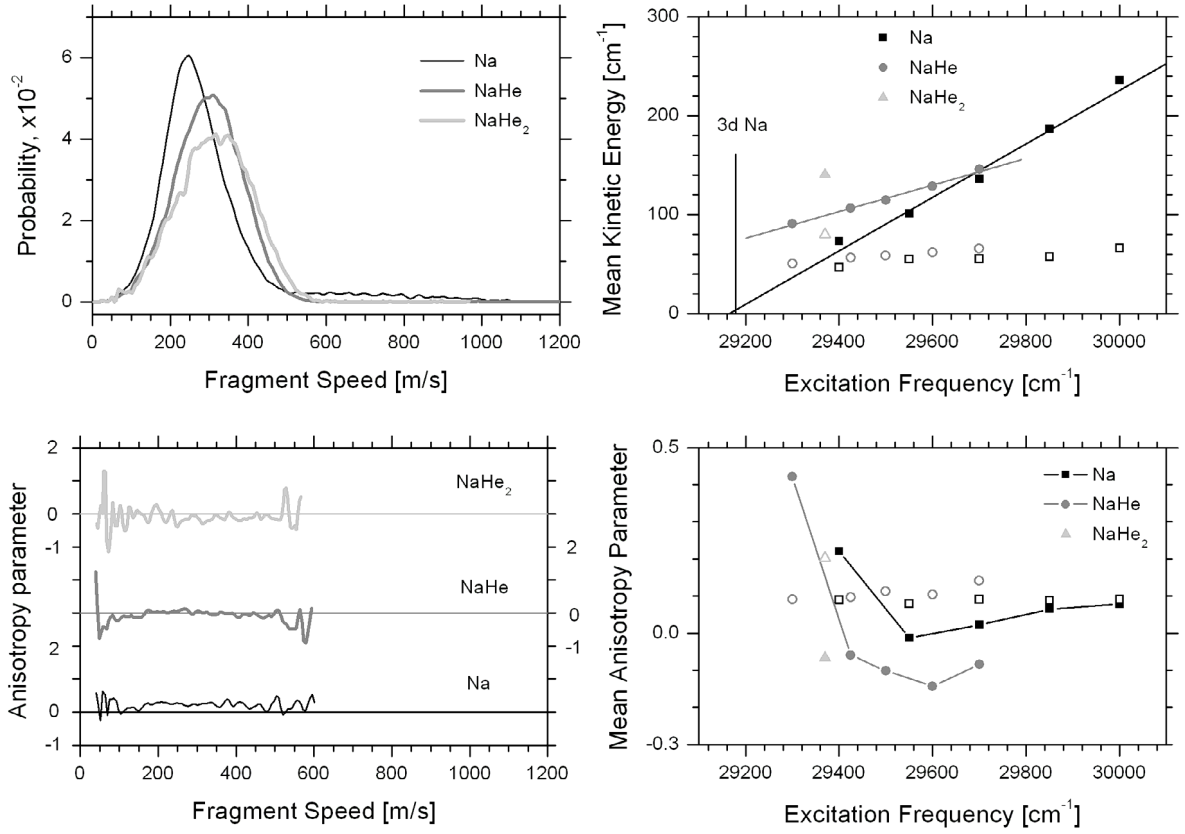

Figure 3.32: Upper panel: speed distributions of desorbed Na NaHe and $NaHe_2$ derived from velocity map ion images recorded following excitation at 29 400, 29 425 and 29 370 cm^{-1}, respectively, of Na-He_N with <r> = 41 Å. Lower panel: corresponding variation of the anisotropy parameter.

Figure 3.33: Upper panel: mean kinetic energy of desorbed Na atoms and NaHe complexes derived from velocity map ion images recorded following excitation of Na-He_N with <r> = 41 Å at different frequencies. Vertical line marks the 3d←3s transition of free sodium. The lines going through experimental points are the fits to the linear function 3.3. Lower panel: corresponding mean anisotropy parameters derived from velocity distributions. The open symbols are values of the standard deviations. The lines through the data points are to guide the eye.

the excitation energy. The <β>-parameters have a less regular behavior: bare Na atoms have small positive value of <β> ≈ 0.1 and <β> ≈ -0.1 for NaHe all along the excitation band except the low frequency part. There is <β> ≈ 0.25 for Na desorbed after excitation at 29 400 cm^{-1} and <β> ≈ 0.25 for NaHe at 29 300 cm^{-1} are at odds with the general trend.

The parameters found by fitting the experimental values of $<E_{kin}>$ to expression 3.3 are presented in Table 7. Extrapolated to zero, $<E_{kin}>$ of desorbed sodium ends within the fitting errors at the corresponding free atomic 3d←3s transition of 29 173 cm^{-1}[99]. This is similar to the $<E_{kin}>$ variations of Na atoms in the 4s-band. The slope a = 0.27 ± 0.02 has the value which is intermediate between those found in the 3p- and 4s-bands, 0.212 ± 0.003 (averaged over 3p $^2P_{1/2,3/2}$ states) and 0.515± 0.002 respectively. The slope a = 0.135 ± 0.007 of the $<E_{kin}>$ for desorbed NaHe is twice smaller than that of Na and the extrapolation to zero kinetic energy yields the onset b = 28 638 ± 43 cm^{-1}, which is red-shifted by ≈ 500 cm^{-1} from the 3d←3s atomic transition.

Table 7 Fitting parameters for $<E_{kin}>$ and $<\Delta E_{kin}>$ within the 3d-band

Species	$<E_{kin}>$		$<\Delta E_{kin}>$	
	a	b [cm^{-1}]	a	b [cm^{-1}]
Na	0.27 ± 0.02	29 165 ± 41	0.028 ± 0.006	27 682 ± 421
NaHe	0.135 ± 0.007	28 638 ± 43	0.037 ± 0.002	27 909 ± 68

3.1.4 4p-band

3.1.4.1 One-photon excitation spectra

Within the excitation band corresponding to 4p←3s atomic transition, bare sodium atoms constitute the major part among the desorbed fragments, see Figure 3.34. The bare sodium desorbs within band with a FWHM ≈ 1500 cm^{-1} centered at ≈ 31 200 cm^{-1}. The shape of the spectrum is asymmetric with the tail on the high frequency side with respect to the maximum, which is similar to the observed excitation spectra correpsonding to the 3p, 4s and 3d excited states of free Na. The NaHe desorbs within a much narrower band with FWHM of ≈ 200 cm^{-1} that peaks at ≈ 30 500 cm^{-1}. The Na excitation spectrum varies with droplet size, see Figure 3.35. The spectrum recorded with <r> = 27 Å is shifted by ≈ 300 cm^{-1} to higher frequency from that recorded at <r> = 60 Å. The shape of the spectrum also changes: at larger droplets the high frequency tail is more intense than at smaller droplets. This might indicate that the spectrum consists of two components, the relative contributions of which change with the size of nanodroplets.

3.1.4.2 Two-photon excitation spectrum

The use of a two-photon excitation in the 4p-band was motivated by the following. As will be explained in section 3.1.5.1, the relative intensities of Σ'←Σ' and Π'←Σ' transitions in one- and two-photon excitation of Na-He_N should be considerably different. This will allow for separation of presumably overlapping transitions. In addition, a one-color scheme is feasible in the 4p-band, where the third photon from the same laser can ionize desorbed Na atoms in the 4p excited state. The application of a one-color shceme is also possible in the 3d-band, but our attempts to record two-photon excitation spectra were not successful due to technical problems.

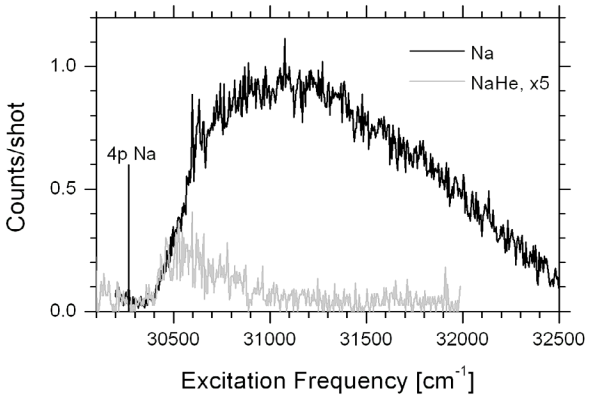

Figure 3.34: One-photon excitation spectrum of the 4p-band of Na-He_N with a <r> = 41 Å recorded by monitoring Na and NaHe. The NaHe excitation spectrum is specially multiplied by a factor of 5 for the visibility. The vertical line indicates position of the free atomic 4p←3s transition.

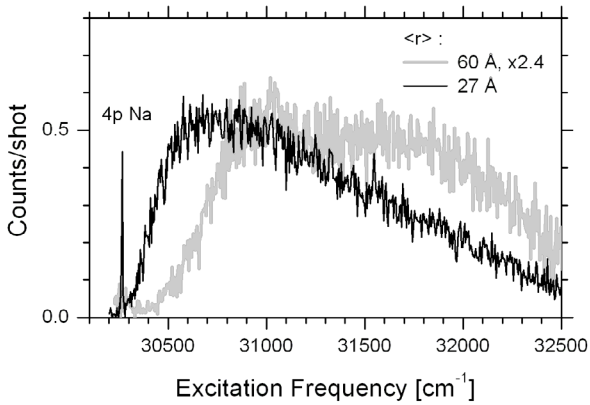

Figure 3.35: One-photon excitation spectra of 4p-band of Na-He_N with <r> = 60 Å and <r> = 27 Å recorded by detection of bare sodium atoms. The sharp peak in the left part of the graph marks the 4p←3s transition of gas phase sodium atoms present in the detection region.

A comparison of the one-color one- and two-photon excitation spectra of Na-He_N within the 4p-band recorded by detecting Na atoms is shown in Figure 3.36. Only desorption of bare sodium has been detected when using two-photon excitation. The two-photon spectrum has the maximum at ≈ 32 300 cm^{-1} and is asymmetric with the tail in the low frequency part. Its FWHM ≈ 1 500 cm^{-1} is practically the same as that of one-photon spectrum, while the onset of the two-photon spectrum is blue-shifted by ≈ 400 cm^{-1} from the 4p←3s atomic transition at 30 270 cm^{-1}[99] compared to 150 cm^{-1} for the one-photon spectrum. The shape of the two-photon transition varies with droplets size, seeFigure 3.37: the low frequency part of the spectrum at <r> = 60 Å is blue-shifted by ≈ 300 cm^{-1}

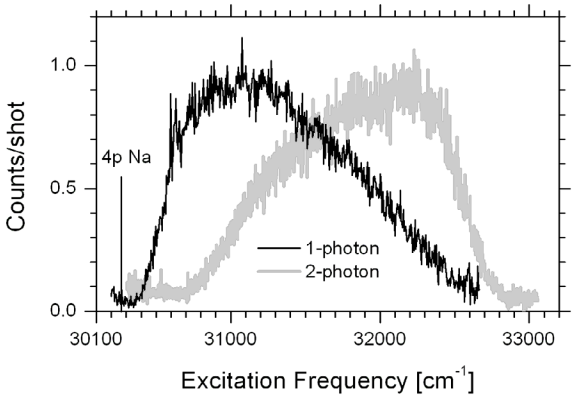

Figure 3.36: Excitation spectra recorded by detecting Na atoms following one-photon and two-photon excitation of Na-He_N with <r> = 41 Å. The vertical line marks the 4p←3s transition of free sodium. The laser fluence is 1.3 J/cm^2 for both spectra.

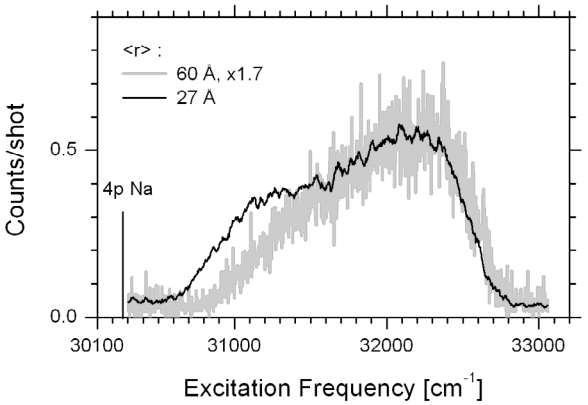

Figure 3.37: Two-photon excitation spectra of the 4p-band of Na-He_N with <r> = 60 Å and <r> = 27 Å recorded by detection of Na. The spectrum recorded at <r> = 27 Å is smoothed by adjacent averaging over 10 points. The vertical line marks the 4p←3s transition of free sodium.

compared to the spectrum obtained at <r> = 27 Å. It is visible that the low frequency part of the spectrum at ≈ 31 000 cm^{-1} increases with the decrease in the mean droplets size.

3.1.4.3 TOF mass spectra

The relative abundances of Na and NaHe obtained from TOF mass spectra recorded following one-color one-photon excitation within 4p-band are presented in Figure 3.38. The two fragments have correlated variations: NaHe attains its maximum abundance of 0.06 at the excitation frequency of 30 500 cm^{-1} at the expense of bare Na, the relative abundance of which drops at this frequency to 0.94. In contrast to the 3p- and 3d-bands, the variation of relative abundances with droplets size was not observed, which was checked by recording TOF spectra at different mean droplet sizes at the excitation frequency of 30 750 cm^{-1}, see Figure 3.39. The $NaHe_n$ exciplexes with n>1 were not detected, which implied that their relative abundances were inferior to 10^{-4}.

3.1.4.4 Photoelectron spectra

The photoelectron spectra derived from photoelectron images recorded by one-photon and two-photon excitation at 32 000 cm^{-1} (16 000 cm^{-1} in case of two-photon excitation) of Na-He_N are presented in Figure 3.40. The energy resolution in the one-photon excitation scheme is not sufficient to fully resolve photoelectron peak originating from the ionization of 3d and 4p sodium levels which are separated by only 1 094 cm^{-1}. In the one-color scheme used photoionization of Na in the lower lying 3p and 4s states is possible. As can be seen in Figure 3.40, within the experimental S/N ratio only photoelectrons from Na(4p) were detected. Photoelectron spectra following one-color one-photon excitation were obtained at various droplet sizes and excitation frequencies within the 4p-band and no variations were observed.

In order to verify the photoionization of Na from the 3d excited state the photoelectron spectrum with two-photon excitation was recorded, see the insert in Figure 3.40. Having a better resolution, it can resolve signals from Na atoms in 4p and 3d states. The signal in the spectrum originates from the ionization of Na atoms in 4p state and any signal araising from ionization of Na(3d) is absent.

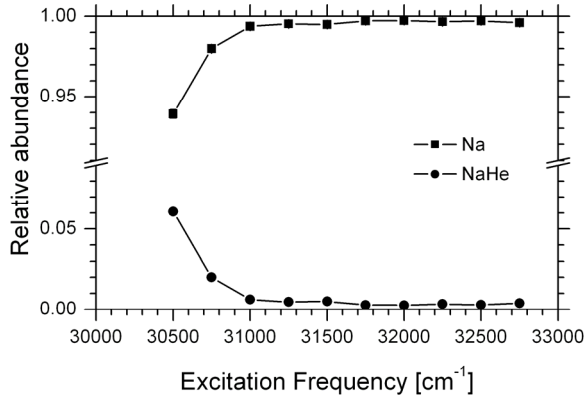

Figure 3.38: Relative abundance of desorbed Na and NaHe after one-photon excitation of Na-He_N with <r> = 41 Å within 4p-band. The lines through the data points are to guide the eye. Errors are smaller than the symbol size and not shown.

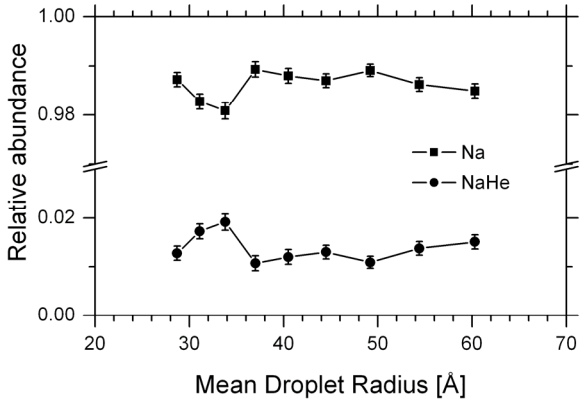

Figure 3.39: Relative abundance of desorbed Na and NaHe after the one-photon excitation of Na-He_N with <r> = 29 - 60 Å at 30 750 cm^{-1}. The error bars reflect the statistical errors in total counts for each species.

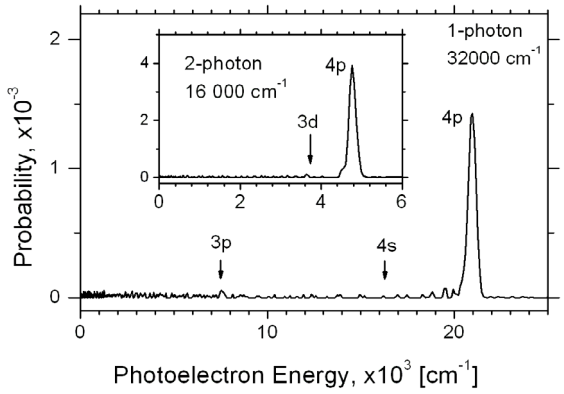

Figure 3.40: One-color photoelectron spectra derived from photoelectron images recorded following 32 000 cm^{-1} excitation of Na-He_N with <r> = 41 Å. Arrows indicate the energies, where photoelectron signal would appear if lower than 4p states of sodium are ionized. In the insert: one-color photoelectron spectrum obtained following two-photon excitation of Na-He_N with <r> = 41 Å at 16 000 cm^{-1}.

3.1.4.5 Ion imaging

Ion images were only recorded for bare desorbed Na. In view of very small abundance, the imaging of NaHe exciplex was not carried out. Pronounced variations of speed and angular distributions of recoiled Na as a function of excitation frequency were observed in 4p-band, see the upper panel of Figure 3.41. Maintaining the same regular shape, the speed distributions become wider with increasing excitation frequency, as was also seen for the other states. The angular anisotropy parameter gradually changes from negative at low frequencies to positive at high frequencies, see the lower panel of Figure 3.41. The variation of $\langle E_{kin} \rangle$ and $\langle \Delta E_{kin} \rangle$ with excitation frequency within the 4p-band is presented in the upper panel of Figure 3.42, while the corresponding $\langle \beta \rangle$-parameter variations are shown in the lower panel.

As can be seen from the graph, the change of $\langle E_{kin} \rangle$ versus excitation frequency can be well approximated by the linear function 3.3. The results are collected in Table 8. The onset b = 30 209 ± 25 cm^{-1} determined from the linear fit of $\langle E_{kin} \rangle$ is red-shifted by ≈ 60 cm^{-1} with respect to the free Na 4p←3s transition at 30 270 cm^{-1}. This result deviates with previous findings in the other excitation bands, when the onset was either blue-shifted as in the 3p-band or corresponded to the free Na transitions as in the 4s- and 3d-bands. The probable cause of this deviation may be a systematic calibration error, for the velocity map ion images for the 4p band were acquired at two different voltages settings in the imaging setup. In the region 30 500 - 31 500 cm^{-1} the Repeller voltage of +1000 V was used to obtain better resolution, see Chapter 2, while in the region of 31 750 - 32 750 cm^{-1} the higher voltage of +4 000V was applied in order to fit the increased velocity map ion image on the detector. The slope a = 0.406 ± 0.006 in the linear dependence of $\langle E_{kin} \rangle$ of desorbed Na has value intermediate between those in the 4s- of and 3d-bands. The width of KE distribution $\langle \Delta E_{kin} \rangle$ also increases with the excitation energy. The fit of $\langle \Delta E_{kin} \rangle$ to the linear function 3.3 yields the slope value a = 0.09 ± 0.01, which corresponds within the fitting error to the results in the other, except the 3d one, bands.

The $\langle \beta \rangle$-parameter demonstrates a regular increase from a negative value of $\langle \beta \rangle$ = -0.68 at 30 500 cm^{-1} in the low frequency part of the excitation spectrum to positive value of $\langle \beta \rangle$ = 1.3 at 32 500 cm^{-1}. The increasing trend in the $\langle \beta \rangle$-parameter versus excitation frequency was previously observed

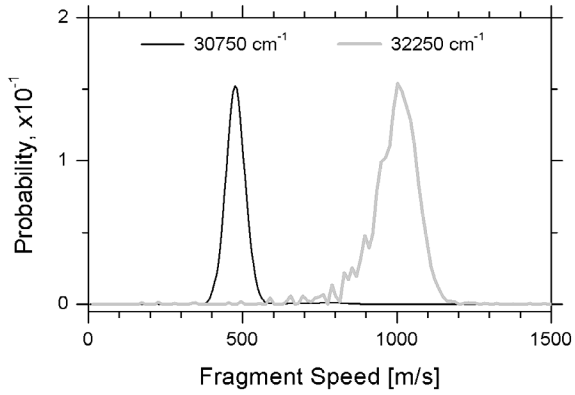

Figure 3.41: Upper panel: speed distributions of desorbed Na derived from velocity map ion images recorded following one-photon excitations at 30 750 and 32 250 cm^{-1} of Na-He_N with <r> = 41 Å. Lower panel: corresponding variation of the anisotropy parameter.

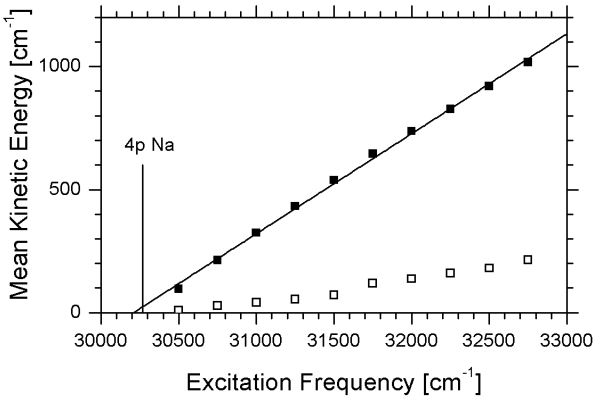

Figure 3.42: Upper panel: Mean kinetic energy of desorbed Na atoms derived from velocity map ion images recorded following one-photon excitation of Na-He_N with <r> = 41 Å within the 4p excitation band shown in Figure 3.34. Vertical line marks the 4p←3s transition of free Na. The open symbols are values of standard deviations. The line going through experimental points is the fit to the linear function 3.3. Lower panel: Corresponding mean anisotropy parameters derived from velocity distributions. The open symbols are values of standard deviations. The lines through the data points are to guide the eye.

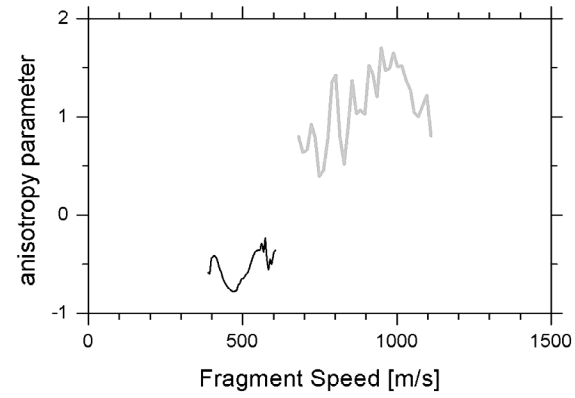

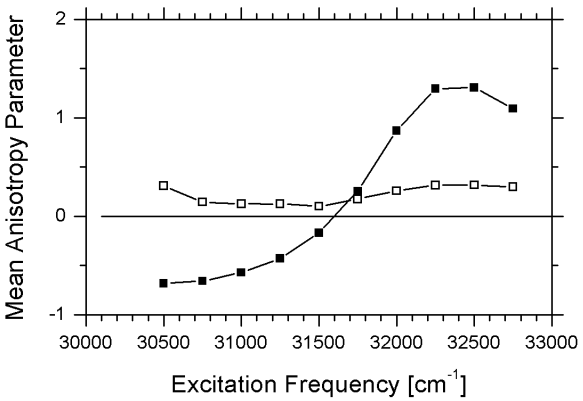

only in 3p-band, while almost no change in $<\beta>$ was found in the 4s-band and decreasing trend was observed in 3d-band. The width of the angular distribution $<\Delta\beta>$ varies little within the range $<\Delta\beta> \approx$ 0.1 - 0.3. A similar behavior was observed for the other bands.

Table 8 Fitting parameters for $<E_{kin}>$ of desorbed Na within 4p-band

Species	$<E_{kin}>$		$<\Delta E_{kin}>$	
	a	b [cm^{-1}]	a	b [cm^{-1}]
Na	0.406 ± 0.006	30 209 ± 25	0.09 ± 0.01	30 513 ± 100

3.1.5 Discussion

3.1.5.1 Modeling of excitation spectra

As was first shown by Ancilotto[44], the alkali atoms in the ground electronic states can be bound to the surface of liquid helium in a dimple-like deformed surface structure. The same holds for alkalis on the surface of helium droplets[110]. The trapping potential of an alkali-droplet system is thus a three-dimensional one with cylindrical symmetry around the "alkali-droplet centre" axis. From this it follows that a rigorous theoretical treatment of Na(nl)-He_N←Na(3s)-He_N transitions requires the construction of 3D interaction potentials and the solution of the 3D Schrödinger equation. The latter task is still challenging as there is no universal method to solve the problem. However, with a number of assumptions described below the 3D problem can be reduced to a one-dimensional diatomic-like problem for which established numerical solvation procedures exist[108, 111]. This approach has allowed to qualitatively reproduce the 0 K excitation spectra of alkali atoms on the surface of helium droplets[70]. In the following of this section we will test the applicability of this simplified one-dimensional approach to higher excited states of Na-He_N.

3.1.5.1.1 Na-He_N interaction potentials

We use the one-dimensional pair-wise additive model to calculate Na-He_N interaction potentials which was first developed for alkali-doped helium droplets by Stienkemeier *et al.*[69] and extended later by Burnemann *et al.*[70]. In this model, the alkali-He_N system is considered as a diatomic molecule, where the alkali atom is acting as one atom and the helium droplet is acting as another. Within this approach the "droplet-sodium atom" interaction potential can be constructed by summing individual Na-He pair potentials over helium atoms constituting the droplet. In practice, the summation is replaced by intergration over the Na-He_N density profile:

$$V_{Na-He_N}\left(n\Lambda,\vec{R}\right)-V_{Na}\left(nl\right)=\int\left[V_{NaHe}\left(n\Lambda,\vec{R}'-\vec{R}\right)-V_{Na}\left(nl\right)\right]\rho_{He}\left(\vec{R}'\right)d\vec{R}' \qquad 3.4$$

where the designation of the integration variables are explained in Figure 3.43, n is the main quantum number and l is the orbital angular momentum of Na atom, Λ is the projection of the orbital angular momentum of Na-He_N onto the quantization z-axis, a cylindrical symmetry axis; $\rho_{He}\left(\vec{R}'\right)$ stands for helium density at the point with coordinates of the vector $\vec{R}'$. In this model, the He-He interaction, three-body and higher order effects are neglected, as well as spin-orbit interaction.

The helium atoms are treated as continuous medium distributed around the sodium atom which is fixed in the Cartesian coordinate system, see Figure 3.43. The cylindrical symmetry of the systems determines the axis “impurity-helium droplet’s centre” as the quantization axis for the projection of electron angular momentum. If the sodium-helium interaction is isotropic then the droplet-sodium interaction potential is just the sum of pair potentials. This is the case for *S* states of sodium. When the sodium is in an electronic states with $l>0$, then the Na-droplet interaction potentials are no more isotropic. They are calculated by taking into account the orientation of each helium atom in the droplet with respect to angularly anisotropic electronic orbital of excited Na. Below we present the elements of quantization of angular momentum in a rotated coordinate system by using the approach of Bunermann *et al.*[66]. This approach allows to construct the Na(nl)-He_N, $l>1$, interaction potentials. An illustration of this method is given for the intuitively simple case of sodium in a *P* state.

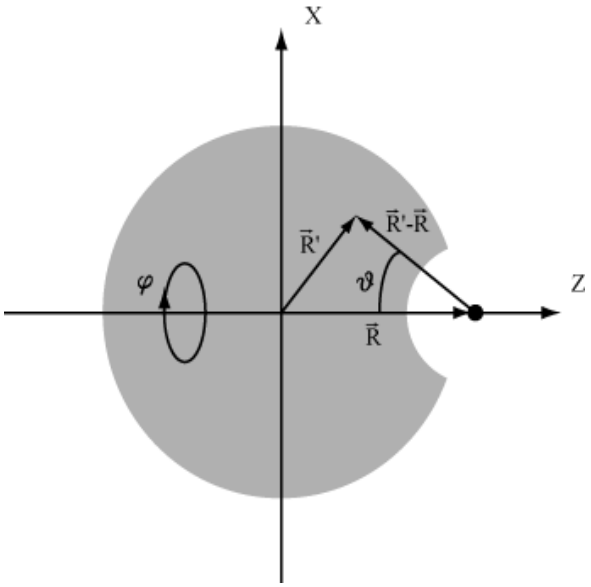

Figure 3.43: Coordinate system used in calculation of Na-He_N interaction potentials.

Let us consider the interaction of an excited Na with a single electron in the 3p-orbital and a He atom in the ground 1s state. For the Na-He system the total electronic angular momentum can be assigned to the angular momentum of Na, so the absolute value of the projection m_l of the Na angular momentum l on the NaHe molecular axis will be equal to the Λ, the absolute value of the projection of the NaHe electronic angular momentum. In the uncoupled basis[112] $|lm_l\rangle$, the Hamiltonian of Na(3p)-He can be expressed in diagonal form by taking into account only electrostatic interactions[113]:

3.5
$$H_{Na-He} = \begin{pmatrix} V_{\Pi} & 0 & 0 \\ 0 & V_{\Sigma} & 0 \\ 0 & 0 & V_{\Pi} \end{pmatrix}$$

where V_Σ and V_Π are the Σ- and Π-type electrostatic interaction potentials. The type of the pair potential depends on the projection Λ = | m_l | of the orbital angular momentum on the molecular axis or, in other words, on the orientation of the p-orbital of the Na atom. The Σ-type (Λ = 0, m_l = 0) potential arises when the 8-shaped p-orbital is parallel to the molecular axis. The perpendicular orientation (Λ = 1, m_l = ±1) of the p-orbital leads to Π potential.

In the case of Na(3p)-He_N, helium atoms can lie at large angles with respect to the quantization z-axis. The eigenvectors $|lm'\rangle$ of the electronic angular momentum in the coordinate system of Na(3p)-He formed by the off-axis helium atom can be expressed as the linear combination of the $|lm\rangle$ eigenvectors in the reference coordinate system[112]:

3.6
$$|lm'\rangle = R^{-1}(\varphi,\vartheta,\chi)\,|lm\rangle = \sum_m D^l_{mm'}(\varphi,\vartheta,\chi)\,|lm\rangle$$

where l is the electronic angular momentum, the m' and m are its projections on the rotated and reference quantization axis respectively; $D^l_{mm'}(\varphi,\vartheta,\chi)$ are the elements of rotational matrix; φ,ϑ,χ

are the Euler's angles of the rotation transformation that changes the old coordinate system to the new one. The rotation matrix elements can be split into three terms:

3.7 $$D^{l}_{mm'}(\varphi,\vartheta,\chi) = e^{-i\varphi m} d^{l}_{mm'}(\vartheta) e^{-i\chi m'}$$

where the analytical expressions for elements $d^{l}_{mm'}(\vartheta)$ upto *l=2* can be found in the *R.N. Zare's* book[112] or can be generated in analytical form for given values of *l, m, m'* with the *Racah* package[114] for the *Maple*[115] software package. The Hamiltonian H'_{Na-He} in new rotated coordinate system is expressed via the old one as:

3.8 $$\boldsymbol{H}'_{Na-He} = \boldsymbol{R}\boldsymbol{H}_{Na-He}\boldsymbol{R}^{-1}$$

The eigenvalues of $\boldsymbol{H}'_{Na-He}$ and $\boldsymbol{H}_{Na-He}$ are the same, since the $\boldsymbol{R}$ matrix is unitary and the eigenvectors are related via the above expression 3.6. The rotation matrix for *P* has follwing form:

3.9 $$\boldsymbol{R} = \begin{pmatrix} e^{-i\varphi}\frac{1}{2}(1+\cos\vartheta)e^{-i\chi} & -e^{-i\varphi}\sqrt{\frac{1}{2}}\sin\vartheta & e^{-i\varphi}\frac{1}{2}(1-\cos\vartheta)e^{i\chi} \\ \sqrt{\frac{1}{2}}\sin\vartheta e^{-i\chi} & \cos\vartheta & -\sqrt{\frac{1}{2}}\sin\vartheta e^{-i\chi} \\ e^{i\varphi}\frac{1}{2}(1-\cos\vartheta)e^{-i\chi} & e^{i\varphi}\sqrt{\frac{1}{2}}\sin\vartheta & e^{i\varphi}\frac{1}{2}(1+\cos\vartheta)e^{i\chi} \end{pmatrix}$$

and the Hamiltonian in new rotated coordinate system is:

3.10 $$\boldsymbol{H}'_{Na-He} =$$

$$\begin{pmatrix} V_{\Pi}\cos^2\vartheta + \frac{1}{2}(V_{\Pi}+V_{\Sigma})\sin^2\vartheta & \sqrt{\frac{1}{2}}e^{-i\varphi}(V_{\Pi}-V_{\Sigma})\cos\vartheta\sin\vartheta & \frac{1}{2}e^{-2i\varphi}(V_{\Pi}-V_{\Sigma})\sin^2\vartheta \\ \sqrt{\frac{1}{2}}e^{i\varphi}(V_{\Pi}-V_{\Sigma})\cos\vartheta\sin\vartheta & V_{\Pi}\sin^2\vartheta + V_{\Sigma}\cos^2\vartheta & -\sqrt{\frac{1}{2}}e^{-i\varphi}(V_{\Pi}-V_{\Sigma})\cos\vartheta\sin\vartheta \\ \frac{1}{2}e^{2i\varphi}(V_{\Pi}-V_{\Sigma})\sin^2\vartheta & -\sqrt{\frac{1}{2}}e^{i\varphi}(V_{\Pi}-V_{\Sigma})\cos\vartheta\sin\vartheta & V_{\Pi}\cos^2\vartheta + \frac{1}{2}(V_{\Pi}+V_{\Sigma})\sin^2\vartheta \end{pmatrix}$$

Due to the azimuthal symmetry of the sodium-helium droplet system the off-diagonal matrix elements of the Hamiltonian in new rotated coordinate system become zero during integration of the expression 3.10 over the azimuthal angle φ. This facilitates the calculations, so one can operate only with diagonal matrix elements, which for the *P* state have the following forms:

3.11
$$V'_{\Sigma}(r,\vartheta) = V_{\Pi}(r)\sin^2\vartheta + V_{\Sigma}(r)\cos^2\vartheta$$
$$V'_{\Pi}(r,\vartheta) = V_{\Pi}(r)\cos^2\vartheta + \frac{1}{2}\left[V_{\Pi}(r)+V_{\Sigma}(r)\right]\sin^2\vartheta$$

where $r = \left|\vec{R}' - \vec{R}\right|$. As one can see from this derivation, the helium atoms, which are off from the symmetry z-axis of "droplet-sodium" complex, will "mix" pure diatomic states of NaHe. In the same manner as described above, the new Hamiltonians for states with higher angular orbital momentum of sodium can be calculated. For *D* state the diagonal matrix elements of the transformed Hamiltonian are the following:

3.12

$$V'_{\Sigma}(r,\vartheta) = V_{\Delta}(r)\frac{3}{4}\sin^4\theta + V_{\Pi}(r)3\sin^2\theta\cos^2\theta + V_{\Sigma}(r)\frac{1}{4}\left(9\cos^4\theta - 6\cos^2\theta + 1\right)$$

$$V'_{\Pi}(r,\vartheta) = V_{\Delta}(r)\frac{1}{2}\sin^2\theta\left(\cos^2\theta + 1\right) + V_{\Pi}(r)\frac{1}{2}\left(4\cos^4\theta - 3\cos^2\theta + 1\right) + V_{\Sigma}(r)\frac{3}{2}\sin^2\theta\cos^2\theta$$

$$V'_{\Delta}(r,\vartheta) = V_{\Delta}(r)\frac{1}{8}\left(1 + \cos^4\theta + 6\cos^2\theta\right) + V_{\Pi}(r)\frac{1}{2}\sin^2\theta\left(\cos^2\theta + 1\right) + V_{\Sigma}(r)\frac{3}{8}\sin^4\theta$$

3.1.5.1.2 Na(3s)-He$_N$ density profiles

The one-dimensional interaction potentials of Na-He$_N$ were calculated by varying the position of Na(n*l*) along the z-axis of the Na(3s)-He$_N$, N = 1000, 5000 density profiles provided by the group of Barranco[116], see Figure 3.44. In their calculations, the zero-point motion of light Na was explicitly taken into account. Details on methods used to calculate these density profiles can be found in an extensive review[19]. The Na atoms perturbs very little the droplet and resides in the shallow dimple at ≈ 6 Å distance from the helium surface.

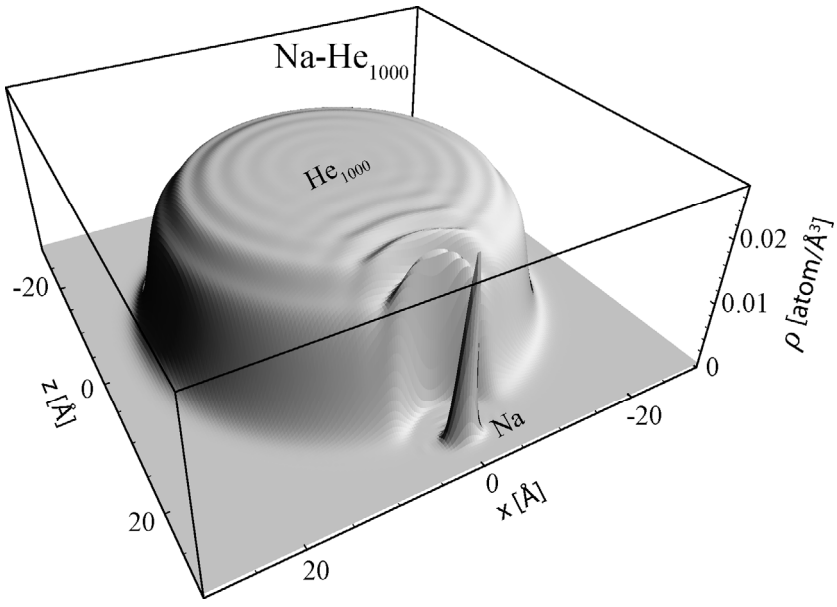

Figure 3.44: Density profile of Na-He1000 used in our calculation. The illustration is reproduced with permission[116]. The visualisation concept is of A. Hernando[117].

3.1.5.1.3 Na-He pair potentials

The mean diameters of nanodroplets produced in our experiments vary from ≈ 50 Å to ≈ 120 Å. This requires the knowledge of Na-He pair potentials at these distances for the correct calculation of Na-He_N interaction potentials. At large internuclear distances the NaHe interaction is very weak but it is never exactly zero. Consequently, the sum of weak interactions of Na with individual He atoms over the whole droplet can result in significant contribution.

For the ground electronic state of Na(3s)-He_N we used the pair potential of Patil[118], see Figure 3.45, because it was used to calculate the density profiles of Na(3s)-He_N (N = 1000, 5000) droplets which we used in our calculations.

There are three sets of Na-He pair potentials for excited states available in the literature: a) Na-He *l*-dependent pseudopotentials of Pascale[106, 119]; b) all-electron *ab initio* Multi-Reference Double excitation Configuration Interaction (MRD-CI) potentials of Jeung and coworkers [120, 121] ; c) *ab initio* MRD-CI pair potentials of Theodorakopoulos *et. al* [122]. The most complete pair potentials are those from Pascale, which include all molecular potential curves correlating to the atomic states from Na(3s) to Na(5g). The potentials of Jeung[120, 121] consist of only $^2\Sigma^+$ states of NaHe correlated to atomic states from Na(3s) to Na(6s). The pair potentials of Theodorakopoulos unfortunately do not extend beyond an internuclear distance of ≈ 10 Å, thus lacking the important information on medium-range sodium-helium interaction.

For our calculations we used the pair potentials of Pascale[106, 119], see Figure 3.45, since they are available at internuclear distances up to ≈ 25 Å and represent all molecular states needed to calculate the effective Na(n*l*)-He_N interaction potentials with $l>0$.

3.1.5.1.4 Calculated Na-He_N interaction potentials

The NaHe pair potentials and calculated effective Na-He_{5000} potentials are presented in Figure 3.45. The energy scales for the pair potentials differ from those for effective potentials in order to show the details of NaHe pair potentials. As can be seen in the figure, the Na-He_{5000} potentials considerably differ from the pair potentials. In contrast to the weakly bound Na(3s)-He_{5000} ground state, the excited Na-He_{5000} states are mainly repulsive. However, the interplay of bound and repulsive pair potentials can also result in bound Na-He_N potentials. This is the case for Na(3p)-He_N interaction: there are two minima with well depths of ≈ 10 cm^{-1} at z = 43 Å for the Π' and ≈ 4 cm^{-1} at z = 45 Å for the Σ' effective potentials. For the isotropic NaHe interaction as in the 4s state of Na, the highly repulsive N(4s)-He_N effective potential is due to the large helium density at the internuclear distance corresponding to the potential barrier in the pair potential. At the same time, at smaller internuclear distances, at which the interaction is attractive, the helium density is almost zero. This leads to the accumulating of the repulsive contribution coming from large Na-He distances according to equation 3.4.

3.1.5.1.5 Calculation of excitation spectra

In the view of difference between the time scale of electron motion of the order of 1 fs and the nuclei' motion of the order of 1 ps, the nuclear configuration of the system is thought to be frozen during the excitation step (Born-Oppenheimer approximation[123]). Furthermore, the Franck-Condon principle[124] is used to calculate the transition probabilities. This means that the transition between electronic molecular states is most probable without changes in the position of the nuclei. The transition involved is called a vertical transition. Thus, strictly speaking, absorption spectra are modeled. Nevertheless, we assume that the excitation spectra do not differ considerably from absorption spectra, so this approach is also applicable to the excitation spectra recorded in this work.

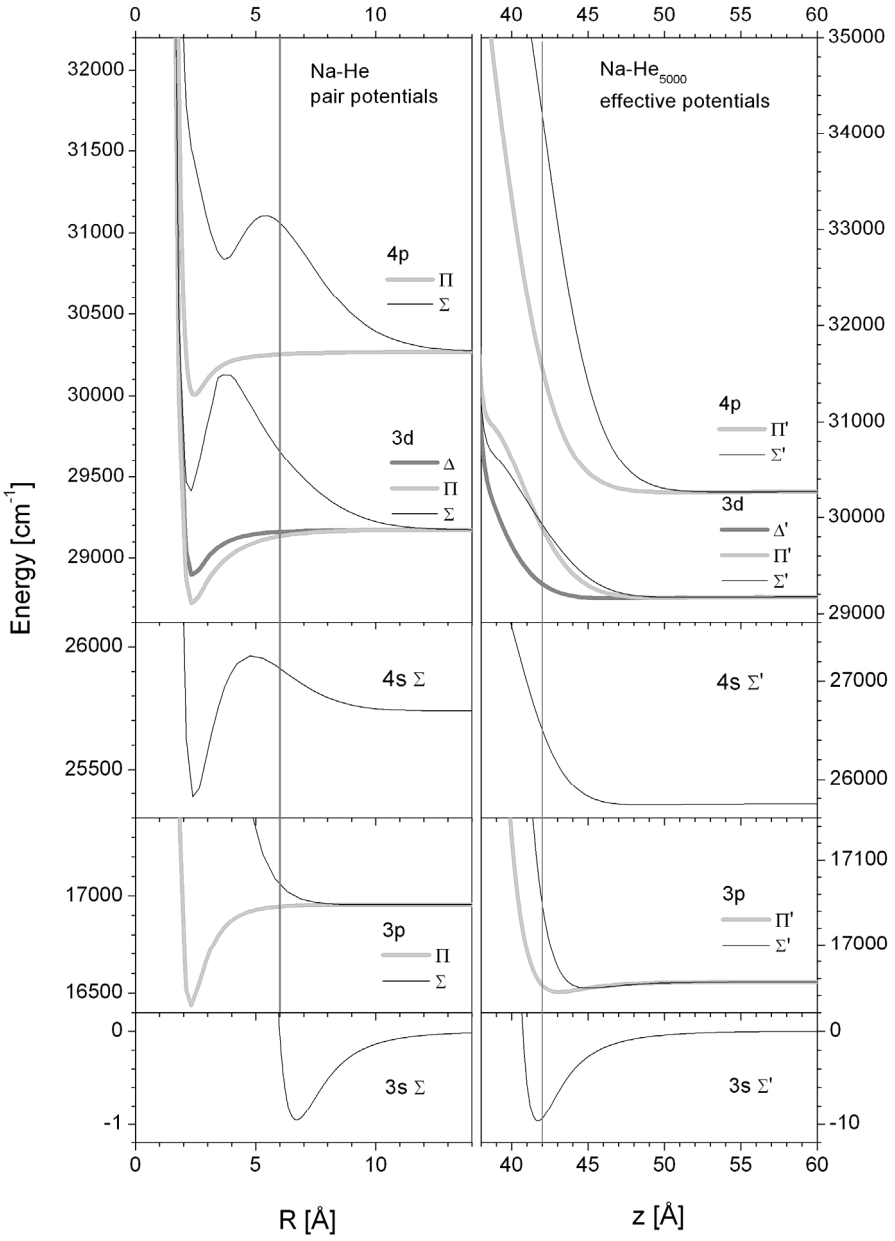

Figure 3.45: Left panels: NaHe pair potentials of Pascale[106, 119]. In the lowest panel the Na(3s)He pair potential is from Patil[118]. The vertical line indicates the distance between Na and the droplet surface in Na-He_N. Right panels: the corresponding Na(n*l*)-He_{5000} effective potentials are shown. The vertical line shows the Na location in the ground Na(3s)-He_{5000} state.

As a consequence of the frozen configuration, the dynamical features of the system such as fluctuations of helium density or excitation of the droplet (phonons, ripplons) are disregarded and are not reflected in the modeled spectra.

Since all effective potentials of the excited states of Na-He_N in Figure 3.45, except 3p, are exclusively repulsive, we will focus on transitions occurring between the bound electronic ground state and the unbound electronic excited states of Na-He_N. In the case of Na(3p)-He_N transitions between bound ground state and bound excited states can also take place and they were previously considered by Bunermann and coworkers in Ref[69]. We assume that the transition dipole moment is

constant within the region of the interaction potentials, where the transition takes place. We also suppose that at the ultra-low temperature 0.4 K of helium droplets only the ground vibrational and "rotational" states (*v"=0, J"=0*) of Na(3s)-He_N are populated. The term "rotation" for the complex system as Na-He_N is used to keep the correspondence to the case of diatomic molecule which is the basis of our approach. The "rotational" degree of freedom will be ignored in the following discussion. Taking into account all above assumptions, the transition probability within the Franck-Condon approximation can be written as:

3.13 $$P_{g,f}(E) \propto g_f \left|M_{gf}\right|^2 \left(\int_0^\infty \psi_g(z)\psi_{f,E}(z)dz\right)^2$$

where ψ_g is the radial wavefunction in the electronic ground state described by the $V_{Na-He_N}(3s\ \Sigma, z)$ bound potential, $\psi_{f,E}$ is the radial wavefunction in the electronic excited state described by the $V_{Na-He_N}(nl\ \Lambda, z)$ repulsive potential at energy E, M_{gf} is the electronic dipole transition moment, g_f is the electronic degeneracy factor in the excited electronic state. Since the diatomic states with $\Lambda>1$ are doubly degenerated, for the Π and Δ states g_f = 2. The Franck-Condon factors (FCF) $\left(\int_0^\infty \psi_g(z)\psi_{f,E}(z)dz\right)^2$ were calculated with the *BCONT 2.2* program of Le Roy[111] which solves one-dimensional Schrodinger equations in the potentials $V_{Na-He_N}(nl\ \Lambda, z)$. The absorption cross-section for a given Na(n*l*)-He_N←Na(3s)-He_N transition can be written as:

3.14 $$\sigma_{3s\to nl}(E) \propto \sum_{l=0}^{n-1} P_{3s,nl}(E)$$

We apply the diatomic approximation of Na-He_N interaction also for electric-dipole selection rules. The weak spin-orbit coupling in Na-He interaction corresponds to the (b) Hund's case[125] with the general rules for one- and two-photon of equal frequency[126] transitions :

$$\Delta S = 0$$

3.15

$\Delta J = 0, \pm 1,\ 0 \not\leftrightarrow 0$	$\Delta\Lambda = 0, \pm 1$	one-photon,
$\Delta J = 0, \pm 1, \pm 2$	$\Delta\Lambda = 0, \pm 1, \pm 2$	two-photon,

where S is the spin multiplicity, J is the total angular momentum and Λ is the projection of the J, apart from spin, on the molecular axis. The above selection rules imply that in one-photon excitation only n*l* Σ'←3s Σ' and n*l* Π'←3s Σ' transitions are allowed, and in the two-photon excitation n*l* Σ'←3s Σ', n*l* Π'←3s Σ' and n*l* Δ'←3s Σ' transitions are allowed. Chen and Yeung[126] evaluated transition probabilities in two-photon absorption and showed that for $|\Delta\Lambda|$ = 1,2 $|\Delta J|$=0,1,2 there is only one term in the expression for the transition probability, while in the case of $\Delta\Lambda$=0 for ΔJ=0 (Q-branch) there a sum of the two terms. The second term can give rise to extra intensity in the Q-branch in the two-photon excitation, which has been observed experimentally[127, 128]. Therefore, we expect stronger electronic transitions with $\Delta\Lambda$=0 compared to $|\Delta\Lambda|$=1,2 in the case of two-photon excitation.

3.1.5.1.6 Comparison of the experimental and calculated excitation spectra

In the following we will test the applicability of the pair-wise additive model for states higher than 3p by comparing the calculated excitation spectra of Na-He_N with experimental ones. The quality

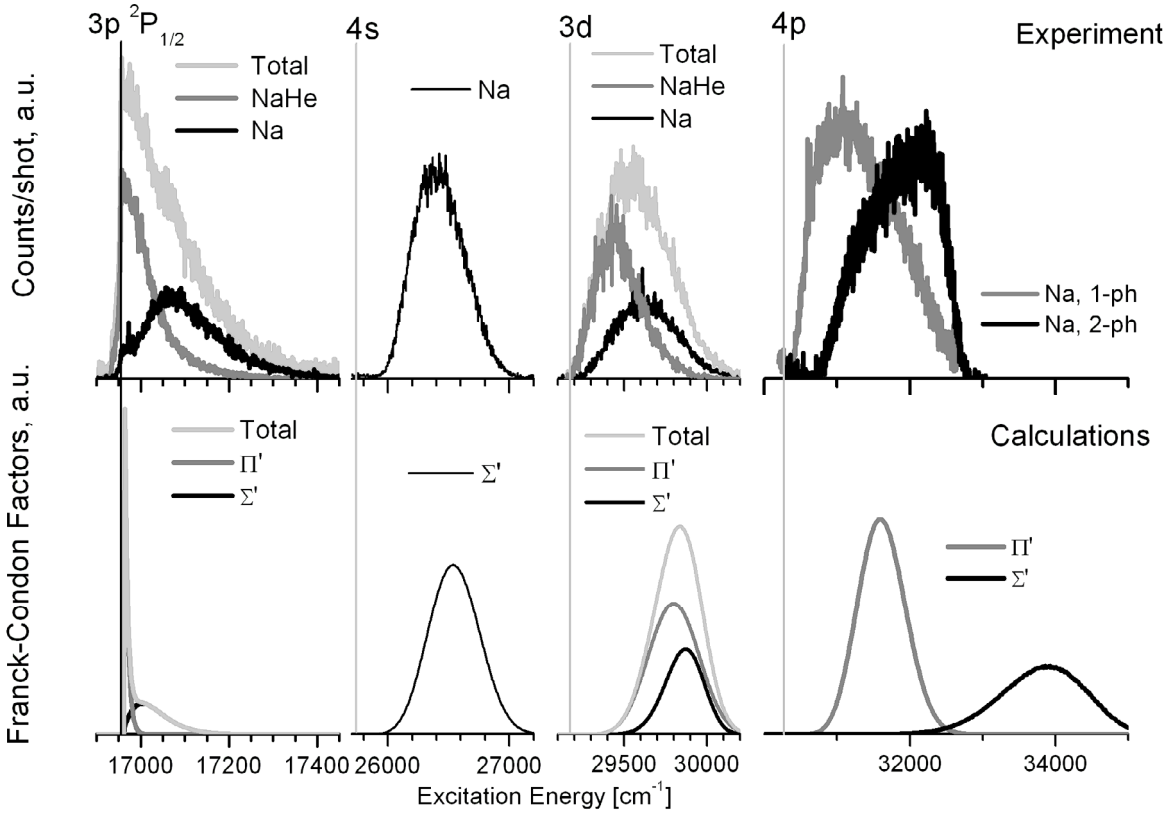

Figure 3.46: Comparison of the experimental excitation spectra recorded at mean droplet size of $\langle N_{He} \rangle$ = 6080 and the calculated spectra with the Na-He_{5000} density profile.

of the calculated spectra depends on several factors. Since the effective potentials are the sum of pair potentials over the helium atoms in the droplet, both the NaHe pair potentials and the Na-He_N density profile have considerable influence on the calculated spectra. On the other hand, the experimental conditions differ also from those used in the modeling. Whereas calculations are performed for single droplet size, the excitation spectra were recorded with the broad droplet size distributions, see section 2.1.2. Saturation may modify the shape of spectra, which is certainly the case in the 3p-band and probably in 4p-band, see section 3.1.5.1.6.5. In view of the arguments mentioned above, only the overall shape and the position of the calculated spectra are expected to match the experiment. Droplet size effects will only by qualitatively discussed.

As can be seen from Figure 3.45, the vertical transitions between the bound ground state and the repulsive excited states will result in considerable shift from the corresponding atomic transitions. Furthermore, the width of the spectrum is determined by the width of ground state wavefunction and the slope of the upper repulsive potential (Franck-Condon mapping). Indeed, the calculated spectra are broad and correspond well to the experiment data upto the 4p-excitation band, see Figure 3.46. In general, the calculated spectra are shifted by several 100 cm^{-1} to higher frequencies compared to the experimental ones. The exception is the 3p-band spectrum, where the calculated $\Sigma \leftarrow \Sigma$ transition is shifted to the red by ≈ 100 cm^{-1}. The discrepancies in the frequency are the largest in the 4p-band for calculated $\Sigma \leftarrow \Sigma$ transition which is blue-shifted by more than 1 000 cm^{-1} with respect to the experimental spectrum.

The widths of the calculated spectra are in general narrower than those of experimental spectra by a factor of 2. Only the calculated 4s spectrum has a width similar to that found experimentally.

The described discrepancies may partially reflect the quality of the Na-He pair potentials. Indeed, the use of Na(4s)-He potential of Jeung et al.[120, 121], which is obtained at a higher level theory than that of Pascale[106, 119], leads to better agreement between theoretical (not shown) and experimental spectrm. This is due to the systematically more repulsive pair potential of Pascale compared to that of Jeung *et al.*. The Na(3s)-He ground state potential is as important as the excited states potentials because it determines the Na-He_N density profile[19], the starting point in our calculations.

It is interesting to note that there is a pronounced correlation between the fragment-specific excitation spectra and the type of calculated transition. The Na-excitation spectra correspond to Σ←Σ while the NaHe-excitation spectra correspond to Π←Σ transitions. This correlation will be discussed in section 3.1.5.2.

It is also interesting to check how well the droplet size effect in the excitation spectra can be reproduced within the pair-wise additive model of Na-He_N interaction. There are a number of factors that limit a quantitative comparison. On the theoretical side, there are only two, Na-He_{1000} and Na-He_{5000}, density profiles are at our disposal. This is obviously not enough to follow the evolution of the size effects along the wide range $<N_{He}>$ ≈ 2 000 - 20 000 of experimental mean droplet sizes, see Chapter 2. Furthermore, the spectra recorded at given mean droplet size are convoluted by the broad droplet size distribution. The latter might result in broader experimental spectra compared to the calculated spectra.

3.1.5.1.6.1 3p-band

A comparison of the calculated and the experimental species-specific 3p←3s spectra is presented in Figure 3.47. The overall agreement between the calculated 3p Σ'←3s Σ' and spectra and experimental Na-specific and NaHe-specific excitation spectra, respectively, is good. The calculated spectra with a FWHM ≈ 100 cm^{-1} are narrower by a factor of 2 than the experimental spectra with a FWHM ≈ 200 cm^{-1}. The 3p Π'←3s Σ' calculated spectra with a FWHM ≈ 10 cm^{-1} are a factor of 5 narrower than the experimental NaHe-specific spectra with a FWHM ≈ 50 cm^{-1}. The possible explanation of these discrepancies may be saturation effects that are discussed in section 3.1.5.1.6.5.

The difference of ≈ 5 cm^{-1} between 3p Σ'←3s Σ' and 3p Π'←3s Σ' transitons calculated with Na-He_{1000} and Na-He_{5000} correctly follows the the trend in the experimental spectra, where the

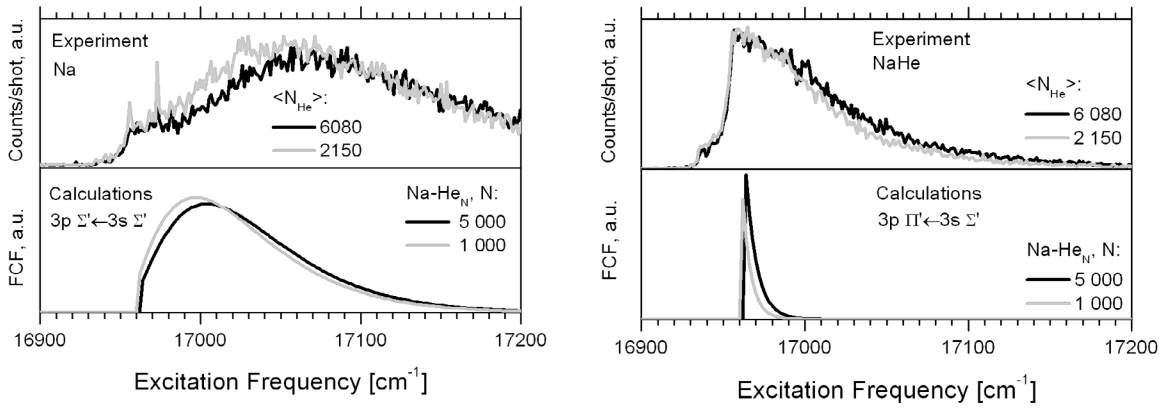

Figure 3.47: Comparison of the experimental excitation spectra of the 3p-band recorded at different droplet sizes and the modeled Na(3p)-He_N←Na(3s)-He_N absorption spectra.

difference can be estimated as ≈ 10 cm^{-1} between relevant mean droplet size of $\langle N_{He} \rangle$ = 2150 ($\langle r \rangle$ = 29 Å) and $\langle N_{He} \rangle$ = 6080 ($\langle r \rangle$ = 41 Å).

The state-selective Na excitation spectra in Figure 3.4 are not well understood. First, the intensity ratio of Na(3p $^2P_{1/2}$) to Na(3p $^2P_{3/2}$) is 3 to 1. This is in contrast to the ratio of Na(3p $^2P_{1/2}$)← Na(3s $^2S_{1/2}$) and Na(3p $^2P_{3/2}$)← Na(3s $^2S_{1/2}$) in the free atomic transitions[99] which equals 1 to 2. Secondly, two contributions clearly correspond to the two spin-orbit (SO) states of Na and not to a single SO state. This indicates that Na in the two sping-orbit states interacts differently with the helium droplet and that these states are mixed due to the helium-induced perturbation. The observed disproportion in the intensities of the excitation spectra might be related to the $NaHe_n$ exciplex formation on the surface of nanodroplets, see section 3.1.5.2.

3.1.5.1.6.2 4s-band

In the case of 4s excitation band there is the best correspondence of the calculated and experimental spectra, see Figure 3.48. There is an overall ≈ 150 cm^{-1} offset of calculated spectra to the high frequencies with respect to experimental spectra. The droplet size dependent shift of ≈ 100 cm^{-1} and the FWHM ≈ 500 cm^{-1} are reproduced correctly. The isotropic character of Na(4s)-He pair potential and the large separation in energy of the Na(4s) state from adjacent excited states are thought to be the origin of this good result within the pair-wise additive model which disregards the droplet-induced perturbations of the Na-He pair potentials.

3.1.5.1.6.3 3d-band

We present a comparison of the species-specific experimental spectra and calculated spectra in Figure 3.49. It is found that the calculated 3d Σ'←3s Σ' transition depends very weakly on the density profile used: the spectrum calculated with $Na\text{-}He_{1000}$ profile is red shifted by ≈ 15 cm^{-1} compared to that of $Na\text{-}He_{5000}$. Such a small difference cannot be distinguished at the energy scale in Figure 3.49. This theoretical finding corresponds well to the very weak droplet size dependent shift of the

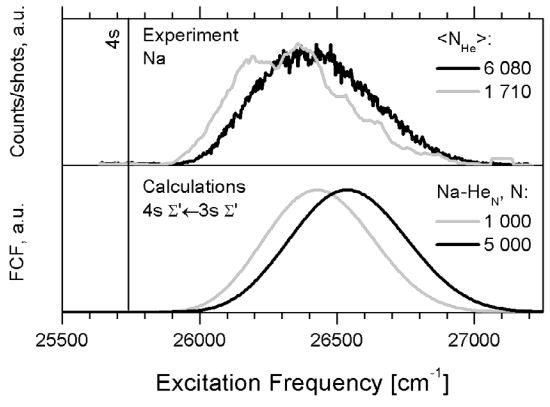

Figure 3.48: Comparison of the experimental excitation spectra of the 4s-band recorded at different droplet sizes and the modeled Na(4s)-He_N←Na(3s)-He_N absorption spectra.

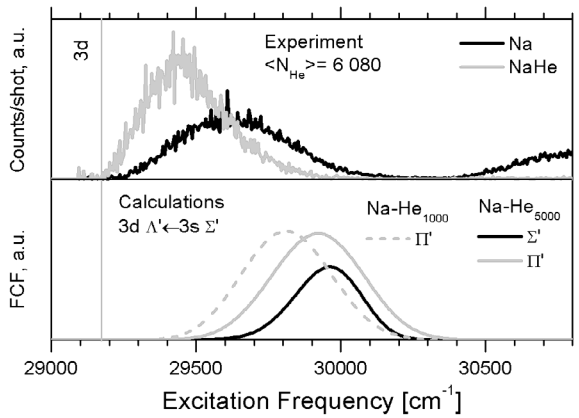

Figure 3.49: Comparison of the experimental excitation spectra of the 3d-band and the modeled Na(3d)-He_N←Na(3s)-He_N absorption spectra. The 3d Σ'←3s Σ' calculated transition depends very weakly on the Na-He_N density profile, so only the spectrum calculated with $Na\text{-}He_{5000}$ density profile is shown.

Na-specific excitation spectrum which is estimated in the experiment to be less than 30 cm^{-1} over $<N_{He}>$ = 1 750 - 20 000 range of helium droplets. The theoretical 3d Π'←3s Σ' transition demonstrates a pronounced size effect. For Na-He_{1000} the calculated 3d Π'←3s Σ' transition is red-shifted by ≈ 150 cm^{-1} compared to that of Na-He_{5000}. This is in contrast to the experimental observation, where such large shift is not observed in any of the species-specific excitation spectra. The 3d Δ'←3s Σ' transitions are not shown because they are forbidden for a one-photon transition in the ideal diatomic molecule, see expression 3.15.

3.1.5.1.6.4 4p-band

A transition-specific droplet size effect was found in the modeled spectra corresponding to the 4p-band, see Figure 3.50. The 4p Π'←3s Σ' and 4p Σ'←3s Σ' transitions calculated with the Na-He_{1000} density profiles are red shifted by ≈ 600 cm^{-1} and ≈ 300 cm^{-1} respectively from those calculated with the Na-He_{5000} profile. The more pronounced dependence of 4p Π'←3s Σ' transition on cluster size correlates well to the experimental one-photon transition. Indeed, in the low frequency part of the experimental one-photon spectrum, which is associated with the 4p Π'←3s Σ' transition, a shift of ≈ 150 cm^{-1} is observed between mean droplet sizes $<N_{He}>$ = 6 080 and of $<N_{He}>$ = 1 710. Additional evidence of the probable location of the 4p Σ'←3s Σ' transition in the high frequency part of the 4p-band is the positive angulare anisotropy parameter of desorbed excited sodium atoms which is characteristic to a Σ←Σ transition in a diatomic molecules, see section 3.1.5.4. This may imply that in the two-photon excitation spectra we observe mainly 4p Σ'←3s Σ'. As a consequence, this may indicate that the probability of the two-photon 4p Σ'←←3s Σ' transition is considerably larger than that of 4p Π'←←3s Σ'.

It is also worth to note the asymmetric shapes of the one- and two-photon experimental excitation spectra in the 4p-band. A possible explanation may the saturation of transition in the experimental spectra. A rough estimation of saturation is considered below.

The revealed discrepancies between the experimental and theoretical spectra in 3d and 4p bands indicate that the pair-wise additive model start to break down for high excited states of Na-He_N and more realistic approach is required.

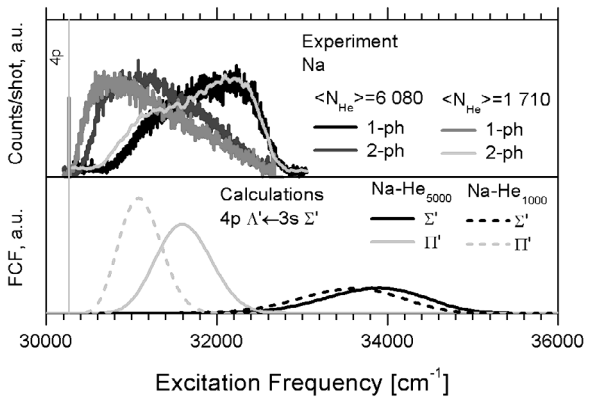

Figure 3.50: Comparison of the experimental excitation spectra in the 4p-band recorded at different droplet sizes and the modeled Na(4p)-He_N←Na(3s)-He_N absorption spectra.

3.1.5.1.6.5 Saturation effects in the 3p- and 4p-bands

The comparison of our Na-He_N excitation spectra of the 3p-band and the excitation spectra recorded with LIF[69] shows that in our case power saturation is probable. Below we estimate on the basis of a classical two-level system[129] the power saturation in Na-He_N transitions that correlate to the allowed atomic 4p, 3p←3s transitions.

It can be shown that the integral absorption cross-section of a two-level system irradiated by a plane wave is a constant, which does not depend on line-broadening process[129]:

3.16 $$\int_{-\infty}^{\infty} \sigma(\omega) d\omega = \frac{\hbar \omega_{12} B_{12}}{c}$$

where ω_{12} is the transition frequency from the lower level 1 to the higher level 2, c is the speed of light, B_{12} is the Einstein coefficient. We will assume that a free Na atom and Na-He_N can be described by a two-level system so that the integral Na np←3s absorption cross-sections are constant even when being perturbed by the helium droplet. For simplicity we approximate both the atomic and Na-He_N frequency dependent cross-section by rectangular profiles with constant values $\sigma^0_{Na}(\omega)$, $\sigma^0_{Na-He_N}(\omega)$ and frequency ranges $\Delta\omega_{Na}$, $\Delta\omega_{Na-He_N}$ which are equal to the FWHM of respective transitions:

3.17
$$\sigma_{Na}(\omega) = \sigma^0_{Na}(\omega), \text{ for } \omega^0_{Na} - \Delta\omega_{Na}/2 \le \omega \le \omega^0_{Na} + \Delta\omega_{Na}/2$$
$$\sigma_{Na-He_N}(\omega) = \sigma^0_{Na-He_N}(\omega), \text{ for } \omega^0_{Na-He_N} - \Delta\omega_{Na-He_N}/2 \le \omega \le \omega^0_{Na-He_N} + \Delta\omega_{Na-He_N}/2$$

where ω^0_{Na} and $\omega^0_{Na-He_N}$ are the centers of the respective transitions. From the expression 3.16 it follows that:

3.18 $$\sigma^0_{Na}(\omega)\Delta\omega_{Na} = \sigma^0_{Na-He_N}(\omega)\Delta\omega_{Na-He_N}$$

So, the magnitude of the absorption cross-section for Na-He_N will be lowered with respect to atomic case as:

3.19 $$\sigma^0_{Na-He_N}(\omega) = \sigma^0_{Na}(\omega)\frac{\Delta\omega_{Na}}{\Delta\omega_{Na-He_N}}$$

For $\Delta\omega_{Na}$ we take the natural line width which relates to the radiative lifetime τ_{rad} as:

3.20 $$\Delta\omega_{Na} = \frac{1}{\tau_{rad}}$$

The absorption cross-section for atomic Na at the center of the absorption line, neglecting any broadening, can be written as[129]:

3.21 $$\sigma^0_{Na}(\omega) = \frac{{\lambda_{Na}}^2}{2\pi} = 2\pi\frac{c^2}{{\omega_{Na}}^2}$$

where ω_{Na} is the frequency of the atomic transition. This result is valid if the lineshape is a Lorentzian, when the linewidth is associated with only one upper level. We will use this assumption for 3p and 4p excited levels of Na.

The saturation condition for the pulsed excitation, when the duration of the laser pulse is shorter than the relaxation time of the upper level, may be expressed as[130]:

3.22 $$I \geq \frac{\hbar\omega}{2\sigma}$$

where I in [J/cm^2] is the fluence of exciting radiation and σ is the cross-section in [cm^2]. The radiation lifetime of np levels of Na are larger than 16 ns[131] compared to the FWHM = 11 ns of the excitation laser pulse, thus we will neglect the population loss during the excitation laser pulse and will use the expression 3.22 for all np states. By substituting the expressions 3.21 and 3.20 into 3.19 and the latter into 3.22 we get:

3.23 $$I \geq \frac{\hbar}{4\pi c^2}\tau_{rad}\omega_{Na}{}^2\omega_{Na-He_N}\Delta\omega_{Na-He_N}$$

where ω_{Na-He_N} is the center of the Na-He$_N$ transition. To simplify the evaluation we take $\omega_{Na-He_N} \approx \omega_{Na}$ and rewrite the above expression for use with frequency $\tilde{\nu}$ in [cm^{-1}], τ_{rad} in [ns]:

3.24 $$I \geq 1.17\cdot 10^{-20}\tau_{rad}\tilde{\nu}^3\Delta\tilde{\nu}_{Na-He_N}$$

We take $\tilde{\nu}$ and $\Delta\tilde{\nu}_{Na-He_N}$ approximately as the center and the FWHM of the experimental excitation spectrum as the starting values. The results of estimation are collected in Table 9.

We conclude that the excitation spectrum in the 3p-band is saturated, which is in agreement with the comparison of our spectrum and the previously reported spectrum recorded with LIF[69]. Furthermore, the excitation transition in the 4p-band seems to be considerably saturated. The power saturation may also explain the asymmetric shape of the one-photon excitation spectrum, since in this case both type of transitions are allowed. This may result in the spectral overlap of two adjacent and saturated transitions into one broad feature.

It is difficult to foresee whether the above approach is applicable for normally forbidden ns←3s and nd←3s atomic transitions. The conservation of the integral absorption cross-section 3.16 in this case cannot be used directly. Instead, the quantum-mechanical calculation of the transition dipole moments for Na-He$_N$ system is required.

Table 9 Estimation of power saturation in the 3p and 4p-bands

	$\tilde{\nu}$ [cm^{-1}]	$\Delta\tilde{\nu}_{Na-He_N}$ [cm^{-1}]	τ_{rad} [ns]	I$_{est}$ [J/cm^2] estimation	I$_{exp}$ [J/cm^2] experiment
3p	17 000	100	16	$9\cdot10^{-5}$	$7\cdot10^{-4}$
4p	31 000	1 000	125	$4\cdot10^{-2}$	1.3

3.1.5.1.7 Conclusion

In conclusion, the excitation spectra of Na-He$_N$ corresponding to 3p, 4s, 3d and 4p excited states of free sodium can be qualitatively reproduced with the pair-wise additive model of Na-He$_N$

interaction. The discrepancy between the calculated spectra and the experimental spectra can be attributed to the quality of the Na-He pair potentials and density profiles of Na-He_N used for modeling, and to the simplicity of the static model that disregards dynamical effects. The saturation of transitions in the experiments could also affect the shape of recorded spectra.

3.1.5.2 Exciplex formation

3.1.5.2.1 A possible model

In the following we will apply the model proposed by Reho and coworkers[74] to describe the Na(3p)-He exciplex formation to the exciplex formation in higher excited states of sodium. In the original model, the authors assume that the excited Na is temporarily bound at the surface of the helium droplet, since the one dimensional Na(3p)-He_N potentials have shallow minima at slightly larger distance than in the ground electronic state. The exciplex formation is then determined by the tunneling of a helium atom along the effective Na-He-He_N potential. The latter results from the folding of the Na-He pair potential and the He-He_N potential representing the interaction of the helium atom with the droplet's surface.

The He-He_N potential was taken from the basic model of Eichenauer and Le Roy[132], in which an atom, described as a hard sphere of the radius a, interacts via $1/r^6$ law with atoms of a semi-infinite liquid with a sharply defined surface. The He-He_N potential is obtained by integration over all He atoms outside the excluded radius a and has the following form:

3.25
$$V(h)=\begin{cases} -\left(\dfrac{\pi\rho C_6}{6}\dfrac{1}{h^3}\right) & a<h<\infty, \\ -\left[\dfrac{\pi\rho C_6}{2a^3}\left(\dfrac{1}{3}+\dfrac{a-h}{a}\right)\right] & -a\le h\le a, \\ -\left(\dfrac{4\pi\rho C_6}{3a^3}\right)+\left(\dfrac{\pi\rho C_6}{6}\dfrac{1}{|h|^3}\right) & h<-a, \end{cases}$$

where h is the height above the helium surface, ρ = 0.0218 Å^{-3} is the bulk helium density of a droplet, a = 3.35 Å is the radius of the He atom chosen such that V(-∞) = - 16.72 cm^{-1}, which is the potential energy of the He atom in bulk helium[1]; C_6 = 6 892 cm^{-1} Å^6 is the dispersion coefficient[133]. Most of the attractive part of *V(h)* potential develops over the - 4 Å ≤ h ≤ 4 Å range, see the upper panel in Figure 3.51.

The NaHe pair potentials of Pascale[106, 119] do not take into account the spin-orbit effects, so they have only one $^2\Pi$ potential curve correlating to the Na(n^2P) + He asymptotes. Reho *et al.*[74] showed that the SO effects play an important role in the exciplex formation. The SO splitting Δ_{SO} is assumed to be independent of internuclear disctance and to equal to the SO splitting in the ^{2}P state of Na. The SO splitted potential curves were calculated on the basis of potential curves $V_\Sigma(R)$ and $V_\Pi(R)$ of Pascale using the approach of Cohen and Schneider[134] by diagonalizating the effective Hamiltonian in the $\left[{}^2\Pi_{3/2}, {}^2\Pi_{1/2}, {}^2\Sigma_{1/2}\right]$ basis set at each internuclear distance R :

3.26
$$\begin{bmatrix} V_{\Sigma}(R) & \frac{\sqrt{2}}{3}\Delta_{SO} & 0 \\ \frac{\sqrt{2}}{3}\Delta_{SO} & V_{\Pi}(R)-\frac{\Delta_{SO}}{3} & 0 \\ 0 & 0 & V_{\Pi}(R)+\frac{\Delta_{SO}}{3} \end{bmatrix}$$

The folding of the NaHe and He-He_N potentials is done by summing the He-He_N and Na-He pair potential using the height of Na atom above the helium droplet surface h = 7 Å extracted from Na-He_N density profiles of Barranco's group[116]. The folding may introduce a potential barrier in the otherwise purely attractive pair potentials as in the case of Na(3p $^2P_{3/2}$)-He-He_N interaction[74], see also lower panel in Figure 3.51. In the folded potential corresponding to Na(3p $^2P_{1/2}$) the barrier is even higher due to the modification of the $V_{\Pi}(R)$ potential curve by SO coupling procedure.

The next important aspect of the model is the location of the excited Na. Reho *et al.*[74] took this distance as 8.56 Å based on the calculations by Kanorski in Ref[69] who approximated the Na-droplet potentials by the "Na-infinite helium surface" potentials using the helium density profiles calculated by Ancilotto[44].

The upper limit of probability for He atom from the helium surface to tunnel through those barriers in Na(3p $^2P_{3/2}$)-He-He_N potentials was estimated with quasi-classical theory as:

3.27
$$T = \exp\left(-\frac{2}{\hbar}\int_a^b \sqrt{2\mu\left(U(x)-E\right)}dx\right)$$

where μ = 3.4 amu is the reduced mass of the NaHe exciplex, $E = E_{kin}/3 \approx 4$ cm^{-1} is the kinetic energy of the helium atom in the reaction coordinate. $E_{kin} = E_{pot} - E_{bound}$ is the kinetic energy determined as the difference between the E_{pot} = 16.72 cm^{-1} potential energy of the He atom in the bulk helium and the E_{bound} = 5 cm^{-1} binding energy of the He to the surface of helium[1]; a and b are the barrier's coordinates at points $U(x) = E$. This probability multiplied by the attempt frequency of the He atom to overcome the potential barrier represents the inverse tunneling time. This frequency was set to be 10^{12} Hz, the Debye frequency of liquid helium[74]. The tunneling time was considered by Reho *et al.*[74] as the formation time of the exciplex.

As was pointed out by Droppelmann *et al.*[75], the above model does not take into account the necessary vibrational relaxation of the created exciplex. The formed exciplex without energy relaxation can dissociate via tunneling through the barrier as well. In addition, we point out that the desorption of the excited Na, which is caused by the overall repulsive interaction of Na(3p)-He_N, is also important if it occurs on the time scale of tunneling and vibrational relaxation. Thus, the exciplex formation may reflect the interplay of the desorption dynamics of excited Na, the tunneling through the potential barrier and the vibrational relaxation of the exciplex.

3.1.5.2.2 Application of the model

Below we will consider how the model of Reho *et al.*[74] presented above is applicable to excited states of Na-He_N higher than 3p. The difference between our calculations and those of Reho is the use of density profile of the droplet instead of infinite helium surface to calculate Na-He-He_N potentials.

3.1.5.2.2.1 3p-band

The use of Na-He_{5000} density profiles of Barranco[116] yields z = 43 Å as the location of the bound potential well in the Na(3p Π')-He_N effective potential. This results in a shorter "Na(3p)-helium surface" distance of 6 Å, compared to 8.56 Å taken by Reho *et al.*[74]. The distance of 6 Å correspond approximately to the distance where the droplet density attains the bulk value. As a consequence, the centering of the He-He_N potential in expression 3.25 at the distance of 6 Å results in lower potential barriers : ≈ 4 cm^{-1} versus 7.8 cm^{-1} along $^2\Pi_{3/2}$ potential curve and ≈ 7 cm^{-1} versus 11.2 cm^{-1} along $^2\Pi_{1/2}$. At the same time, the positions of the potential barriers at R = 7.5 Å and R = 7 Å did not practically change. Thus, the exciplex formation in the configuration of Na-He_{5000} should be barrierless, which contradicts to the results of Reho *et al.*[74]. The contradiction originates from the assumed static location of the excited Na(3p) by the droplet surface and from the implicit

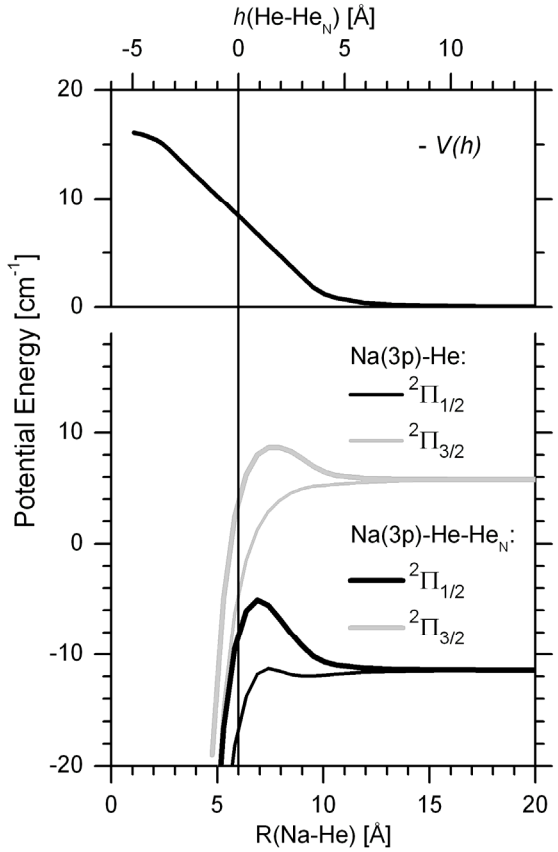

Figure 3.51: Upper panel: He-He_N potential. h = R(Na-He) - R_e(Na*-He_N), where R_e(Na*-He_N) = 6 Å is the distance between excited Na(3p) and He_N in the bound well along Na(3p Π')-He_N effective potential, see Figure 3.45. Lower panel: Comparison of the Na(3p)-He pair potentials with the effective Na(3p)-He-He_N potentials obtained by folding the Na(3p)-He with He-He_N potential. The vertical line shows R_e(Na*-He_N).

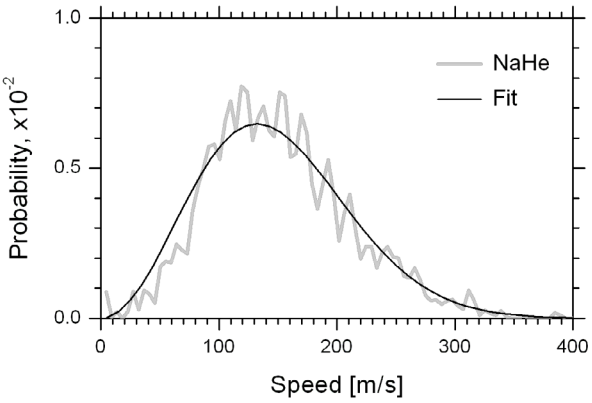

Figure 3.52: Comparison of the experimental speed distributions of the desorbed NaHe from Figure 3.20 with the fitted Maxwell-Boltzmann speed distribution yielding T = 28.6±0.6 K.

immediate stability of the formed exciplex. Below we will discuss these two issues.

Timescale of the species desorption. First, we consider the desorption timescale of the bare excited sodium and exciplexes. It is important to realize that only the final velocity distribution, which reflects the situation several nanoseconds after the excitation, is recorded in our experiment. Thus, the estimated time scale given below is based on the velocity distributions of excited Na and NaHe which reflects the Na-He_N configuration at the moment when presumably all dynamics on the surface of helium droplet has been accomplished.

The experimental data presented in section 3.1.1.4 show that the lowest mean kinetic energy of desorbed Na(3p ^2P) $\langle E_{kin}(Na)\rangle \approx 5$ cm^{-1} at the excitation frequency of 17 000 cm^{-1}. That kinetic energy corresponds to the mean speed $\langle v(Na)\rangle \approx 73$ m/s. We take the Na(3p)-He_N distance, at which the excited Na is considered as complitly desorbed so that its interaction with helium droplets stops and the exciplex formation is no more possible, to be 16 Å compared to the initial 6 Å in the electronic ground state, see the lower panel in Figure 3.51. For the simplicity, we also assume that the excited Na atoms leave the droplet surface always along z-axis shown in Figure 3.43. Thus, the excited Na(3p) should pass the distance of 10 Å to leave definitely the droplet, after which the exciplex formation is thought to be impossible. The resulting time $\left\langle \tau_{desorp}\left(\mathrm{Na}\right)\right\rangle \approx$ 14 ps is thus the upper limit of the desorption time scale for the slowest Na(3p). The $\langle E_{kin}(Na)\rangle$ reaches the value of ≈ 50 cm^{-1} at the excitation frequency of 17 250 cm^{-1}, so the desorption time decreases as $1/(\langle E_{kin}\rangle)^{1/2}$ by a factor of ≈ 3 down to 4.4 ps, which is taken as the low limit of the desorption timescale. The estimated desorption times are in line with the 70 ps upper limit of the onset time of Na atomic fluorescence measured by Reho *et al.*[72].

The mean kinetic energy $\langle E_{kin}(NaHe)\rangle = 28$ cm^{-1} of the NaHe exciplex does not vary with excitation frequency, see Figure 3.22. This yields the $\langle v(NaHe)\rangle \approx 160$ m/s and the desorption time $\left\langle \tau_{desorp}\left(\mathrm{NaHe}\right)\right\rangle \approx$ 6 ps which is two orders of magnitude smaller than the 700 ps onset of the NaHe fluorescence measured in the experiments of Reho *et al.*[72]. A possible explanation of this discrepancy may be the "thermal" desorption of the formed exciplex from the droplet surface. In this case, the NaHe may be temporarily bound to the helium surface, which allows for vibrational relaxation of the formed exciplex by the cold droplet. The subsequent desorption is thus caused by the conversion of vibrational to translational energy. The isotropic speed distribution of NaHe, see Figure 3.20 and Figure 3.22, and the Maxwell-Boltzmann profile of the speed distribution with the effective temperature of T = 28.6±0.6 K, see Figure 3.52, support this hypothesis.

Contrary to the case of exciplex desorption, the velocity distribution of Na resembles the fast diatomic-like dissociation event, since the mean value of angular anisotropy parameters for desorbed Na species correlate with that in the dissociation of diatomic molecules via Π'←Σ' and Σ'←Σ' transitions, see section 3.1.5.4. This way, the desorption of bare Na(3p) is thought to be "direct".

Population of the vibrational levels of NaHe. Second, we consider the population of the vibrational levels of the desorbed NaHe. The spectral analysis of the NaHe fluorescence by Reho *et al.*[71, 72] showed that mainly the lowest four vibrational levels of desorbed Na(3p)He, v"=0-3, are populated. They also found that the population of the vibrational level depends on the excitation frequency. At higher excitation frequencies higher vibrational levels with v"=2-3 are more populated. Our experimental data on the ZEKE spectroscopy of desorbed NaHe, see section 3.1.1.3, is in agreement with those results. The population of low vibrational states indicates that the relaxation of NaHe should take place on the surface of nanodroplet prior to the desorption, which necessitates the temporal trapping of NaHe on the droplet surface. During the relaxation, the correlation between the

transition dipole moment and the direction of the desorption, see section 3.1.5.4.1.2, is lost. This may lead to the isotropic angular distribution of the desorbed exciplexes.

Droplet size effects and $NaHe_n$, n>1, exciplexes. In their analysis of the fluorescence from desorbed species, Reho *et al.*[71] suggested that, apart from NaHe exciplex, a small amount of the $NaHe_2$ was formed as well. In our experiments, we discovered the formation of even heavier $NaHe_n$, n = 3 - 4, exciplex at appreciable quantities. The absence of exciplexes with n > 4 is in agreement with the work of Enomoto *et al.*[105] who found that heavier exciplexes are unstable. If we assume that the formation energy of $NaHe_n$ exciplexes equals to the sum of the pair NaHe energies then the cooling of the vibrationally excited heavy exciplexes on the droplet surface should be more efficient compared to that of NaHe in order to stabilize them. The small, less than 8%, relative abundance of $NaHe_n$, n = 3 - 4, see Figure 3.8 and Figure 3.9, indicates that the vibrational relaxation may be incomplete. In addition, the droplet size effects points to the fact that at larger droplets the relaxation is more efficient, resulting in higher outcome of heavy exciplexes. This can be seen in Figure 3.9, where the relative abundances of Na and $NaHe_n$, n = 2 - 4, obtained at fixed excitation frequency but at different droplet sizes are strongly correlated: an increase in the mean droplet size results in the decrease of Na abundance and in the corresponding increase of exciplexes' abundances. However, there is only small variation of the NaHe abundance against droplet size. This may originate from the interplay of the dissociative ionization of heavier exciplexes in our detection scheme and the droplet size effects.

3.1.5.2.2.2 4s-band

The absence of exciplexes formation within the 4s-band, see section 3.1.2, may be explained by the hindrance of Na-He formation due to the potential barrier in the Na(4s)-He pair potential. It is centered at 5 Å of internuclear distance and has the height of ≈ 226 cm^{-1}, see Figure 3.53. The barrier is rather broad with the FWHM ≈ 4 Å. The Na atom after the excitation is located on the repulsive side of the potential barrier. Furthermore, the Na(4s)-He_N effective potential is strongly repulsive

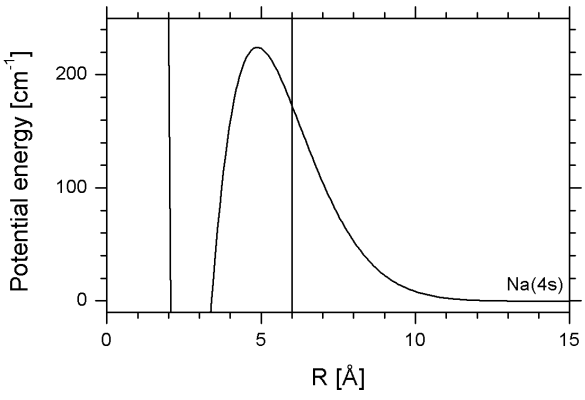

Figure 3.53: Na(4s)He pair potential of Pascale[106, 119] in relative energy scale in order to show the potential barrier and the assumed internuclear distance (vertical line) for the estimation of the tunneling probability. See the text for details.

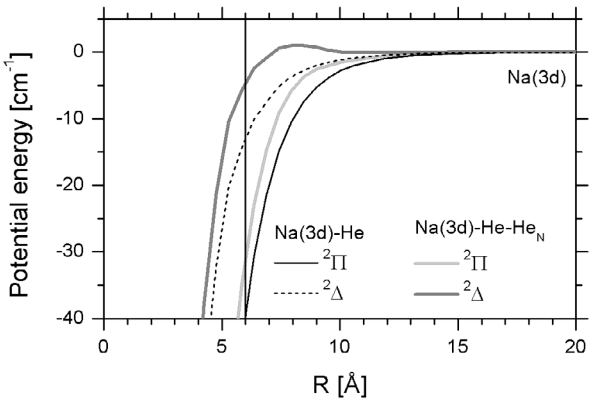

Figure 3.54: Na(3d)He pair potentials of Pascale[106, 119] and the effective Na(3d)-He-He_N potentials in relative energy scale in order to show the effect of folding the pair potentials and the He-He_N potential. The vertical line shows the assumed initial NaHe internuclear position after the excitation of Na-He_N.

without any bound well. Therefore, the excited Na should rapidly leave the droplet surface and the exciplex formation will be quenched by the barrier. This picture corresponds to the experiment.

We will estimate the upper limit of the probability of exciplex formation within the model of Reho *et al.*[74] according to equation 3.27. We assume that after the excitation the Na(4s) stays at the same location, 6 Å from the droplet surface. The height of the potential barrier is much larger than the 16.72 cm^{-1} depth of the He-He_N potentials, so we will neglect the folding procedure, which will make it even higher. Instead, we will use only the original Na(4s)He pair potential of Pascale[106, 119]. The internuclear distance of 6 Å corresponds to the tunneling of Na(4s) through the effective potential barrier of ≈ 54 cm^{-1} height and ≈ 2 Å width, see Figure 3.53. The numerical integration of the expression 3.27 over this barrier yields $T \approx 2 \cdot 10^{-4}$. The inverse of the product of this probability and 10^{12} s^{-1} of the attempt frequency yields the tunneling time of 5 ns. We will compare this time with the mean desorption time of the slowest Na, the velocity distribution of which was recorded at 26 100 cm^{-1} of excitation frequency. Following the approach from the previous section, we find that the $\langle v(Na) \rangle \approx 440$ m/s at $\langle E_{kin}(Na) \rangle \approx 180$ cm^{-1} from Figure 3.27. The mean desorption time is then $\left\langle \tau_{desorp}\left(\mathrm{Na}\right)\right\rangle \approx 2$ ps. This is three orders of magnitude smaller than the estimated tunneling time. Thus, the fast desorption of excited sodium from the surface of helium nanocluster, caused by the overall strong repulsive interaction with the entire droplet, quenches the local exciplex formation via tunneling through the potential barrier in Na(4s)-He-He_N potential.

3.1.5.2.2.3 3d-band

Within the 3d-band the relative abundance of NaHe reaches a value of 0.7 at the excitation energy of 29 300 cm^{-1}, see Figure 3.29, which is similar to the case of 3p-band. Droplet size effects on the relative abundances of exciplexes were observed as well. In contrast, there is no pronounced formation of heavier $NaHe_n$, n > 1, exciplexes: the abundance of the $NaHe_2$ is inferior to 0.1, see section 3.1.3.2. Below we again apply the same approach used above for the 3p and 4s bands to analyze the exciplex formation in the 3d band.

To generate the Na(3d)-He-He_N effective potentials we used the original 3d $^2\Delta$ and $^2\Pi$ NaHe pair potentials of Pascale[106, 119], since they exhibit strong bound wells. We discarded the $^2\Sigma$ potential curve, since it is strongly repulsive in 3-10 Å range of the internuclear distances relevant for exciplex formation. The SO effects are neglected because in the free Na the SO splitting is only 0.05 cm^{-1}[99], so the expected SO effect will be of the same order of magnitude. Such small effects are negligible with the energy scale of 1 cm^{-1} under consideration. The folding of Na(3d)He and He-He_N potentials results in the general raising of 3d $^2\Pi$ NaHe potential by ≈ 10 cm^{-1} and in a more pronounced modification of 3d $^2\Delta$ NaHe potential, see Figure 3.54. In the latter case, the potential curve is not only raised by ≈ 10 cm^{-1} , but also forms a small, ≈ 1 cm^{-1} potential barrier at the internuclear distance of 8 Å. The Na(3d)-He_N effective potentials are all strongly repulsive in the ground state geometrical configuration, see Figure 3.45, which will lead to a fast increase of "Na-helium surface" distance after the Na excitation. However, in order to qualitatively consider the upper limit of the exciplex formation probability, we assume that the exciplex formation takes place in that fixed configuration. This implies that the Na(3d)He internuclear distance is set to 6 Å. As can be seen in Figure 3.54, this should lead to barrierless formation of the NaHe exciplex along both 3d $^2\Pi$ and 3d $^2\Delta$ Na(3d)-He-He_N potential curves. Nevertheless, the formed exciplexes will have different binding energies: NaHe formed along 3d $^2\Pi$ potential curve will be ≈ 30 cm^{-1} below the dissociation limit corresponding to the energy of the Na(3d), while NaHe formed at 3d $^2\Delta$ potential curve will be bound by only ≈ 5 cm^{-1}. The 3d $^2\Pi$ NaHe exciplex formed on the droplet surface may survive the fast

desorption of excited Na, since the assumed binding energy of He to the droplet is only ≈ 5 cm^{-1} compared to the estimated ≈ 30 cm^{-1} binding energy of He to the excited Na. Thus, the desorption of exciplex would be"direct".

The above hypothesis about "direct" formation of NaHe exciplex is supported by the peculiar velocity distributions of NaHe exciplexes, see section 3.1.3.4. These distributions are more characteristic to those of bare Na and which we attribute to the "direct" desoption or diatomic-like dissociation of Na-He_N, see section 3.1.5.4. Indeed, the $<E_{kin}(NaHe)>$ has linear dependence on the excitation energy, the 28 638 ± 43 cm^{-1} onset of which correlates within three standard deviations to the minimum in the bound 3d $^2\Pi$ NaHe potential curve at 28 729 cm^{-1}. This situation resembles the linear behavior of $<E_{kin}(Na)>$, the onset of which correlates to the energy of the atomic excited state. In that sense the NaHe acts as the single entity and the energy at the minimum of the potential well is the analog of the atomic energy level. In addition, the desorbed Na and NaHe have practically the same mean estimated desorption times: taking the $<E_{kin}(Na)> \approx 70$ cm^{-1} and $<E_{kin}(NaHe)> \approx 90$ cm^{-1} at excitation frequencies of 29 400 and 29 300 cm^{-1} respectively from Figure 3.33, one obtains $\left\langle \tau_{desorp}\left(\mathrm{Na}\right)\right\rangle \approx 3.7$ ps and $\left\langle \tau_{desorp}\left(\mathrm{NaHe}\right)\right\rangle \approx 3.5$ ps.

Droplet size effects. The experimentally observed droplet size effect on relative abundance of exciplexes, see Figure 3.30, is quite interesting. In contrast to the Na(3p)-He_N effective potentials, the Na(3d)-He_N potentials do not possess any bound wells and are strongly repulsive. In addition, the fast and "direct" desorption of exciplexes observed in the experiment, which has an estimated time scale of 3.5 ps, would reduce vibrational relaxation of an exciplex on the surface of helium droplet.

As was pointed out above, the formation of the exciplex should be barrierless. The exciplex formed along 3d $^2\Pi$ Na-He-He_N effective potential is relatively strongly bound by ≈ 30 cm^{-1} compared to the ≈ 5 cm^{-1} binding energy of He to the droplet. Since the binding energy of a He atom to Na(3d) is larger than that to helium droplet, the exciplex formation may happen by the "direct" pick-up of the helium atoms from the droplet's surface. So, the creation of Na(3d)He should be mainly determined by the probability to pick-up the He atom by the departing excited Na. The nearest to the Na helium atoms constitute the surface of the dimple, where Na resides in the electronic ground state. The area of this surface obviously depends on the droplet's size, so does the number of helium atoms forming the dimple's surface. Accordingly, the probability to pick-up one of helium atoms from the dimple surface by excited Na will depend on the droplet size. It is likely that the formation of heavier Na(3d)He_2 exciplex occurs in the similar way.

3.1.5.2.2.4 4p-band

The experimentally observed exciplex formation in the 4p excitation band is special in many respects, see section 0. First, only the lightest NaHe exciplex was observed. Second, no droplet size effect on the relative abundance of exciplex was detected. Unfortunately, the velocity ion imaging of the desorbed NaHe were not recorded, so the important information related to the desorption of exciplex is missing. However, we will follow the common procedure to construct Na(4p)-He-He_N potentials to get an insight into the dynamics of NaHe formation in the 4p-band.

To start with, we generated the SO-specific Na(4p)-He pair potentials on the basis of $^2\Sigma$ and $^2\Pi$ Na(4p)He potentials of Pascale[106, 119] by diagonalizing the Hamiltonian of expression 3.26. The Na(4p)-He_N effective potentials are highly repulsive, see Figure 3.45, so the Na-He_N separation will rapidly increase on the picosecond timescale from the initial 6 Å. As in the case of 4s and 3d-bands, we assume that the exciplex formation starts in the ground state helium configuration in order to determine an upper limit for the exciplex formation. That is why we folded the $^2\Pi_{1/2}$ and $^2\Pi_{3/2}$ pair

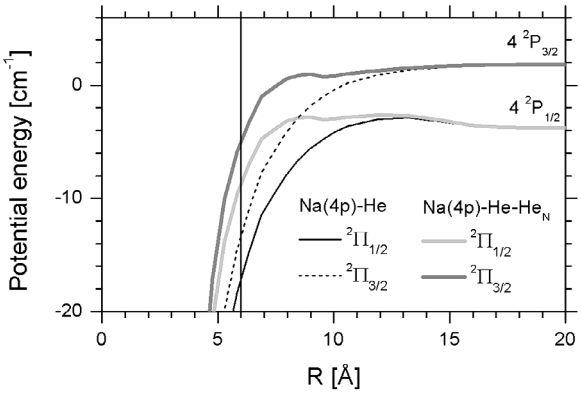

Figure 3.55: Na(4p)He pair potentials with SO splitting generated from potentials of Pascale[106, 119] and the effective Na(4p)-He-He$_N$ potentials in relative energy scale in order to show the effect of folding the pair potentials and the He-He$_N$ potential. The vertical line shows the assumed initial NaHe internuclear position after the excitation of NaHe$_N$.

potentials with the He-He$_N$ potential from expression 3.25 centered at a internuclear distance of R = 6 Å. As can be seen in Figure 3.55, the effect of folding the He-He$_N$ and NaHe potentials is a reduction of the bound energy of exciplex by ≈ 8 cm^{-1}, so the bound energies of Na(4p)He will be ≈ 5 cm^{-1} and ≈ 8 cm^{-1} along the $^2\Pi_{1/2}$ and the $^2\Pi_{3/2}$ curves respectively. From the folded potentials we conclude that the exciplex formation should be barrierless. It is likely that the Na(4p)He are formed by the "direct" pick-up of He atoms from the dimple's surface by departing excited Na atom similar to the case of 3d band. The following estimation of the desorption time of Na(4p) is in favor of this hypothesis.

The upper limit of the mean desorption time for Na we estimate as previously: from $\langle E_{kin}(Na)\rangle \approx 100$ cm^{-1} at excitation frequency of 30 500 cm^{-1}, see Figure 3.42, one finds $\langle v(Na)\rangle \approx$ 327 m/s which results in $\left\langle \tau_{desorp}\left(\mathrm{Na}\right)\right\rangle \approx 3$ ps. This mean desorption time is comparable to that in the 3d band, where the formation of Na(3d) is likely to be "direct". However, in contrast to the 3d band, neither heavier NaHe$_n$, n>1, exciplexes nor droplet size effects in the exciplex formation were experimentally observed in the 4p-band. The origin of this peculiarity is unclear.

3.1.5.2.3 Conclusion

The NaHe$_n$, n=1-4, exciplex formation upon excitation of Na-He$_N$ can be qualitatively understood considering the pair interactions of excited sodium with the neighboring helium atoms. In this way, NaHe pair potentials at an internuclear distance of ≈ 6 Å, corresponding to sodium-helium surface distance, determine the bound energy of the nascent exciplex. According to this hypothesis, the exciplex should be formed in highly vibrational states, since the energy at an internuclear distance of ≈ 6 Å is close to the dissociation limit. This assumption is supported by our ZEKE spectroscopy of Na(3p)He, where transitions from the upper vibrational levels with v"=5-6 were tentatively identified.

To a first approximation, the influence of the helium droplet on the exciplex formation can be taken into account using the static model of Reho *et al.*[74], where the energy of ≈ 5 cm^{-1} needed for the extraction of a helium atom from the droplet surface is explicitly introduced. The additional extraction energy may inhibit NaHe formation. In addition, a fast desorption of exciplex from droplet's surface revealed in our experiments may hinder exciplex formation via extraction of a helium atom from the droplet. Droplet size effects observed in the experiments are attributed to the droplet-induced

vibrational relaxation of nascent exciplex and to geometry of the dimple where sodium resides in the ground state, which are thought to depend on the droplet size.

3.1.5.3 Modeling of photoelectron spectra

The perturbation of the atomic excited states of sodium by helium droplet leads to a shift of the Na-He_N excitation spectra to higher frequencies compared to those in the free Na. This makes it energetically possible the Na atoms desorb from the droplet in the same states to which it was excited. Indeed, in the photoelectron spectra recorded after the excitation of Na-He_N within the 4s-4p bands photoelectron peaks originating from the photoionization of Na in the corresponding excited states were observed. However, additional photoelectron peaks were also detected. They originated from lower excited states. The population of these low states may be caused either by droplet-induced relaxation or by radiative decay of the free excited Na after its recoil from the helium surface. The latter fact is certainly possible. First, the desorption happens on the picosecond time scale as can be estimated from the observed speed distributions of recoiled Na. Second, the duration of the laser pulse of 11 ns in the one-color detection scheme, used throughout the 4s-4p excitation bands, is comparable to the radiative life times of the 3p-4p excited states of free Na which fall in the range 40-125 ns[131, 135]. This implies that after the excitation with the first photon the desorbed excited Na may radiatively relax to the lower excited states before being ionized by the second photon from the same laser pulse.

The population of the low excited states also depends on the saturation of the transition, since in the case of saturation all Na atoms will be populated in the highest excited state at the beginning of the laser pulse. This will result in a higher probability for the excited sodium atoms to radiatively relax to lower states. In addition, independently from the population process of the excited states of desorbed Na, the intensities of the corresponding photoelectron peaks are convoluted by photoionization cross-sections of those states. Furthermore, the exciplex formation may affect the ionization cross-section of respective excited states of Na. This implies that the intensity of the observed photoelectron peaks deoes not directly reflect the populations of the excited states of desorbed bare Na.

In order to better understand the population process of the low excited states of desorbed Na we have modeled the relative intensities of the photoelectron peaks, assuming only radiative decay. In the modeling of photoelectron spectra the following assumptions were made:

- Na atoms are ionized in the gas phase, after having desorbed from helium droplets
- The desorption is instantaneous
- The sodium atoms desorb only in the excited state corresponding to the excitation band
- The population of the states lower than those corresponding to the excitation band occurs only by spontaneous radiative decay

The comparison of the modeled results with the experimental data will help to determine the importance of droplet-induced relaxation.

Based on these assumptions, the population rate equations were written for a given excitation band. The resulting systems of coupled differential equations are specific to the particular excitation band. Below, we will present an example of the system for the 4s excitation band. The approach is easily extensible for higher excited states of sodium by including additional equations and terms for

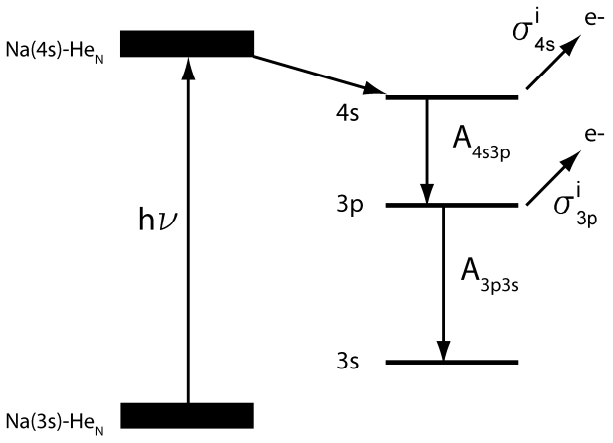

Figure 3.56: State population scheme used to model photoelectron spectrum recorded within 4s-band. The energy scale is exaggerated.

optically allowed transitions and ionization channels.

The population scheme within the 4s-band is illustrated in Figure 3.56. The system of coupled differential equations for this band is given below:

$$
\begin{aligned}
\frac{dN^d_{3s}}{dt} &= -\frac{\sigma^d_{4s\leftarrow 3s} I(t)}{h\nu} N^d_{3s} \\
\frac{dN_{4s}}{dt} &= -A_{4s3p} N_{4s} - \frac{\sigma^i_{4s} I(t)}{h\nu} N_{4s} + \frac{\sigma^d_{4s\leftarrow 3s} I(t)}{h\nu} N^d_{3s} \\
\frac{dN_{3p}}{dt} &= -A_{3p3s} N_{3p} - \frac{\sigma^i_{3p} I(t)}{h\nu} N_{3p} + A_{4s3p} N_{4s} \\
\frac{dN^i_{4s}}{dt} &= \frac{\sigma^i_{4s} I(t)}{h\nu} N_{4s} \\
\frac{dN^i_{3p}}{dt} &= \frac{\sigma^i_{3p} I(t)}{h\nu} N_{3p}
\end{aligned}
\qquad 3.28
$$

where N^d_{3s} is the number of ground state Na(3s)-He$_N$ droplets which is depleted by excitation to Na(4s)-He$_N$ having a cross-section $\sigma^d_{4s\leftarrow 3s}$. As was assumed before, the excitation leads to instantaneous desorption of Na(4s). Thus the increase in the number of free Na(4s) N_{4s} is equal to the decrease of Na(3s)-He$_N$. On the other hand, N_{4s} is depleted by : a) the spontaneous radiative decay to 3p state, and b) photoionization. N_{3p} is the number of Na atom in the 3p excited state depopulated by : a) spontaneous decay to Na(3s) and b) photoionization. N_{3p} is populated only by radiative decay of Na(4s). N^i_{4s} and N^i_{3p} are the numbers of ionized Na atoms from 4s and 3p states, respectively. A_{4s3p} and A_{3p3s} are Einstein's coefficients[99] or the rates of spontaneous radiative decay of Na(4s) and Na(3p). σ^i_{4s} and σ^i_{3p} are the ionization cross-sections[109, 136, 137] of Na atoms in the corresponding excited states at ionization frequency ν. $I(t)$ is the laser light intensity in Watt/m^2 in the ionization volume. The equation for the Na(3s) state was not included into the system, because

sodium atoms in the 3s state cannot be one-photon ionized at excitation frequencies used. The system of coupled differential equations 3.28 was numerically integrated in the Maple 9[115] software package with initial conditions:

3.29 $$t = 0 : N_{3s}^{d} = 1, N_{4s} = 0, N_{3p} = 0, N_{4s}^{i} = 0, N_{3p}^{i} = 0$$

The time dependences of $I(t)$ is assumed to be Gaussian with the measured FWHM = 11±1 ns. It is expressed as:

3.30 $$I(t) = I_0 \exp\left(-(t - t_0)^2 / 2b^2\right)$$
$$I_0 = \frac{2E_{pulse}}{S}\sqrt{\frac{1}{\sqrt{2}\pi b}}$$
$$b = 2\sqrt{2\ln 2} / FWHM$$

where $t_0 = 20$ ns is the time of maximum power of a laser pulse, E_{pulse} is the averaged measured energy of the laser pulse in Joule, $S = 0.37$ mm^2 is the area of the focused laser beam at the crossing point with helium droplet beam, c is the speed of light. The equations were integrated until $t = 60$ ns and the relative ratios of Na atoms ionized from particular excited state were calculated as:

3.31 $$\mathrm{I}_{\mathrm{theor}}(4\mathrm{s}) = \frac{N_{4s}^{i}}{N_{4s}^{i} + N_{3p}^{i}}$$
$$\mathrm{I}_{\mathrm{theor}}(3\mathrm{p}) = 1 - \mathrm{I}_{\mathrm{theor}}(4\mathrm{s})$$

in order to compare them with experimental relative intensities of photoelectron peaks.

3.1.5.3.1 Application of the model to Na-He$_N$

The input parameters, which were used to calculated the relative intensities of photoelectron peaks in the 4s-4p bands, are listed in Table 11. The ionization cross-sections of excited states of Na were obtain from several sources. The cross-sections for Na(3p) were read from Fig.2 in Ref.[138]. Prof. M. Aymar kindly provided[136, 137] the numerical data for the photoionization cross-section of the 3d and 4p states of sodium. The ionization cross-section for Na(4s) was read from Fig.6 in Ref.[109]. The cross-section $\sigma_{nl\leftarrow 3s}^{d}$ for the Na(n*l*)-He$_N$←Na(3s)-He$_N$ excitation transition is taken to be $1\cdot10^{-20}$ cm^2 in order to avoid saturation effects at the laser fluences used in the experiment. The chosen value results in less than 10% depletion in the initial number of Na(3s)-He$_N$.

The effect of saturation in the excitation step was checked by increasing the $\sigma_{nl\leftarrow 3s}^{d}$ by three orders of magnitude to $1\cdot10^{-17}$ cm^2. This resulted in complete depletion of Na(3s)-He$_N$ in the beginning of the laser pulse when the intensity has ≈ 30% of its peak value.

We found that the calculated relative ratios of photoelectron peaks were sensitive to the values of the laser pulse energy and the ionization cross-section of the excited states of Na. In order to take into account those dependences the cross-sections and the energy of laser pulse were varied by ±50% from the tabulated values. The ±50% variation in the ionization cross-sections was taken as the upper limit of deviation of experimental values[139-141] from the theoretical values[109, 137]. The ±50% variation in the pulse energy comprises 20% errors in measurements of the pulse energy and in the area of the focused laser beam at the ionization point. The input parameters used in the calculations are collected in Table 10 and the results in Table 11.

Table 10 Input parameters for modeling the PE spectra in 4s-4p bands

Excitation band	Ionization frequency [cm^{-1}]	Excitation cross-section $\sigma^{d}_{nl\leftarrow 3s}$ x10^{-18} [cm^2]	Laser pulse energy [mJ]	Ionization cross-section x10^{-18}, [cm^2]			
				3p	4s	3d	4p
4s	26 316	0.01	4	6.5±0.5	$(13\pm2)\cdot10^{-3}$	-	-
3d	29 400		8	6.0±0.5	-	7.5±0.1	-
4p	32 000		6	2.5±0.5	$<1\cdot10^{-3}$	6.2±0.1	0.51±0.05
4p	16 000		15	-	0.1±0.03	72±1	5.6±0.1

Table 11 Experimental and calculated relative intensities of photoelectron peaks in 4s-4p bands

Excitation band		3p	4s	3d	4p
4s 1-photon	Experiment	0.956±0.002	0.0434 ± 0.0004	-	-
	Theory	0.89±0.04	0.11 ± 0.04	-	-
3d 1-photon	Experiment	0.20±0.05	-	0.80 ± 0.05	-
	Theory	0.02±0.01	-	0.98 ± 0.01	-
4p 1-photon	Experiment	0.01±0.01	-	-	0.99±0.01
	Theory	0.007±0.001	$< 1\cdot10^{-4}$	$< 1\cdot10^{-3}$	0.993 ± 0.001
4p 2-photon	Experiment	-	-	-	1.00 - 0.01
	Theory	-	$< 7\cdot10^{-4}$	$< 1\cdot10^{-5}$	0.999 ± 0.001

3.1.5.3.1.1 4s-band

The modeled relative intensities of photoelectron peaks in the ionization of 3p and 4s states of desorbed sodium correspond qualitatively to the experimental ones: $I_{theor}(4s) = 0.11 \pm 0.04$, $I_{theor}(3p) = 0.89 \pm 0.04$ versus $I_{exp}(4s) = 0.0434\pm0.0004$ and $I_{exp}(3p) = 0.956\pm0.002$. The increase of the $\sigma^{d}_{4s\leftarrow 3s}$ by three orders of magnitude in order to imitate the saturation of the excitation transition does not produce considerable effect. The result is a small decrease of $I_{theor}(4s)$ from 0.11 ± 0.04 to 0.10 ± 0.04.

The discrepancy between calculations and the experiment may be partially due to the approximate value of the ionization cross-section for the Na(4s), which is close to its zero minimum at the ionization frequencies used. According to Aymar[109] the largest deviation of theoretically calculated values from real ones are expected in this region. Based on this fact we conclude that there is no droplet induced relaxation of the Na in the 4s excited state.

3.1.5.3.1.2 3d-band

In the 3d excitation band, there is a quite large deviation of the theoretical relative intensities $I_{theor}(3d) = 0.98 \pm 0.01$ and $I_{theor}(3p) = 0.02 \pm 0.01$ versus experimental ones $I_{exp}(3d) = 0.80\pm0.05$ and $I_{exp}(3p) = 0.20\pm0.05$. The theoretical values demonstrate a very weak dependence on the ionization cross-section of Na(3p) and Na(3d). The saturation of the excitation step reduces the $I_{theor}(3d)$ down to

0.90 ± 0.02 and increases $I_{theor}(3p)$ up to 0.10 ± 0.02. This is still not sufficient to explain the experimental relative intensity of photoelectron peak from ionization of Na(3p). It is not excluded that the pronounced formation of exciplexes, which constitute ≈ 55% of the desorbed species, see Figure 3.29, in the 3d band may be at the origin of the discrepancy. The Na(3d)He exciplex may have different photoionization cross-section and different radiative life time compared to bare Na(3d). Alternatively, helium droplet induced relaxation may cause the enhanced population of desorbed sodium atoms in the 3p state.

3.1.5.3.1.3 4p-band

The best correspondence between experimental and theoretical values of relative photoelectron peak intensities is in the 4p-band for both one- and two-photon excitations, see Table 11. The variation of the input parameters described above do not change the $I_{theor}(4p) = 0.99 \pm 0.01$. This is owing to the 125 ns[131] lifetime of Na(4p), which is substantially longer than the laser pulse width of 11 ns. In addition, in contrast to the 3d-band, in the 4p-band the main outcome product is the bare Na atoms, so the influence of exciplexes is very small.

3.1.5.3.2 Conclusion

Based on the results of modeling of photoelectron spectra recorded in the experiments, we conclude that there is no helium droplet induced relaxation of excited sodium atom upon desorption in the 4s and 4p excitation bands. In the 3d band, the revealed discrepancy may be caused by helium droplet induced relaxation during the desorption of excited Na atom or by the exciplex formation.

3.1.5.4 Velocity distributions of desorbed Na

As was shown in section 3.1.5.1, the Na-He_N excitation spectra can be well reproduced on the basis of diatomic model of Na-He_N interaction, when Na acts as one atom and the helium droplet acts as the other. In addition, the observed velocity distributions of bare sodium atoms desorbed from the droplet's surface are particularly regular. The pronounced anisotropic angular distribution and linear dependence of the mean kinetic energy versus excitation frequency are commonly observed in the photodissociation of diatomic molecules. These two facts motivated us to consider the application of a diatomic photodissociation model to the desorption of excited Na from the nanodroplet's surface.

3.1.5.4.1 A possible model

3.1.5.4.1.1 Energy balance

In a diatomic molecule AB, the photon energy $h\nu$ is partitioned in a dissociation event in the following way:

3.32
$$AB \xrightarrow{h\nu} A + B$$
$$h\nu = E_{\text{int}}^{A} + E_{\text{int}}^{B} + E_{kin}^{A} + E_{kin}^{B} + D$$

where D is the dissociation energy, $E_{\text{int}}^{A}, E_{\text{int}}^{B}$ are the internal energies of the fragments, $E_{kin}^{A} = \frac{m_A v_A^2}{2}, E_{kin}^{B} = \frac{m_B v_B^2}{2}$ are their kinetic energies. The total available kinetic energy $E_{kin} = E_{kin}^{A} + E_{kin}^{B}$ is determined by the excess photon energy with respect to the dissociation and internal energies:

3.33 $$E_{kin} = h\nu - \left(D + E_{\text{int}}^{A} + E_{\text{int}}^{B} \right)$$

Assuming that the internal energies of the photofragments do not vary with the photon energy, the kinetic energy of the fragments depends linearly from the photon energy. From energy and momentum conservation laws it follows:

3.34 $$E_{kin}^{A} = E_{kin} \frac{m_B}{m_A + m_B} = \left[h\nu - \left(D + E_{\text{int}}^{A} + E_{\text{int}}^{B} \right) \right] \cdot \frac{m_B}{m_A + m_B}$$

3.1.5.4.1.2 Angular distribution of photofragments

The center-of-mass angular distribution of fragments in one-photon photolysis reflects the **E-μ-v** correlation, where **E** stands for electric field vector, **μ** is the electronic transition dipole moment of the parent molecule, and **v** is the fragment velocity. This distribution is expressed by the known formula[94]:

3.35 $$I(\theta) = \frac{1}{4\pi} \left[1 + \beta P_2 (\cos\theta) \right]$$

where $I(\theta)$ is the angular distribution of photophragments, θ is the angle between velocity vector **v** and the polarization vector **E**, β denotes the anisotropy parameter, and P_2 is the second-order Legendre polynomial, $P_2(x) = \left(3x^2 - 1\right)/2$. The anisotropy parameter reflects the **μ-v** correlation and is expressed as expectation value:

3.36 $$\beta = 2 \left\langle P_2 (\cos\chi) \right\rangle$$

where χ is the angle between vectors **μ** and **v**, P_2 is the second-order Legendre polynomial given above. As can be seen from the expression, the anisotropy parameter can take on values $-1 \le \beta \le 2$.

The following approximations make the angular distributions of the dissociated fragments particularly simple. The first two are axial and instantaneous recoil of fragments and hold when the bond rupture is fast compared to the rotation period of the molecule. The third one is the orientation of the transition dipole moment with respect to the bond axis: perpendicular or parallel. The last two limiting cases result in anisotropy parameter $\beta = -1$ and $\beta = 2$ respectively, so the angular distributions have the following forms: $I_{\perp}(\theta) \propto \sin^2\theta$ and $I_{||}(\theta) \propto \cos^2\theta$.

From the symmetry reason in diatomic molecules the transition dipole moment must lie either along the molecular axis corresponding to the parallel transition or in the plane perpendicular to the axis corresponding to the perpendicular transition. So, parallel type transition such as Σ-Σ, Π-Π manifest anisotropy parameter $\beta = 2$, whereas perpendicular transitions such as Σ-Π, Π-Δ manifest $\beta = -1$.

3.1.5.4.2 Application of the model to Na-He$_N$

3.1.5.4.2.1 Kinetic energy distributions of desorbed Na

Energy balance. From the analysis of experimental photoelectron spectra in section 3.1.5.3 we can conclude that the Na desorbs in the same excited state to which it was excited on the surface of helium droplets. Based on this fact and on the small ≈ 10 cm^{-1} binding energy of Na to the helium droplet in the ground state, we approximate the sum of the dissociation energy of Na-He$_N$ and the

internal energy of Na in the equation 3.34 as being equal to E_{Na}, the energy of the electronic excited state of desorbed Na:

3.37 $$E_{Na} = D + E_{\text{int}}^{Na}$$

We also assume the helium droplet to be hard sphere, the internal modes of which (phonons, ripplons) are not excited:

3.38 $$E_{\text{int}}^{He_N} = 0$$

From the above assumptions we obtain from equation 3.33 that:

3.39 $$E_{kin} = h\nu - E_{Na}$$

and from the equation 3.34:

3.40 $$E_{kin}^{Na} = E_{kin}\frac{m_{He_N}}{m_{He_N} + m_{Na}} \approx h\nu - E_{Na} \quad , \quad m_{He_N} >> m_{Na}$$

where m_{He_N} and m_{Na} are masses of the helium droplet and the sodium atom respectively. From the above equation it follows that within the diatomic picture of Na-He_N dissociation, Na should carry all total available kinetic energy. We should also observe a sharp kinetic energy distribution of the desorbed Na, the width of which is limited by the resolution of our imaging setup. Furthermore, a slope of unity should be observed in the linear dependence of E_{kin}^{Na} versus photon energy.

In contrast, the experimental data demonstrate that the kinetic energy distribution of desorbed Na is broader than the resolution of our setup. In addition, in the linear behavior of the average kinetic energy of desorbed Na $\left\langle E_{kin}^{Na} \right\rangle$ versus excitation frequency the slopes do not exceed 0.6. These slope values indicate that an appreciable amount of available kinetic energy, comparable or superior to the kinetic energy of the desorbed Na, must be deposited into the droplet.

The obvious origin of the noted discrepancies is the approximation of the helium droplet as a hard sphere without excitation of the internal modes. However, the role of phonon and ripplon excitations is not clear. The typical ≈ 1 cm^{-1} and ≈ 0.1 cm^{-1} energy scales of phonon and ripplon of the helium droplet[37] will require multi-phonon and multi-ripplon excitation in order to account for the missing kinetic energy of desorbed Na.

An alternative hypothesis may be the interaction of the excited Na atom with only a limited number of the nearest helium atoms instead of the whole droplet. In support of this hypothesis is the absence of droplet size effects in the experimental velocity distributions. The effective number N_{eff} of helium atoms represents the counterpart of the sodium with the effective mass m_{eff}:

3.41 $$m_{eff} = m_{He} N_{eff}\left({}^4\text{He}\right)$$

Having introduced the effective mass and neglecting again the excitation of the helium droplet, we rewrite equation 3.40 as:

3.42 $$E_{kin}\left(Na\right) = \frac{m_{eff}}{m_{eff} + m_{Na}}\left(h\nu - E_{Na}\right)$$

The effective masses, which were calculated according to the above equation from the experimental slopes of $\left\langle E_{kin}^{Na} \right\rangle$ versus excitation energy, are presented in Table 12. The obtained effective masses do not correspond to integer number of ^{4}He atoms because N_{eff} represents their averaged number. The set of m_{eff} manifests an interesting trend as the m_{eff} increases with the energy of the electronic excited state. The odd point in this trend is the m_{eff} = 24.4 in the 4s-band, which has the largest value of the whole set at the intermediate $E_{Na(4s)}$ = 25 740 cm^{-1} energy compared to the limiting values $E_{Na(4s)}$ = 16 956 cm^{-1} and $E_{Na(4p)}$ = 30 273 cm^{-1}[99].

Table 12 m_{eff} in Na-He$_N$ photodissociation in 3p-4p bands

State of desorbed Na	Experimental slope	m_{eff} [amu]
3 $^2P_{1/2}$	0.195 ± 0.002	5.6
3 $^2P_{3/2}$	0.228 ± 0.002	6.8
4s	0.515 ± 0.002	24.4
3d	0.27 ± 0.02	8.5
4p	0.406 ± 0.006	22.9

Width of kinetic energy distributions. The width of the kinetic energy distribution is wider than the energy resolution of our imaging setup, so it is unlikely to be an artifact. In all excitation bands the width increases almost linearly with the excitation energy. We do not well understand the nature of the width, but qualitatively it might stem from density fluctuations of helium in the vicinity of the adsorbed sodium. The very crude estimation can be made for the case of an ideal gas, where the relative fluctuation of number of particles N in a given volume is:

3.43
$$\frac{\left\langle \Delta N^2 \right\rangle^{\frac{1}{2}}}{N} = \frac{1}{\sqrt{N}}$$

Table 13 Estimation of the relative width of kinetic energy distributions

State of desorbed Na	m_{eff} [amu]	$N_{eff}(^4He)$	ΔE_{kin} ideal gas	ΔE_{kin} experiment
3 $^2P_{1/2}$	5.6	1.4	0.85	0.65 - 0.45
3 $^2P_{3/2}$	6.8	1.7	0.77	0.65 - 0.35
4s	24.4	6.1	0.4	0.12 ± 0.02
3d	8.5	2.125	0.69	0.6 - 0.3
4p	22.9	5.725	0.42	0.1 - 0.2

Assuming that the effective number of helium atoms fluctuates, we take in the above expression $N = N_{eff}(^4He)$ in order to estimate the relative width of the kinetic energy distribution as:

3.44
$$\Delta E_{kin} = \frac{\left\langle \left(\Delta E_{kin}^{Na} \right)^2 \right\rangle^{1/2}}{\left\langle E_{kin}^{Na} \right\rangle} \propto \frac{1}{\sqrt{N_{eff}\left({}^4\mathrm{He} \right)}}$$

The results of estimation are collected in Table 13. The relative width ΔE_{kin} calculated with N_{eff} corresponds well for the 3p and 3d-band and systematically higher by a factor of 3 for the 4s and 4p band. This state-specific behavior of relative width is difficult to interpret in view of the crude approximations made. More elaborate model is required which will take into account the quantum nature of the helium atoms at ultra-low temperature and the state-specific interaction of excited Na with the helium droplet.

3.1.5.4.2.2 Angular distribution of recoiled Na

The anisotropic angular distributions of excited Na atoms desorbed from helium droplets can be qualitatively understood using the model of diatomic-like sodium-droplet photodissociation and the calculated spectra from section 3.1.5.1.

We start with the simplest case of the 4s band, where ground and electronic excited state of Na-He_N have Σ symmetry. Therefore, the resulting angular distribution of detached sodium in the 4s Σ'←3s Σ' transition should have anisotropy parameter $\beta = 2$ (parallel transition), see section 3.1.5.4.1.2. The experimental value of mean anisotropy parameter $\langle\beta\rangle = 1.81\pm0.06$, see Figure 3.27, is fairly close to theoretical limit. A small deviation of ≈ 0.2 from the diatomic limit may be caused by the droplet rotation and the breaking of Σ symmetry due to the fluctuation of helium density or the displacement of Na atom from the symmetry axis. We speculate that the perturbation of the spherical symmetry of the 4s orbital of Na on the surface of helium droplet may cause its deformation resulting in non-zero projection of the electronic angular momentum on the symmetry axis. This deformation may lead to the non-parallel character of Na(4s)-He_N←Na(3s)-He_N transition and as a result to the reduced value of angular anisotropy parameter.

In the cases of 3p and 4p band, there is a correspondence between the positions of the calculated Σ'←Σ' and Π'←Σ' transitions and the variation of the mean anisotropy parameters $\langle\beta\rangle$ of the recoiled Na. In the theoretical spectra, Π'←Σ' transitions are always in the low frequency part of the excitation band, while Σ'←Σ' transitions are in the high frequency part, see Figure 3.46. Assuming that the Na-He_N photodissociation is similar to a diatomic case, we expect $\beta = -1$ in the low frequency part of a band and $\beta = 2$ in the high frequency part. However, the experimentally obtained values of $\langle\beta\rangle$ are inferior to these limits, though at the high frequency part of the 3p and 4p excitation band the mean anisotropy parameter of $\langle\beta\rangle \approx 1.6$ and $\langle\beta\rangle \approx 1.4$, respectively, are close to the theoretical limit of $\beta = 2$. In the low frequency part of the 4p band $\langle\beta\rangle \approx -0.7$ is close to the theoretical limit of $\beta = -1$, while in the 3p band $\langle\beta\rangle \approx 0$. The deviation of the $\langle\beta\rangle$ from the limiting values we attribute to the mixing of Σ' and Π' excited states of Na-He_N. The increasing trend of $\langle\beta\rangle$ with excitation frequency within the bands may stem from the spectral overlap of the Π'←Σ' and Σ'←Σ' transition.

Within the 3d band the mean anisotropy parameter $\langle\beta\rangle$ is close to a zero value which may indicate larger state mixing or spectral overlap of the Π'←Σ' and Σ'←Σ' transition.

Spin-orbit specific mean anisotropy parameter within the 3p-band, see Figure 3.21, remains a not well understood phenomenon. A small difference of ≈ 0.3 between values of $\langle\beta\rangle$ for desorbed Na in the 3p $^2P_{1/2}$ and 3p $^2P_{3/2}$ state is likely caused by droplet-induced state mixing.

3.1.5.4.3 Conclusion

The velocity distributions of excited Na atoms desorbed from the surface of helium droplets can be qualitatively explained using the model of diatomic-like sodium-droplet interaction. In this model, a helium droplet is considered as a sodium rigid counterpart in a instantaneous photodissociation event. From this model the linear dependence of mean kinetic energy on excitation

energy and anisotropic angular distribution characteristic of recoiled Na atoms follow directly. This corresponds qualitatively well to the experimental data. The deviations from the diatomic model with a rigid droplet are following. In the linear dependence of the mean kinetic energy of Na on excitation energy the slope is less that unity. This indicates that the droplet does not interact as rigid entity in the dissociation event and that a considerable amount of available kinetic energy is dissipated into the droplet. Anisotropy parameters of angular distributions of recoiled Na are inferior with respect to those in the true diatomic case, β = 2 for $\Sigma \leftarrow \Sigma$ and β = -1 for $\Pi \leftarrow \Sigma$ transition. The revealed discrepancy may indicate that $\Pi' \leftarrow \Sigma'$ and $\Sigma' \leftarrow \Sigma'$ transitions may overlap within an excitation band. Furthermore, the real Na-He_N interaction potential is a 3D one, thus the diatomic symmetry of an electronic state of Na-He_n is not totally true. This may also lead to a deviation of the anisotropy parameter observed in the Na-He_N photodissociation from the true diatomic case. Smearing of the angular anisotropy due to rotations of the droplet is not excluded, too. The broad kinetic energy distribution of desorbed excited Na does not follow the diatomic case. It can be caused by the helium density fluctuation in the vicinity of the Na atom. The absence of droplet size effects on velocity distribution of desorbed Na is not well understood.

3.1.6 Summary

The features in the excitation spectra of Na-He_N recorded in the region of 17 000 - 33 000 cm^{-1} can be assigned to the corresponding atomic excited states of free sodium. We have labeled them according to atomic energy level as 3p, 4s, 3d and 4p band. Within excitation bands we recorded internal energy and velocity distributions of photoproducts. The formation of $NaHe_n$, n=1-4, exciplexes observed in these bands depends on the corresponding excited state of free sodium. In all excitation bands the mean kinetic energy of desorbed Na has a linear dependence with excitation frequency, the slope of which is specific to the corresponding excited state of free sodium. The anisotropy of angular distributions of desorbed fragments is species- and band-specific.

The excitation spectra can be qualitatively reproduced using a pair-wise additive model of sodium-helium interactions. The one-dimensional Na-He_N interaction potentials are constructed by summing Na-He pair potentials over helium atoms constituting the droplet while changing the Na-droplet distance along axis connecting the droplet's center and the Na atom. These Na-He_N effective potentials for sodium excited states are highly repulsive, giving rise to the bound-free transitions, which explains the desorption of excited sodium from the droplet. The spectra calculated using this model are very sensitive to the NaHe pair potentials and Na-He_N density profiles used. The best correspondence between calculated and experimental spectra is in the 4s and 3d band. In the 3p and 4p band the observed spectra differ considerably from the theoretical ones due to the saturation of transition. An especially large difference between experimental and calculated spectra for the 4p band is thought to originate from the breakdown of the model that disregards excited state mixing due to droplet-induced perturbations.

The exciplex formation can be qualitatively understood as a pair interaction of excited sodium with the neighbor helium atoms constituting the dimple where Na in the ground state resides. Therefore, the nascent exciplexes should be created in high vibrational states close to the dissociation limit corresponding to a excited level of free Na. The droplet influence on the NaHe formation can be taken into account as an additional energy needed to extract a helium atom from the droplet's surface. The introduction of this energy can modify the NaHe interaction by forming potential barriers at the internuclear distance corresponding to the "sodium-helium surface" separation. Within the considerations given above, the complete absence of exciplexes in the 4s band is due to a high potential barrier in Na(4s)He pair potential at the internuclear distance close to that of "sodium-droplet

surface". The large relative abundance of exciplexes in the 3p band is due a combination of two processes. The formation of NaHe on the attractive part of droplet-induced potential barriers in the NaHe effective potentials above the dissociation limit. The exciplexes are then stabilized by following vibrational relaxation into the droplet, since the Na(3p)-He_N potential has a weakly bound well at corresponding internuclear distance, where NaHe is thought to be temporarily trapped. This picture is supported by experimentally observed Na(3p)He in the high vibrational states using ZEKE and a Maxwell-Boltzmann-like isotropic speed distributions of desorbed exciplexes with an effective temperature of 28 K. The high abundance of NaHe in the 3d band is thought to originate from the exciplex formation on the droplet surface already in bound states, so the fast desorption of excited Na is not a limiting factor. In contrast, the low abundance of NaHe in the 4p band is thought to be combination of the fast desorption and very weak binding of nascent exciplexes. Droplet size effects are observed only in the 3p and 3d band, when larger droplets yielded enhanced abundances of exciplexes. These effects are tentatively attributed to the droplet-size dependent number of helium atoms within the dimple surface where Na resides, which mediates the probability to pick-up a helium atom by recoiling Na upon excitation.

The internal energy distributions of desorbed photofragments recorded using photoelectron spectroscopy represent the combination of the initial states distribution of excited sodium, their radiative decay upon desorption from the helium droplet and ionization cross-section. They can be reproduced assuming instantaneous recoil of the excited sodium that decays radiatively to lower excited states within the laser pulse of 11 ns during which excitation and ionization take place subsequently. Based on this modeling, droplet-induced relaxation is expected to occur only in the 3d band. The vibrational state distribution of Na(3p)He exciplexes recorded in the 3p band using ZEKE spectroscopy clearly demonstrated droplet-induced vibrational relaxation of nascent exciplexes created in highly vibrational states close to dissociation limit.

The speed and angular distributions of recoiled excited Na atoms can be understood using diatomic approximation of Na-He_N dissociation, when the helium droplet acts as a counterpart without internal energy structure of the excited sodium atom. The linear dependence of the mean kinetic energy of desorbed Na follows directly from this approximation, but the expected slope of unity is not observed experimentally. The discrepancy indicates that a considerable part of the available energy is deposited into the droplet, so the droplet acts as a "soft" counterpart in the dissociation event. Assuming that the excited sodium interacts only with nearest helium atoms, the experimental slopes can be converted to an average number of these atoms which depends non-regularly on a particular exited state of free sodium. The angular anisotropy of desorbed excited Na follows in general the type of calculated transition within a diatomic molecular picture of Na-He_N photodissociation. The difference between the theoretical picture and that observed experimentally, is attributed to state mixing and spectral overlap of different transitions.

3.2 Medium excited states

In this section we present the experimental results obtained in the excitation bands correlating to excited states of sodium which are higher than the 4p state. The frequency region under consideration is 33 500 - 38 000 cm^{-1}. The medium states are selected in a separate section because same features observed in this energy region, like the linear dependence on the excitation frequency of the mean kinetic energy of excited Na desorbed from helium droplets, resemble those of the lower excited states. At the same time, photoelectron spectra reveal population of states that cannot be populated by the radiative decay of desorbed excited Na. In this respect, the results differ from the

situation for the lower excited states. The results for medium excited states will be discussed within the models developed for the lower excited states.

3.2.1 5s and 4d-5p bands

3.2.1.1 Excitation spectra

The excitation spectra recorded by monitoring desorbed bare Na atoms, NaHe, $NaHe_2$ and all fragments following one-color excitation of Na-He_N in the frequency region of 33 200-34 500 cm^{-1} are shown in Figure 3.57. The feature centered at 34 200 cm^{-1} we tentatively assign to a state corresponding to the 5s excited state of sodium. The band is shifted by ≈ 1 000 cm^{-1} to higher frequencies with respect to the atomic 5s←3s transition at 33 201 cm^{-1}[99]. The excitation within the 5s-band results mainly in the desorption of bare sodium atoms with small fraction of NaHe exciplexes. The second feature starts at ≈ 34 500 cm^{-1} and seems to continue almost to 36 000 cm^{-1}, see section 3.2.2. The assignment of this feature is not straightforward, since there are three excited sodium states in this frequency region: Na(4d) at 34 549 cm^{-1}, Na(4f) at 34 587 cm^{-1} and Na(5p) at 35 041 cm^{-1}[99]. We will call that part of the Na-He_N excitation spectrum the 4d-5p-band. Within this 4d-5p-band a pronounced NaHe and $NaHe_2$ exciplex formation was observed.

Among the species-specific excitation spectra only that of bare Na shows a droplet size dependence, see Figure 3.58: the maximum of the 5s-band shifts by ≈ 200 cm^{-1} to higher frequencies by going from droplets with <r> = 29 Å to <r> = 60 Å. At the same time, the Na excitation spectrum in the 4d-5p-band shifts to higher frequencies at most by ≈ 50 cm^{-1}. In contrast, the NaHe and $NaHe_2$ excitation spectra hardly change with droplet size.

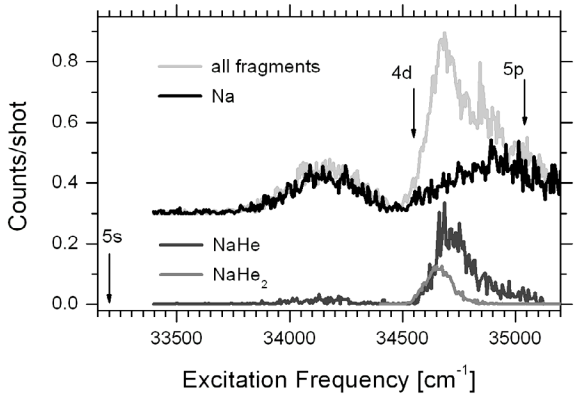

Figure 3.57: Excitation spectrum of 5s-4d-5p-band of Na-He_N with <r> = 41 Å recorded by monitoring Na, NaHe, $NaHe_2$ species and all products. The spectra are scaled such as to reflect the relative abundances found in TOF mass-spectra. The arrows indicate positions of free atomic 5s←3s, 4d←3s and 5p←3s transitions.

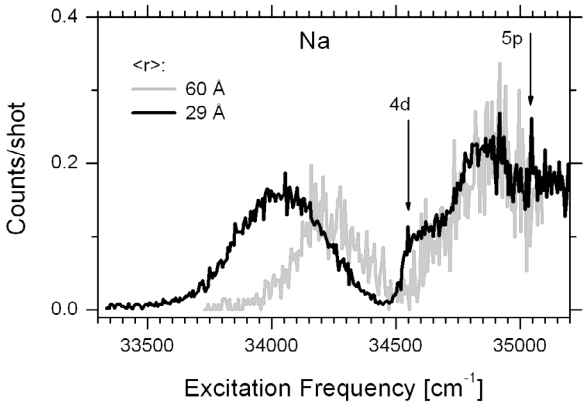

Figure 3.58: Excitation spectrum of 5s-4d-5p-band of Na-He_N at <r> = 60 Å and 29 Å recorded by monitoring bare Na atoms.

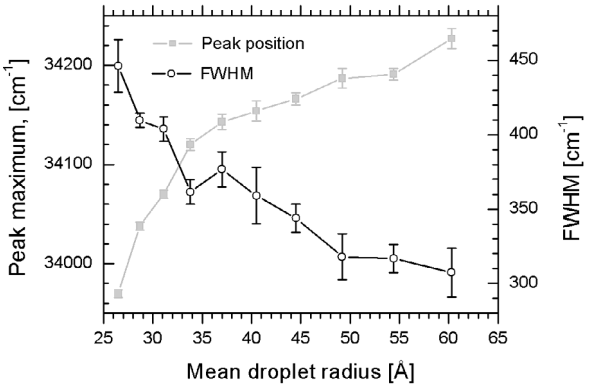

Figure 3.59: Variations of the peak position and its FWHM of the 5s-band excitation spectrum, which was fitted to Gaussian function 3.45, with the mean droplet size. The error bars represent the fitting errors.

The shape of the 5s-band is relatively symmetric and can be fitted quite well to the standard Gaussian function as:

3.45
$$f(\nu) = a\exp\left(-\frac{(\nu-\nu_0)^2}{2c^2}\right),$$
$$FWHM = c\cdot 2\sqrt{2\ln 2}$$

where ν is excitation frequency, a is the amplitude, ν_0 is the maximum of the Gaussian, and c is the effective width which can be expressed via the full width at half maximum (FWHM). In order to overview the evolution of the 5s dependence on the helium cluster size, the excitation spectrum was recorded at different mean droplet radii from <r> = 27 Å to <r> = 60 Å, see Figure 3.59. The variation of the band's maximum is more pronounced at smaller cluster sizes. The variation of the band's width is more regular: it decreases gradually with increasing droplet size from FWHM ≈ 450 cm^{-1} at <r> = 27 Å to FWHM ≈ 310 cm^{-1} at <r> = 60 Å.

3.2.1.2 TOF mass spectra

The TOF mass-spectra in the 5s and 4d-5p bands were recorded at two excitation frequencies for different droplet sizes. These frequencies were 34 143 cm^{-1} and 34 686 cm^{-1}, corresponding to the maximum of the Na excitation spectrum in the 5s-band and the maximum of NaHe excitation spectra in 4d-5p band, respectively. In the 5s-band only two species were detected: Na and NaHe. The heavier exciplexes $NaHe_n$, n>1, were not observed, implying that their relative abundances are inferior to 10^{-4}. In the 4d-5p band, heavier exciplexes $NaHe_n$, n=1-3, were detected. In both the 5s and the 4d-5p bands droplet size effects on the relative abundances of species were not observed, see Figure 3.60 and Figure 3.61.

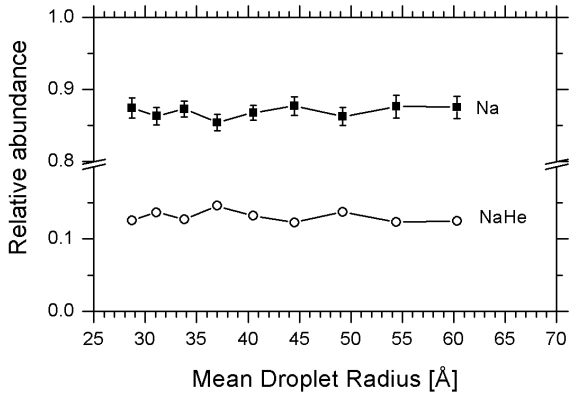

Figure 3.60: Relative abundance of desorbed Na and NaHe after 34 143 cm^{-1} excitation of Na-He_N at different droplet sizes. The lines through the data points are to guide the eye. Error bars are shown only if they are larger than the symbol size.

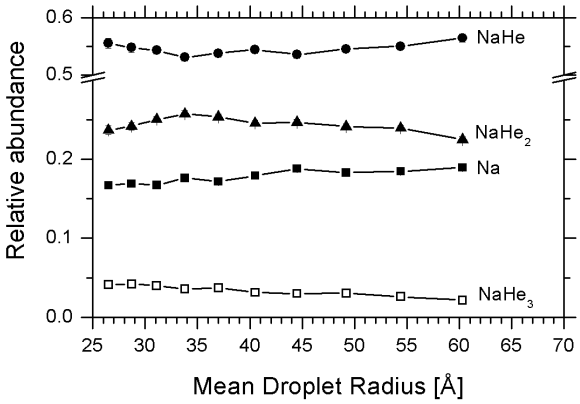

Figure 3.61: Relative abundance of desorbed Na, and $NaHe_n$, n=1-3, after 34 686 cm^{-1} excitation of Na-He_N at different droplet sizes. The lines through the data points are to guide the eye. Error bars are not shown because they are inferior to the symbol size.

3.2.1.3 Photoelectron spectra

3.2.1.3.1 5s-band

The photoelectron spectrum obtained following one-color 34 201 cm^{-1} excitation of Na on helium droplets with <r> = 54 Å is presented in Figure 3.62. Photoelectrons originating from the

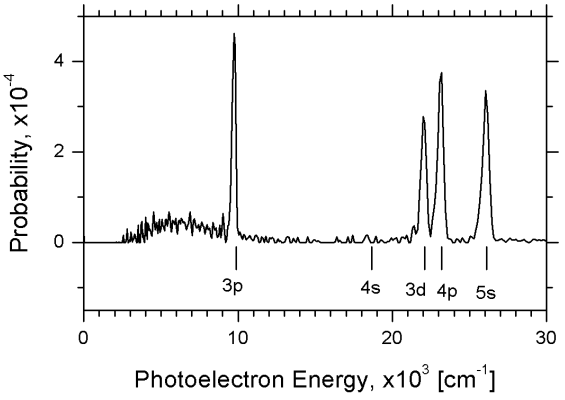

Figure 3.62: One-color photoelectron spectrum derived from photoelectron images recorded following 34 201 cm^{-1} excitation of Na-He_N with <r> = 54 Å. At the bottom the lines mark the energy of photoelectrons originating from the photoionization of excited states of Na with 34 201 cm^{-1} photon.

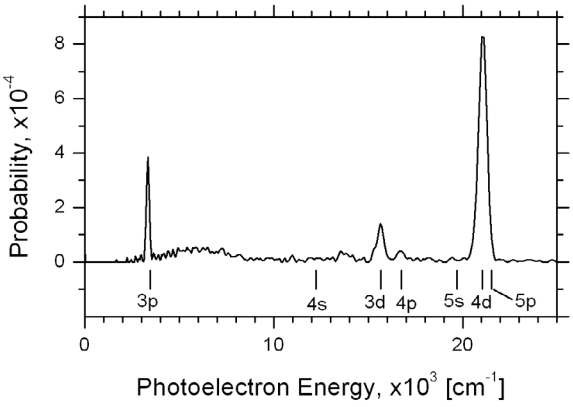

Figure 3.63: Two-color photoelectron spectra derived from photoelectron images recorded following 35 200 cm^{-1} excitation of Na-He_N with <r> = 41 Å. The ionization frequency is 27 778 cm^{-1}. At the bottom the lines mark the energy photoelectrons originating from the photoionization of soduim excited states with that photon. The line corresponding to the 4f excited state is not shown due to its closeness of 38 cm^{-1} to 4d states.

ionization of all energetically accessible states, except 4s, were observed. The broad feature at energies 2 000 - 9 000 cm^{-1} is due to the background photoelectrons created by light scattering on the copper parts in the imaging setup. The relative intensities of the photoelectron peaks do not vary with droplet size within the experimental errors, remaining the same at <r> = 54 Å and <r> = 34 Å, see Table 14.

Table 14 Photoelectron peak intensities in 5s-band

Na excited state	Experimental relative intensity	
	<r> = 34 Å	<r> = 54 Å
3p	0.232 ± 0.005	0.227 ± 0.005
4s	$<1\cdot10^{-3}$	$<1\cdot10^{-3}$
3d	0.210 ± 0.005	0.210 ± 0.005
4p	0.283 ± 0.005	0.283 ± 0.005
5s	0.275 ± 0.005	0.280 ± 0.005

3.2.1.3.2 4d-5p-band

A two-color scheme was used to obtain the photoelectron spectra following 35 200 cm^{-1} excitation within the 4d-5p band, see Figure 3.63. The ionization laser with frequency a of 27 778 cm^{-1} did not cause any background but at the same time the photon energy was enough to ionize excited Na down to 3p states. However, the background from scattered light of 35 200 cm^{-1} frequency was still present as broad feature in the 4 000 - 9 000 cm^{-1} energy region, but did not almost interfere with the signal of interest. The limited resolution of the photoelectron spectrum does not allow to resolve the photoelectron peak centered at 21 000 cm^{-1} into contributions from 4d-4f-5p excited states of Na. For the lower states, 3p-5s, the resolution is enough to separated the photoelectron peaks. Apart from the strong peak at 21 000 cm^{-1}, the other prominent peaks come from photoionization of Na in 3p and 3d excited states. Only a weak feature is distinguishable at the energy corresponding to the 4p state of Na. The relative intensities of the experimental photoelectron peaks are collected in Table 15.

Table 15 Photoelectron peak intensities in 4d-5p-band

Na excited state	3p	4s	3d	4p	5s	4d
Experimental relative intensity	0.118 ± 0.007	0.0	0.107 ± 0.007	0.033 ± 0.012	0.0	0.743 ± 0.003

3.2.1.4 Ion imaging

3.2.1.4.1 5s-band

As was mentioned above, at the excitation frequencies like in the 5s-band a considerable background in photoelectron images arises from scattered excitation light. So, we tried to employ several frequencies in the ionization step. For ion imaging the photoelectron background is not important, so both one-color and two-color schemes are applicable. With respect to ion imaging, the question about the detection of low excited states of desorbed Na arises. In principle, the velocity

distribution may consist of several contributions correlating to particular excited states of Na. Depending on the ionization frequency in the two-color scheme, some lower states cannot be ionized, which may change the velocity distribution. In the 5s-band we tried one- and two-color schemes, where frequencies of ≈ 34 000 cm^{-1} and 13 423 cm^{-1}were used, respectively. In both cases the velocity distributions of desorbed Na were practically identical. Since the signal-to-noise ration in the two-color scheme was better than that in one-color, we will present the velocity ion images in the 5s band recorded with the latter scheme.

The ion imaging within the 5s-band has revealed two components in the speed distribution of desorbed Na atoms, see Figure 3.64. Each component has a positive anisotropy parameter approaching a value of ≈ 1.5. The ion images were recorded at different excitation frequencies within the 5s-band, but only the slow component revealed a significant variation with excitation frequency. The weak high speed component near 2 000 m/s might originate from dissociation of sodium dimer on the surface of nanodroplets. The dimer formation was difficult to suppress by lowering the sodium vapor pressure without considerably loosing monomer signal. At the 34 143 cm^{-1} the ion images were recorded at three different droplet sizes with <r> = 29 Å, 41 Å and 60 Å. No droplet size effects on the

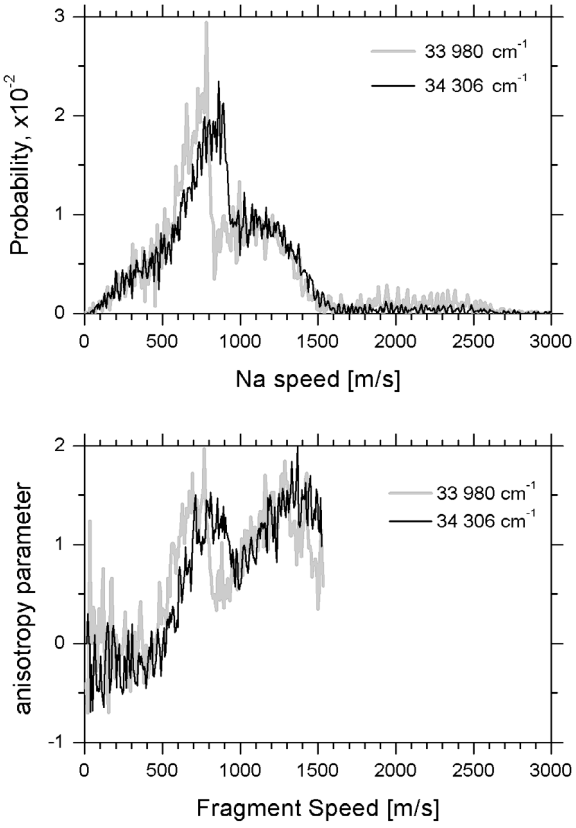

Figure 3.64: Upper panel: speed distributions of desorbed sodium atoms derived from velocity map ion image recorded following 33 980 and 34 306 cm^{-1} excitations of Na-He_N with <r> = 41 Å. The ionization frequency is 13 423 cm^{-1}. Lower panel: corresponding variation of anisotropy parameter.

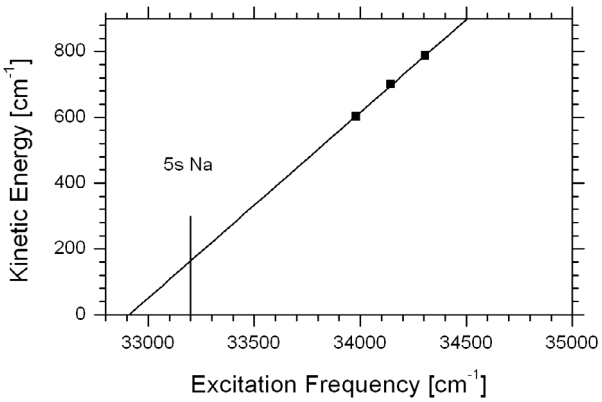

Figure 3.65: The variation of the sharp onset in the kinetic energy distributions of recoiled Na atoms.

velocity distributions were observed. Ion images of the NaHe exciplex were not recorded in view of their low signal level.

The slow component, which has the sharp threshold in the 800-900 m/s region, varies regularly with excitation energy and in this resopect is similar to the speed distributions found in the lower excited states. However, it is difficult to separate the two speed components in order to extract the variable one, and therefore impossible to plot the mean kinetic energy $<E_{kin}>$ versus the excitation frequency for the slow component. Instead of $<E_{kin}>$, the sharp onset in the E_{kin} with a width of only 50 cm^{-1} may serve as the replacement. The kinetic energies measured at half height of this onset are plotted versus the excitation frequency in Figure 3.65. A straight line can be easily drawn through the points, so the fitting to our usual linear function 3.3 yields the slope $a = 0.56\pm0.02$ and the onset $b =$ 32 910±50 cm^{-1}. Since instead of $<E_{kin}>$ the threshold is plotted, the ≈ 300 cm^{-1} deviation in the onset from the energy of the 5s←3s atomic transition at 33 200 cm^{-1}[99] can be considered as tolerable for attributing the slow speed component to desorbed excited Na in 5s state. The value of the slope for the 5s state is also reasonable, since it is close to those found in the 4s- and 4p-bands, see sections 3.1.2.3 and 3.1.4.5.

3.2.1.4.2 4d-5p-band

We used two schemes for recording ion images in the 4d-5p-band: a two-color scheme as in the 5s-band to record velocity map images at 34 800, 35 000, 35 200 and 35 400 cm^{-1} excitation frequencies, and a one-color scheme to record images at 35 060, 35 130, 35 600-36 000 cm^{-1}. We did not record the images at the same excitation frequency using both schemes. However, taking into account the results in the 5s-band, we believe that the velocity distributions will be the same independent of the scheme used. The regular behavior of $<E_{kin}(Na)>$ obtained with both schemes supports our hypothesis (all data points follow the same linear trend).

We will present the mean kinetic energies of desorbed Na at the excitation frequencies beyond those shown shown in the excitation spectrum, see Figure 3.57, since they follow the linear dependence which continues much further than the 35 200 cm^{-1}. The excitation spectrum in that frequency region will be shown in the next section 3.2.2.1. The ion images of NaHe and $NaHe_2$ exciplexes were recorded only at the maximum of their excitation spectra.

We begin with the presentation of the speed and anisotropy parameter distributions of Na, NaHe and $NaHe_2$ obtained following the 34 686 cm^{-1} excitation of Na-He_N in Figure 3.66. The speed distribution of NaHe and $NaHe_2$ exciplexes are similar, demonstrating a single component with a FWHM ≈ 200 m/s. In contrast, the speed distribution of desorbed Na has two contributions. The narrow one has a FWHM ≈ 150 m/s and is centered at ≈ 200 m/s. The second broad feature is centered at ≈ 800 m/s. It spans up to 1500 m/s and has a FWHM ≈ 650 m/s. The desorbed Na manifests an anisotropy parameter of zero, while thr exciplexes have slightly negative values in the range of -0.1-0.2.

The speed and angular distributions of desorbed Na obtained at 35 060 cm^{-1} and 35 800 cm^{-1} excitation frequencies are shown in Figure 3.67. The broad component of the speed distribution still remains, though its contribution is reduced compared to the data taken at 34 686 cm^{-1}. The most pronounced part of the speed distribution has a FWHM ≈ 150 m/s. It shifts to higher speeds with increasing excitation frequency. The angular anisotropy parameter also correlates to the narrow frequency-dependent speed component. It has a $\beta \approx 0.5$ - 1 for this component, whereas outside the region it mainly oscillates around zero.

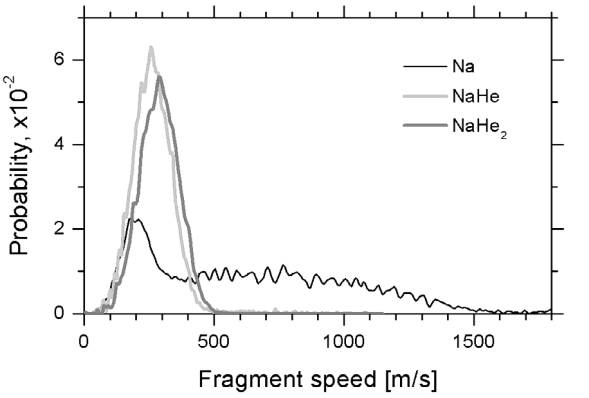

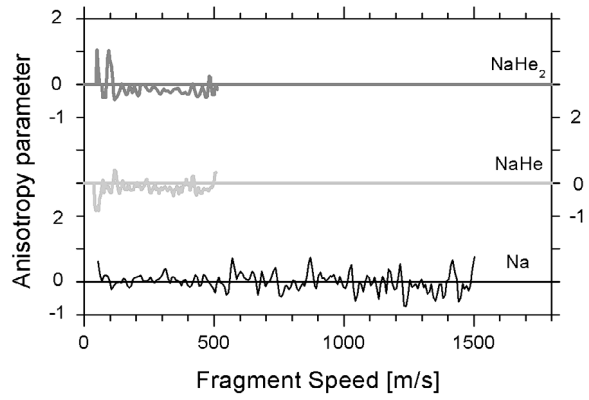

Figure 3.66: Upper panel: speed distribution of desorbed Na, NaHe and $NaHe_2$ derived from velocity map ion images recorded following 34 686 cm^{-1} excitation of Na-He_N with <r> = 41 Å. The ionization frequency is 13 423 cm^{-1}. Lower panel: corresponding variation of the anisotropy parameter.

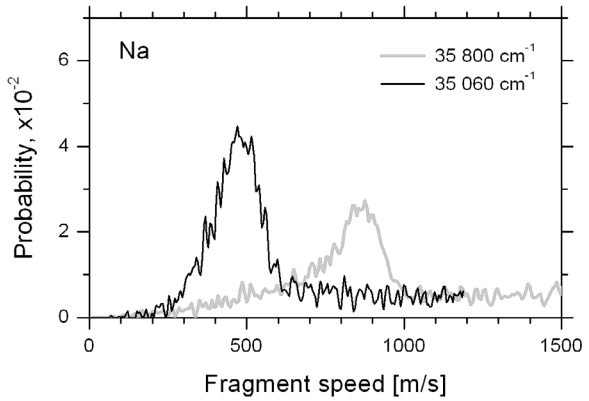

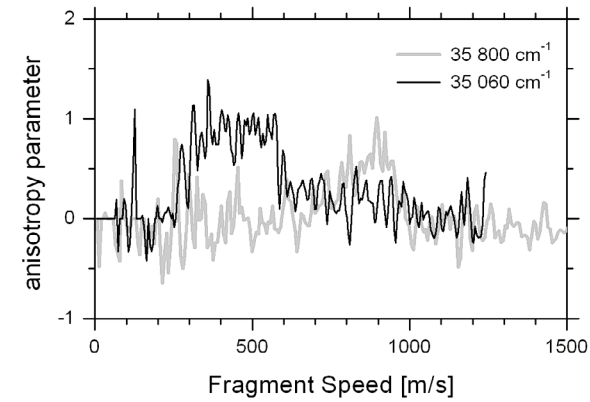

Figure 3.67: Upper panel: speed distribution of desorbed Na derived from velocity map ion image recorded following 35 060 cm^{-1} and 35 800 cm^{-1} excitations of Na-He_N with <r> = 41 Å. The ionization frequencies are equal to excitation ones. Lower panel: corresponding variations of the anisotropy parameters.

The mean kinetic energies $<E_{kin}>$ and anisotropy parameters $<\beta>$ of desorbed Na at excitation energies higher than 34 800 cm^{-1} are presented in Figure 3.68. To avoid the contribution of the broad speed component, the averaging was made up to the high speed onset of the narrow component, where it decreases to the background level. For the speed distributions shown in Figure 3.67 the onsets are 600 m/s and 1 000 m/s for speed distributions recorded at 35 060 and 35 800 cm^{-1} respectively. The $<E_{kin}>$ manifest a linear dependence versus excitation frequency, which is similar to the situation observed in the low energy 3p-4p bands. The fitting to linear function 3.3 yielded the following parameters: the slope a = 0.499±0.007 and the onset b = 34 637±10 cm^{-1}. The onset value is shifted to high frequencies with respect to the 4d←3s atomic transition by 88 cm^{-1}. The standard deviation of the mean kinetic energy, shown in open symbols, linearly rises at excitation frequencies higher than ≈ 35 300 cm^{-1}. The $<\beta>$ starts at positive values around unity at low frequencies and varies considerably around the 5p←3s atomic transition of sodium, see the low panel in Figure 3.68. It decreases from ≈ 1 to ≈ -0.3 within ≈ 150 cm^{-1} frequency region centered at 35 000 cm^{-1}. After 35 400 cm^{-1} the $<\beta>$ steadily increases from ≈ -0.5 to ≈ 0.3.

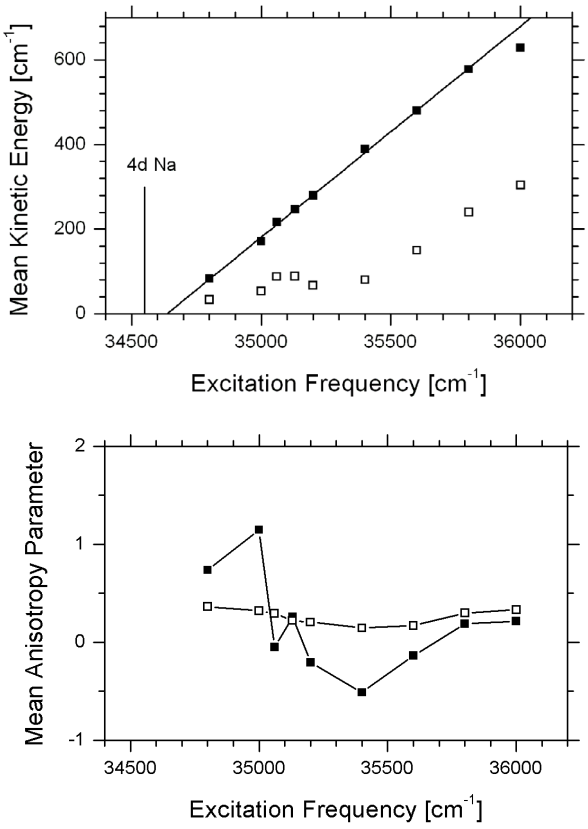

Figure 3.68: Upper panel: Mean kinetic energy of desorbed Na atoms derived from velocity map ion images recorded following excitation of Na-He_N with <r> = 41 Å at different frequencies within the 4d-5p-band. The ionization frequency is 13 423 cm^{-1}. Vertical line in the left part of the graph marks the 4d←3s transition of free sodium. The open symbols are values of standard deviations. The line going through experimental points is the fit to the linear function 3.3 in the 34 800-35 800 cm^{-1} region. Lower panel: Corresponding mean anisotropy parameters. The open symbols are values of standard deviations. The lines through the data points are to guide the eye.

3.2.2 6s and 5d-6p bands

The next group of features in the excitation spectrum of Na-He_N in the 36 500 - 38 000 cm^{-1} frequency region we will call 6s- and 5d-5p bands in analogy with the previous 5s- and 4d-5p-bands. This choice should not be considered as an assignment, since the experimental data do not demonstrate clear correspondence to a particular excited state of free Na.

3.2.2.1 Excitation spectra

This time we used one- and two-photon excitation schemes. For the excited states of Na-He_N higher than 36 500 cm^{-1} in energy, the two-photon excitation does not interfere with lower states, because there is no absorption of Na-He_N between 3p and 4s-bands in the 18 000 - 25 700 cm^{-1} frequency region. The two-photon excitation spectrum is needed to record a photoelectron spectra within a particular band, see section below. The comparison of one- and two-photon excitation spectra allowes to conclude, within propensities of transition probabilities (see section 3.1.5.1), that essentially the same states are probed in both schemes.

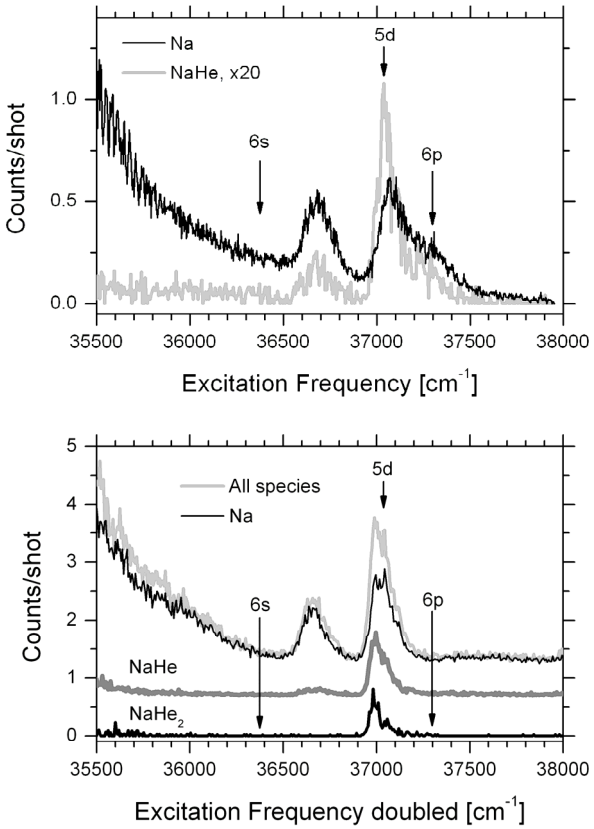

Figure 3.69: Upper panel: one-photon excitation spectrum of 6s-5d-6p-band of Na-He_N with <r> = 41 Å recorded by monitoring Na and NaHe species. Lower panel: the same spectrum obtained by two-photon excitation and by monitoring Na, NaHe, $NaHe_2$ and all products. The arrows indicate frequencies of free atomic 6s←3s, 5d←3s and 6p←3s transitions.

The excitation spectra recorded by detecting Na and NaHe products following one-photon excitation of Na-He_N are shown in the upper panel of Figure 3.69. The first feature, which is centered at 36 700 cm^{-1}, we will call the 6s-band, since it is located close to 6s←3s transition in free Na atom at 36 373 cm^{-1}[99]. The feature in the 36 900 - 37 500 cm^{-1} we will call 5d-6p band because it spans over the corresponding atomic 5d←3s and 6p←3s transitions of Na at 37 037 cm^{-1} and 37 297 cm^{-1} frequencies respectively[99]. The 6s and 5d-6p bands overlap with the signal correlating to lower excited states of sodium. It is not clear whether this signal is the continuation of the spectrum in 4d-5p band after 35 200 cm^{-1}, see Figure 3.57, or it is the part of a new feature. We were not able to record an excitation spectrum of Na-He_N between 35 200 cm^{-1} and 35 500 cm^{-1} due to the technical problems.

The two-photon excitation spectra, which were recorded also by detecting $NaHe_2$, are presented in the lower panel of Figure 3.69. The differences between the one- and two-photon excitation spectra are twofold. First, in the 5d-6p-band the high frequency part of the spectrum in the 37 200 - 37 600 cm^{-1} region, which is visible in the one-photon excitation, disappears in the two-photon excitation. Second, the $NaHe_n$, n=1-2, exciplexes are more abundant in the two-photon excitation spectrum compared to that in one-photon. This may be caused by the probing of different types of transitions or by the different ionization cross-sections of the desorbed species. Indeed, in the latter case ionization frequencies differed by a factor of two because of one-color detection scheme used: ≈ 37 000 cm^{-1} and 18 500 cm^{-1} for one- and two-photon excitations respectively. In contrast to the 5d-6p-band, the 6s-band does not change its shape in both type of excitation spectra. In addition,

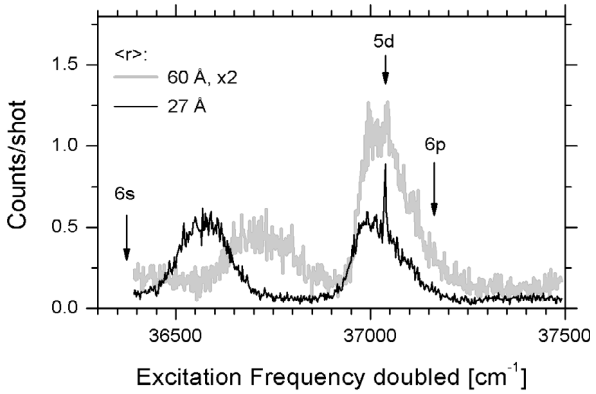

Figure 3.70: Two-photon excitation spectra of 6s-5d-6p-band of sodium atoms on the surface of helium nanodroplets with <r> = 60 Å and <r> = 27 Å recorded by monitoring bare Na atoms. The arrows indicate positions of free atom 6s←3s, 5d←3s and 6p←3s transitions.

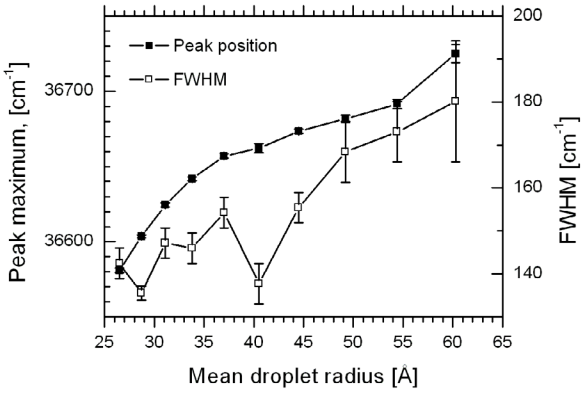

Figure 3.71: Variations of the peak position and its FWHM of the 6s-band excitation spectrum with droplet size as fitted to a Gaussian in expression 3.45. Error bars show fitting errors.

the main desorbed species in both case are bare Na atoms. In this respect, it resembles the Σ←Σ transitions observed in the lower 3p-4p bands.

The influence of the droplet size on the excitation spectra is shown in Figure 3.70. The two-photon excitation is shown as it has a lower background and less overlap with the broad low frequency feature. The one-photon excitation spectra yields similar results. The change in the position of 6s-band by ≈ 150 cm^{-1} from ≈ 36 550 cm^{-1} at <r> = 29 Å to ≈ 36 700 cm^{-1} at <r> = 60 Å is obvious. In contrast, the 5d-band keeps almost the same position and the shape. The 6s-band excitation spectrum was recorded at different droplet sizes. The shape of the band stays well symmetric over <r> = 27 - 60 Å droplet sizes and can be easily fitted to Gaussian profile in expression 3.45. The peak positions of fitted profiles and their FWHM are presented in Figure 3.71. The shift and the FWHM of the 6s-band to higher frequencies increase with the increasing mean droplet radius. The shift in frequency between the smallest and the largest droplets amounts to 144 cm^{-1}. The FWHM shows a smaller difference of ≈ 40 cm^{-1}.

The relative abundances of desorbed species were not specially studied in the 6s-5d-6p bands. However, the qualitative abundances can be obtained from the signal level in the excitation spectra shown in Figure 3.69. We estimate the abundances in the two-photon excitation spectrum at the 37 000 cm^{-1} as: ≈ 0.5, ≈ 0.4 and ≈ 0.1 for Na, NaHe and $NaHe_2$ respectively. We believe that there is no droplet size effects on the relative abundances of species, since it was not observed in the lower 4p and 5s-4d-5p excitation bands. In support of this hypothesis is the general absence of droplet size effects for the higher excitation bands considered in section 3.3.

3.2.2.2 Photoelectron spectra

In order to avoid large background signal, we used the one-color two-photon scheme to obtain photoelectron spectra in the 6s-5d-6p bands.

It should be noted that the two-photon scheme favors detection of the nd excited states of desorbed Na because of their much larger ionization cross-sections compared to those of ns and np states. In the frequency range of 18 000 - 21 000 cm^{-1} the ionization cross-sections of nd states are of

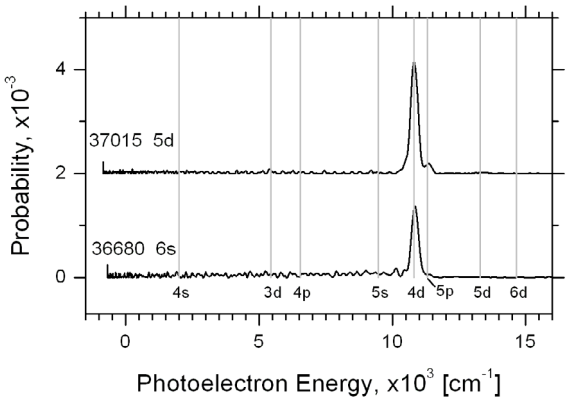

Figure 3.72: Photoelectron spectra derived from photoelectron images recorded following one-color two-photon excitation of Na-He_N with <r> = 60 Å. The spectra are shifted according to expression 3.46 so that the photoelectrons, originating from the same atomic levels of Na, are aligned at the same energy. The corresponding Na levels are indicated at the bottom of the graph. Text labels in the left part of the graph indicate the doubled excitation frequencies and designation of the Na-He_N excitation band.

the order of $1 \cdot 10^{-18}$ cm^2 , which is an order of magnitude larger than those for np states and two orders of magnitude larger than for ns states[109, 136, 137]. It is not excluded that Na atoms desorb in the 4f excited state. However, we can not resolve the photoelectron peak from the ionization of the 4f state from that of the 4d state, which differ by only 48 cm^{-1}, due resolution in the photoelectron spectra, see Chapter 2. In the following we will consider only the nd excited states.

In view of the many peaks which may appear in photoelectron spectra from various excited states of desorbed Na, we have shifted the experimental spectra so that the peaks from the same excited state are aligned at fixed energy. This makes the comparison of photoelectron spectra recorded at different excitation energies much easier. For the conversion we assume that the ionization photon has a fixed frequency $\tilde{\nu}_0$ = 17 500 cm^{-1}. The new photoelectron energy E' [cm^{-1}] is then calculated by subtracting from the original energy E the energy difference between the real ionization photon of frequency $\tilde{\nu}$ [cm^{-1}] and the one fixed at $\tilde{\nu}_0$:

3.46 $$E' = E - \left(\tilde{\nu} - \tilde{\nu}_0\right)$$

The photoelectron spectra recorded with two-photon excitation at 36 680 cm^{-1} and 37 015 cm^{-1} (doubled frequencies) of Na-He_N with <r> = 60 Å are shown in Figure 3.72. These frequencies correspond to: a) the centre of 6s-band and b) the maximum in the 5d-6p-band, respectively. In the center of the 6s-band only photoelectrons originating from the 4d excited state of Na were detected. In the maximum of the 5d-6p band, the 4d peak and a distinct weak peak corresponding to the 5p state of sodium are present. The droplet size effect was checked by comparing the photoelectron spectra recorded with <r> = 60 Å and <r> = 29 Å. Within the experimental S/N ratio both spectra are identical.

3.2.2.3 Ion imaging

We will focus on ion imaging of desorbed species after the one-photon excitation of Na-He_N. Considering the Na-He_N interaction as in a diatomic molecule, the angular distribution of the excited

sodium desorbed from the helium droplet is directly related to the upper excited molecular state, Σ or Π, see section 3.1.5.4.

3.2.2.3.1 6s-band

We present first in Figure 3.73 the speed and anisotropy parameter (β-parameter) distributions of Na and NaHe obtained by excitation of Na-He_N in the center of the 6s-band at 36 680 cm^{-1}. The velocity distributions of desorbed species demonstrate mixed features. The speed distribution of Na has one component, while that of NaHe has two. The slower component, in the speed range of 100 - 400 m/s, hasaf β-parameter of zero. At high speeds, in the range 700-1 400 m/s, both Na and NaHe have $\beta \approx 1.5$. The speed distribution of the desorbed excited Na demonstrates weak dependence on the excitation frequency, see Figure 3.74. By going from 36 620 cm^{-1} to 36 740 cm^{-1}, it shifts by ≈ 100 m/s to higher speeds. The extracted mean kinetic energy $\langle E_{kin} \rangle$ of desorbed sodium, see Figure 3.75, can be fitted to the linear function of expression 3.3. As in the case of the 4d-5p-band, the averaging was made from zero to high speed onset at ≈ 1 400 m/s in order to avoid the contribution

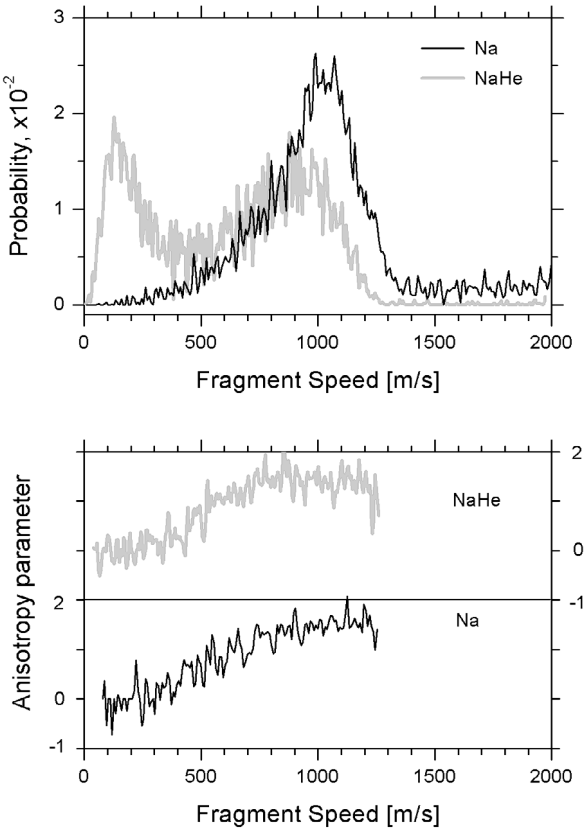

Figure 3.73: Upper panel: speed distributions of desorbed Na and NaHe derived from velocity map ion images recorded following one-photon 36 680 cm^{-1} excitation of Na-He_N with $\langle r \rangle$ = 41 Å. Lower panel: corresponding variation of the anisotropy parameter.

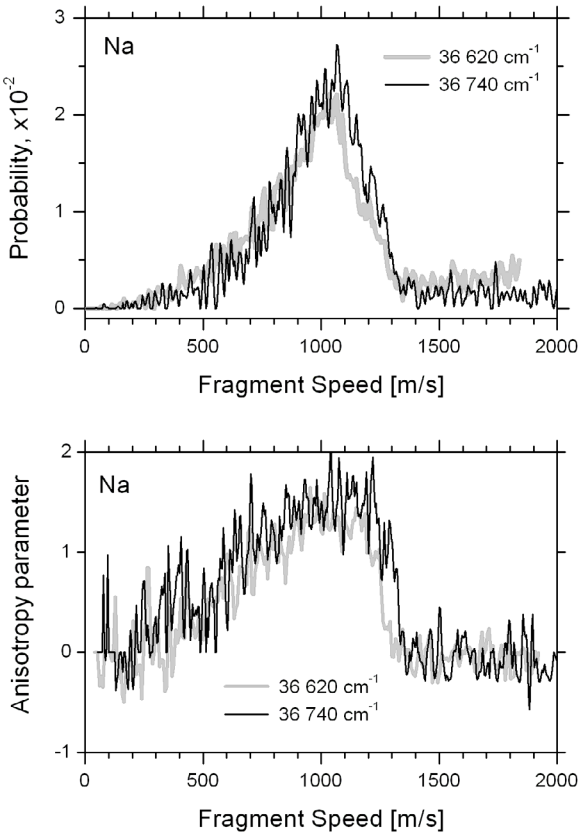

Figure 3.74: Upper panel: speed distribution of desorbed Na derived from velocity map ion images recorded following one-color one-photon 36 620 cm^{-1} and 36 740 cm^{-1} excitation of Na-He_N with $\langle r \rangle$ = 41 Å. Lower panel: corresponding variation of the anisotropy parameters.

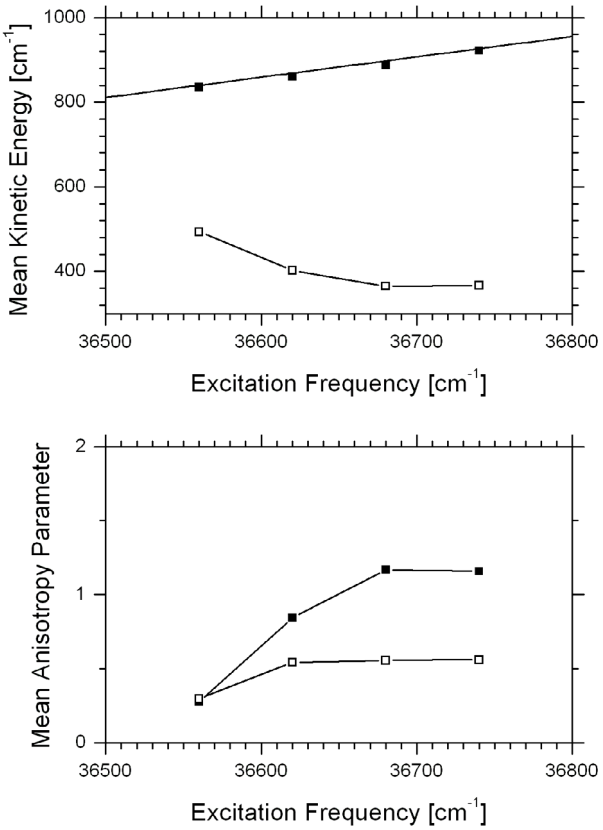

Figure 3.75: Upper panel: Mean kinetic energies of desorbed bare Na atoms derived from velocity map ion images recorded following one-photon excitation of Na-He_N with <r> = 41 Å within 6s-band. The open symbols are values of standard deviations. The straight line through the experimental points is a fit to the linear function 3.3. Lower panel: Corresponding mean anisotropy parameters derived from the velocity distributions of bare Na atoms. The open symbols are the values of the standard deviations. The lines through the data points are to guide the eye.

from the high speed background. The obtained slope and offset values are $a = 0.48 \pm 0.03$, $b = 34\,810 \pm 100$ cm^{-1}, respectively. The value of the onset falls between the 34 549 cm^{-1} and 35 041 cm^{-1} energies of 4d and 5p excited states of Na atom, respectively. The slope value is close to $a = 0.499 \pm 0.007$ found in the 4d-5p-band. The variation of the standard deviation of the $<E_{kin}>$, shown in open symbols in Figure 3.75, is quite interesting. It decreases at higher excitation energies, which is opposite to all previous observation in lower excitation bands. The variation of the mean anisotropy parameter $<\beta>$ within the excitation band is shown in the lower panel of Figure 3.75. The $<\beta>$ gradually increases from ≈ 0.3 to ≈ 1.2. Its standard deviation remains practically at the same value of ≈ 0.5, excepting the lowest frequency with the value of ≈ 0.3. The droplet size effect on the velocity distribution was not specially checked, but we do not expect any effect in view of its absence in the lower excitation bands of Na-He_N.

3.2.2.3.2 5d-6p band

In the 5d-6p band we recorded the velocity distributions of desorbed Na and NaHe at the maximum and in the high frequency shoulder of the corresponding species-specific excitation spectra, see Figure 3.76 and Figure 3.77. Both species have two-component speed distributions. The slow ones, in the range of 100 - 500 m/s, appear after the excitation in the high frequency part of the 5d-6p

band. The slow component of the Na speed distribution changes its position with the excitation frequency: at 37 292 cm^{-1} it peaks at ≈ 300 m/s while at 37 400 cm^{-1} it peaks at ≈ 400 m/s. Taking these two values and assuming linear dependence of corresponding E_{kin}, one can extract the slope and the onset in the expected linear dependence according to expression 3.3 similar to the lower excited states of Na-He_N: $a \approx 0.6$ and $b \approx 37\ 200$ cm^{-1}. The slope value is in reasonable agreement with the previous cases in the 5s, 4d and 6s-bands. The onset value falls between the energies of Na in the excited 5d and 6p state at 37 037 cm^{-1} and 37 296 cm^{-1}[99]. The anisotropy parameters corresponding to slow components are negative with $\beta \approx -0.5$ for Na and positive with $\beta \approx 0.5$ for NaHe.

The high speed components, in the range of 500 - 1400 m/s, are present at all excitation frequencies. The β-parameters corresponding to the fast components show a frequency dependence and have opposite signs: for Na species $\beta \approx 0.2$ at 37 071 cm^{-1} and $\beta \approx -0.3$ at 37 292 cm^{-1} and 37 400 cm^{-1}; for the NaHe the anisotropy parameters are $\beta \approx -0.2$ and $\beta \approx 0.3$ for 37 037 cm^{-1} and 37 137 cm^{-1} respectively. Droplet size effects on the velocity distributions of Na and NaHe were not checked.

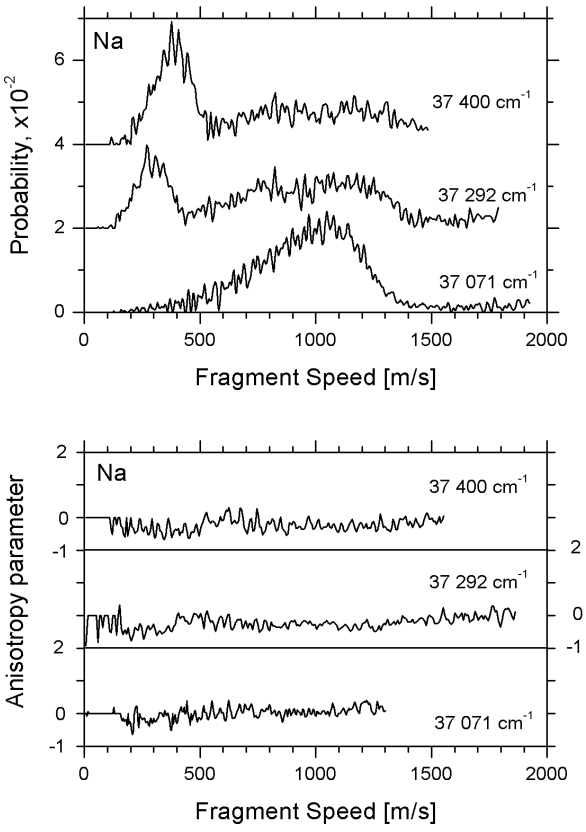

Figure 3.76: Upper panel: speed distribution of desorbed Na derived from velocity map ion images recorded following one-photon 37 071, 37 292 and 37 400 cm^{-1} excitations of Na-He_N with <r> = 41 Å. Lower panel: corresponding variations of the anisotropy parameters.

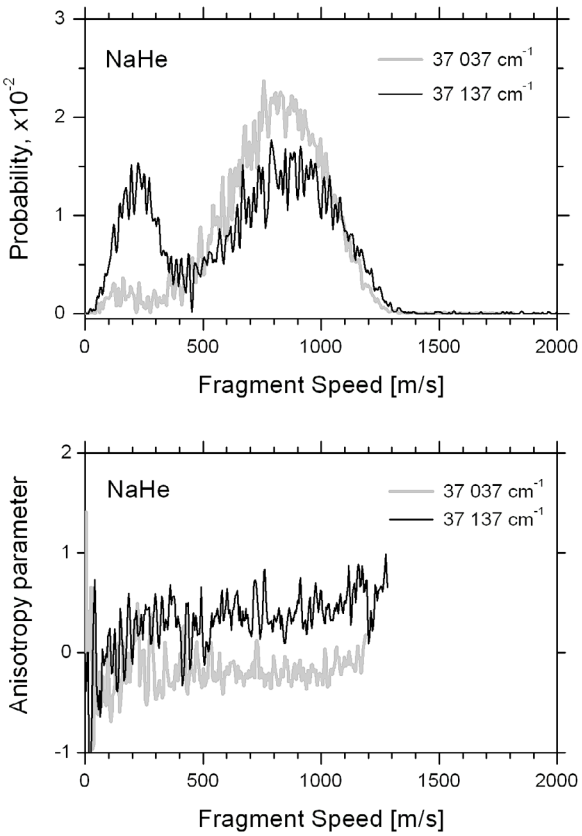

Figure 3.77: Upper panel: speed distribution of desorbed NaHe derived from velocity map ion images recorded following one-photon 37 037 cm^{-1} and 37 137 cm^{-1} excitations of Na-He_N with <r> = 41 Å. Lower panel: corresponding variations of the anisotropy parameters.

3.2.3 Discussion

Dynamics within the 5s-4d-5p and 6s-5d-6p bands in the Na-He_N excitation spectrum are found to be much more complex compared to the relatively simple situation in the lower 3p-4p excitation bands. We will explore below the applicability of the models, which were developed for the lower excitation bands, for the medium bands. For simplicity we will consider only the ns, np and nd excited states of Na and neglect the nf and ng states. Their influence is not clear in view of the already complex picture were the ns, np and nd states are not well distinguishable.

3.2.3.1 Excitation spectra

3.2.3.1.1 Na-He_N potentials

We start with the presentation of the NaHe pair potentials and Na-He_N effective potentials, see Figure 3.78. As before in section 3.1.5.1, we used the pair potential of Pascale[106, 119] and the Na-He_{5000} density profile of the group of Barranco[19, 116] to generate the effective potentials within pair-wise additive model for the Na-He_N interaction. As can be seen in the right panel in Figure 3.78, the Na-He_{5000} effective potentials correlating to 5s, 5p and 6s excited states of Na are strongly repulsive. In contrast, the effective potentials corresponding to the 4d and 5d states demonstrate more complex character with a sort of broad potential barriers. The observed peculiarities are due to the "mixing" between the Σ and Π, Δ potential curves of NaHe in the generation procedure of Na-He_N potentials, see expression 3.12. The Σ potential curves of the Na(nd)-He, n=4-5, pair potentials have an undulatory character in the 10-30 Å region of internuclear distance. Here the potential energy is higher than the energy of the corresponding excited atomic states. At the same time the Π, Δ potential curves do not have such undulation and they smoothly approach the atomic energy level within 10 Å of internuclear distance. The "mixing" of these states results in the broad barriers for the effective potentials in the region of z = 40-60 Å.

3.2.3.1.2 Comparison of the calculated and experimental spectra

The absorption spectra corresponding to the bound-free transition between the Na(3s)-He_{5000} and the repulsive potentials Na(5s,5p,6s)-He_{5000} were calculated with the BCONT 2.2 program[111] in the same way as was done for the low excited states of Na-He_N, see section 3.1.5.1.5.

As was shown previously, the simple one-dimensional pair-wise model to describe the Na-He_N interaction reproduced successfully the 3p, 4s and 3d excitation spectra. However, for the 4p-band the deviation of the calculated spectrum from the experiment was considerable. Partially this is caused by the quality of pair potentials. It is expected that for higher excited states the discrepancy will become even larger. Indeed, the 5s Σ' ← 3s Σ' calculated absorption spectrum, which is centered at ≈ 35 700 cm^{-1}, is shifted by ≈ 1 500 cm^{-1} to higher frequencies from the experimental spectrum in the 5s-band centered at ≈ 34 100 cm^{-1}, see Figure 3.79. Nevertheless, the FWHM ≈ 300 cm^{-1} of the calculated spectrum is quite close to the experimental width of FWHM ≈ 350 cm^{-1}, see Figure 3.59. The rest of the experimental excitation spectra could not be directly related to the calculated spectra. The experimental data do not manifest clear characteristics which can be attributed to a particular excited state of Na, as was the case in the low excited states of Na-He_N. For instance, the calculated 6s Σ'←3s Σ' absorption spectra is centered at ≈ 39 600 cm^{-1}, which is shifted by ≈ 3 900 cm^{-1} to higher frequency with respect to the 6s-band. Furthermore, its FWHM ≈ 300 cm^{-1} is twice larger than the experimental value of FWHM ≈ 150 cm^{-1}, see Figure 3.71. The calculated 5p Π'←3s Σ' spectrum, which is centered at ≈ 39 600 cm^{-1}, is too broad having a FWHM ≈ 1 500 cm^{-1} and shifted to higher

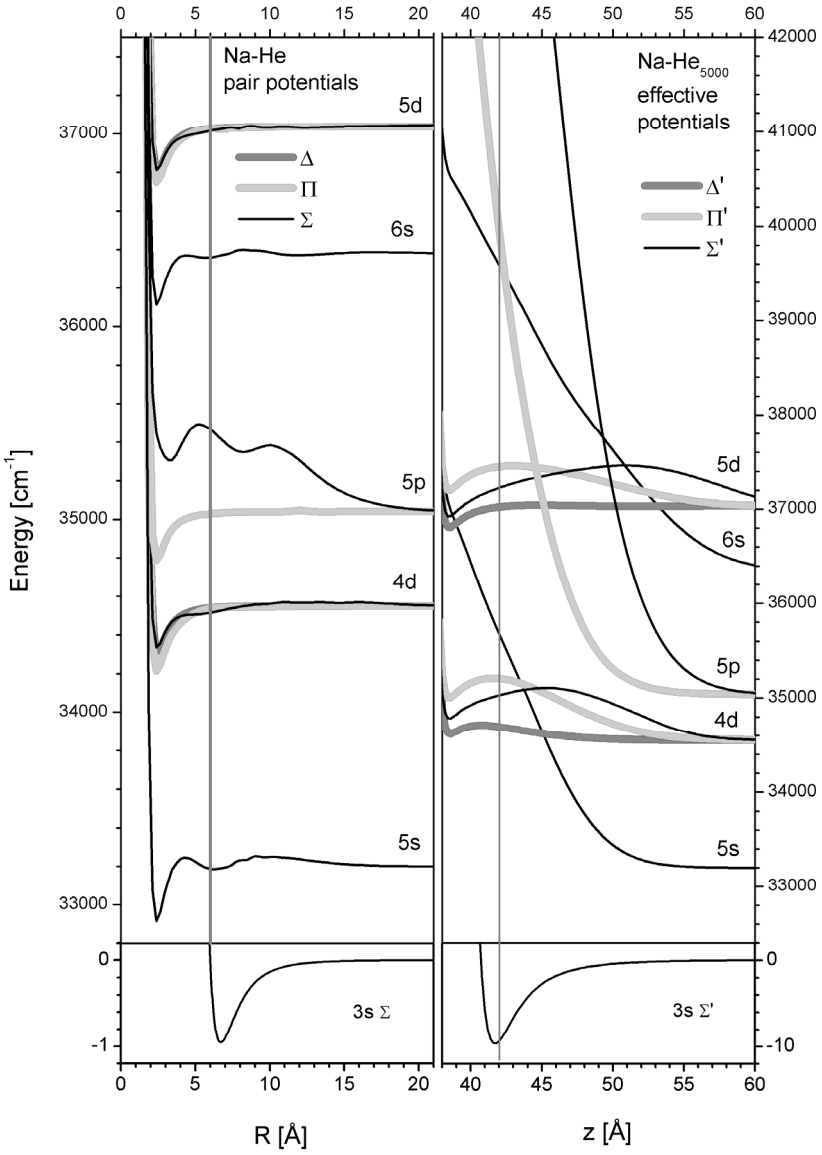

Figure 3.78: Left panels: NaHe pair potentials of Pascale[106, 119]. In the lowest panel the Na(3s)He pair potential of Patil[118] is depicted. The vertical line indicates the distance between Na and the droplet surface. Right panels: the corresponding Na(n*l*)-He_{5000} effective potentials are shown. The vertical line shows the Na location in the ground Na(3s)-He_{5000} state.

frequencies by 4 000 cm^{-1} from the 4d-5p experimental located near 35 000 cm^{-1}. The 5p Σ'←3s Σ' calculated absorption spectrum lies even above the Na atomic ionization potential at 41 449 cm^{-1}[99] and is not shown.

The attempts to calculate 4d Λ'←3s Σ' and 5d Λ'←3s Σ', Λ= Σ, Π, Δ, absorption spectra were not successful because of unphysical results obtained using the standard options of BCONT 2.2 program[111]. However, considering the inner levels in the 4d,5d Σ' states as bound, which seems justified in view of the large potential barriers, the 4d Σ'←3s Σ' and 5d Σ'←3s Σ' absorption spectra were calculated with the LEVEL 8.0 program[108]. They correspond approximately to the experimental Na-He_N excitation spectra, but their physical meaning is not clear.

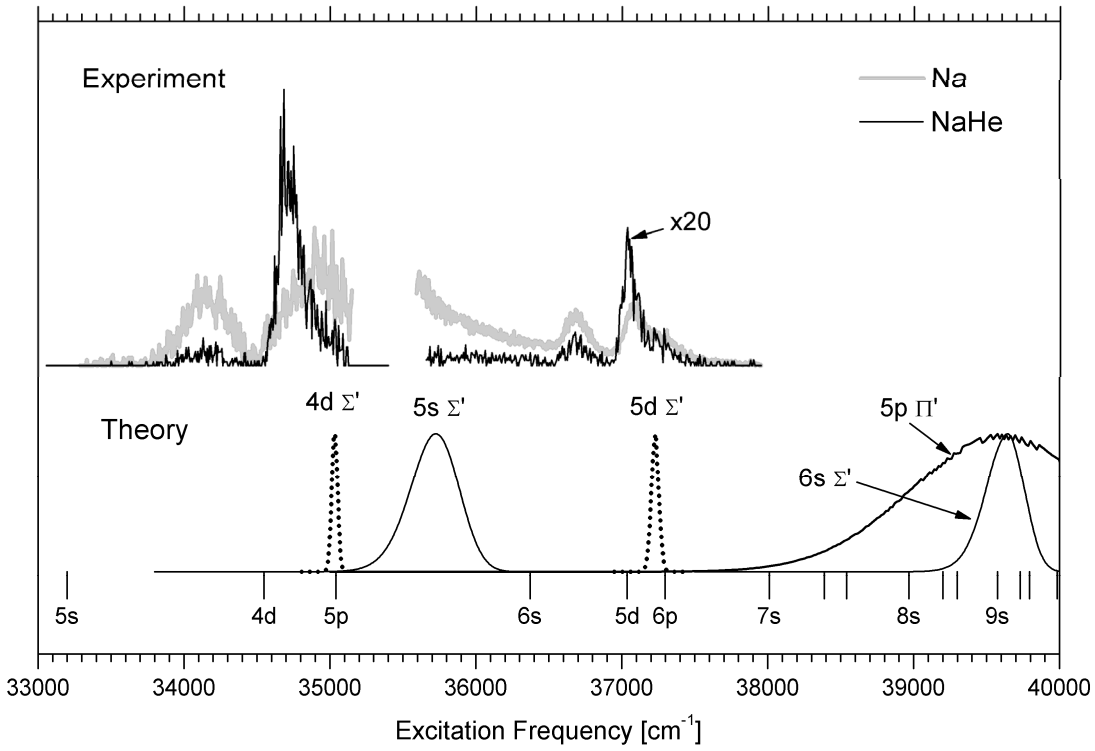

Figure 3.79: Comparison of the one-photon experimental excitation spectra of Na-He_N with <r> = 41 Å in the 5s-6p bands with the calculated spectra. The 4d Σ' and 5d Σ' spectra represent bound-bound transitions while the other spectra are of the bound-free type. At the bottom, the energies of atomic levels are marked with vertical lines. After the levels 7s - 6d - 7p, only the ns-levels of the following ns - (n-1)d - np sequences are labeled.

In view of the obvious breakdown of the pair-wise additive model for medium excited states of Na-He_N we do not consider the droplet size dependence of the theoretical spectra. A possible reason of the breakdown may be related to higher density of states in the atomic sodium. It is expected that these levels, perturbed by the helium droplet, will be broadened, mix and overlap. This may give similar results to that observed experimentally. Contrarily, in the pair-wise additive model the state mixing is ignored and therefore can not be reproduced.

3.2.3.2 Exciplex formation

We will consider the exciplex formation using Na-He-He_N effective potentials, which where presented in section 3.1.5.2 for the 5s and 4d excited states of sodium. The experimental photoelectron spectra and velocity distributions of desorbed excited Na following excitation within the 5s and 4d-5p bands demostrated that these bands may correlate to Na(5s) and Na(4d). In contrast, there is no definitive experimental evidence that in the 4d-5p, 6s- and 5d-6p bands the Na-He_N are excited to states that correlate to 5p, 6s, 5d, 6p states of free Na atoms. Therefore, exciplex formation in excited states of free Na higher than 4d will be not considered here. In addition, there is no NaHe pair potentials available in the literature for excited states higher than 5g.

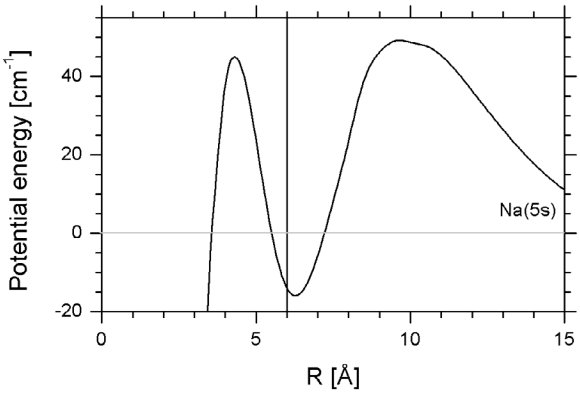

Figure 3.80: Na(5s)He pair potential of Pascale[106, 119] in relative energy scale in order to show the potential barrier and the assumed Na-He internuclear distance (vertical line) after the excitation of Na-He_N.

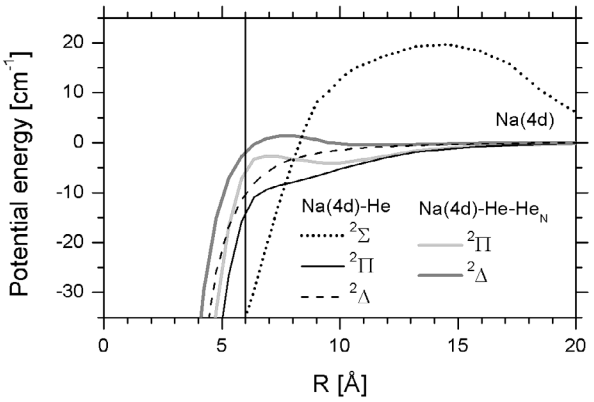

Figure 3.81: Na(4d)He pair potentials of Pascale[106, 119] and the effective Na(4d)-He-He_N potentials.

3.2.3.2.1 5s-band

The Na(5s)-He pair potential is presented in Figure 3.80, where the vertical line marks the initial internuclear distance after the excitation of Na-He_N. Following this line, one finds that the excited Na atom will be in the quasi-bound well between two potential barriers centered at ≈ 4.2 Å and ≈ 10 Å. Thus, we encounter here an interesting situation for the exciplex formation. On the one hand Na(5s) should be trapped in that well, meaning it should stay close by the surface. On the other hand, the strong repulsion between the Na(5s) and the whole droplet, see Figure 3.78, should lead to the fast desorption of excited sodium and thus decrease the probability of Na(5s)He formation. Below we will estimate the time scales for these processes.

First, we estimate the mean desorption time: the $\langle E_{kin}(Na)\rangle \approx 600$ cm^{-1} at 33 980 cm^{-1} of excitation frequency, see Figure 3.65, results in the mean speed of recoiling excited sodium $\langle v(Na)\rangle \approx$ 800 m/s. We find the mean desorption time for Na atom $\left\langle \tau_{desorp}\left(\mathrm{Na}\right)\right\rangle \approx 1.2$ ps with the assumptions stated previously for lower excited states in section 3.1.5.2. Second, we estimate the upper limit of tunneling probability through the narrowest barrier. As in the case of lower, 4s-4p Na excited states, we assume that after the excitation Na stays at the fixed distance of 6 Å from the droplet's surface. In view of the much higher energies of potential barrier around ≈ 60 cm^{-1} compared to the ≈ 17 cm^{-1} energy of the He atom in the bulk liquid helium[1] we will neglect the folding of NaHe and He-He_N potentials and will use only the NaHe pair potential. For the bound well one needs to take into account the zero point energy (ZPE). We estimate this energy by approximating the well as a parabolic potential, which leads to ZPE ≈ 17 cm^{-1}. Adding the 4 cm^{-1} of kinetic energy of He atom along the reaction coordinate, we find the transition probability $T \approx 4.7\cdot10^{-17}$ according to expression 3.27. The tunneling time, which is the inverse of the product of T and the attempt frequency of 10^{12} s^{-1}, is thus ≈ $2\cdot10^{5}$ s. This is too long time compared to the nanosecond time scale in the experiment determined by the duration of the laser pulse. The tunneling through the second larger barrier will be even less probable.

We conclude that the tunneling probabilities via any of the two potential barriers are negligibly small, so the exciplex should be formed in that intermediate potential well between barriers

on the picosecond time scale. On the basis of the estimated fast desorption of the Na(5s) from the helium droplets we also conclude that the formation should occur via direct pick-up of He atom by the departing Na(5s). However, the experimental relative abundance of NaHe in the 5s-band of only ≈ 10% indicates that this assumed pick-up process may be not very efficient.

3.2.3.2.2 4d-5p-band

We present in Figure 3.81 the Σ, Π, Δ Na(4d)He potentials of Pascale[106, 119] and he folded Π, Δ Na(4d)-He-He_N effective potentials. The Σ Na(4d)He potential has an undulation at an internuclear distance of ≈ 6 Å, where the energy is ≈ 20 cm^{-1} lower than those along the Π and Δ potentials. The folding of the Σ Na(4d)He pair potential with the He-He_N potential does not thus significantly modify the NaHe potential. In contrast, the folding reduces the binding energies of exciplex formed along the Π and Δ Na(4d)He potentials curves at an internuclear distances of 6 Å by ≈ 20 cm^{-1}. That internuclear distance we take as fixed after the excitation of Na-He_N. From the Σ Na(4d)He and Na(4d)-He-He_N potentials in Figure 3.81 one can see that the exciplex formation will be barrierless. The strongest binding energy of ≈ 30 cm^{-1} will be along Σ Na(4d)He potential and only ≈ 6 cm^{-1} and ≈ 3 cm^{-1} along Π, Δ Na(4d)-He-He_N potentials. The strong binding of exciplex formed along Σ Na(4d)He may explain the large abundance of NaHe in the 4d-5p band, where even heavier exciplexes $NaHe_2$ and $NaHe_3$ were detected.

3.2.3.3 Photoelectron spectra

We calculated the photoelectron peak intensities following excitation in the 5s and 4d-5p-bands by using the model presented in section 3.1.5.3. The input parameters for the calculation are listed in Table 16 and Table 17. As before, the ionization cross-sections for the 3p excited state of Na were read from Fig.2 in Ref.[138]. For the ns states they were read from Fig.6 in Ref[109]. For the 4p, 3d and 4d excited states the cross-section were taken from the data kindly provided by M.Aymar[136, 137]. The laser pulse duration, the cross-section of the laser beam at the ionization point were kept the same as for the lower excites states, see section 3.1.5.3. The errors for the calculated intensities reflect the variation of the ionization cross-sections and the laser power by 20 %.

3.2.3.3.1 5s-band

As can be seen form the Table 16, there is a dramatic difference between the experimental and the calculated photoelectron peak intensities or states lower than the 5s. The most pronounced deviation occurs for the 3d state, where the experimental relative intensity is three orders of magnitude larger than the calculated one. The experimental intensity of peaks from the Na(4p) and Na(5s) are a factor of ≈ 1.8 and ≈ 1.3 higher than predicted by the model. In contrast, the photoelectron peak corresponding to 3p excited state of sodium is a factor of three smaller than theoretical one. The reasonable variation of the input parameters does not compensate the remarkable difference in the relative intensities of photoelectrons from lower excited states. This indicates that the enhanced population of recoiled excited Na in the 3d state is caused by effects related to the helium droplets rather than to the laser pulse energy or ionization cross-sections.

Table 16 Relative intensities of photoelectron peaks in the 5s-band

Na excited state	Ionization cross-section at 34 201 cm^{-1} $x10^{-18}$ $[cm^2]$	Experimental relative intensity	Calculated relative intensity
3p	2 ± 0.5	0.227 ± 0.005	0.62±0.02
4s	$(3±0.5)\cdot10^{-3}$	0.0	$(8±1)\cdot10^{-5}$
3d	4.25 ± 0.05	0.210 ± 0.005	$(4±0.2)\cdot10^{-4}$
4p	0.345 ± 0.003	0.283 ± 0.005	0.160 ± 0.005
5s	0.011 ± 0.001	0.280 ± 0.005	0.22 ± 0.01
One color experiment. The energy of the laser pulse is 12 mJ.			

3.2.3.3.2 4d-5p band

The experimental photoelectron spectrum recorded in the 4d-5p band following 35 200 cm^{-1} excitation demonstrates relative peak intensities which are quite different from the theoretical ones, see Table 17. As in the 5s-band, the experimental intensity of the 3d peak is three orders of magnitude larger than calculated. In contrast, the intensities of 3p and 4p experimental peaks are a factor of three larger than those predicted by the model. The intensity of the experimental 4d photoelectron peak is only 25% smaller than that from calculations. Within reasonable variations of input parameters it was not possible to obtain the enhanced intensity of 3d photoelectron peak. This again indicates that the droplet induced effects may play a significant role in the population of the excited states of desorbed sodium atoms.

Table 17 Relative intensities of photoelectron peaks in 4d-5p-band

Na excited state	Ionization cross-section at 27 778 cm^{-1} $x10^{-18}$ $[cm^2]$	Experimental relative intensity	Calculated relative intensity
3p	4.5 ± 0.5	0.118 ± 0.007	0.06 ± 0.02
4s	0.006 ± 0.001	0.0	$<10^{-3}$
3d	9.4 ± 0.1	0.107 ± 0.007	$<10^{-3}$
4p	0.76 ± 0.01	0.033 ± 0.012	0.010 ± 0.002
5s	0.004 ± 0.001	0.0	0.0
4d	4.20 ± 0.05	0.743 ± 0.003	0.93 ± 0.01
Two-color experiment. The excitation frequency is 35 200 cm^{-1}. Energy of the ionization laser pulse is 2 mJ.			

3.2.3.4 Velocity distributions of desorbed species

In this section we will first consider the velocity distributions of the desorbed bare Na atoms following one-photon Σ'←Σ' and Π'←Σ' excitations of Na-He_N by using the same diatomic-like approach as for the low bands. Then we will discuss the velocity distributions of the desorbed exciplexes.

3.2.3.4.1 Velocity distributions of desorbed Na

5s band. The slow component in the speed distributions recorded in the 5s-band seems to correlate to the 5s excited state of Na. First, the angular anisotropy parameters $\beta \approx 1.5$, see Figure 3.64, correlates to $\Sigma \leftarrow \Sigma$ type of transition as expected to the 5s Σ' Na-$He_N \leftarrow$3s Σ' Na-He_N dissociation transition within the diatomic model of Na-He_N interaction presented in section 3.1.5.4.1. Second, the speed of component varies with the excitation frequency. The variation of the high energy onset in the kinetic energy distribution is linear and has its onset close to the energy of free Na(5s), see Figure 3.65. Third, the photoelectron spectroscopy reveals the presence of recoiled Na in the 5s states, see Figure 3.62. The unclear feature in the slow speed component is its sharp onset at high speed. Overall behavior of the slow speed component of Na in the 5s-band resembles that in the lower 3p-4p bands.

The origin of the high speed component is not clear: it does not depend on the excitation frequency but has anisotropy parameter $\beta \approx 1.5$. This component might be related to the desorbed Na(3d), the presence of which was revealed by PES and which cannot be accounted for by radiative decay of recoiled Na(5s).

4d-5p band. The speed distributions of Na excited within the 4d-5p band demonstrate two speed components similar to the 5s-band: the slow and narrow one depends on the excitation frequency, see Figure 3.67. The linear dependence of the mean kinetic energy of the components shown in Figure 3.68 indicates that it might be related to the desorption of Na(4d). Furthermore, the photoelectron spectrum shown in Figure 3.63 of the 4d-5p band reveals mainly the Na(4d). In addition, the variation of the anisotropy parameter, see Figure 3.68, is similar to the 3d-band: the β-parameter varies from positive to negative values with the excitation frequency. The broad high-speed component is still present and might be related to the Na atoms desorbed in the 3d excited state, since the corresponding peak was observed in the photoelectron spectrum in Figure 3.63 and cannot be produced by radiative decay of Na(4d) as we showed in section 3.2.3.3.

6s band. In the 6s-band only one broad, high-speed component with anisotropy parameter $\beta \approx 1.5$ was observed, see Figure 3.74. The positive β-parameter indicates that a n*l* Λ' Na-$He_N \leftarrow$3s Σ' Na-He_N transition of the $\Sigma \leftarrow \Sigma$ type may be involved. The linear dependence of the mean kinetic energy against an excitation frequency, shown in Figure 3.75, and photoelectron spectrum, see Figure 3.72, indicate that excitation of Na-He_N may be related to the 4d excited state of Na perturbed by the droplet.

5d-6p band. The slow and narrow component in the speed distribution of recoiled Na in the high frequency part of the 5d-6p band has a pronounced frequency dependence, see Figure 3.76. The negative anisotropy parameters point to a $\Pi \leftarrow \Sigma$ type transition. The variation of the peak kinetic energy against the excitation frequency indicates that it may originate from the Na atoms recoiling in the 5d or 6p state. However, the photoelectron spectrum reveals the presence of Na atoms only in the lower 4d and 5p states, see Figure 3.72. The results of PES should be taken with care in view of the two-photon excitation that may probe different excited states. The broad high-speed component is present in speed distributions at all excitation frequencies within the 5d-6p band. It is almost not dependent from the excitation frequency and has β-parameter close to zero value, see Figure 3.76. At the current state its assignment to a particular excited state of Na is not possible.

3.2.3.4.2 Velocity distributions of desorbed exciplexes

The obtained set of velocity distributions of desorbed exciplex in the 5s-6s excitation bands is not as complete as for the bare sodium. Ion images were not recorded for the 5s-band and in the other bands images were only recorded at the maximum of NaHe excitation spectra. We can only comment

on some common features for the speed distributions of Na and NaHe and the evolution with excitation frequency.

In the 4d-5p band the speed distributions of NaHe and $NaHe_2$ demonstrate only slow and narrow components and the corresponding anisotropy parameters are practically zero, see Figure 3.66. In this respect, it resembles the situation in the 3d band. The variation of the speed distribution with the excitation frequency is not known and additional experiments are required.

The speed distribution of NaHe in the 6s band is peculiar, see Figure 3.73. In contrast to desorbed Na atoms, the NaHe has two components. The slow one has almost zero β-parameter, while the high speed component has $\beta \approx 1.5$. The fast component correlates to that of the recoiled Na and might originate from the "direct" pick-up of the He atom by excited Na during the desorption process. The slow component might be related to the some lower or not resolved in the PES excited state of Na.

In the 5d-6p band the speed distribution of NaHe has an evolution which is similar to that of Na, see Figure 3.77. In the low frequency part of the band there is only one broad high-speed component, while in the high frequency region the slow and narrow component appears. In contrast to Na, the anisotropy parameters for NaHe at low frequencies is positive with $\beta \approx 0.3$. This might be the sign of the spectral overlap of two different n*l* Λ' Na-He_N←3s Σ' transition, one of which leads to the formation of exciplex and the other to the desorption of bare excited sodium.

3.2.4 Summary

In this section we have presented and discussed the dynamics observed in the medium excited states of Na-He_N in the energy region of 33 500 - 38 000 cm^{-1}. A mixed behavior was revealed in this frequency region, where some features, e.g. linear dependence of the mean kinetic energy of desorbed Na on excitation frequency, correspond to excited states of free sodium, while others, e.g. photoelectron spectra, do not. From the ensemble of the data acquired, only two bands in the lower frequency part of the excitation spectrum could be related to 5s and 4d excited state of free sodium. The correspondence of the rest of the features in the spectrum to particular excited levels of Na can not be determined at the current state of research. This is why the naming of the excitation bands in this section should not be considered as an assignment.

The application of models developed for the lower excited states of Na-He_N to the medium states was partially successful. For the excitation spectra only the 5s-band is qualitatively reproduced within pair-wise additive model of Na-He_N interaction. Other calculated spectra corresponding to excited states of free sodium higher than the 5s states, namely 5p and 6s are too broad and too blue-shifted with respect experimental spectra. The calculated spectra corresponding to 4d and 5d excited states of Na are a special case, as they match approximately two narrow features in the recorded spectrum, but their correspondence to atomic states is doubtful in view of physically unusual calculated Na-He_N potentials. A possible explanation of the revealed discrepancy between the modeled and the experimental data is the higher density of states of free sodium in that energy region, which leads to the helium droplet-induced mixing.

The distribution of the internal energy states of desorbed photofragments revealed with photoelectron spectroscopy can not be reproduced with an assumption of instantaneous recoil of Na in the corresponding atomic excited state. The strong photoelectron signal from the Na in the 3d state observed in the 5s and 4d-5p bands indicates a droplet-induced relaxation.

The exciplex formation within the identified 5s and 4d-5p band can be qualitatively understood with the model developed for lower excited states of Na-He_N. Na(4d)He pair potentials allows barrierless formation of exciplex for the Na(4d) on the droplet's surface upon excitation, which correspond to a high observed abundance of exciplexes in the band. In the case of Na(5s), the situation

is not clear. the pair potential shows that the exciplex should be formed in the strongly bound intermediate potential well above dissociation limit between two potential barriers. However, the observed abundance of NaHe of ≈ 12% is quite low, which indicates that either the quality of the pair potential is poor or that some other unforeseen mechanisms govern formation of exciplex.

The velocity distribution of photofragments remains specific to free Na atoms and exciplexes as in the case of lower excitation bands. However, new features appear. In the 5s band the speed distribution of desorbed Na has two components with angular anisotropy parameters close to a value of 2, indicating their origin from Σ'←Σ' transition. The slow one has a sharp onset for the highest kinetic energy and depends on the excitation frequency. This dependence allows to attribute the slow component to Na desorbing in the 5s state. The high speed component does not depend on the excitation frequency and attributed to Na(3d). In the 4d-5p excitation band the speed distribution of desorbed Na also contains two components. The variation of the mean kinetic energy of the slow component indicates its origin to the 4d excited state of free sodium. The variation of the angular anisotropy within the band is also observed, which, however, does not allow to extract additional information. The speed distribution of exciplexes in the 4d-5p band demonstrates single component with anisotropy parameter close to zero. In the higher excitation bands, the speed distributions of photofragments show mixed character, having mainly two speed components for free Na atoms and exciplexes. The slow component depends on excitation frequency, though the acquired data do not always suffice to attribute the component to a particular excited state of atomic Na.

3.3 High excited states

In this section we present and discuss our results obtained in the energy region of 38 000 - 41 500 cm^{-1} of Na-He_N excitation spectrum. A number of spectral features with similar shapes and dynamical features were observed in this region. Their discussion is based on the properties of Rydberg states of free sodium with the principle quantum number n>8.

3.3.1 Excitation spectra

The excitation spectra recorded by detecting bare Na atoms and $NaHe_n$, n=1-4, exciplexes are presented in the upper panel of Figure 3.82. They were obtained under field-free conditions. Excitation and ionization take place within the laser pulse while no accelerating voltages are applied to electrodes, see Chapter 2. An electric field is applied 200 ns later to accelerate the created ions towards the MCP detector. These conditions were chosen to avoid effects of state mixing and lifetime shortening of high Rydberg states by the static electric field.

In each species-specific excitation spectra one can see a series of features. The common structure of each feature upto 40 000 cm^{-1} consists of two peaks. Exciplex formation is enhanced for the low frequency peak compared to the high frequency peak. As the excitation frequency increases, the separation between the two peaks decreases so that they overlap to form one single peak with a FWHM ≈ 100 cm^{-1}. After 40 800 cm^{-1} the peaks are spaced too close to each other and form one broad feature. The high frequency onset of this broad feature in the $NaHe_n$, n=1-4 excitation spectra is red-shifted by ≈ 150 cm^{-1} from the 41 449 cm^{-1} ionization threshold of free Na[99].

In the lower panel of Figure 3.82 we present the two-photon excitation spectra recorded by detecting Na, NaHe and $NaHe_2$ species with the constant electric field of 1 485 V/cm present in the ionization volume. The $NaHe_3$ and $NaHe_4$ exciplexes were also detected but their signal levels were not sufficient to record spectra. The Na and NaHe two-photon spectra have a common repeating group of features. The two most distinct groups can be seen in the 37 900 - 39 400 cm^{-1} region. In the low

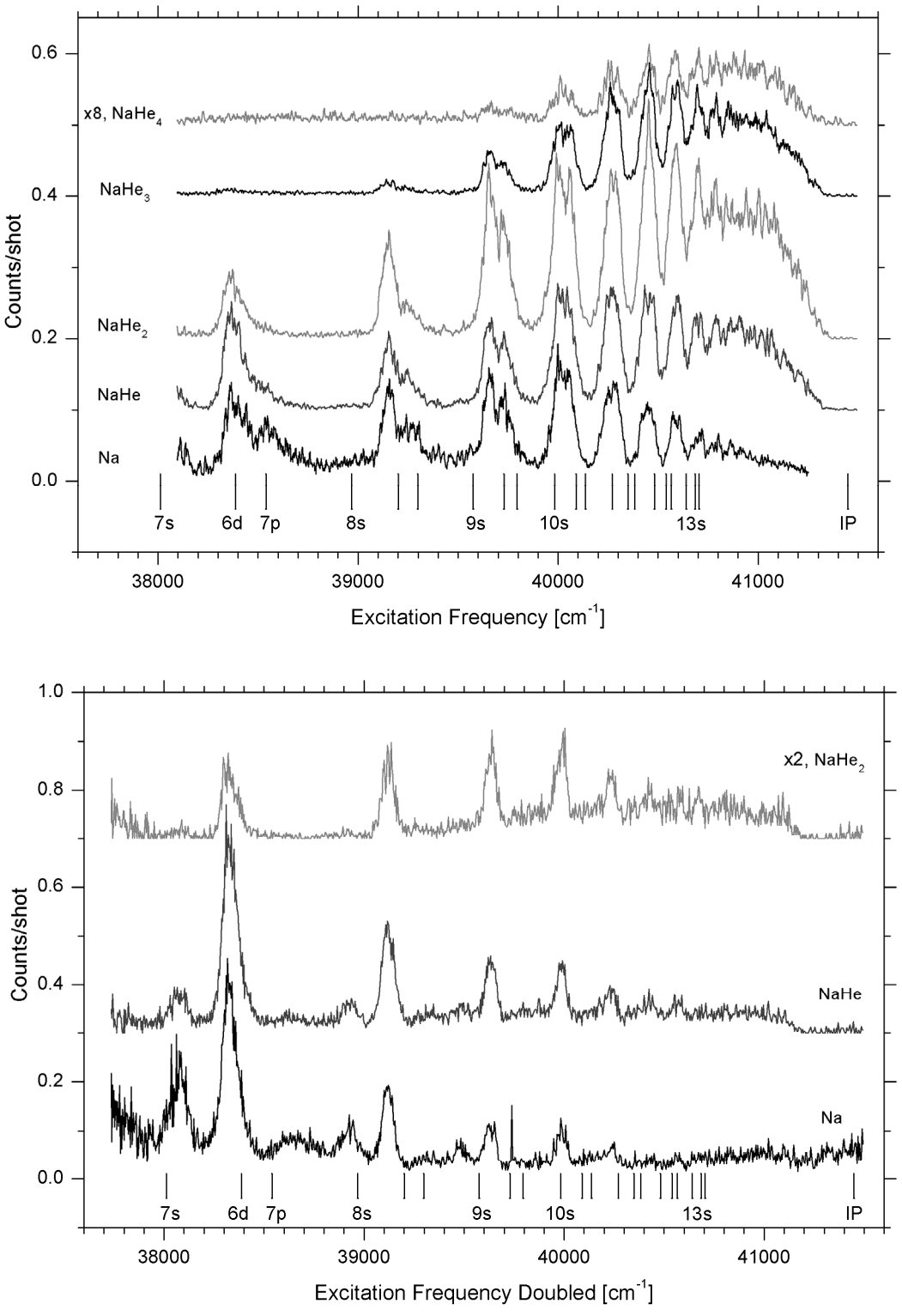

Figure 3.82: Upper panel: one-photon excitation spectrum of Na-He_N with <r> = 41 Å recorded by monitoring bare Na atoms and $NaHe_n$, n=1-4, under the field-free conditions. Lower panel: Two-photon exciation spectrum of Na-He_N with <r> = 41 Å recorded by monitoring bare Na atoms, NaHe and $NaHe_2$ with constant electric field of 1 485 V/cm. At the bottom of the graphs the vertical lines mark the energies of the atomic levels. After the first labeled sequence of levels 7s - 6d - 7p, only the ns-levels of the following ns - (n-1)d - np sequences are labeled.

frequency part of each group there is the medium intensity peak followed by the twice more intense peak, where the exciplex formation is the highest. At frequencies above 39 400 cm^{-1} the pattern is no longer distinguishable due to the low signal levels and only the strongest medium peaks persist. As in the one-photon excitation spectra, the separation between peaks decreases at higher frequencies and after 40 700 cm^{-1} there is only one broad feature. Comparing the one- and two-photon excitation spectra, one can see that of the low frequency peak in each group of two-peaks in one-photon spectra corresponds to the strongest middle peak in the group of two peaks in the two-photon spectra. The correspondence of two other peaks in two photon spectra to the features in the one-photon spectra is less obvious due to noise in the latter.

Comparison of the Na and NaHe excitation spectra recorded in the presence of a constant electric field of 1 485 V/cm with those recorded under field-free conditions is presented in Figure 3.83. Within the experimental signal-to-noise ratio there is almost no difference between field-free and field-present excitation spectra. The only observed effect is a shift in spectra' onsets in the region close to the ionization threshold of free Na atom. This shift ≈ 150 cm^{-1} is clearly visible in the NaHe excitation spectra. In the Na-specific spectrum the onset is less distinguishable due to the presence of the sharp features corresponding to the high Rydberg (HR) states of free Na atoms effused from the oven. The value of the shift is a factor of 1.6 smaller than that of 237 cm^{-1} according to equation 2.20. We think that the deviation of the experimental value from the theoretical one is due to the non-uniform electric field.

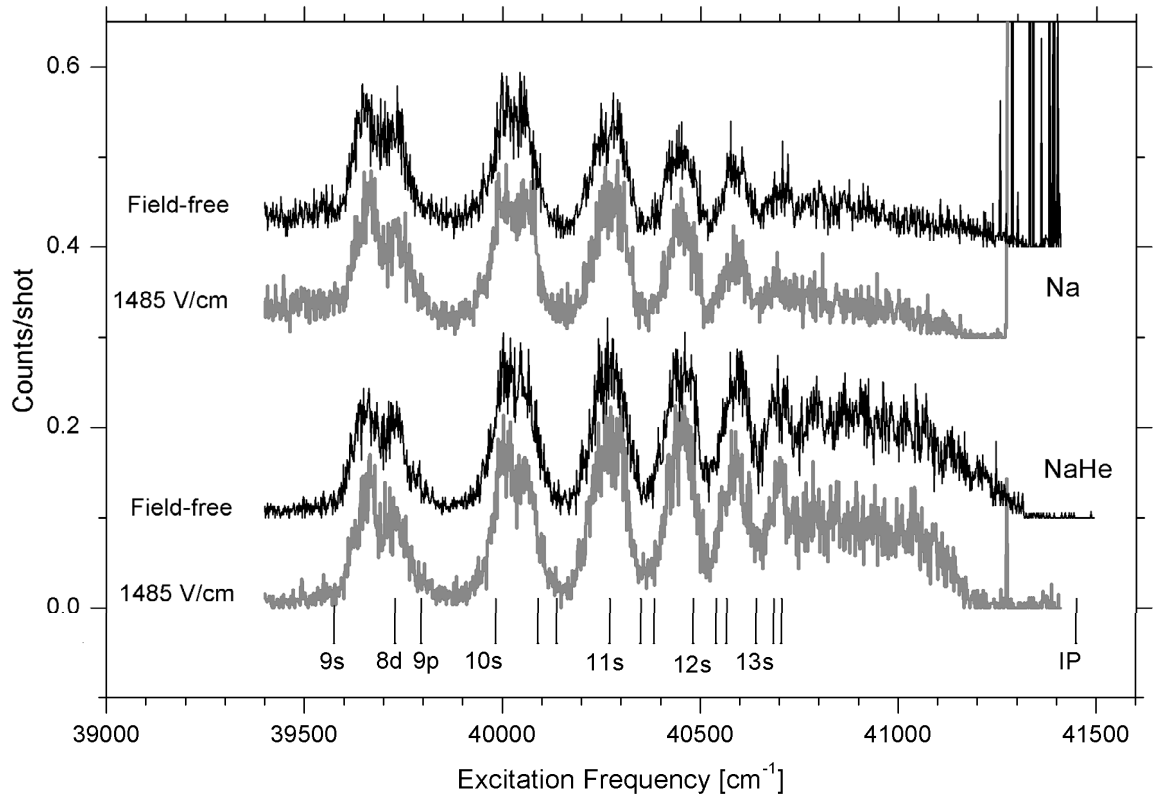

Figure 3.83: Field-free and field-on one-photon excitation spectra of Na-He_N with <r> = 41 Å recorded by monitoring bare Na atoms and NaHe. The peaks in the field-free Na spectrum after 41 200 cm^{-1} originate from pulsed field ionization of high Rydberg states of gas phase Na in the effusive beam coming from the oven.

The one-photon excitation spectra of Na-He_N with <r> = 54 Å and <r> = 29 Å recorded under field-free conditions by detecting Na and NaHe are illustrated in Figure 3.84. The droplet size effects are two-fold. First, in the 38 000 - 40 200 cm^{-1} frequency range the intensities of peaks in a group of two adjacent peaks varies: the high frequency peak gains the intensity at smaller droplets by a factor of two. Second, each group shifts as a whole to higher frequencies at smaller nanodroplets. In the 38 000 - 40 200 cm^{-1} frequency range the shift is inferior to ≈ 50 cm^{-1}, but attains almost 100 cm^{-1} around 41 000 cm^{-1}.

In the NaHe-specific two-photon excitation spectrum of Na-He_N the three strongest peaks centered at 39 100 cm^{-1}, 39 650 cm^{-1} and 40 000 cm^{-1} were recorded at different droplet sizes in the <r> = 27 - 60 Å range. We will respectively refer to these peaks as 7d, 8d and 9d bands according to the nearest nd excited state of Na. They keep essentially the same FWHM ≈ 100 cm^{-1} over the droplet size range but their positions changes: at larger droplet sizes they shift to lower frequencies. In Figure 3.85 the differences between the peak position for those bands determined by fitting to Gaussian function 3.45, and the energies of corresponding nd state of Na are plotted versus the mean droplet radius. All three bands show a similar behavior. The peak positions change most within the 26 - 40 Å range of droplet sizes and a sort of plato is reached for larger nanoclusters. The difference in peak position between the smallest and the biggest droplets increases with excitation energy: for the 7d-band it is ≈ 25 cm^{-1}, for the 8d-band it is ≈ 35 cm^{-1} and for the 9d-band it is ≈ 40 cm^{-1}. The revealed effect resembles those we found in the 5s and 6s-bands in the medium excited states of Na-He_N, see section 3.2.

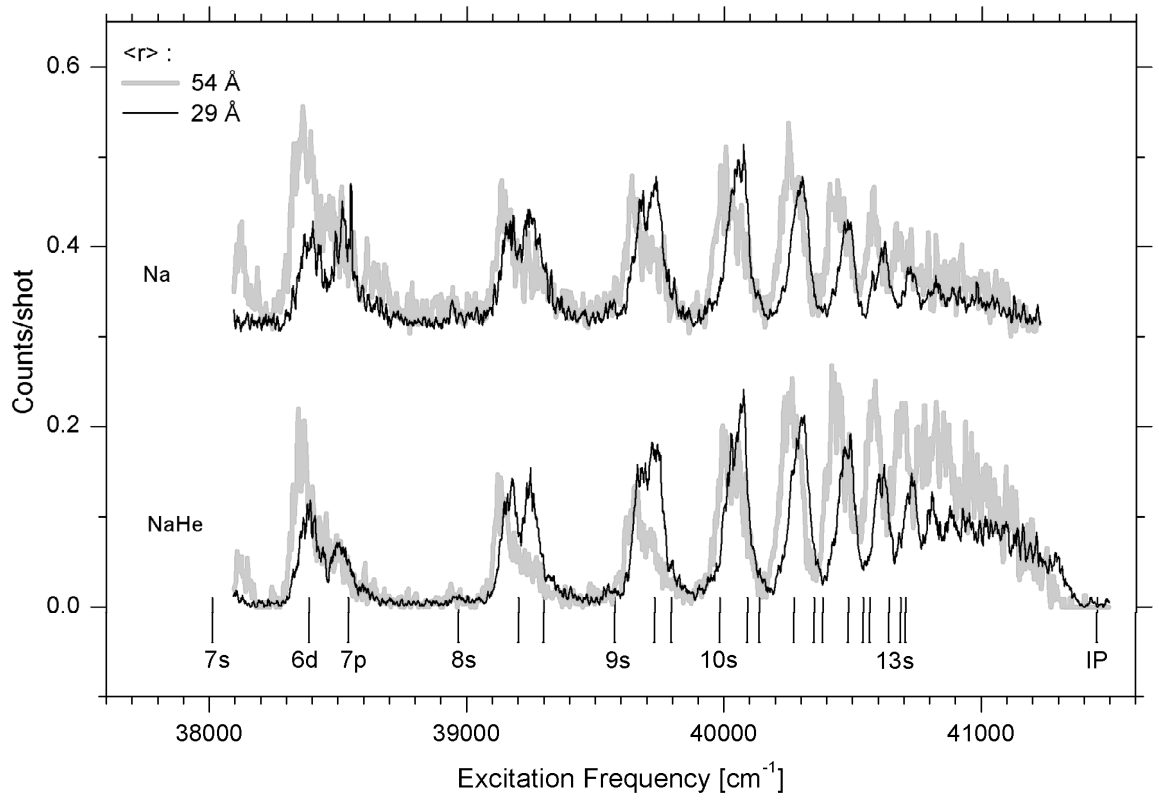

Figure 3.84: Field-free one-photon excitation spectrum of Na-He_N with <r> = 54 Å and <r> = 29 Å recorded by monitoring bare Na atoms and NaHe exciplexes.

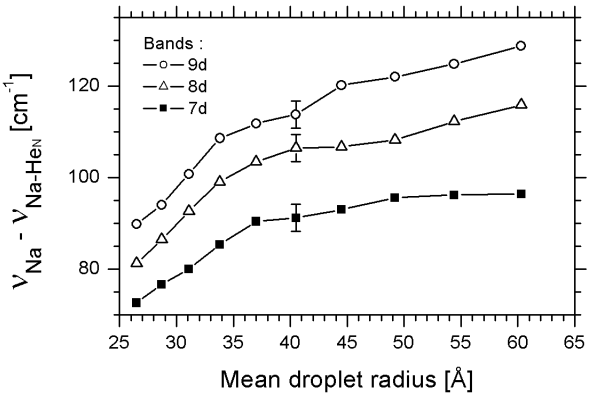

Figure 3.85: Variation of the peak position for the nd-bands, n=7-9, for excitation spectra recorded by detecting NaHe after two-photon excitation of Na-He_N with <r> = 41 Å. The error bars comprise the fitting errors and the reproducibility error in the experiment. The lines through the data points are to guide the eye.

3.3.2 TOF mass spectra

The two-photon excitation was chosen to obtain the time-of-flight mass spectra in order to have the same experimental conditions as for the photoelectron spectroscopy (PES) which will be

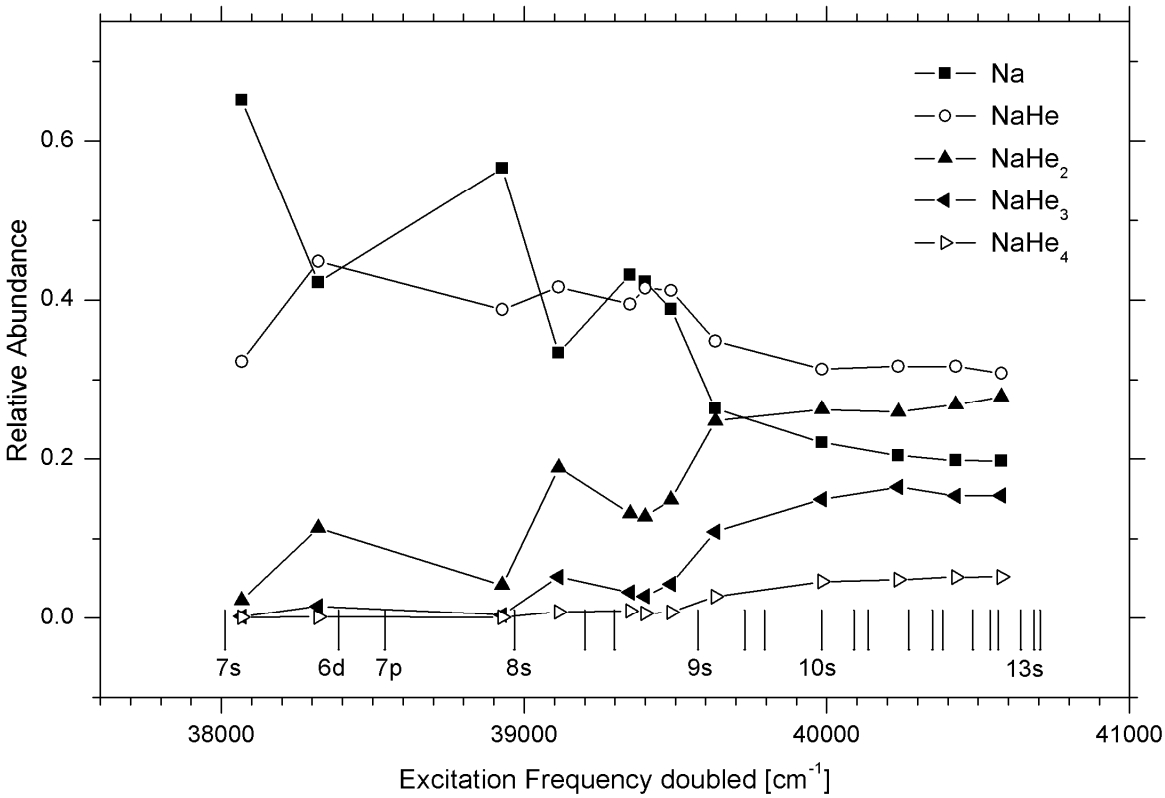

Figure 3.86: Relative abundance of desorbed Na and $NaHe_n$, n=1-4, after the one-color two-photon excitation of Na-He_N with <r> = 41 Å. The lines through the data points are to guide the eye. Errors at the current scale are inferior the symbol size, so error bars are not shown.

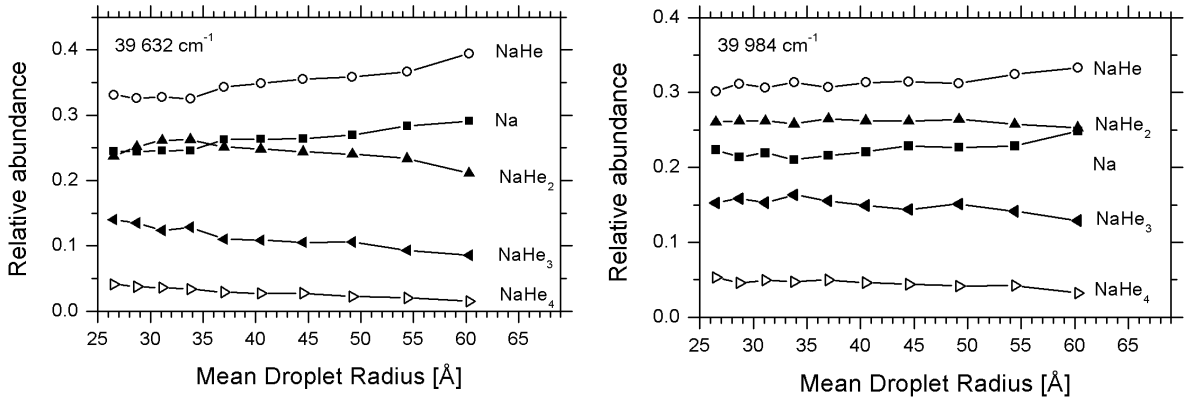

Figure 3.87: Relative abundance of desorbed Na, $NaHe_n$, n=1-4, after one-color two-photon excitation of Na-He_N with <r> = 26-60 Å at 39 632 cm^{-1} and 39 984 cm^{-1} doubled frequencies. The lines through the data points are to guide the eye. Errors at the current scale are inferior the symbol size.

presented later. In this way, a direct correspondence between the internal states of the species revealed by PES and the relative abundances in TOF is provided.

The relative abundances of species desorbed from Na-He_N following two-photon excitation at the maxima of the observed transitions are presented in Figure 3.86. The bare Na atoms and $NaHe_n$, n=1-4, exciplexes are the main detected species. The relative abundances of heavier exciplexes $NaHe_n$, n=5-6, are below $1 \cdot 10^{-3}$. Extra-heavy species with masses more than 10^3 amu, which would correspond to the photoionization of helium droplet with attached excited Na, were not observed. The variations in the abundances of Na-$NaHe_n$, n=1-4, seem to be related to a particular peak within the two-peak group described in the previous section : at the low frequency peaks bare Na atoms dominate, while at the strongest medium peaks the exciplexes are the main products. The oscillations of relative abundances disappear at excitation frequencies higher than ≈ 39 700 cm^{-1}, the point after which the $NaHe_n$, n=3-4, exciplexes are formed at appreciable quantities. That frequency also marks the limiting frequency after which the relative abundances become practically stable.

The droplet size effects were checked at the frequencies of 39 632 and 39 984 cm^{-1}, see Figure 3.87. Those points are the onset of heavy $NaHe_n$, n=3-4, exciplexes and the point where the relative abundances reach stable values, respectively. As can be seen from the graphs there is very weak size effect at the doubled excitation frequency of 39 632 cm^{-1}. Here the abundances of $NaHe_n$, n=2-4, systematically increase and those of Na and NaHe decrease at smaller droplets. This effect is opposite to that found in the low 3p and 3d excitation bands of Na-He_N. At the doubled excitation frequency of 39 984 cm^{-1} no systematic variation in the relative abundances with droplet size was observed.

3.3.3 Photoelectron spectra

To record the photoelectron images in the 38 000 - 41 100 cm^{-1} frequency region we used the one-color two-photon excitation scheme in order to minimize the background caused by the scattered light on the copper parts of our imaging setup, see section 3.2.2.2. The two-photon scheme limits the detection of low excited states of Na down to 4s states.

The photoelectron (PE) spectra recorded at the maxima of peaks in the two-photon excitation spectrum, see Figure 3.82, of Na-He_N with <r> = 41 Å are presented in Figure 3.88. For each spectrum the doubled excitation frequency and the label of the nearest excited states of Na are shown

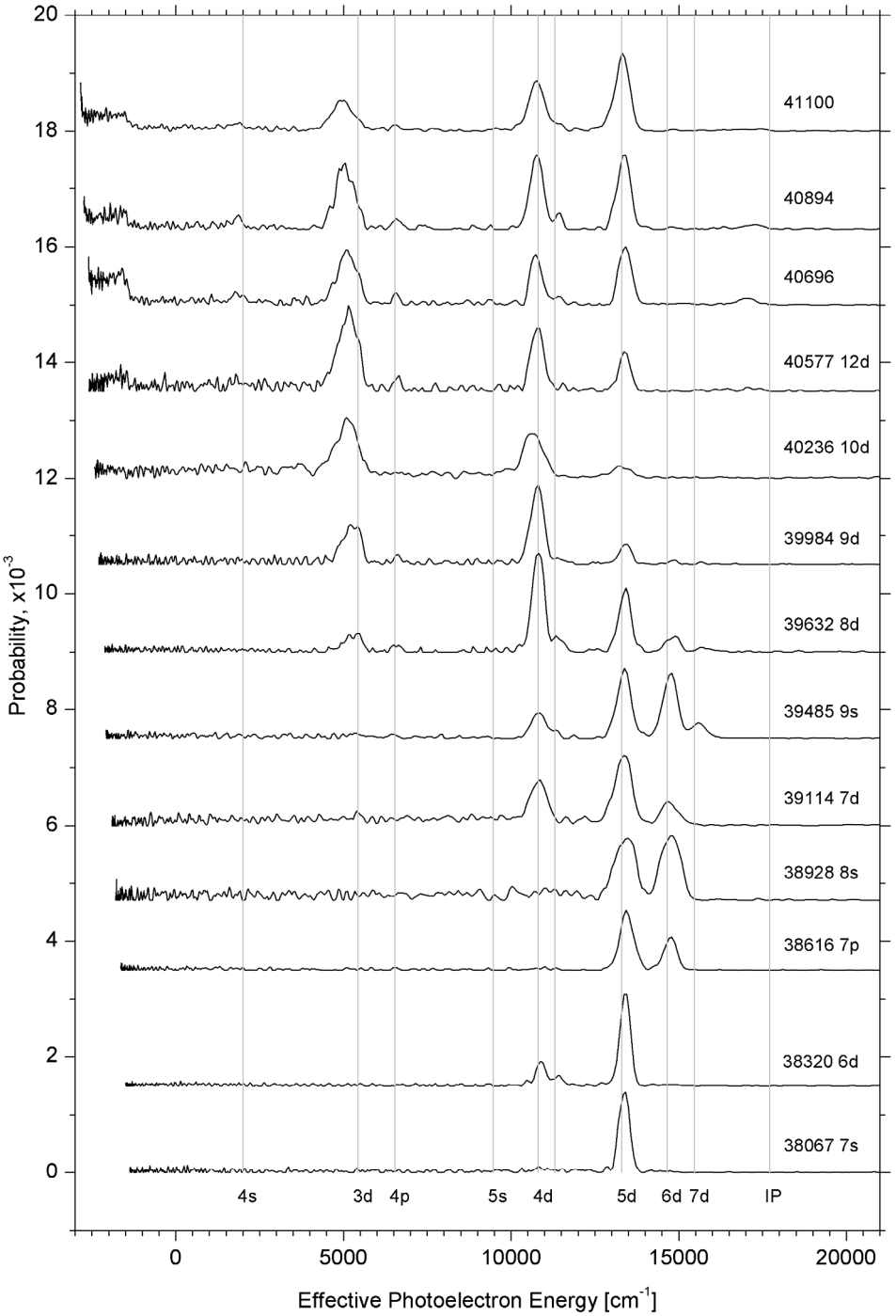

Figure 3.88: Photoelectron spectra derived from photoelectron images recorded following one-color two-photon excitation of Na-He_N with <r> = 41 Å. The spectra are shifted so that the photoelectron peaks, originating from the same atomic levels of Na, have the same position. The vertical lines show the energies of these photoelectrons if the ionizing photons would have 17500 cm^{-1} of energy. The corresponding Na levels are indicated at the bottom of the graph. Text labels in the right part of the graph indicate doubled excitation frequencies and the energy of the nearest excited states of free sodium.

for reference purposes. For an easier assignment of the peaks to particular excited states of Na we converted the kinetic energy of photoelectrons into an effective energy according to the expression 3.46. As a results, photoelectrons originating from the same excited state of Na have the same effective energy irrespective of the ionization frequency. The vertical lines and labels at the bottom of Figure 3.88 mark the corresponding excited states of free Na. After the 5p state only nd states are labeled, since the energy resolution of 3% in the PE spectra is not sufficient to separate the photoelectron peaks from the adjacent (n+1)s and (n+1)p states. Furthermore, the ionization cross-sections for the nd state are at least an order of magnitude larger than those for ns and np states[109, 136, 137]. The same applies for higher *l*-states of Na.

The broad feature in the -3 000 - 1 000 cm^{-1} region of PE energy, which is visible in spectra recorded in the 40 500 - 41 100 cm^{-1} range of excitation frequency, is likely related to the sodium dimers formed on the droplet's surface. The intensity of this feature depends on the temperature of the oven with sodium sample: at higher temperatures, when higher vapor pressure of Na in the doping cell facilitates the dimer's formation, its intensity increases with respect to most peaks in the photoelectron spectrum. The intensity of the PE peaks correlating to 4p, 5p and 5d excited states of Na also increase with increasing oven temperature, indicating that they also originate from sodium dimers.

Now we will discuss the features which, as we think, correspond to the excitation of singly doped nanodroplets. The common aspect of all PE spectra is the presence of peaks correlating to excited states of Na which are lower in energy compared to the nearest, with respect to the excitation energy, state of free sodium. This is similar to the case of the 6s and 5d-6p excitation bands, see section 3.2.2. In the evolution of PE spectra with the excitation frequency two distinct regions can be selected. The first region comprises low frequencies, 38 000 - 39 500 cm^{-1}, of the excitation spectrum. The PE peaks there correspond only to medium and high, 4d-7d, excited states of Na. In contrast, in the second region of 39 500 - 41 100 cm^{-1}, a prominent signal correlating to the 3d state appears. The FWHM ≈ 700 cm^{-1} of this peak is a factor of five larger than the resolution of ≈ 150 cm^{-1} at the PE energy of 5 000 cm^{-1}. Furthermore, the peaik shifts to lower PE energies increasing with excitation energy and attains ≈ 500 cm^{-1} at 41 100 cm^{-1} (doubled) excitation frequency. The transition between the two types of PE spectra coincides with the excitation frequency at which the heavy $NaHe_n$, n=3-4, exciplexes start to appear, see Figure 3.86. It is not unlikely that the broad PE peak at ≈ 5 000 cm^{-1} reflects the ionization of $NaHe_n$, n=2-4, exciplexes which are the most abundant species in the 39 500 - 41 100 cm^{-1} region of excitation.

3.3.4 Ion Imaging

The velocity distributions of the desorbed species were obtained following one-photon excitation of Na-He_N at the excitation frequencies corresponding to peaks in the spectrum shown in the upper panel of Figure 3.82. The one-photon excitation makes possible a direct comparison of the speed and angular distributions corresponding to high excited states of Na-He_N with those in the lower and medium excitation region.

We present the evolution of speed distributions of bare Na and $NaHe_2$ exciplex with excitation frequency in Figure 3.89 and Figure 3.90, respectively. These species represent two major product types: bare Na atoms and $NaHe_n$, n=1-4, exciplexes which have particular speed distributions. In addition, their large relative abundances facilitate ion imaging. The anisotropy parameters are not shown, since for all species at all frequencies they are featureless and oscillate around zero value. Below we will highlight some important aspects of speed distributions.

The Na speed distribution recorded at an excitation frequency of 38 363 cm^{-1} has only one fast broad component. It is centered at ≈ 800 m/s and has a FWHM ≈ 500 m/s. The speed distribution of

$NaHe_2$ at the same excitation frequency also has a fast and broad component, though it is centered at a lower ≈ 650 m/s speed and is not as broad having a FWHM ≈ 400 m/s as in the case of Na. The next speed distribution of Na at 38 572 cm^{-1} excitation frequency has two components. The fast one is asymmetric and centered at ≈ 1 000 m/s. It has a sharp high speed onset compared to the fast component of Na speed distribution at 38 363 cm^{-1}. The slow component is centered at ≈ 200 m/s and has a FWHM ≈ 200 m/s. Having two components, the speed distribution recorded at 38 572 cm^{-1}

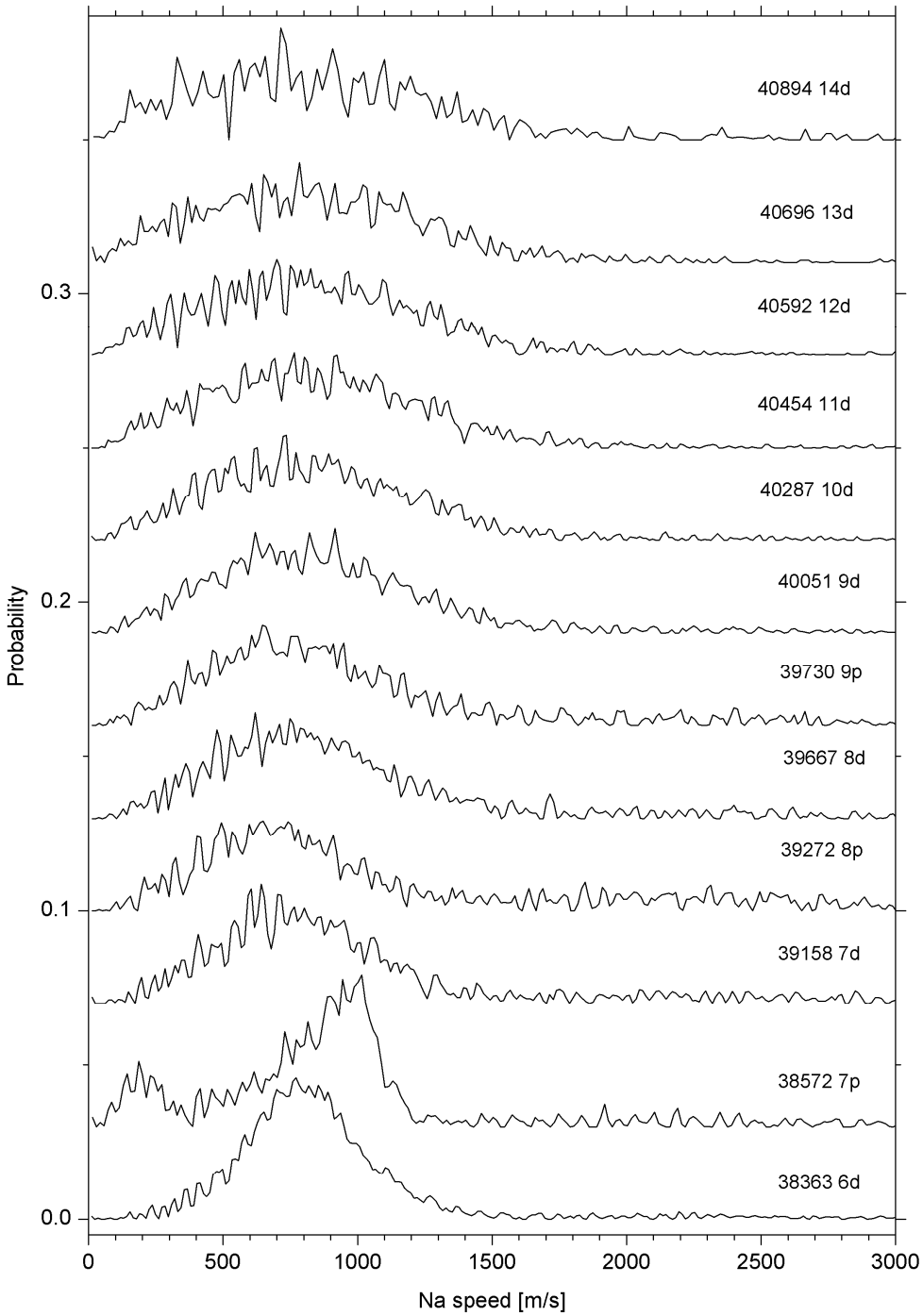

Figure 3.89: Speed distributions of desorbed Na derived from velocity map ion images recorded following one-photon excitation of Na-He_N with <r> = 41 Å. Text labels in the right part of the graph indicate excitation frequencies and the energy of the nearest excited states of free sodium.

resembles that obtained at 37 292 cm^{-1} in the high frequency part of the 5d-6p band, see Figure 3.76. The rest of speed distributions of desorbed Na in Figure 3.89 has only one fast and broad component centered at ≈ 750 m/s and a FWHM ≈ 800 m/s. In contrast to Na, in the speed distributions of $NaHe_2$ a slow component appears while the fast one gradually disappears starting at an excitation frequency of

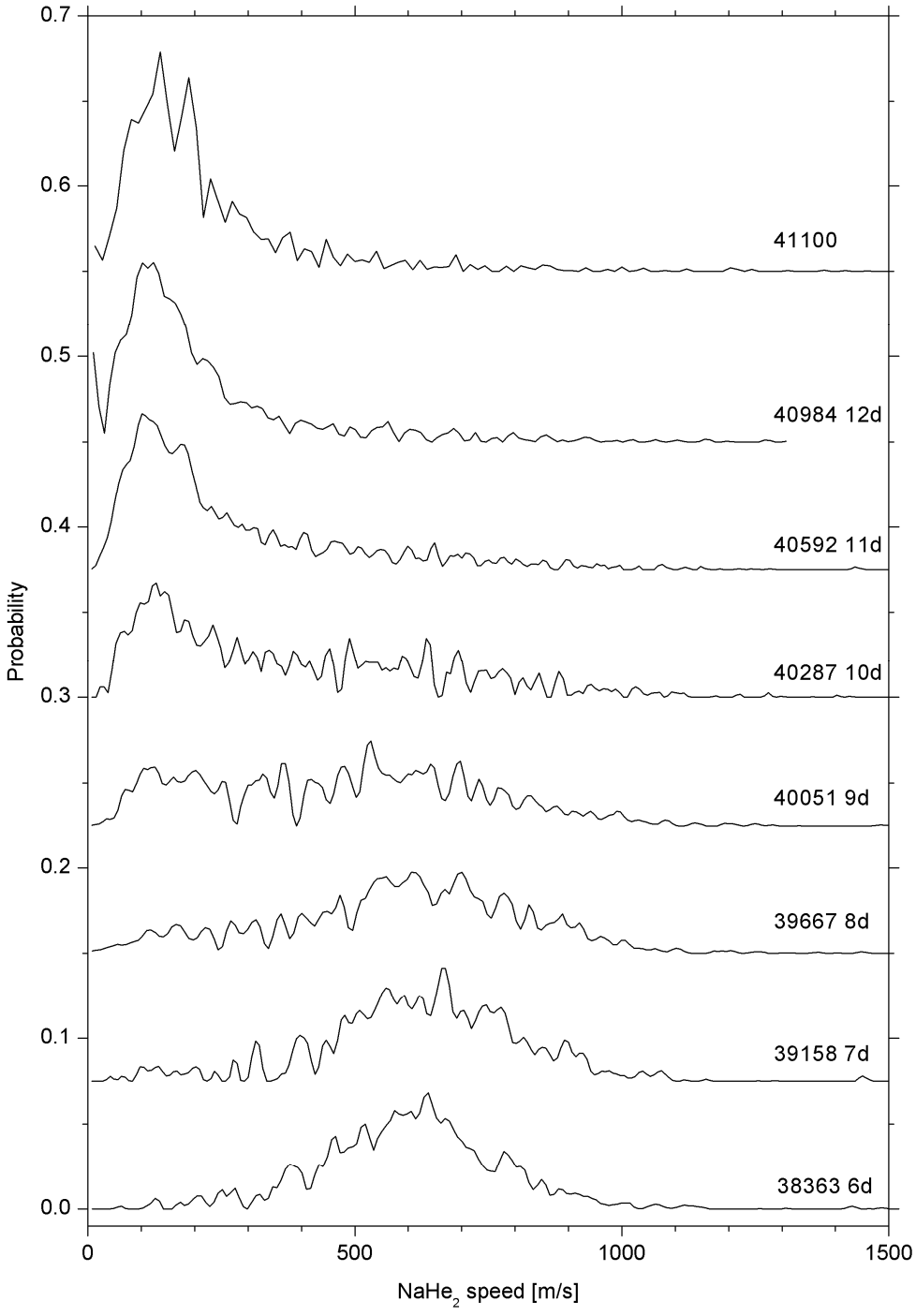

Figure 3.90: Speed distributions of desorbed $NaHe_2$ derived from velocity map ion images recorded following one-color one-photon excitation of Na on helium droplets with <r> = 41 Å. Text labels in the right part of the graph indicate doubled excitation frequencies and the energy of the nearest nd excited states of free sodium.

39 667 cm^{-1}, see Figure 3.90. The slow component is centered at ≈ 150 m/s and has a FWHM ≈ 150 m/s. The changes in the speed distributions of $NaHe_2$ after an excitation frequency around 39 500 cm^{-1} coincide with the enhanced formation of $NaHe_n$, n=3-4, exciplexes, see Figure 3.86, and with the appearance of the broad peak correlating to Na(3d) in the photoelectron spectra, see Figure 3.88.

In the 40 000 - 41 100 cm^{-1} region, the speed distribution of the desorbed species depends on the number of helium atoms attached to the excited Na in a regular way. In Figure 3.91 we present the speed and angular anisotropy parameter distributions of Na and $NaHe_n$, n=1-4, obtained following 40 592 cm^{-1} excitation of Na-He_N with <r> = 41 Å. As was mentioned before, the β-parameter distributions are featureless. In contrast, the speed distributions demonstrate gradual evolution with the increase in the number of He atoms in the exciplexes. There is only one fast broad component in the case of bare Na, while the speed distributions of exciplexes consist of a narrow slow and broad fast components. The latter gradually disappears by going from NaHe to $NaHe_4$ where it becomes the dominant component. This effect has no analog in the lower excited states of Na-He_N.

The evolution of the mean kinetic energies of desorbed fragments with excitation frequency is illustrated in Figure 3.92. It is clear that the mean kinetic energies of the $NaHe_n$, n=1-4, exciplexes decrease from a quite stable value of ≈ 500 cm^{-1} in the 38 000 - 39 500 cm^{-1} region to 50-150 cm^{-1} at 41 100 cm^{-1}. In contrast, the $<E_{kin}>$ of bare Na stays relatively constant around 800 cm^{-1}. At a given excitation frequency, the bare Na has the largest mean kinetic energy followed by NaHe, $NaHe_2$ and $NaHe_3$.

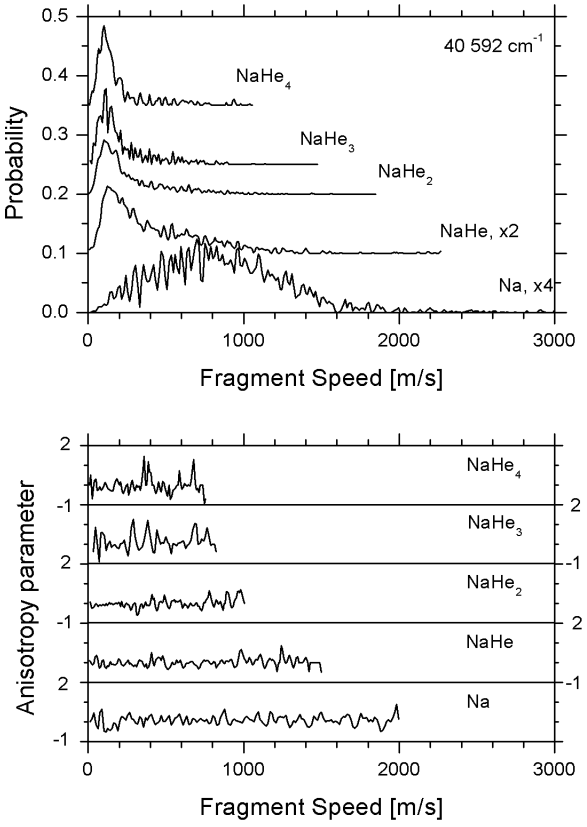

Figure 3.91: Upper panel: speed distribution of desorbed Na, NaHe, $NaHe_2$,$NaHe_3$ and $NaHe_4$ derived from velocity map ion image recorded following one-photon 40 592 cm^{-1} excitation of Na-He_N with <r> = 41 Å. Lower panel: corresponding variation of the anisotropy parameter.

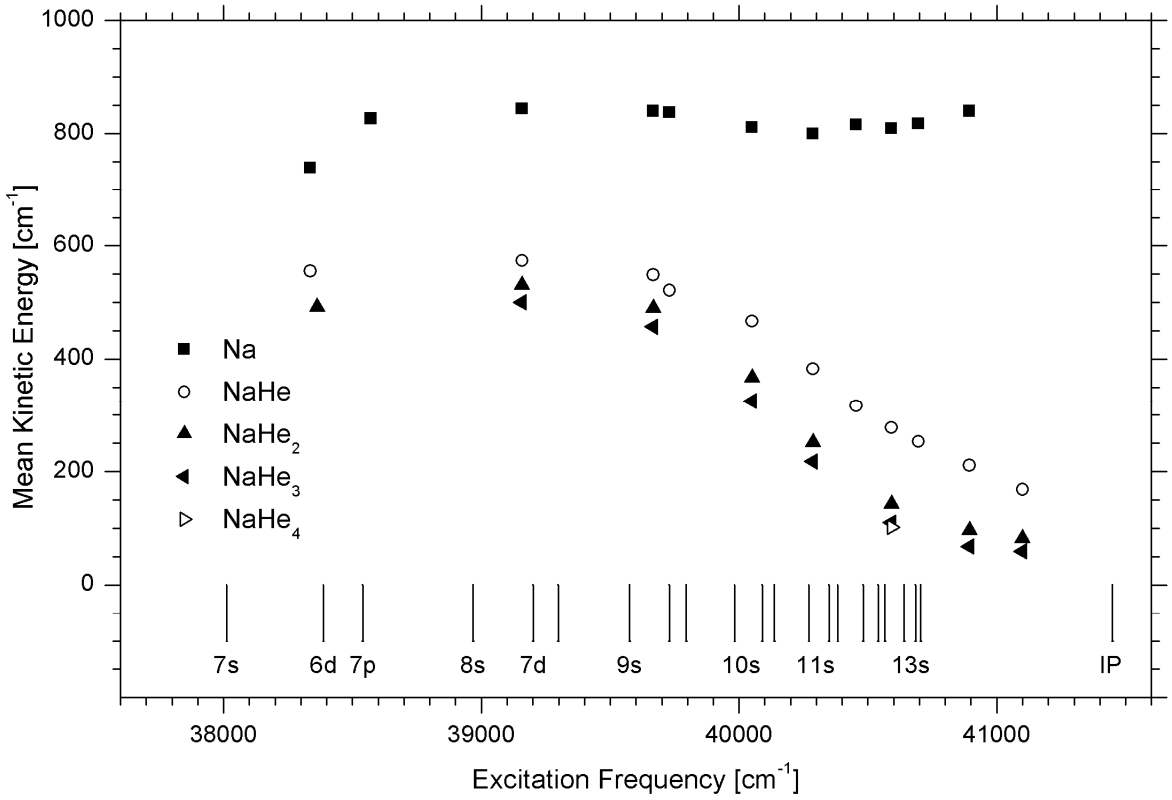

Figure 3.92: Mean kinetic energy of desorbed Na and $NaHe_n$, n=1-4, derived from velocity map ion images recorded following one-color one-photon excitation of Na-He_N with <r> = 41 Å.

In order to check the effect of droplet size on the speed distributions of the desorbed species, the speed distribution of Na, NaHe and $NaHe_2$ were obtained at 40 287 cm^{-1} excitation of Na-He_N with <r> = 29 Å and <r> = 54 Å. At an excitation frequency of 39 667 cm^{-1}, the speed distributions of Na and NaHe were also recorded for the same mean droplet sizes. In all cases no differences between the speed distributions were discernible within the signal-to-noise ratio.

3.3.5 Discussion

3.3.5.1 Excitation spectra

The assignment of peaks in the 38 000 - 41 000 cm^{-1} frequency region of the excitation spectrum is not straightforward. As we demonstrated before for the medium excited states, the fact that features in the excitation spectra are close to a particular atomic transition of free Na atom does not mean that other experimental data, like photoelectron spectra and velocity distribution of desorbed species, will correlate to this state. A possible explanation for this observation is related to the high density of excited states of Na in this energy region and state mixing induced by helium droplet.

The absence of appropriate NaHe potentials for states higher than 5d state makes it impossible to calculate the absorption spectra of Na-He_N within the pair-wise additive model of sodium-helium interaction. We can only try to extrapolate the general trend by analyzing the evolution of the experimental and calculated spectra together with the evolution of NaHe pair potentials. Firstly, the Na(n*l*)-He pair potentials will approach to the Na^+-He potential with the increase in main quantum number n. The same holds for the Na-He_N effective potential. Indeed, the line shape of the highest

excitation transition of Na-He_N in the 40 000 - 41 000 cm^{-1} region resemble the profile of direct ionization, see section 3.4 below. Furthermore, the droplet size effects on the line positions are also similar. Both show an increasing red shift with increasing droplet size, see Figure 3.85. In addition, the high density of states may be in the origin of the broad unresolved feature in the excitation spectrum in the 40 500 - 41 300 cm^{-1} region, see Figure 3.82.

3.3.5.2 Dynamics

We will consider together the TOF mass-spectra, photoelectron spectra and the velocity distributions of species desorbed after the excitation of Na-He_N. All these three pieces of information indicate a qualitative change in the desorption dynamics at excitation frequencies above ≈ 39 500 cm^{-1}. Below this frequency the data shows the characteristics of medium excited states of Na-He_N presented in the section 3.2. $NaHe_n$, n=1-2, exciplexes are most abundant, see Figure 3.82 and Figure 3.86. The PE spectra in Figure 3.88 shows mainly photoelectron peaks from the 4d-7d excited states of free Na. The speed distributions of desorbed species consist of a broad high-speed component, see Figure 3.89 and Figure 3.90. At frequencies above 39 500 cm^{-1} the abundance of heavier exciplexes $NaHe_n$, n=3-4, becomes significant and comparable to that of bare Na atoms. In the photoelectron spectra, a peak correlating to Na(3d) appears. The speed distribution of desorbed bare Na does not almost change, while in the speed distributions of exciplexes a slow component appears which becomes the main feature. In addition, the mean kinetic energies of desorbed species shown in Figure 3.92 are substantially lower at frequencies of 39 500 cm^{-1}. All listed features indicate that the appearance of $NaHe_3$ and $NaHe_4$ may be related to the excited Na in the 3d state. The mechanism behind this is not clear, since the Na-He_N are excited to states that should correlate to states higher than 4d. Obviously, some complex droplet-induced relaxation is involved. At the current state of the research it is not possible to draw a definitive picture of this relaxation process.

We put forward the following tentative explanaiton that is based on the solvation of the ionic core of the Na atom excited to Rydberg states with the principle quantum number n>10 into the helium droplet. The solvation is possible, since mean orbital radius $\langle r_e \rangle$>50 Å, see section 3.4.3.2.2, of these Rydberg states will be comparable or larger than the mean droplet radius in the experiment. In this situation, the repulsive interaction between outer electron and the helium droplet should be considerably reduced due to the low probability of electron penetration into the region of ion core. The

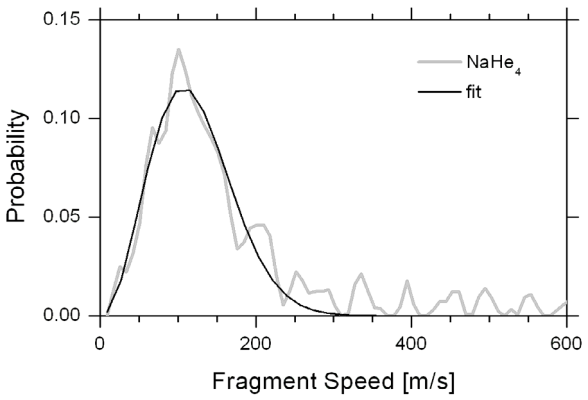

Figure 3.93: Comparison of the experimental speed distributions of the desorbed $NaHe_4$ from Figure 3.91 to a Maxwell-Boltzmann speed distribution corresponding to a temperature of 28 K.

formation of $NaHe_n$, n>2, exciplexes following the solvation of the core may induce relaxation of electronic energy into the droplet as vibrational energy of the solvation shell. The Na atom relaxed to lower states will be ejected into vacuum with some helium atoms still attached to it. The ejection might be due to the local overheating of the helium droplet which results in a sort of thermal "explosion". The narrow speed distribution of $NaHe_4$ supports this hypothesis, since it can be fitted to Maxwell-Boltzmann distribution with the temperature 28±2 K, see Figure 3.93. This temperature is similar to that extracted from the speed distributions of NaHe in the 3p band, where relaxation is important.

3.3.6 Summary

In this section, we presented and discussed the excitation spectrum and dynamics of $Na\text{-}He_N$ in the frequency range of 38 000 - 41 500 cm^{-1}. This range comprises excited states of free Na with the principle quantum number n>8 up to the ionization threshold. However, it is impossible to perform an unambiguous correspondence of the observed features to particular excited states of free sodium at the current state of research. The features observed in the spectrum have similar shape with a typical width of ≈ 100 cm^{-1} and close to the ionization potential of $Na\text{-}He_N$ overlap, forming a broad structure. Starting from a frequency of ≈ 39 500 cm^{-1}, the features in the spectrum become droplet size dependent. They shift to lower frequency at larger mean droplet sizes, resembling in this to the variation of the ionization threshold of $Na\text{-}He_N$ considered in the next section 3.4. The overall behavior of these features can be understood by taking into account the mean orbital radius of $\langle r_e \rangle >$ 50 Å of the Na atom excited to Rydberg states with the principle quantum number n>8 in the frequency region of interest. The mean orbital radius is larger than the mean droplet radius in the experiment, thus reducing the electron-helium droplet repulsive interaction. The electron density close to the ion core of excited sodium in Rydberg states with n>8 is greatly reduced, which facilitates its solvation in the droplet. The electronic energy of the excited sodium can be efficiently relaxed into the droplet via vibrations in the solvation shell of the ionic core. The sodium atom relaxed to the low more repulsive electronic states can the be ejected from the droplet. This mechanism can explain the recorded photoelectron spectra that demonstrates the presence of the excited states not higher in energy than that of 7d state of free sodium. The ejection can also happen via thermal desorption of vibrationally excited exciplex formed around the ionic core, when the local overheating of the helium environment results in the ejection of exciplex together with the evaporating helium atoms. The enhanced abundance of $NaHe_n$, n = 3-4, observed in the region of 39 500 - 41 500 cm^{-1} can be explained by this mechanism. In addition, the recorded speed distributions of $NaHe_4$ with the Maxwell-Boltzmann profile corresponding to a temperature of 28 K supports this hypothesis. The two relaxation mechanism proposed can explain the reduced angular anisotropy and broad speed distributions of desorbed photofragments observed for high excited states of $Na\text{-}He_N$.

3.4 Photoionization of $Na\text{-}He_N$

As was shown in the previous section, the excitation spectrum of Na on the surface of helium nanodroplets recorded by detecting the desorbed bare Na atoms and $Na\text{-}He_n$ exciplexes ends approximately 150 cm^{-1} before the ionization potential of the free sodium atom. This brings up the following questions: what determines this shift of ≈150 cm^{-1} in the ionization potential and what happens with the ionized sodium? We will show how these two questions may be answered with photoelectron and ZEKE spectroscopy and TOF mass-spectroscopy. We will demonstrate that the simple pair-wise additive model introduced in section 3.1.5.1 can semi-quantitatively reproduce the

experimental data. In addition, indirect evidence will be presented on the observation of so-called Scolium states of helium nanodroplets, a helium cluster with an embedded positive ion and an electron orbiting around in a high Rydberg state[18, 142].

3.4.1 Photoelectron and ZEKE spectroscopy

The advantage of the photoelectron spectroscopy lies in the fact that ionic states can be probed directly. On the time scale of excitation we can neglect the motion of helium atoms (Born-Oppenheimer approximation) and consider the shape of photoelectron peak as the projection of the ground state wavefunction onto the ionic potential (Franck-Condon principle). However, in our experimental setup the disadvantage of PES is the limited resolution at low kinetic photoelectron energies, which makes it difficult to reveal the structure of a narrow photoelectron peak. In contrast to PES, zero electron kinetic energy (ZEKE) spectroscopy, which is normally considered as a high-resolution variant of PES[97], yields in our setup a much better resolution. Nevertheless, the shape of the molecular ZEKE spectrum is subjected to interaction dynamics of high Rydberg (HR) states with rovibrational states of the molecular ionic core[102]. This can lead to the detection of transitions which are normally forbidden by the Franck-Condon principle[143]. A considerable shortening of the life time of HR states may also take place, which could make it impossible to record a ZEKE spectrum. This is why we perform both ZEKE and PES measurements to gain an additional insight into effects which may be caused by the dynamics of high Rydberg states of Na-He_N.

For imaging of photoelectrons upon ionization of Na-He_N we used a two-photon ionization scheme in order to avoid the background present in the one-photon ionization, see Chapter 2. At the same time, for ZEKE spectroscopy we used one-photon excitation. The time delay of 1 μs between the photoexcitation and the ionization of HR states by pulsed electric field allows to suppress the background. Attempts to record a two-photon ZEKE spectrum of Na-He_N were not successful due to the presumably low excitation cross-section.

First, we present in the upper panel of Figure 3.94 the photoelectron spectra of Na-He_N with $\langle r \rangle$ = 37 Å and that of free Na recorded following two-photon ionization at 20 742 cm^{-1} frequency. The spectrum of doped helium droplets consists of a strong broad peak centered at a photoelectron energy ≈ 180 cm^{-1} and a shoulder at lower energies. The weak peak in this shoulder, which is centered at ≈ 50 cm^{-1}, originates from the ionization of free Na atoms effused into the detection volume from the oven. The origin of the low energy peak was confirmed by recording the photoelectron spectrum at the same ionization frequency with the helium droplet beam switched off which is shown in gray in the same graph.

The one-photon ZEKE spectrum of Na-He_N with $\langle r \rangle$=37 Å is shown in the lower panel of Figure 3.94. The energy scale of ZEKE spectrum is kept the same as for the photoelectron spectrum. The ZEKE spectrum is positioned with respect to the photoelectron spectra so that the peaks that correspond to the ionization of free Na, coincide. This arrangement will facilitate the comparison of the PES and ZEKE spectra below.

The sharp feature at 41 445±3 cm^{-1} in the ZEKE spectrum can be readily assigned to the ionization threshold (IT) of the free sodium atoms[99] and corresponds to the peak in the PE spectrum of free Na. The broad red-shifted peak is centered at ≈ 41 320 cm^{-1} and correlates to a similar feature in the photoelectron spectrum of Na-He_N. The resolution of 5 cm^{-1}, which is determined from the gas phase peak, is a considerable improvement compared to the resolution of 30 cm^{-1} in the photoelectron spectrum. The broad features in the ZEKE and PES spectra change their position with droplet size in a regular way, see Figure 3.95: at smaller droplets the shift between the broad feature and the peak

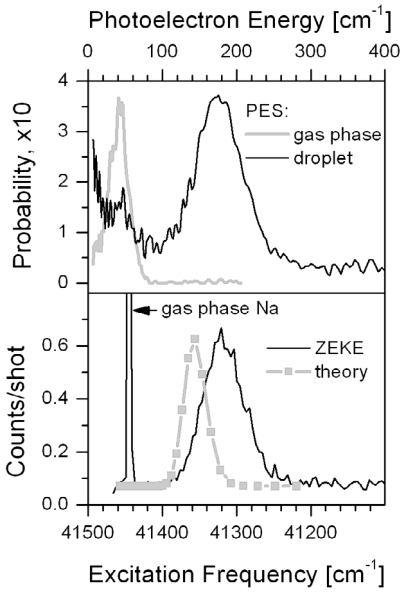

Figure 3.94: Upper panel: photoelectron spectra derived from photoelectron images recorded by one-color two-photon ionization of Na-doped helium nanodroplets with $\langle N_{He} \rangle$ = 4 620 (<r>=37 Å) and of gas phase free Na atoms. The photon energy is 20 742 cm^{-1}. Lower panel: ZEKE spectrum recorded at the same mean droplet size by one-photon excitation of $Na\text{-}He_N$. The theoretical absorption spectrum obtained within the pair-wise additive model for $Na\text{-}He_{5000}$ is also presented. The data points are the Franck-Condon Factors and the line connecting them is to guide the eye.

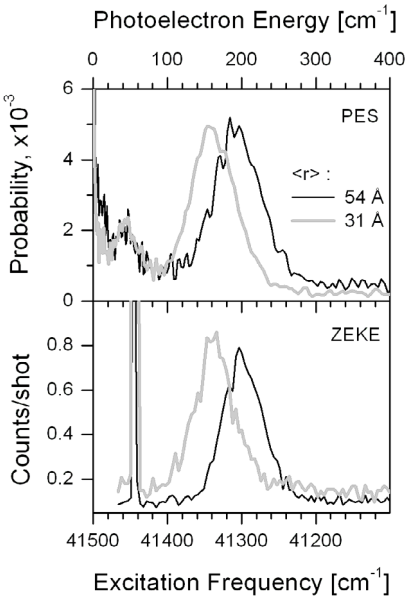

Figure 3.95: Upper panel: photoelectron spectra derived from photoelectron images recorded by one-color two-photon ionization of Na-doped helium nanodroplets with <r> = 31 Å and <r>=54 Å. The photon energy is 20 742 cm^{-1}. Lower panel: ZEKE spectra recorded at the same mean droplet sizes by one-photon excitation of $Na\text{-}He_N$.

corresponding to free Na decreases. Therefore, we assign the broad feature to sodium-doped helium droplets. The theoretical spectra, see section 3.4.3.1, corresponds well to the experiment, which supports our assignment. The fact that the droplet features have identical positions and shapes in the PES and ZEKE shows that dynamical effects of HR states of $Na\text{-}He_N$ play a minor role.

3.4.1.1 Droplet size effect

The shape of the droplet peak in the ZEKE spectrum does not practically depend on the mean droplet size and can be readily fitted to Gaussian function in expression 3.45. The FWHM = 65 ± 2 cm^{-1} of the droplet peak in the ZEKE spectrum stays fairly constant in the 26-54 Å range of mean droplet radius. In the PE spectrum, the width of droplet peak is influenced by the signal from the free Na atoms and does not show regular variations with the mean droplet size. In contrast, the peak in the ZEKE and PES vary in a similar manner as was shown in the previous section. The shifts of the droplet peaks with respect to the atomic peaks in the PE and ZEKE spectra we define as :

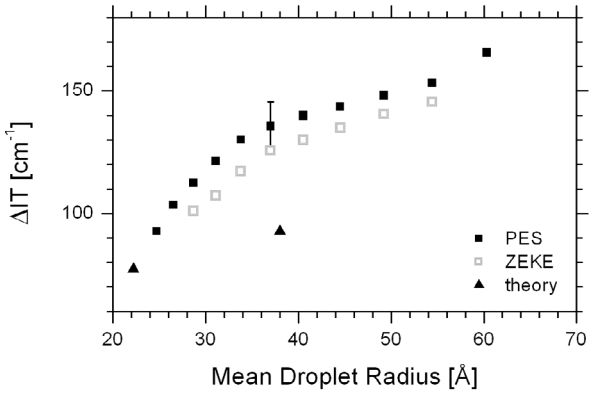

Figure 3.96: The variation of the absolute shift of the ionization threshold (IT) of Na-doped helium nanodroplets with respect to the IT of free Na atoms as defined in expression 3.47. The error bars for the PES data are shown only at one data point for the visibility. The errors for ZEKE data points of 3 cm^{-1} are inferior to the symbol size.

3.47
$$\Delta IT = \tilde{\nu}(Na) - \tilde{\nu}(Na\text{-}He_N)\ , \text{ZEKE}$$
$$\Delta IT = E_{PE}(Na) - E_{PE}(Na\text{-}He_N)\ , \text{PES}$$

where ΔIT is the shift between ionization threshold (IT) of free Na and the maximum of $Na\text{-}He_N$, feature; $\tilde{\nu}(Na) = 41\ 445 \pm 3\ cm^{-1}$ is the ionization threshold of free Na as measured in the ZEKE experiment, $\tilde{\nu}(Na\text{-}He_N)$ is the maximum of the droplet peak in the ZEKE spectrum obtained from fitting it to the Gaussian function in expression 3.45; $E_{PE}(Na) = 41 \pm 5\ cm^{-1}$ and $E_{PE}(Na\text{-}He_N)$ are the maxima of free Na and droplet photoelectron peaks obtained by fitting them tothe Gaussian function mentioned above. The shifts were determined at different mean droplet radii and are shown in Figure 3.96. As can be seen, the PES and ZEKE yields essentially the same dependence. The small persistent difference of $\approx 10\ cm^{-1}$ between PES and ZEKE data points may be attributed to calibration errors of our ion imaging setup.

The variation of ΔIT in photoionization of $Na\text{-}He_N$ with the mean droplet size is similar to variations of 5s, 6s and 7d-9d excitation bands, see sections 3.2.1.1, 3.2.2.1 and 3.3.1: at small droplet sizes in the range of 25-40 Å the droplet peak position varies the most by $\approx 40\ cm^{-1}$, while at larger droplets with <r> = 40 - 60 Å it varies only by $\approx 25\ cm^{-1}$. The overall change of ΔIT within the <r> = 25 - 60 Å range obtained from photoelectron imaging is $\approx 70\ cm^{-1}$. This value is a factor of two larger than in the 7d-9d bands, a factor of two smaller than in the 6s-band and a factor of four smaller than in the 5s-band.

3.4.1.2 Lifetime of high Rydberg states of $Na\text{-}He_N$

The lifetime of the HR states probed in ZEKE was determined in the experiment at three mean droplet sizes. The excitation frequency was fixed at the corresponding maxima of the droplet peaks in the ZEKE spectra. Figure 3.97 shows the signal level as function of the time delay between the optical excitation and the ionization by the pulsed electric field. The data for the largest droplets with <r> = 54 Å was corrected for background signal from gas phase atoms effused from the oven. The correction was done by subtracting from the data recorded with helium droplets the signal recorded

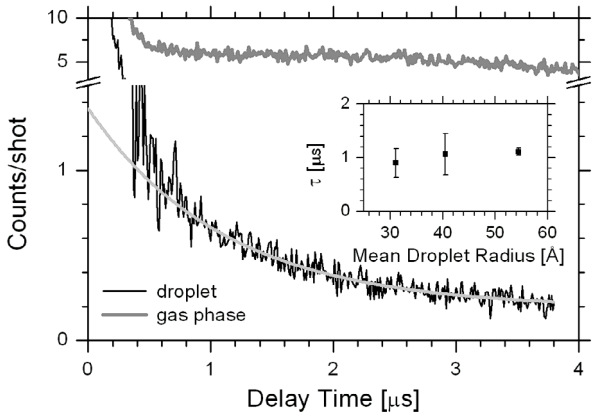

Figure 3.97: The measuring of lifetime of high Rydberg states created by excitation of Na-doped helium nanodroplets with <r> = 54 Å by varying the delay time between the photoexcitation at 41 304 cm^{-1} and the ionization by the pulsed electric field of 5 V/cm. The light-gray line represents the fit to exponential decay function in expression 3.1, from which the lifetime was determined. In the insert: the variation of the lifetime with droplet size is shown.

with the helium droplet beam switched off. This resulted in the smallest fitting error in determination of the lifetime by fitting the data points to exponential function 3.1, see the inset in Figure 3.97. As one can see in the figure, the lifetime does not depend on the mean droplet size within experimental errors.

The value of $\tau \approx 1$ μs is quite short for the HR states with main quantum number n ≈ 100 probed in our experiment, see section 2.2.5. In the case of unperturbed sodium atom the radiative lifetime of such states is more than 1 ms[100]. To insure that the short lifetime of the HR states of Na-He_N is not an artifact, which is often the case due to the stray electric fields in the experimental setup, the lifetime of HR states of free sodium atoms was also measured with the helium droplet beam switched off, see upper graph in Figure 3.97. As can be seen in the figure, the gas phase signal stays practically constant, thus we can rule out the influence of stray field as the origin of the short lifetime of HR states of Na-He_N. The discussion of the possible cause of the lifetime shortening in HR states of Na-He_N will be renewed after the presentation of the TOF mass-spectra recorded under the field-free conditions.

3.4.2 Time-of-flight spectra

In the experiments presented below, we investigate the fate of the Na^+ ion in the direct photoionization of Na-He_N and the fate of the sodium ionic core upon exciting the Na on the droplet's surface to HR states. Before presenting the experimental result we will explain the choice of the techniques used.

The direct way to probe the mass content of species optically probed in ZEKE spectroscopy is to use a mass analyzed threshold ionization (MATI)[103], which is the mass-selected variant of the ZEKE technique. Instead of electrons, in MATI the direct photoions are separated by an external constant electric field. However, it was not possible to implement MATI in our experimental setup in order to detect species with masses ≈ 10^4 amu relevant to helium droplets. We used another approach that allows to establish the relation between the features in the ZEKE and the ion-yield spectra, see 2.2.5.1. According to the principle of ZEKE spectroscopy, the ZEKE spectrum of a given species is the energy derivative of the ion-yield spectrum of that species. From this it follows that in the case of

Na-He_N the ion-yield spectrum of fragments with masses ≈ 10^4 amu, which corresponds to helium droplets, should appear in the same frequency region as that of broad droplet feature in the ZEKE spectrum. The detection of ions with masses ≈ 10^4 amu is possible in our setup by applying high voltage of ≈ 4 000 V to the Repeller electrode. We will proceed as following. First we will provide evidence that after the direct ionization of Na-He_N the heavy species with masses relevant to helium droplet can be detected. Second, we will present the ion-yield excitation spectrum of those species and compare it with the integrated ZEKE spectrum.

3.4.2.1 Direct photoionization of Na-He_N

The TOF mass spectrum of species created after excitation of Na-He_N at 41 398 cm^{-1} is presented in the left panel of Figure 3.98. We used excitation under field-free conditions followed by a delayed pulsed electric field for ionization, see section 2.2.5.1. In this case, the ionization threshold of Na-He_N is not lowered by the external field. The frequency of 41 398 cm^{-1} used is ≈ 50 cm^{-1} below the 41 449 cm^{-1} ionization threshold of free Na[99], but above the expected ionization threshold of Na-He_N represented by the droplet peak in the ZEKE spectrum. So, we expect that the recorded mass-spectrum reflects only the ionization of Na-He_N.

As one can see in the left panel of Figure 3.98 there is no prominent signal at light masses. The weak peaks at mass of 23 amu and 46 amu can be attributed to the Na^+ and Na_2^+ ions created by ionization of sodium dimers formed on the droplet surface. The most interesting feature in the mass-spectrum is the weak signal corresponding to species with masses of ≈ 10^4 amu, which we assign to the helium droplets with the attached positive Na^+ ion. In order to increase the S/N ratio for this weak signal, the output of the multichannel scaler was summed over 125 bins (each bin is of 8 ns duration) so that the resulting signal corresponds to a larger time-bin of 1 μs. This increased the sensitivity at the expense of mass resolution. The outcome of the binning, after conversion of masses to the number of helium atoms, is presented in the right panel of Figure 3.98. One can easily distinguish the signal from heavy species which we attribute to the helium droplets with embedded sodium ion. The extracted atom number distribution of helium atoms has its maximum at 3 500 which is a factor of two smaller than the mean droplet size of $\langle N_{He} \rangle$ = 6 080 presumed in the experiment. This can be attributed to low sensitivity of MCP for such heavy masses. The observation of heavy species with masses relevant

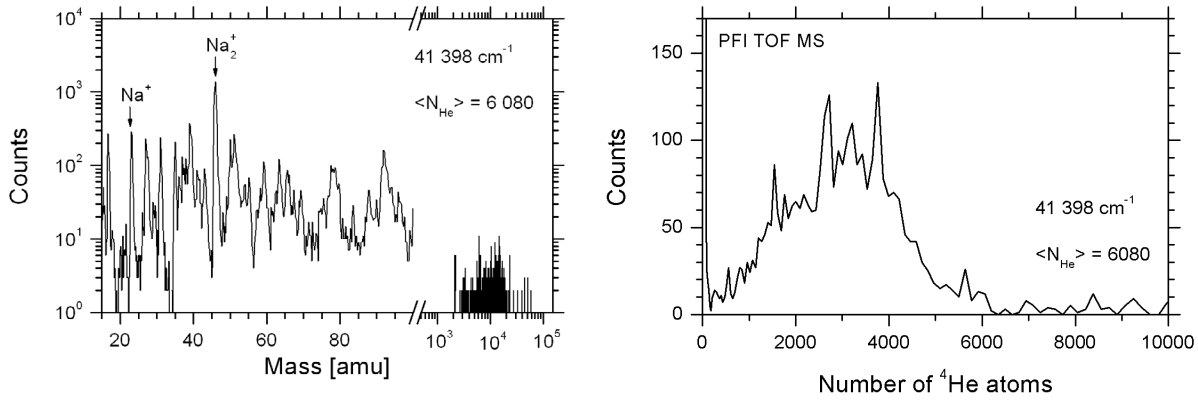

Figure 3.98: Time-of-flight mass-spectrum of Na-He_N with $\langle N_{He} \rangle$=6080 (<r>=41 Å) recorded following one-photon ionization at 41 398 cm^{-1}. Left panel: overview of the full mass spectrum. Right panel: heavy masses region of the spectrum converted to the number of ^{4}He atoms

to helium droplets with embedded positive ion indicates that after direct photoionization of Na-He_N the Na^+ will be solvated inside the cluster.

3.4.2.2 Ion yield excitation spectrum of Na-He_N

By recording the ion yield versus excitation frequency, two regions of interest were set in the TOF: the first comprised the exciplexes Na*-He_n , n=1-5, at masses m = 27-43 amu and the second was set for masses relevant to helium droplets at m = 3 000-25 000 amu. The ion yield spectrum for exciplexes is shown in the upper panel and that for heavy fragments in the lower panel of Figure 3.99. In the upper panel, the ZEKE spectrum is plotted for the comparison of the onset in the exciplexes yield spectrum. The low S/N ratio in heavy fragments spectrum is due to the reduced detection efficiency of slow and heavy ions by the MCP. The integrated ZEKE spectrum is also presented in the lower panel to compare its shape with the ion yield spectrum. The integration was done after the subtraction of the background determined as the offset in the low frequency region of the ZEKE spectrum. Two important observations can be made from the data in Figure 3.99: a) the integrated ZEKE spectrum of Na-He_N coincides with the heavy ion yield spectrum; b) the onset of desorbed exciplexes matches the high frequency onset of the ZEKE spectrum. From the first observation we conclude that in the ZEKE experiments the droplet-related broad peak originates from excitation of Na-He_N to HR states just below its ionization threshold. The meaning of the second observation will be discussed later.

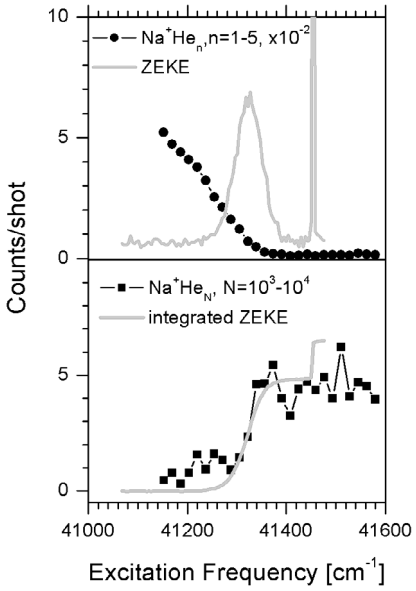

Figure 3.99: Upper panel: One-photon ZEKE spectrum of Na-He_N with <r>=41 Å and the ion-yield excitation spectrum recorded by monitoring Na^+-He_n exciplexes. Lower panel: ion-yield spectrum recorded by gating on fragments with masses in the region of 3 000-25 000 amu and the integrated ZEKE spectrum.

3.4.3 Discussion

3.4.3.1 Modeling of the Na^+-He_N←Na(3s)-He_N photoionization transition

For modeling of the ionization spectrum of Na-He_N we used the same pair-wise additive approximation for the Na-He_N interaction developed previously for the low and medium excited states of sodium-doped droplets, see section 3.1.5.1. We used the Na-He_{5000} and Na-He_{1000} density profiles of Barranco[116] that include the effect of zero-point motion of the light impurity and the pair potential of Na(3s)-He of Patil[118] and that of Na^+-He of Soldan et el.[107] to construct the Na(3s)-He_N and Na^+-He_N effective potentials, see Figure 3.100. The transition probabilities (Franck-Condon Factors, FCF) from the vibrational ground state of Na(3s)-He_N to the vibrational levels of Na^+-He_N were calculated with the LEVEL 8.0 program[108]. The spectra are represented as the envelope over FCF, see the lower panel in Figure 3.94. The comparison of the calculated and experimental ZEKE spectra is presented in Table 18.

The position and the shape of the ionization spectrum of Na-He_N can be understood on the basis of Franck-Condon mapping principle applied to the transition between the ground state level of Na(3s)-He_N potential and the energy levels of Na^+-He_N potential shown in the right panel of Figure 3.100. The width of the ground state wavefunction projected onto the ionic potential defines the width of the ionization transition in frequency space. Even though the calculated energy levels in the Na^+-He_{5000} potential at the projection region are separated by more than 5 cm^{-1}, the resolution in the ZEKE spectrum, no level structure was observed in the experiment. A possible explanation may be the approximate nature of the used one-dimensional effective potentials, neglecting the sodium motion parallel to the helium surface that will result in much denser spacing between energy levels. The wide droplet size distribution in the experiment will also contribute to the smearing of the theoretical level structure.

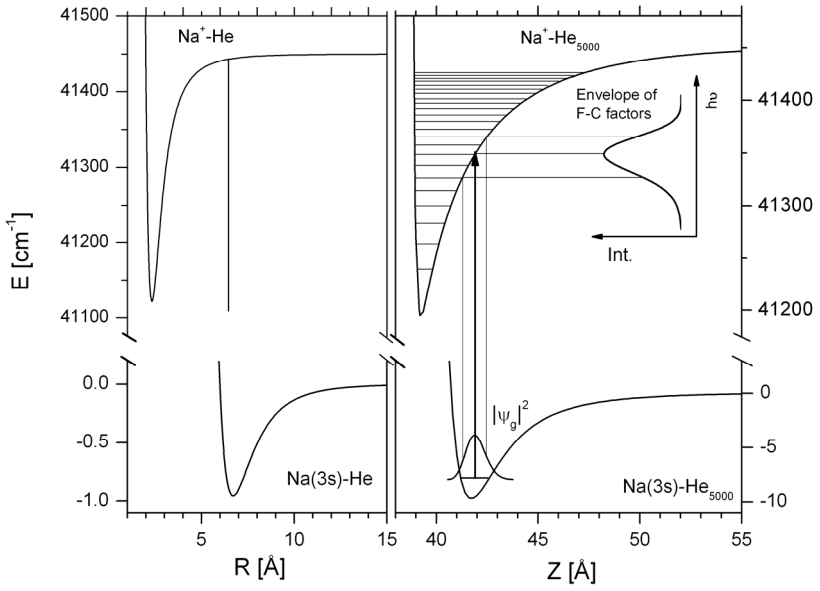

Figure 3.100: Left panel: pair potentials of Na(3s)-He and Na^+-He. Right panel: corresponding Na(3s)-He_{5000} and Na^+-He_{5000} effective potentials calculated as sum of the pair potentials.

In view of the availability of only two theoretical density profiles, Na-He_{1000} and Na-He_{5000} which are relevant to the droplet sizes in the experiment, we can only remark that the shifts in the ionization thresholds obtained with these profiles follow the experimental trend. We also attempted to describe the lowering of the IT with a variant of the polarizable continuum model[144]. The expression of polarization energy of the helium droplet, which had a sharp surface, in the field of Na^+ ion was obtained containing three parameters: a) the radius of the droplet, b) the radius of the dimple, and c) the distance between the ion, which resides in the centre of sphere that forms the dimple, and the unperturbed droplet's surface. However, it was not possible to extract reliable information from fitting the experimental data points to the expression.

Table 18 Comparison of experimental and theoretical photoionization transitions of Na-He_N

		Peak position as fitted to Gaussian [cm^{-1}]	FWHM as fitted to Gaussian [cm^{-1}]
Experiment ZEKE	$\langle N_{He} \rangle$ = 4 620	41 318 ± 1	65 ± 2
Theory	N_{He} = 5 000	41 356 ± 1	35 ± 1
	N_{He} = 1 000	41 372 ± 1	32 ± 1

The photoelectron spectra and ZEKE spectra reflect mainly the configuration of the ground state of Na-He_N, for the electronic excitation can be considered instantaneous on the time scale of nuclear motion. In contrast, the fate of the Na^+ in the direct photoionization and the fate of sodium ion core after the excitation of Na-He_N to HR states are expected to be determined by the time scale of nuclear motion. Thus, it is not possible to obtain information about the location of sodium ion after the photoionization of Na-He_N from our spectroscopic data. We expect that Na^+ will move towards the droplet surface since the Na^+-He_N effective potential is attractive. It will finally be located in the droplet's interior because of the confining potential of the ionic impurity in the droplet[49]. During this confining process, the shell of He atoms[13], "snowball", will be formed around the Na^+. Finally the solvated ion will be confined inside the droplet, the size of which will be somewhat reduced by evaporative cooling of helium atoms from the nanocluster due to the release of ≈ 2 852 cm^{-1} , the solvation energy of Na^+ in bulk liquid helium[145]. Very approximately the low limit of the time scale of nuclear motion can be taken as the period of vibration in the Na^+-He_{5000} effective potential. Taking the vibrational frequency to be 100 $cm^{-1} \approx 3 \cdot 10^{12}$ s^{-1}, we obtain the lower limit of the confining time of $\approx 0.3 \cdot 10^{-12}$ s = 0.3 ps.

3.4.3.2 Dynamics of high Rydberg states of Na-He_N

3.4.3.2.1 Exciplex desorption

Before the discussion of the peculiar complex of sodium atom in a HR state attached to a helium nanodroplet, we will consider the desorption of exciplexes formed after the excitation of Na to HR states.

A possible reason that $NaHe_n$, n = 1-4, exciplexes are observed in the 41 250 - 41 400 cm^{-1} region of the Na-He_N ZEKE spectrum in Figure 3.99, where solvation of Na^+ core in the helium droplet is expected, may be the spectral overlap with transitions corresponding to the lower excited

states of Na. The high frequency parts of Na-He_N transitions in the 41 000 - 41 500 cm^{-1} region are not resolved, see Figure 3.82, but we expect that their width will be similar to the FWHM ≈ 65 cm^{-1} of the droplet ZEKE spectrum. So, the excitation of Na-He_N close to its ionization threshold will produce both Rydberg states with n ≈ 10-15 and states with n ≈ 100. The former cannot be ionized with the weak pulsed electric field in the ZEKE scheme nor by the stronger field of 1 500 V/cm used for the ion-yield measurements. Since this field can ionized only Rydberg states with n>31. As we suggested in section 3.3.5, the relaxation of the sodium excited states with n=10-15 in the helium droplets may lead to the ejection of $NaHe_n$, n = 1-4, exciplexes in the low lying states which are then ionized with the second photon. In contrast, the Na(n)-He_N in the HR states with n ≈ 100 are expected to be much more stable and are detected only via the ionization by pulsed field of 5 V/cm.

3.4.3.2.2 Solvation of Na^+ ion core in the helium droplet in HR states of Na-He_N*

Now we will return to the discussion of the solvation of sodium ion core in HR states of Na-He_N. The ion-yield spectrum recorded by detecting heavy fragments contains both directly photoionized and field-ionized ions due to the short delay between photoexcitation and pulsed-field ionization of HR states. The variation of the ion-yield spectrum with frequency reflects the accumulation of ions across the ionization transition. The coincidence of the integrated ZEKE spectrum with the ion-yield spectrum of heavy fragments confirms that the same ionization threshold, *i.e.* the threshold of Na-He_N, is probed in these experiments. Still, this observation does not provide direct evidence that the Na^+ ion core become solvated in the droplet, while the outer weekly bound electron continues to orbit around. Let us estimate the low limit of the mean electron orbit radius in the HR states probed in ZEKE. We will use the simplest approach, considering the energy levels of hydrogen atoms, see equation 2.18. The mean radius of an electron orbit in the hydrogen atom is[98]:

3.48 $$\langle r_e \rangle = \frac{a_0}{2}\left[3n^2 - l(l+1)\right]$$

where a_0 = 0.529 Å is the Bohr radius, n is the main quantum number and l is the orbital angular momentum. To further simplify the estimation we will consider only the $l=0$ orbits. The applied external electric field modifies the Coulomb potential by lowering the ionization potential and forming a saddle point in the resulting potential. The energy at the saddle point is given by equation 2.20. Neglecting the tunneling through the formed potential barrier, the external field ionizes all HR states down to the saddle point, so we can consider the energy level corresponding to the saddle point as the highest states not affected by field ionization or the lowest one that can be ionized. The main quantum number of this survived energy level is determined as:

3.49 $$n = \left(\frac{Ry}{6.1\sqrt{F}}\right)^{\frac{1}{2}}$$

In our experiments at F = 5 V/cm, n ≈ 90 is the smallest quantum number of the initially created high Rydberg states which can be ionized, so the corresponding mean orbital radius $\langle r_e \rangle$ equals 6 400 Å. This radius is two orders of magnitude larger than the maximal mean droplet radius of 54 Å used in the ZEKE experiment. Furthermore, at n ≈ 90 the electron barely penetrates the ion core region, being largely insensitive to the ion core dynamics[100]. The electron density around the positive charge at a distance comparable to the mean droplet radius of the droplet is so low that the sodium ion core may be considered as free. So, the interaction of the Na^+ core with He_N in the HR

states of Na-He_N is thought to be like in the case of Na^+-He_N. This implies that it will be solvated in the helium nanodroplet. In support of the sodium ion core solvation in the droplet is the ≈1 μs lifetime of Na-He_N in HR states measured in ZEKE experiments. It is three orders of magnitude smaller than predicted life time of free Na atoms under similar conditions but is comparable to that of molecular systems in HR states [102]. The origin of the observed life time we will discuss below.

3.4.3.2.3 Possible relaxation mechanism of Na-He_N HR states*

The Rydberg states of complexes consisting of a positive ion embedded in a helium droplet and an electron in a HR state orbiting outside the helium cluster, also known as Scolium[18, 142], have already been studied theoretically. A short but comprehensive review on the subject appeared recently in the latest publication of Ancilotto et al.[142].

The previous works were mainly devoted to the energy level structure of Scolium with the ion placed exactly in the cluster's centre. Golov and Sekatskii developed a Rydberg-like formulae of the cluster size dependent energy levels[146, 147] and suggested that the states with principal quantum number n≈10-20 should be stable against the ion displacement from the droplet centre. They predicted that the radiative lifetime of the HR states with n≈10 should be larger than the radiation lifetime of 1 μs. The authors explained the increased lifetime by the required tunneling of the outer electron through the helium surrounding the ion core. The assumed potential barrier for electron was taken≈1 eV, as in the case of injection of free electron into liquid helium[148]. The decay mechanism by ripplon and phonon emissions was also considered but judged to be unimportant.

Ancilotto and coworkers[142] investigated the solidification of Be^+-doped helium clusters by additional pressure due to the outer Rydberg electron. They focused on low energy states, i.e. states with principal quantum number n≈7-8, where the electron is confined outside the small Be^+-He_N, N<350, cluster. They estimated the radiative lifetime to be of the order of 0.3 ns. Contrary to the conclusion of Golov and Sekatskii it was found that the Rydberg states of Be*-He_N were not stable against the other recombination mechanism via ion displacement from the cluster centre. As the ion leaves the centre, the electron density localizes on the side of the displacement. This exerts an additional force pulling the ion towards the surface, reducing the helium barrier between the electron and the ion, which can lead to rapid ion-electron recombination. For big droplets with N_{He} ≈ 14 000, R ≈ 53 Å the recombination time via ion pulling was estimated to be a few picoseconds. It should be noted that this recombination time was obtained for the lowest energy Rydberg state. In this case, the orbit's radius is approximately the droplet radius, so the principle quantum number for this state can be estimated as n ≈ 10.

As for the HR states detected in our ZEKE experiments on the ionization of Na-He_N, they differ from those studied theoretically: the estimated principal quantum number n ≈ 100 is considerably larger than that in the reported works. The mechanisms leading to the lifetime of ≈ 1 μs compared to ≈ 1 ms of free Na are not completely clear. The radiation-limited lifetime can be discarded in view of very small transition probability mentioned above. The ion-electron recombination as discussed by Golov and Sekatskii can be also neglected in view of larger droplet sizes used in the experiment and the negligible electron density in the vicinity of the droplet for the HR states with n ≈ 100. Recombination by ion pulled to the cluster surface by the electron suggested by Ancilotto et al.[142] may be extrapolated to higher Rydberg states with n>8. If one assumes that the rate of the recombination via this mechanisme is proportional to the mean radius of the electron orbit, then the recombination time will increase by a factor of $(n/n_0)^2=10^2$, $n_0=10$ being the characteristic principal quantum number for the states studied by Ancilotto. Thus, the recombination time will be of the order of 1 ns, which is three orders of magnitude smaller compared to the

experimental value of ≈ 1 μs. In view of the very crude scaling assumption, the difference is thought to be tolerable and is in line with expected increase in the lifetime of HR states.

3.4.4 Summary

In this section we presented our results on the photoionization of Na-He_N studied with the photoelectron, ZEKE and TOF mass-spectrometry. The ionization threshold of Na-He_N has a red shift of ≈ 150 cm^{-1} with respect to that of free sodium atom and depends on droplet size. Its shape and shift can be semi-quantitatively reproduced within the pair-wise additive model of Na-He_N and Na^+-He_N interaction. We showed using TOF that upon direct ionization the created Na^+ ion is solvated inside the helium droplet. With a combination of ZEKE and ion yield spectra the high Rydberg (HR) states of Na-He_N with the principle quantum number n ≈ 100 were studied. Indirect evidence of existence of so-called Scolium states, when an electron resides in a high orbital outside a helium cluster with embedded positive ion, was obtained. The evidence comprises two facts. The first is a life time of ≈ 1 μs of HR states of Na-He_N created in the experiment. This correlates well with estimations of the life time of Scolium in the recent theoretical studies. The second is the coincidence of the integrated ZEKE spectrum of Na-He_N with the heavy ion yield spectrum (ion mass $m>10^3$ amu corresponding to helium droplet with solvated Na^+). This implies that the ionic core of Na in HR states may be solvated in the droplet while the electron is still orbiting outside the droplet during measured life time of ≈ 1 μs.

Chapter 4 : Ionization of aromatics-doped helium nanodroplets

In this chapter, we will focus on the influence of the helium droplet on the photoionization of embedded molecules. The aim of our experiments is to understand the effect of helium environment on the ionization process by comparing the photoionization of the gas phase molecules with those embedded in helium droplets.

The investigation of molecular dynamics requires that the initial and final states of the system under study are well defined[149]. In practice, this is rarely achievable for complex systems. In helium droplets the ground state can be considered as the best defined state in view of the ultracold, 0.4 K, helium environment that restricts the internal molecular excitations only to rotations. The internal degrees of the droplet alone can also be considered as well defined at such low temperatures[150]. In this respect, the rotational and vibrational energy states of the free molecule at 0.4 K temperature are better defined than the states of the joint system "molecule-helium droplet". The additional degrees of freedom are the radial position of the impurity in the droplet and the energy in the confinement potential of nanocluster, the distributions of which are quite broad[48].

In view of the considerations given above it is preferable to use one-photon ionization of the doped helium droplets. Otherwise, additional effects related to intermediate excited states can not be excluded. However, experimentally it is more advantageous to use resonance-enhanced multiphoton ionization (REMPI) schemes via intermediate electronic excited states. The REMPI scheme can be routinely implemented to ionize molecules with conventional pulsed tunable dye lasers[151]. The ionization of molecules embedded in helium droplets via the intermediate electronic excited state may complicate the extraction of information that is relevant exclusively to the photoionization dynamics. Indeed, the study of electronically excited molecules in helium droplets showed that their properties are affected by the helium environment[55]. Nevertheless, in the following we will show that valuable information about the photoionization dynamics of doped helium droplets can be obtained with multi-photon ionization via intermediate electronic excited states.

We chose three readily available aromatic molecules: aniline, phenol and toluene as model systems, since all these molecules were previously studied in the gas phase. The use of three molecules allows selecting out the general effects from those that may arise from the properties of a particular molecule. In general, these systems match to the following requirements, which are important in the experiment:

- bulk substances have high enough vapor pressure at room temperatures, so it is easy to embed molecules into droplets by passing the droplet beam through the scattering cell filled with the vapors of given substance
- the resonance-enhanced multiphoton ionization (REMPI) schemes via the intermediate electronic excited S_1 states are known
- the vibrational energy structure of the electronic ground S_0 state, intermediate electronic excited S_1 state and of the ionic state were studied experimentally and theoretically

We would like to emphasize that due to the dynamics in the intermediate electronic excited state S_1 affecting the ionization, the obtained data and the developed models can be essentially understood only all together. From methodological point of view, this makes difficult the presentation of our results. We chose to present the results on the dynamics in the S_1 states first, though here we will already use the results related to the ionization dynamics. Then, in the second part, we will concentrate on the ionization process studied by photoelectron spectroscopy.

4.1 S_1 excited state dynamics

4.1.1 $S_1 \leftarrow S_0$ excitation spectra

The REMPI spectra of the $S_1 \leftarrow S_0$ transitions in aniline, phenol and toluene in the gas phase and in helium droplets are recorded by monitoring as a function of the laser frequency the total electron yield for aniline and the molecular ion yield for phenol and toluene, see Figure 4.1. In the phenol and toluene cases, the background using photoelectron detection was too high to record spectra. The spectra of aniline recorded by detecting photoelectrons or ions were found to be essentially the same. The upper graphs show the spectra of gas phase molecules. These spectra demonstrate vibrational progressions that have been analyzed previously, see references for aniline[152], phenol[153] and toluene[154]. The lower graphs show the excitation spectra of molecules embedded in helium droplets. The spectra of aniline and phenol are dominated by asymmetric broad features that follow, largely, the gas phase spectra. Contrarily, in the spectrum of toluene sharp peaks dominate. The droplet spectra are shifted to higher frequencies with respect to the spectra of free molecules. In the aniline case, it is difficult to determine whether the shift is the same for all vibrational transition in view of their broad structure. In contrast, for the phenol and toluene droplet spectra that exhibit sharp features the shift is the same for all transitions in the spectra. We will determine these shifts below.

Closer inspection of the band origins of the droplet spectra of aniline and phenol, see Figure 4.2, also reveals the presence of sharp lines which are shifted to higher frequencies compared to gas phase transitions. Their parameters are collected in Table 19. Analogous to the spectra of other aromatic species dissolved in helium droplets, the sharp lines can be interpreted as the zero-phonon lines and the broad features as phonon wings[64].

Table 19 Positions of ZPL in excitation spectra

Molecule	Gas phase band origin [cm^{-1}]	ZPL in the excitation spectrum of molecules in He droplets [cm^{-1}]	Shift [cm^{-1}]
Aniline	34 030	34 065	+ 35
Phenol	36 347	36 393	+ 46
Toluene	37 474	37 522.5	+ 48.5

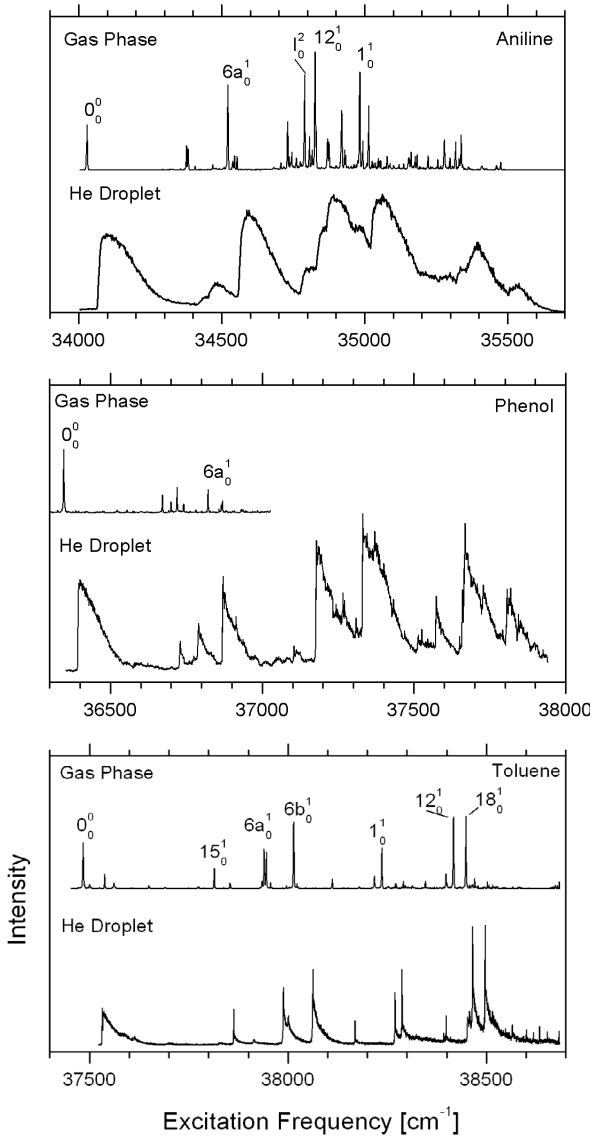

Figure 4.1: $S_1 \leftarrow S_0$ 1+1 REMPI excitation spectra of aniline, phenol and toluene in the gas phase (upper spectra in the graphs) and in helium droplets (lower spectra in the graphs) with <r> = 41 Å for aniline and <r> = 37 Å for phenol and toluene. Laser intensities in helium droplet spectra were 72 MW/cm^2 for aniline and toluene and 36 MW/cm^2 for phenol.

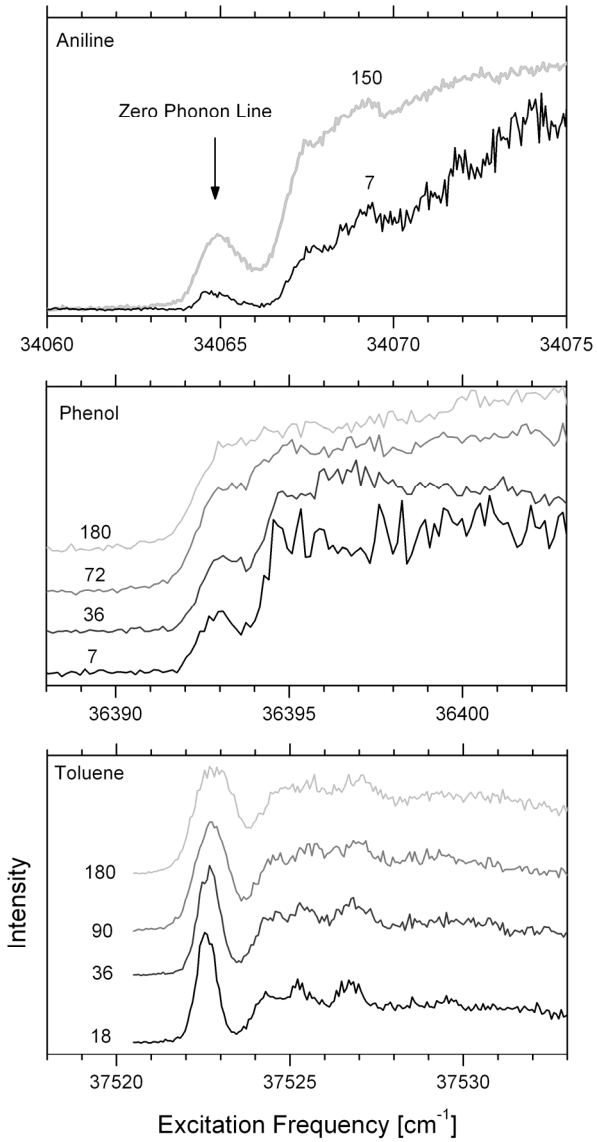

Figure 4.2: The enlarged regions of the excitation spectra with zero-phonon lines located to the red of the phonon wings corresponding to the band origins. The numbers indicate light intensities in MW/cm^2.

4.1.1.1 A possible explanation of ZPL shifts

The differences in shifts between the band origins in the gas phase and in helium droplets for aniline, phenol and toluene may be due to changes in the electron density that occur within a molecule upon excitation as was shown by Boatwright *et al.*[155]. The authors measured the lineshift for a series of substituted benzene derivatives and found that it was correlated to the increase of electronic density in the excited molecules along the axis going through the centre of aromatic ring. The proposed explanation relied on the fact that in the electronic ground state two helium atoms can be

near completely localized above and below the molecular plane of the benzene. Upon the electronic excitation, the helium-plane distance is increased, so two localized helium atoms move away from the ring. Applying this principle to the molecules embedded in the droplets, a magnification of the effect is expected, since the full solvation shell of the molecules should be rearranged. Indeed, Boatwright *et al.* demonstrated that the larger is the change in electron density the larger is the shift. The largest blue shift of 45.7 cm^{-1} was found for toluene and the smallest of 16.06 cm^{-1} for benzonitrile. The lineshifts found in our experiments lie within that range, though Boatwright and coworkers did not reported on lineshifts for aniline and phenol.

Within the set of molecules studied, red and blue shifts were discovered, see the compilation of results in review of Toennies and Vilesov[20]. The red or blue shifts are not unambiguously related only to the properties of the excited state of a molecule in helium droplets, but rather to the combination of both ground and excited electronic states. Practically all molecules reside inside helium droplets, meaning that the energy of the solvated molecules with respect to the free one is lowered by solvation. The solvation of the excited molecule also means that the energy level of the embedded molecule is again lower than in the gas phase. Then the red or blue shift depends on the interplay between solvation energies in both states.

4.1.1.2 Intensities of ZPL and PW

In contrast to other systems[156, 157], the zero-phonon line in aniline spectrum is much weaker than the phonon wing. The saturation behavior of the observed features is also opposite to that observed for other aromatic systems[157-159], see Figure 4.2. While for phenol and toluene the intensity ratio of zero-phonon line to phonon wing decreases with increasing light intensity, this is not the case for aniline where the ratio increases with the increasing light intensity. Both these observations on the relative intensities can be attributed to the large geometry change of the aniline molecule upon electronic excitation. Whereas aniline in the ground electronic state is nonplanar with the hydrogen atoms of the amine group pointing out of the aromatic plane, it becomes planar upon electronic excitation to the S_1 state[160]. The large geometry change of the aniline upon electronic excitation requires a substantial reorganization of the helium environment around the molecule, which will give rise to an intense phonon wing and relative weak zero-phonon line[64].

The geometry modifications in the electronic excited S_1 states of phenol and toluene with respect to the ground S_0 states are less pronounced than in aniline. In the S_0 and S_1 states, the phenol molecule has planar structures[161, 162]. The geometry of phenol is modified upon the excitation to S_1 level by slightly increasing the C-O-H angle and shortening the C-O distance[162] and the expansion of the aromatic ring due to the increase in the C-C bonds. In toluene, the geometry changes are the shortening of “C-methyl group” bond and the overall expansion of the benzene ring by increasing of the C-C bonds[163, 164]. The methyl group has the same orientation in the ground and in the electronic excited states, when the hydrogen atoms of the group are all out of plane with one of the C-H bond forming the right angle with the aromatic ring.

The geometry modifications upon electronic excitation of doped molecules may qualitatively explain the observed difference in the intensities of ZPL and PW within the configuration coordinate model.

4.1.1.3 Configuration coordinate model

The vibrational frequencies of molecules are, in general, of the order of 100 cm^{-1} and are much higher than the phonon frequencies in liquid helium which are of the order of 1 cm^{-1}. This means that

the low frequency modes of liquid helium nanodroplets can be treated independently from the high frequency of molecular vibrations (adiabatic approximation). Each vibronic state of the molecule can be associated to an intermolecular potential energy surface, which describes the equilibrium position and the motion of the surrounding helium atoms when the dopant is in this state. These potential surfaces determine the lineshapes of vibronic transitions of "dopant-liquid helium nanodroplet" system. According to Keil[165], the normalized lineshape function for the transition from an electronic state $|a\alpha\rangle$ to an electronic state $|b\beta\rangle$ of the molecule-droplet system, which we associate to the $|a\rangle \rightarrow |b\rangle$ transition in the free molecule and designate as $I_{|a\rangle\rightarrow|b\rangle}(E)$, is written as:

4.1 $$I_{|a\rangle\rightarrow|b\rangle}(E) = \left\langle \sum_{\beta} \left|\langle a\alpha|b\beta\rangle\right|^2 \delta\left(\varepsilon_{|b\beta\rangle} - \varepsilon_{|a\alpha\rangle} - E\right) \right\rangle_{T,|\alpha\rangle}$$

In the expression, $|\alpha\rangle$ and $|\beta\rangle$ represent the phonon levels in the states $|a\rangle$ and $|b\rangle$, respectively. E is the transition energy of the molecule in the helium droplet, $\varepsilon_{|b\beta\rangle}$ and $\varepsilon_{|a\alpha\rangle}$ are the eigenenergies of the system, when the molecule is in one of the electronic states $|a\rangle$ or $|b\rangle$ and the surrounding medium is in the respective phonon states $|\alpha\rangle$ or $|\beta\rangle$. The outer brackets $\langle ... \rangle_{T,|\alpha\rangle}$ indicate that the thermal average on the initial state $|\alpha\rangle$ is taken. In the Franck-Condon approximation, the electronic transition dipole moment $\vec{\mu}$ is independent from the internuclear separation: $\langle a\alpha|\vec{\mu}|b\beta\rangle = \vec{\mu}_0 \langle a\alpha|b\beta\rangle$, where $\vec{\mu}_0$ is the constant transition dipole moment. Consequently, $\left|\vec{\mu}_0 \langle a\alpha|b\beta\rangle\right|^2$ are intermolecular Franck-Condon factors describing the overlap of the phonon wavefunctions involved in the transition. Thus, the expected dependence of $I_{|a\rangle\rightarrow|b\rangle}$ on $\vec{\mu}$ is absorbed in the normalization. The defined lineshape function consists of discrete lines centered at different energies determined by delta-functions, but in reality, these lines are smeared into a quasi-continuum due to factors as high density of phonon states, the limited lifetimes of excitations and droplet size effects in view of broad size distribution of nanocluster in the cluster beam source.

The energies $\varepsilon_{|b\beta\rangle}$ and $\varepsilon_{|a\alpha\rangle}$ satisfy the condition (only the expression for $|a\alpha\rangle$ state is shown) :

4.2 $$\left[T_N + E_{|a\rangle}(\vec{x})\right]\psi_{a\alpha}(\vec{x}) = \varepsilon_{|a\alpha\rangle}\psi_{a\alpha}(\vec{x})$$

where T_N is the kinetic energy operator for helium atoms, $\vec{x}$ represents the nuclear coordinates of helium atoms. $E_{|a\rangle}(\vec{x})$ is the adiabatic potential in which the helium atoms move ($E_{|a\rangle}$ is the eigenenergy of the electronic part of the Hamiltonian for the $|a\alpha\rangle$ state). This potential for the ground state can be expanded in a Taylor series in terms of the displacements of the helium atoms from the equilibrium positions. With a normal mode transformation, the adiabatic potential becomes:

4.3 $$E_{|a\rangle}(\vec{x}) = \frac{1}{2}\sum_i m_i \omega_{|a\rangle i}^2 q_i^2$$

where q_i are normal coordinates, m_i are normal masses and $\omega^2_{|a\rangle i}$ are normal frequencies. In the upper electronic state $|b\beta\rangle$ it is also possible to obtain the adiabatic potential $E_{|b\rangle}(\vec{x})$ in the quadratic form given above, but the normal coordinates will be not necessary the same as in the ground state. Equation 4.1 thus involves the evaluation of multi-dimensional integrals. To simplify the situation we expand the adiabatic potential $E_{|b\rangle}(\vec{x})$ for the excited state $|b\beta\rangle$ in the normal coordinates q_i for the ground state:

4.4 $$E_{|b\rangle}(\vec{x}) = E^0_{|a\rangle\rightarrow|b\rangle} + \sum_i A_i q_i + \frac{1}{2}\sum_i m_i \omega^2_{|b\rangle i} q_i^2 + \frac{1}{2}\sum_{j\neq i} B_{ij} q_i q_j$$

where $E^0_{|a\rangle\rightarrow|b\rangle}$ is the electronic part of the energy difference between potential surfaces, A_i and B_{ij} are the expansion coefficients, $\omega^2_{|b\rangle i}$ are the normal frequencies. We neglect for further simplicity the cross-terms $B_{ij}q_iq_j$, which makes the expression 4.4 the sum of harmonic oscillator potentials differing in their equilibrium positions from those in the expression 4.3.

The problem is still complicated, since the number of normal modes in the expressions 4.3 and 4.4 is of the order of 3N, where N is the number of helium atoms in the droplet. It is possible to simplify the analysis of the lineshapes by reducing the number of normal coordinates, hence the number of potential energy surfaces of multiple harmonic oscillators, to one effective coordinate and respective energy surface of a single harmonic oscillator. However, the effective or configuration coordinate does not necessarily have a straightforward physical interpretation. In our case, we adopt the interpretation of Hartmann *et al*.[64]. They suggested that the impurity in the droplet is represented by a spherical cavity that undergoes expansion from radius R_g in the electronic ground state of the dopant to the radius $R_e>R_g$ in the electronic excited state. We take additionally into account the rearrangement that is caused by both electron density redistribution and the geometrical change in the excited molecule. In summary, the electronic excitation of the dopant molecule in the droplet leads to the rearrangement of helium atoms surrounding the molecule, which can be viewed within the configuration coordinate model as the transition between vibrational levels of two one-dimensional harmonic potentials.

Now we are able to qualitatively interpret the different intensity ratios of ZPL to PW in the band origins of recorded excitation spectra of aromatic molecules with the configuration coordinate model, taking into account only the first three terms in the expression 4.4. First, we point out that the size of the molecules does not change much upon excitation, so the size change is not the main factor in the helium rearrangement around the electronically excited molecule. Second, the electronic density redistribution in the molecule upon excitation may contribute to the change of the solvation structure. However, we are not able to estimate its importance at the current stage. The geometry change of the molecular structure is the third source of the rearrangement of the helium atoms around the molecule. The last factor is thought to be in the origin of the weak ZPL in the aniline spectrum. As was mentioned above, upon excitation the aniline changes from non-planar to planar configuration. This will result in a considerable change of the normal coordinates in the molecule-droplet system in the electronic excited state compared to the ground state. According to expression 4.4, this implies large A_i coefficients (strong coupling) and a shift of the effective harmonic oscillator potential in the excited

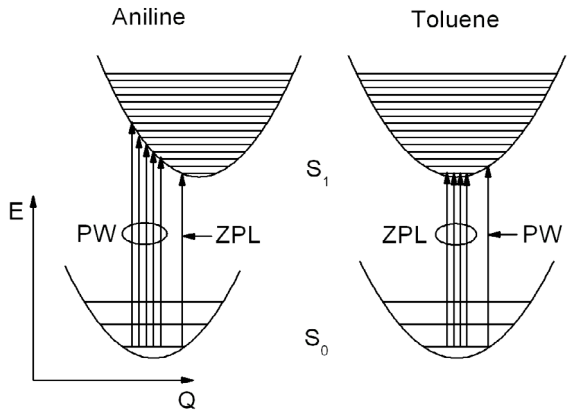

Figure 4.3: Schematic illustration of the configuration coordinate model for aniline and toluene in helium droplets.

state with respect to the ground state potential, see the left graph in Figure 4.3. Consequently, one finds applying the Franck-Condon principle that upon the electronic excitation of the embedded molecule the helium environment (phonons) will be efficiently excited. In contrast, toluene does not change much the geometry upon electronic excitation, so one expects almost unshifted effective potentials, see the right graph in Figure 4.3. In this case, the phonon excitation is greatly reduced. The situation in the excitation of doped phenol is not well explained with only geometrical change in the excited molecule, since there is no big geometry change as in the toluene but the photon wing is quite strong. It might indicate that electronic density redistribution plays an important role in the rearrangement of the surrounding helium atoms.

4.1.1.4 Vibrational relaxation timescale

In our experiments, the ZPLs are strong enough and well separated from the PWs only in the toluene excitation spectrum. The $S_1 \leftarrow S_0$ vibrational excitations of toluene in helium droplets demonstrated systematically wider lineshapes compared to the ZPL of the band origin, see Figure 4.4. Only data points of ZPLs that are well separated from the PWs are presented in the above figure. The lowest laser intensity was used to avoid power broadening effects as much as possible. Assuming that the additional line-broadening is exclusively due to vibrational relaxation of excited toluene in the S_1 electronic state in helium droplets, a time scale may be estimated by fitting the zero-phonon lines of the vibrational transitions to Voigt profile, a convolution of Gaussian and Lorenzian functions. The Gaussian part in Voigt profile is thought to represent the inhomogeneous broadening mainly due to the impurity location within the droplet and the size distribution of droplets. It might also include the unresolved rotational structure. The Lorenzian part is assumed to represent the homogeneous broadening due to the shortening of the level's lifetime by helium-induced vibrational relaxation. It should be emphasized that the energy path, along which the system relaxes, is not known *a priori*. This means that the line broadening represents only the fact of system relaxation to some lower energy levels, but not the nature or energies of these levels.

The ZPL of the origin transition serves as the reference profile. The Gaussian width found for the origin ZPL is used as a fixed parameter when fitting the ZPL of higher vibrational transitions to Voigt profile, see Figure 4.4. We are expecting that the unresolved rotational profile, which is included in the Gaussian width, is the same for all higher vibrational levels. The increase in the Lorenzian width of the ZPLs in $S_1 \leftarrow S_0$ vibrational transitions is attributed to the helium-induced

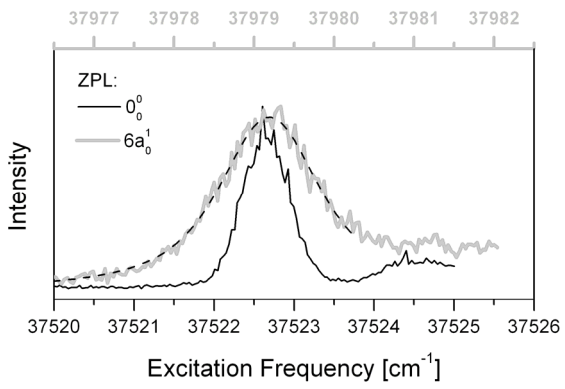

Figure 4.4: Profiles of zero-phonon lines in the $S_1 \leftarrow S_0$ transition of toluene in helium droplets with <r>=37 Å recorded by 1+1 REMPI at a laser light intensity of 2 MW/cm^2. The dotted line is a Voigt fit to the data points. The extracted Gaussian and Lorenzian widths are following: for 0_0^0: 0.64 ± 0.05 cm^{-1} and 0.10 ± 0.02 cm^{-1}; for $6a_0^1$: 0.64-fixed and 1.21 ± 0.04 cm^{-1}.

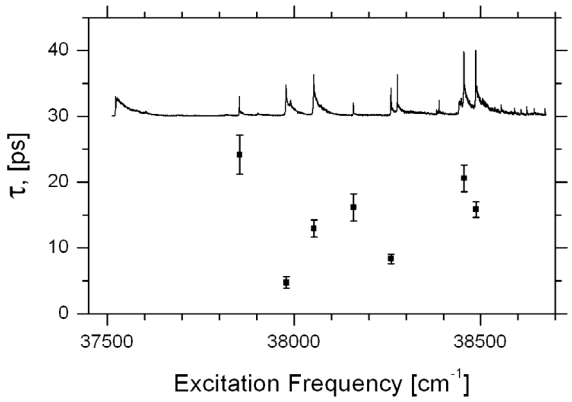

Figure 4.5: The time of the vibrational relaxation of toluene in helium droplets with <r>=37 Å extracted according to equation 4.5 from the lineshapes of zero-phonon lines in the $S_1 \leftarrow S_0$ transitions recorded by 1+1 REMPI at laser light intensity of 2 MW/cm^2. Upper graph represents the $S_1 \leftarrow S_0$ excitation spectrum of toluene in helium droplets from Figure 4.1 for reference purpose.

relaxation. The difference between the Lorenzian widths of the ZPL of given vibrational transition and the band origin is used to determine the relaxation time according to expression:

4.5
$$\tau_i = \frac{1}{2\pi c} \frac{1}{\tilde{w}_L(i) - \tilde{w}_L\left(0_0^0\right)}$$

where $\tilde{w}_L$ is the Lorenzian width expressed in wavenumbers, i stands for a particular vibrational transition and c is the speed of light. The scales of vibrational relaxation are found to be of the order of 10 ps, see Figure 4.5. There is no systematic variation of the relaxation times with the excited energy level. The obtained picosecond time scale of vibrational relaxation is the low limit of the relaxation time, since the level to which the system relaxes cannot be deduced from the excitation spectrum.

4.1.2 Photoelectron spectra

Photoelectron spectra are acquired by imaging the photoelectrons onto the detector at a fixed laser frequency. For the images taken with a gas phase molecule the frequency is set to the 0_0^0 band origin of $S_1 \leftarrow S_0$ transition. For aniline and phenol in helium droplets, the frequency is fixed to the maximum of the PW corresponding to the band origin in the gas phase molecules. For the embedded toluene, the frequency is set to the ZPL corresponding to the band origin. As an example we present the raw photoelectron images for aniline in Figure 4.6.

Already the visual inspection of these raw images yields several important conclusions. The rings in images correspond to the vibrational energy levels of the aniline ion. They are sharp and well distinguished in the photoelectron images of free aniline molecules and are smeared but still recognizable in the helium droplet images. The angular distribution of photoelectrons is practically

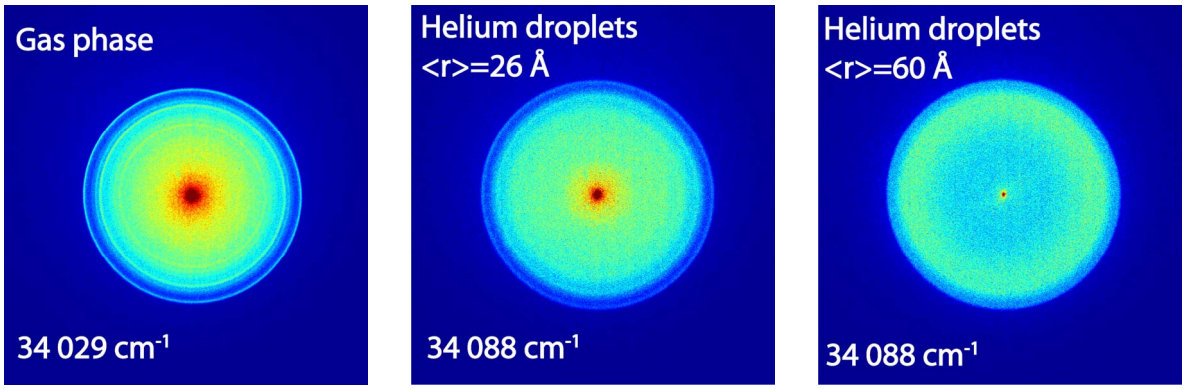

Figure 4.6 (color): Photoelectron images recorded by 1+1 REMPI of aniline in the gas phase and in helium droplets via band origin of the $S_1 \leftarrow S_0$ transition. The frequency of the photon and the mean droplet size are indicated on the images. The images show the central part of 680x710 pixels of the full frame consisting of 1000x1000 pixels. Images are normalized to the total number of counts within each image and have the same color scale in order to emphasize the features in the helium droplet images at <r> = 60 Å. The red color corresponds to the highest number of counts.

anisotropic in the gas phase, implying that several rotational states are probed. The helium droplet images do not demonstrate any angular anisotropy either. This makes it impossible to investigate the dynamics of the photoelectron escape from helium droplets with such a straightforward parameter as the angular distribution that proved to be very fruitful in the study of molecular dissociation in nanodroplets carried out previously in our laboratory[82]. Another interesting observation from the raw images is the strong signal depletion in the central part of helium droplets images, at which slow photoelectrons are projected. We neglect the very slow photoelectrons visible as the very small red spot (saturated in the left and the middle images) in the center of the images for the rest of our discussion. The feature seems to be droplet size dependent because at the large mean droplet sizes, slow electrons are remarkably absent. At the same time, in the images recorded with small droplets, the intensity of slow photoelectrons is comparable to the gas phase. The origin of this phenomenon will be specially considered in section 4.1.2.2 below.

The radii squared of rings correspond to the energy of photoelectrons. It is clearly visible that in helium droplet images the outer radii, corresponding to the most energetic photoelectrons, are larger than those in the gas phase image. This might originate from two factors: a) simply due to the higher energy of photons in 1+1 REMPI, 34 088 cm^{-1} versus 34 029 cm^{-1}, and b) due to the lowering of the ionization threshold in helium droplets. To disentangle these two possibilities it is necessary to know the intermediate energy level in helium droplets from which the ionization takes place.

4.1.2.1 Vibrational relaxation timescale

The excitation spectra of molecules in helium droplets revealed that the intermediate levels are affected by helium environment: the lines in $S_1 \leftarrow S_0$ transition of molecules in helium droplets are blue-shifted and broadened due to the helium excitations. Evidence of vibrational relaxation was obtained from the excitation spectrum of toluene in helium droplets, see section 4.1.1.4.

In order to determined the origin of the shift in the ionization threshold it is necessary to know the energy of the intermediate level from which the ionization takes place. It is therefore important to determine whether complete relaxation of helium and molecular excitation is complete within the laser pulse.

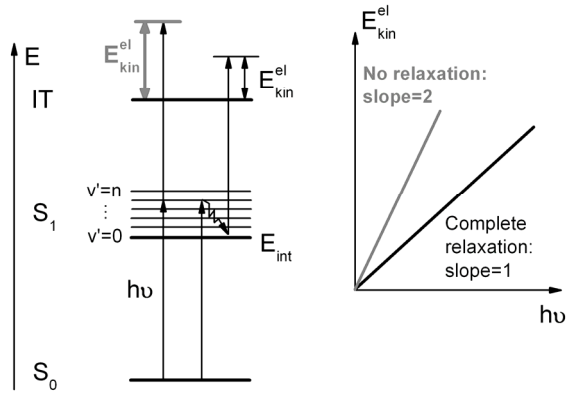

Figure 4.7: Scheme illustrating the influence of vibrational relaxation in the S_1 excited state of molecules embedded in helium droplets on the dependence of the photoelectron kinetic energy on the excitation frequency.

It can be determined by varying the photon energy in the one-color two-photon ionization experiment and monitoring the energy of photoelectrons, see Figure 4.7. If there is no relaxation at all during the time between the excitation and the ionization, then the kinetic energy of photoelectron will depend on the total energy of both the excitation and the ionization photon. In this case, the kinetic energy E_{kin}^{el} of photoelectrons has linear dependence versus the photon energy. The slope equals to two and the energy is written as:

4.6 $$E_{kin}^{el} = 2h\nu - \mathrm{IT} - E_{ion}$$

where E_{ion} stands for the internal energy of the ion, IT is the ionization threshold of the species. On the other hand, if the relaxation relaxes completely to some lower lying state within a time shorter than the duration of the laser pulse, the kinetic energy of the photoelectrons will be independent of the photon energy in the excitation step and only dependent on the energy of the ionization photon. In this case, see Figure 4.7, the photoelectron energy will have linear dependence versus the photon energy with unity slope:

4.7 $$E_{kin}^{el} = h\nu - \left(\mathrm{IT}\text{-}E_{\mathrm{int}}\right) - E_{ion}$$

where E_{int} is the energy of the state to which the system relaxes. We proceed now to the analysis of the photoelectron kinetic energy distribution to verify whether relaxation is coplete on the time scale of the laser pulse.

The electron energy distributions derived from the photoelectron images are presented in Figure 4.8. To minimize the background, a two-color scheme was used to record the photoelectron spectra of phenol and toluene. The upper graphs of Figure 4.8 show the photoelectron spectra of gas phase molecules obtained by ionizing the molecules via the band origins of the $S_1 \leftarrow S_0$ transition. The spectra show several peaks that can be correlated to various vibrational levels in the ions, see for details the references for aniline[166], phenol[167] and toluene[89]. The peaks at the highest kinetic energy, corresponding to the vibrational ground state of ions, can be used to determine the ionization potentials with expression 4.6, see Table 20. The values found agree within the absolute uncertainty of 120 cm^{-1} with the literature values.

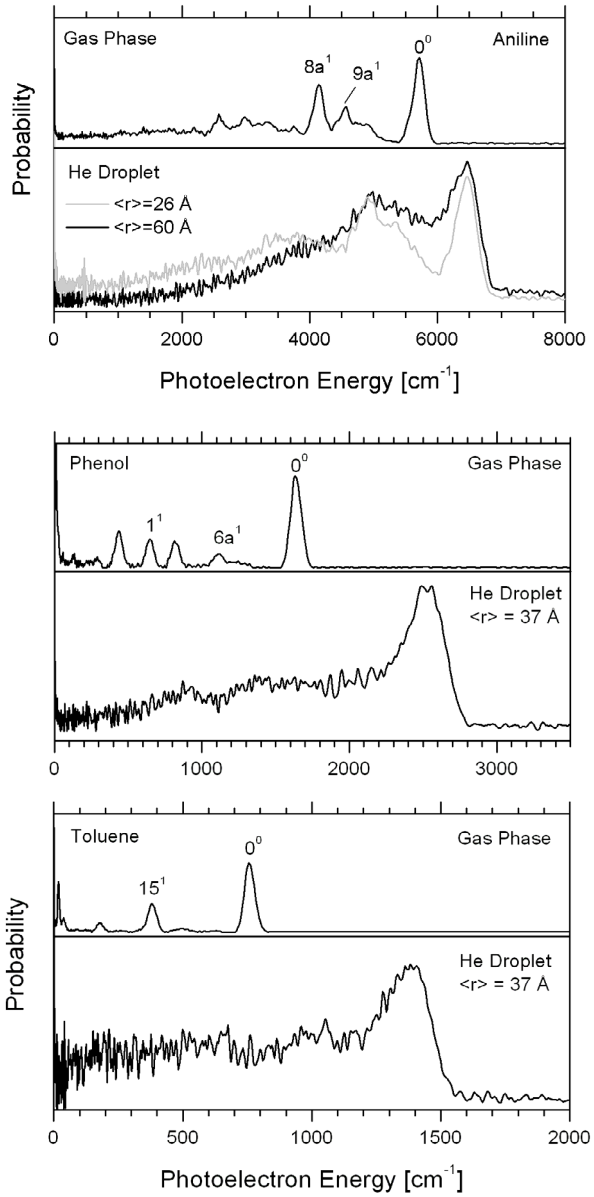

Figure 4.8: One-color (top) and two-color (middle and bottom) photoelectron spectra of aromatic molecules in the gas phase (upper graph) and in helium nanodroplets (lower graphs) recorded by resonance-enhanced multiphoton ionization via the band origin of the $S_1 \leftarrow S_0$ transition.

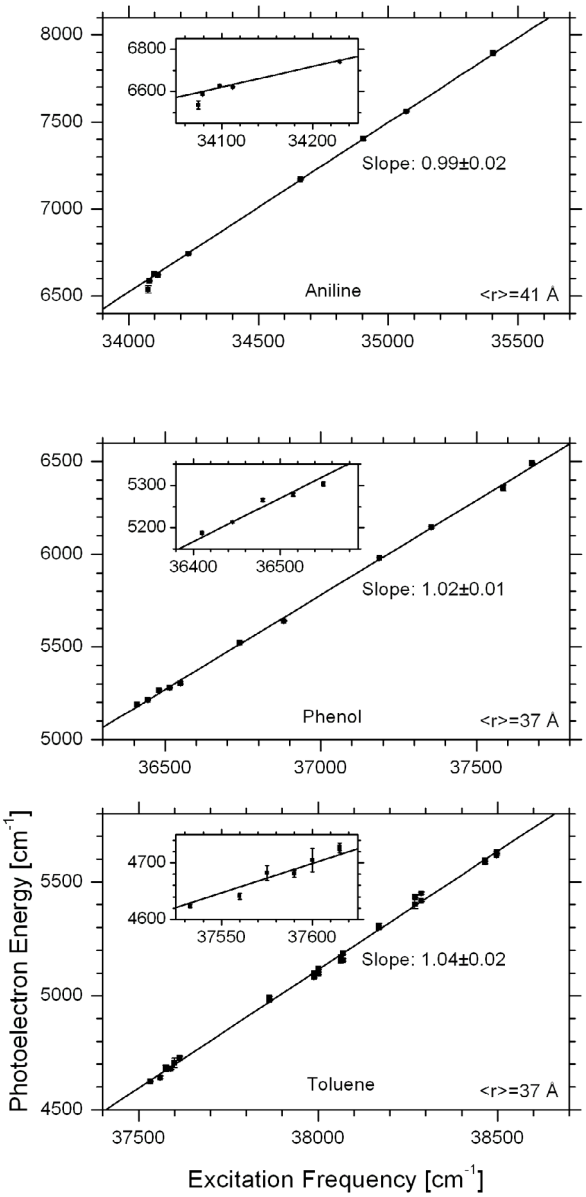

Figure 4.9: Positions of the photoelectron peak, which corresponds to the ground vibrational state of the ion, obtained from fitting the peak to the expression 4.8 as a function of the laser frequency. The points at high frequencies correspond to excitations of vibrational states in the S_1 states of molecules. The regions of low excitation frequencies are enlarged in the insets. They correspond to excitations in the zero-phonon lines and to excitations at different positions within the phonon wings. The straight lines are linear fits to the data points.

Table 20 Ionization potentials of aromatic molecules in the gas phase

Molecule	Gas phase IP from PES, this work [cm^{-1}]	Gas phase IP from ZEKE, previous measurements [cm^{-1}]
Aniline	62 335 ± 120	62 271 ± 2 *
Phenol	68 682 ± 120	68 623 ± 4 **
Toluene	71 495 ± 120	71 344 ± 24 ***
* Ref[168] ** Ref[169] *** Ref[170]. PES measurements.		

The lower panels in Figure 4.8 show the photoelectron spectra of molecules dissolved in helium droplets. These spectra are obtained for aniline and phenol by ionizing species via the maxima of the phonon wings, which are blue shifted by several tens of cm^{-1} from the ZPLs, corresponding to the band origins of the $S_1 \leftarrow S_0$ transition. For toluene, the ionization was via the ZPL of the band origin, since it is the strongest transition. The first point to note in photoelectron spectra of embedded molecules is that the onsets are shifted by about 800 cm^{-1} to higher energies with respect to the gas phase. Otherwise, the droplet spectra resemble largely those of gas phase molecules. However, there are some subtle differences. Upon closer inspection, the high kinetic energy peaks appear to be asymmetrically broadened, especially for the larger droplets, see Figure 4.8 for aniline. The shift of the photoelectron spectrum to higher energies can be attributed to a lowering of the molecular ionization threshold in helium droplets with respect to the gas phase. In order to determine the actual shift of this threshold it is important to know whether relaxation of the helium excitations occurs on the time scale of the laser pulse.

To address this issue and that of the relaxation of molecular vibrations, photoelectron spectra were recorded at frequencies corresponding to the zero-phonon line, several positions in the phonon wing of the band origin and to various vibrational excitations in the S_1 state. Every photoelectron peak at the highest energy was fitted to an empirical function which is the convolution of exponential, $\exp(E/b)$, and Gaussian functions, $\exp(-(E-E_0)^2/d^2)$:

4.8
$$I(E) = A\frac{\sqrt{\pi}}{2} d \exp\left(\frac{E-E_0}{b} + \left(\frac{d}{2b}\right)^2\right)\left(1 - \mathrm{erf}\left(\frac{E-E_0}{d} + \frac{d}{2b}\right)\right)$$

where I is the intensity at photoelectron energy E, A is the amplitude, E_0 and d stand for the centre and the width of the Gaussian peak and b is the exponential constant. The empirical function fits very well the photoelectron peaks, see as an example Figure 4.14. Figure 4.9 shows the value of the E_0 parameter as a function of the laser frequency. The linear fits to the data points with practically unity slopes imply that complete relaxation of molecular vibrations and helium excitations occurs before ionization with the second photon during the 11 ns laser pulse.

The nanosecond time scale of the vibrational relaxation of aromatic molecules in our experiments should be considered as the upper limit of the relaxation time. The lower limit of the order of 10 ps was previously estimated from the line broadening of ZPLs in different vibrational transitions of the $S_1 \leftarrow S_0$ excitation of toluene. Our findings are in accord with other works[79, 81, 158, 171, 172]. However, in our experiments it is not possible to clarify the relaxation mechanism. To elucidate further the nature of vibrational relaxation in the S_1 state a dedicated time-resolved

photoelectron spectroscopy will be useful to map out the relaxation path along the energy levels of the "dopant-helium droplet" system.

4.1.2.2 Depletion of low energy electrons in photoelectron spectra

In this sub-section we will discuss possible origins of the depletion of the low energy electron signal in the photoelectron spectra of aniline, see raw photoelectron images in Figure 4.6, and the resulting photoelectron spectra in Figure 4.8. Already in the raw images, one can see that there is a prominent depletion of slow electronss manifested as a drop in intensity in the central region of the photoelectron image, of aniline in large droplets. The effect seems to be dependent on droplet size: at smaller droplet sizes, there is more signal in the centre of the image, showing a weaker depletion of low energy photoelectrons. The very small intense spot in the centre of the images represents very slow electrons with the kinetic energy of less than 10 cm^{-1}. These ultra-slow electrons show up both in photoelectron images of aniline in the gas phase and helium droplets, thus they may originate both from the thermalization of fast electrons during their escape from helium droplets or directly from the creation of highly vibrationally excited aniline ions in the gas phase or in droplets. Previously, Neumark and coworkers[173, 174] observed similar ultra-slow electrons in the photoionization of pure droplets and assigned them to the thermalization of the created photoelectrons inside the nanoclusters.

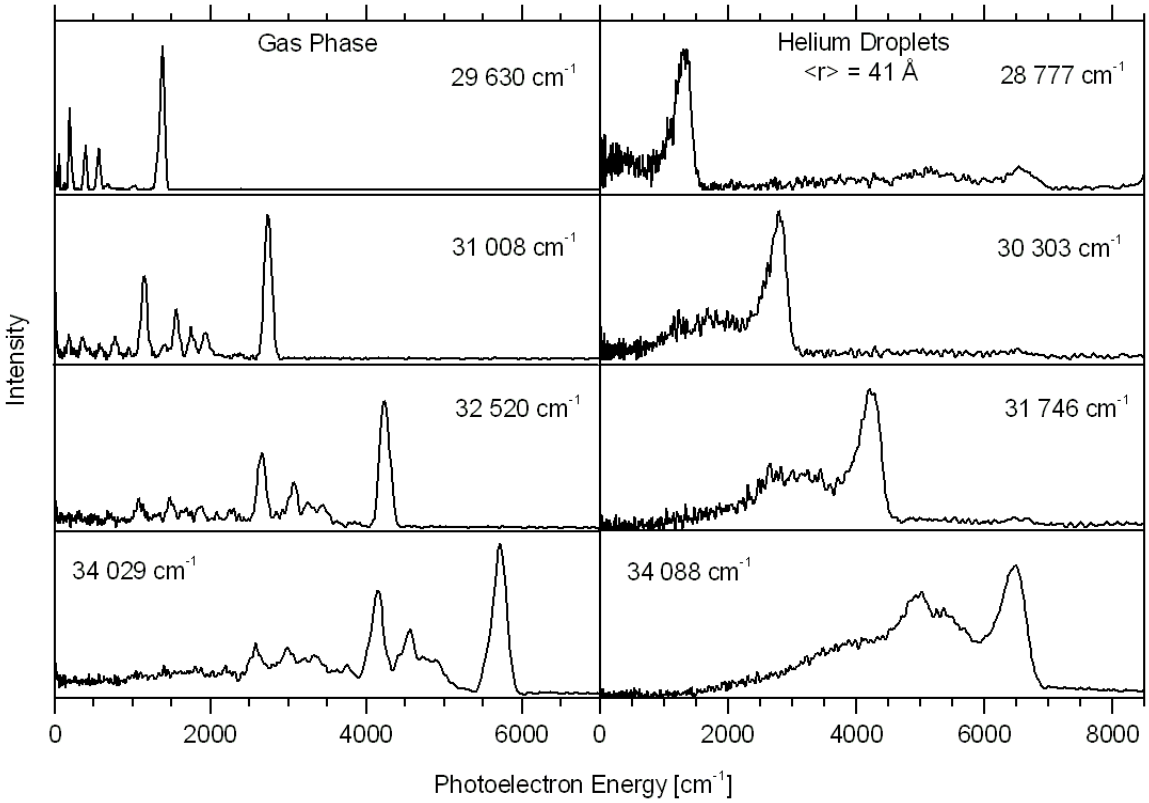

Figure 4.10: Photoelectron spectra of aniline in the gas-phase (left) and embedded in helium droplets (right) recorded in 1+1' (upper three) and 1+1 (bottom) REMPI. The numbers in graphs indicate the energy of the ionization photons.

In the photoelectron spectra of aniline in helium droplets, see Figure 4.8, derived from the raw images, the depletion of slow electrons manifests as the onset of signal at approximately 1 200 cm^{-1} of kinetic energy. This onset is most pronounced at the largest droplets and disappears at small cluster sizes. The explanations of the observed effects cannot be exclusively attributed to the thermalization of photoelectrons in the helium droplet. Two-color experiments allowed to vary the energy of created photoelectrons in a large energy range, 700-7000 cm^{-1}, and slow electrons with E_{kin}<1000 cm^{-1} were readily detected, see Figure 4.10. An alternative explanation to electron thermalization in the droplet may be related to the inter-system crossing (ISC) in aniline between singlet S_1 and triplet T_1 states.

The general idea of the ISC is the following[175]. Molecular states, which are usually considered in theory of molecular spectroscopy, like the S_1 state, are eigenstates of the zero-order Hamiltonian discarding spin-orbit coupling and result from the Born-Oppenheimer approximation. There are two main advantages of using the zero-order states: a) their energies are easily determined by simple formulae with a limited number of parameters and thus can be calculated with the analytical or numerical tools of quantum chemistry; b) the selection rules are rigorous in the zero-order approximation. The zero-order approximation also implies that there is no interaction between vibrational states from different electronic energy potentials. In reality, the Born-Oppenheimer approximation is not fulfilled and electronic states do interact (curve crossing), so the exact stationary states are superpositions of the zero-order states. If several stationary states are created in the optically allowed transitions, the interference between these states will evolve in time. This time evolution is observed as relaxation in terms of zero-order states.

In the case of aniline, the optically accessed singlet S_1 state is "immersed" in a bath of vibrational states from lower triplet states[176] to which transitions are forbidden according to selection rules, see the left panel in Figure 4.11. During the time between excitation and ionization, the energy is transferred to high vibrational states of low-lying triplet states. The photoionization from

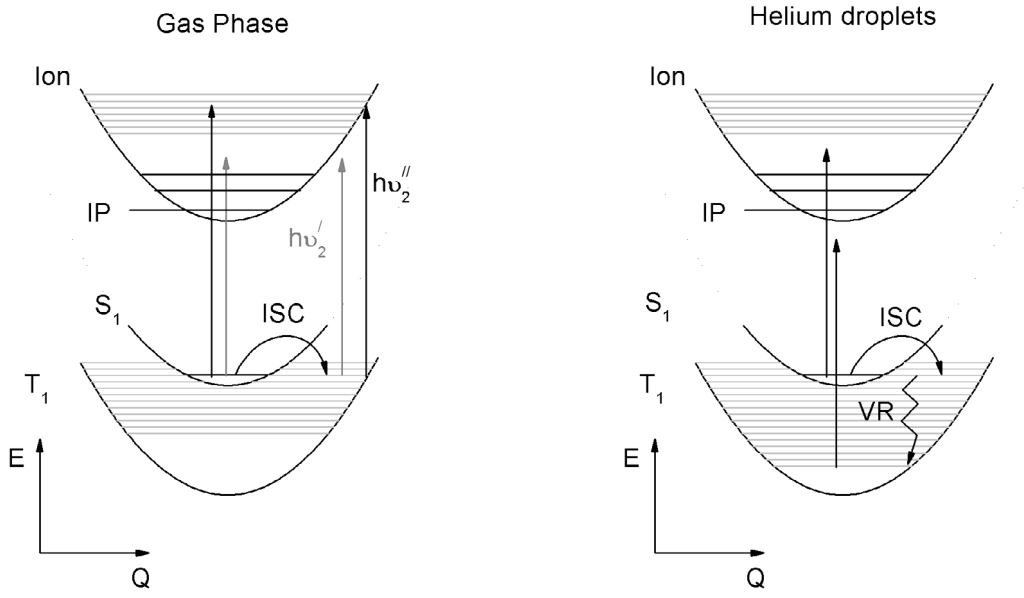

Figure 4.11: Scheme of the inter-system crossing (ISC) that may explain the photoelectron spectra of aniline in the gas-phase (left) and embedded in helium droplets (right) with vibrational relaxation (VR). Here the Q represents a generalized coordinate.

these states will differ from that of the S_1 state in view of different Franck-Condon factors and higher density of vibrational states. For instance, see the left panel in Figure 4.11, the photoionization from the ground vibrational level in the S_1 electronic state will produce a photoelectron spectrum with a well-resolved structure corresponding to low vibrational levels of the ion owing to favorable Franck-Condon factors. In contrast, the ionization from vibrational levels of the triplet state will create highly vibrationally excited ions, giving rise to a dense photoelectron spectrum. If the energy of the ionization photon is not large enough (gray arrows in the left panel of Figure 4.11) then the ionization from the triplet levels will be not as efficient as from the singlet state due to unfavorable Franck-Condon factors. In this case, the dense part of the photoelectron spectrum will be almost absent and the sparse peaks will represent the ionization from the S_1 state to low well-separated ionic vibrational levels. The described processes was experimentally observed in the time-resolve photoelectron spectroscopy of gas phase aniline[177] and occurred on a nanosecond time scale. Our two-color photoelectron spectra of aniline are in line with the above interpretation, see left graphs in Figure 4.10. The spectra demonstrate well-resolved peaks without structureless background at ionization frequencies below ≈ 32 000 cm^{-1}.

Let us consider aniline in helium droplets. The high vibrational levels in the triplet state will be efficiently relaxed by the helium environment on a sub-nanoseconds time scale, so the photon energy will be not sufficient to ionize aniline from the low vibrational level in the T_1 state, see the right panel in Figure 4.11. In the two-color scheme, using less energetic ionization photons, aniline will be ionized to low ionic vibrational levels from the ground vibrational level in the S_1 state similar to the gas phase situation in the left panel of Figure 4.11. Indeed, the experimental results are in line with this hypothesis, see the right graphs in Figure 4.10. In the two-color scheme the low energy part of photoelectron spectrum reappears when the ionization frequency is below ≈ 31 000 cm^{-1}, which corresponds to the gas phase by taking into account the lowering of the ionization threshold.

An interesting issue is the pronounced droplet size dependence as can be seen in Figure 4.8. Here, the low energy background is present at small droplets with <r> = 26 Å. It looks like the relaxation efficiency depends on droplet size and at small droplets it is not complete. Thus the molecule is ionized from high vibrational levels of the triplet state. The crude estimation of this effect given below show that it is not unfeasable. First, the T_1 electronic state of aniline[177] lies ≈ 10 000 cm^{-1} below the S_1. Second, the release of this energy into the droplet will result in the evaporation of ≈ 2 000 helium atoms, assuming that the evaporation of single helium atom from the droplet's surface costs 5 cm^{-1}[37]. The number of evaporated He atoms found corresponds well to the mean droplet size in the experiment.

4.2 Ionization dynamics of aromatic molecules in helium droplets

4.2.1 ZEKE spectrum of aniline embedded in helium droplets

Having established the important aspects of the dynamics in the intermediate states, we can return to the ionization dynamics and analyze the shape of the highest energy photoelectron peak. The choice of this peak is related to its isolation from other photoelectron peaks, so its shape is the least affected by overlap with adjacent peaks. The changes induced by the helium droplets on the shape of a single photoelectron peak are assumed to consist of two contributions:

- the kinetic energy relaxation of the photoelectrons due to scattering off helium atoms during the escape process. This modifies the original shape of the photoelectron peak as it broadens and shifts to lower energies

- phonon wings, which are caused by the excitation of helium environment. They result from the rearrangement of helium atoms around the created ions (snowball formation) and from the change in the molecular geometry between the S_1 state and the ionic state

The electron-helium scattering effects should dependent on droplet size. Taking the helium droplet as a dense gas and assuming that binary elastic collision formalism is valid, the relative energy loss will depend on the traveled through the helium distance. It is expected that the PW related to the helium rearrangement is independent on the droplet size and internal vibrations of the molecular ion, since it should affect mainly the first solvation shells of the dopant in the helium droplet. The sizes of these solvation shells are expected to contain no more than several tens of helium atoms. Therefore, the size of a solvated neutral or ionic dopant should be much smaller than the typical size of helium clusters in our experiments having $\langle N_{He} \rangle \approx 10^3$. The interaction of the neutral or ionic dopant with the rest of helium atoms is expected to be much smaller than that with the helium atoms in the solvation shells. Thus, the rearrangement in the solvation shells should not influence much the whole droplet.

In order to separate in the photoelectron spectrum the effect of kinetic energy relaxation from the phonon wing due to helium excitation we need to know the shape of "pure" photoionization transition. A possible way to measure the "pure" shape of the ionization transition is to use the ZEKE spectroscopy. A deviation of the photoelectron peak from the ZEKE lineshape would indicate that relaxation of the electron's energy during the escape from the droplet occurs. However, the difference between the ZEKE and PE peak must considered with care, since the intensities in the ZEKE spectrum can be affected by the dynamics of high Rydberg states[102].

The relationship between ZEKE and photoelectron spectra is illustrated in Figure 4.12 and Figure 4.13. Here again, we employ the concepts of the configuration coordinate model, see section 4.1.1.3, to explain the shape of the photoionization transition of aniline in helium droplets. The first figure

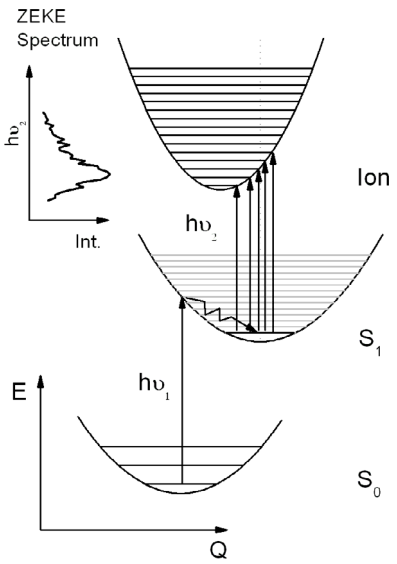

Figure 4.12: Scheme that illustrates the nature of lineshape in the two-color ZEKE spectrum of aniline in helium nanodroplets.

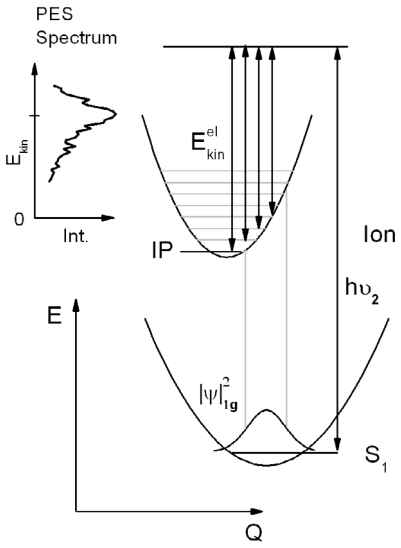

Figure 4.13: Scheme that illustrates the nature of photoelectron peak shape obtained by 1+1 REMPI via S_1 state of aniline in helium nanodroplets.

illustrates the principle of the two-color scheme used, when the frequency of the first photon is fixed and the frequency of the second photon is scanned over the ionization transition. Whenever the photon matches the ionization threshold associated with a particular ionic level, the created high Rydberg states are ionized with a delayed pulse field. Figure 4.13 focuses only on the second, ionization, step in photoelectron spectroscopy in order to emphasize the shaping of the photoelectron kinetic energy distribution by Franck-Condon factors. Here the second photon has a fixed energy above the ionization thresholds of several ionic states. The transition takes place within the overlap of the ground state wavefunction and those of ionic energy levels. The kinetic energy of the photoelectron is simply determined by the energy balance:

4.9 $$E_{kin}^{el} = h\nu_2 - E_{ion} - E_{droplet}$$

where E_{ion} is the energy of an ionic state, $E_{droplet}$ is the energy that is deposited into the droplet by phonon excitation. E_{kin}^{el} is subsequently modified by electron scattering.

The ZEKE and high-resolution photoelectron spectra of aniline in the gas phase and in the helium droplets with <r> = 31 Å recorded by 1+1' REMPI are presented in Figure 4.14. The photoelectron and ZEKE spectra correspond to the ground vibrational state of the aniline ion. The lineshapes in the helium droplet spectra are thought to consist of the analog of ZPL with the high-frequency tail in the ZEKE spectrum corresponding to the PW. The geometry change between the S_1 and ionic states of aniline is rather small, since the bond lengths change by no more than 10%. There only a minor shortening of the C-N bond and small expansion of the aromatic ring, while the overall structure stays planar[168]. The width of the ZPL, which we tentatively relate to the effective Gaussian width $d \approx 90$ cm^{-1} in expression 4.8, is thought to originate from the wide distribution of

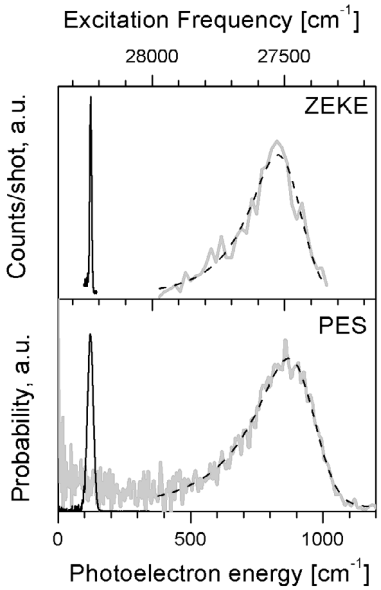

Figure 4.14: Comparison of the two-color photoelectron and ZEKE spectra of aniline in helium droplets with <r> = 31 Å recorded by 1+1' REMPI via the band origin of the $S_1 \leftarrow S_0$ transition. The frequency of the second photon in PES is 28 360 cm^{-1}. The ZEKE and PES spectra have the same energy scale. They are up lined in order to match the gas phase spectra that are seen as sharp peaks in the left part of the graphs. The dashed lines are fits to the function 4.8.

initial conditions like impurity location within the droplet. The strong PW is likely to originate from the enhanced impurity-helium interaction, for the ion creation entails a considerable increase of helium density around the positively charge aniline.

It should be noted that a very short lifetime of high Rydberg states of aniline-He_N around 300 ns was found in our experiments. The use of low pulsed electric field of ≈ 5 V/cm and long time-delay of ≈1 μs, which are our normal settings in ZEKE spectroscopy for ionization Na-doped droplets, were not possible due to the unpractical S/N ratio. A time delay of ≈ 150 ns and the field strength of 38 V/cm yielded the best signal, though the spectral resolution dropped from ≈ 8 cm^{-1} to ≈ 20 cm^{-1}. The elevated noise level still required 100 seconds integration time per data point to obtain the droplet ZEKE spectrum in Figure 4.14. For this reason, the ZEKE spectrum at the best quality was recorded only at the mean droplet size of <r>=31 Å, but spectra at other droplet sizes demonstrated similar shape, though their quality was not good enough to obtain a good fit to expression 4.8.

As can be seen in Figure 4.14, the photoelectron peak and the ZEKE spectrum have practically the same shapes. This implies that the effects of kinetic energy relaxation for photoelectrons with the energy of ≈ 850 cm^{-1} are rather weak for small droplets with <r> = 31 Å. The variation of shape of photoelectron peak with the mean droplet size and initial kinetic energy will provide valuable information on the droplet-induced loss in kinetic energy of photoelectrons. Before presenting the experimental data on this subject, we will discuss the difference in the ionization threshold of molecules in the gas phase and those embedded in helium nanoclusters.

4.2.2 Ionization threshold of aromatic molecules in helium nanodroplets

Although the fit of the highest kinetic energy photoelectron peak versus excitation frequency in section 4.1.2 yields directly the energy difference between the ionization threshold and the level the system has relaxed to, it does not provide the absolute energy of this level. If one assumes complete relaxation of the helium and molecule excitations then the energy of this level corresponds to the frequency of the zero-phonon line in the excitation spectrum. Taking this into account, we can write the equation for the vertical ionization threshold:

4.10 $$\mathrm{IT}\left(X - He_N\right) = E_{ZPL} + E_{ph} - E_{kin}^{el}$$

where X stands for the impurity molecule, E_{ZPL} is the energy of the zero-phonon line of the molecule in helium droplets, E_{ph} is the ionization photon energy and E_{kin}^{el} is the kinetic energy of photoelectron. In the gas phase experiments, the vertical ionization threshold is determined in the absence of relaxation as:

4.11 $$\mathrm{IT}(X) = h\nu_1 + h\nu_2 - E_{kin}^{el}$$

To minimize the influence of systematic errors caused by the calibration of our imaging setup we calculate the difference between ionization thresholds of molecules in helium droplets and in gas phase as:

4.12 $$\Delta\mathrm{IT} = \mathrm{IT}(X - He_N) - \mathrm{IT}(X)$$

The contribution of calibration errors is further reduced by using the same settings of imaging setup for photoelectron spectroscopy of both gas phase molecules and molecules embedded in helium droplets. This way, the errors are those of laser frequencies, which are much smaller than 1 cm^{-1}, and fitting errors, which arise in fitting the photoelectron peaks to the expression 4.8. The latter are usually several wavenumbers. This implies that the errors in the difference of ionization thresholds are smaller

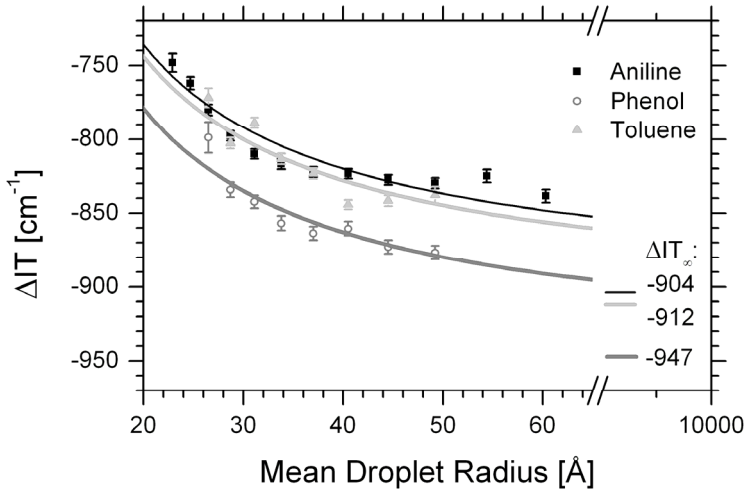

Figure 4.15: Difference between ionization thresholds of molecules in helium nanodroplets and in gas phase obtained by 1+1 REMPI PES via S_1 states. The solid lines represent fits to equation 4.13.

than the errors in the absolute values of these thresholds, which are typically 100 cm^{-1}. With the above mentioned procedure the differences in vertical ionization thresholds have been determined as function of droplet radius, see Figure 4.15.

4.2.2.1 The model

The observed trend can be understood with the simplest variant of the polarizable continuum model, where the ionic impurity resides exactly in the cluster centre and the ionization threshold is lowered due to the polarization of dielectric environment. With increasing of cluster size, the bulk limit is attained. Within this model, the vertical ionization threshold in clusters depends on the cluster radius *R* as:

4.13
$$\mathrm{IT}(R) = \mathrm{IT}_\infty - \frac{e^2\left(1-\varepsilon^{-1}\right)}{8\pi\varepsilon_0 R}$$

where IT_∞ is the ionization threshold in bulk helium, *e* is the electron charge, ε_0 is the permittivity of free space, and ε is the dielectric constant of the cluster [144]. To determine the ionization threshold of molecules in bulk helium, the observed thresholds were fitted to expression 4.13. The constant describing the *R* dependence was found for the aniline case to equal 3 050±350 cm^{-1}/Å, which is in a good agreement with the theoretical value of 3 361 cm^{-1}/Å. In the cases of phenol and toluene, this constant was fixed to the theoretical value because of the smaller range of droplet sizes used in the experiments. This led to much larger fitting errors of ≈ 1 000 cm^{-1}/Å of the extracted values around 3 000 cm^{-1}/Å which are still in good agreement with the theory. The bulk ionization thresholds IT_∞ are listed in Table 21.

We have tested a more realistic model that takes into account the effect of the off-center location of the ion on the polarization energy of the droplet from Lehmann[49]. He reported a new expression that includes the radial position of the ion in the droplet. However, we were not able to extract physically meaningful values of dopant location in the droplet from the fitting of our experimental data to Lehmann's formulae because of the relatively large errors on our data points.

The shift in ionization threshold can also be assessed by theoretical methods. Using the Gaussian software package[178] the ionization thresholds of gas phase and dissolved molecules have been calculated within the framework of the polarizable continuum model. Since for aniline and its cation B3LYP (Becke three-parameter Lee-Yang-Parr) density functional calculations are found to yield more accurate results than *ab initio* calculations at the MP2 (second-order Møller-Plesset) level of theory[88], the calculations have been performed using the former method. In a first step the geometries of aniline and its cation were optimized using the 6-311++*G(df; pd)* basis set. The ionization threshold, given by the difference in energy between the neutral and cation at their optimized geometries, is calculated to equal 60 765 cm^{-1}, a value somewhat smaller than found experimentally. Subsequently, the energies in the presence of the helium solvent were calculated using the polarizable continuum model. Comparison of the ionization threshold found in these calculations to those without helium solvent gives a shift of 993 cm^{-1} for the ionization threshold, which is close to the experimental value. Similar calculations were performed for phenol and toluene systems, see Table 21. These results show that the observed ionization thresholds can be readily related to the gas phase ionization potential by taking into account the polarization effects.

Table 21 Experimental and theoretical ionization thresholds

Molecule	IT_∞ experiment [cm^{-1}]	ΔIT experiment [cm^{-1}]	IT_∞ calculations [cm^{-1}]	ΔIT calculations [cm^{-1}]
Aniline	61 573 ± 20	-904 ± 3	59 772	-993
Phenol	67 640 ± 10	-947 ± 4	66 171	-1103
Toluene	70 391 ± 10	-912 ± 4	68 959	-937

4.2.3 Droplet size effects on photoelectron spectra

As it was already mentioned above, the peaks in the photoelectron spectrum are asymmetric, see Figure 4.8. They show a droplet size-dependent tail extending 100–300 cm^{-1} towards lower kinetic energies. Based on the rather small shifts of the ionization threshold with droplet size and on the already asymmetric shape of ZEKE spectrum of aniline-He_N in Figure 4.14, it can be ruled out that this asymmetry reflects, via the droplet size dependence of the ionization threshold, the rather wide cluster size distribution[84]. Since the ionization of the molecules results in a considerable rearrangement of the surrounding liquid ("snowball" formation[13]), the broadening of peaks in the photoelectron spectrum may be ascribed to excitations of helium giving rise to a phonon wing. This broadening is expected to be independent of droplet size and can therefore only be partially responsible for the observed peak shapes. To clarify the importance of elementary excitations in helium droplets, the two-color experiments are useful as they allow to control the energy of the second ionization photon and hence the kinetic energy of photoelectrons.

Following this approach, the photoelectron spectra of aniline and phenol were recorded at different energies of the ionization photon for a range of mean droplet sizes. The photoelectron peak related to the ground vibrational state of the ion was fitted to the expression 4.8.

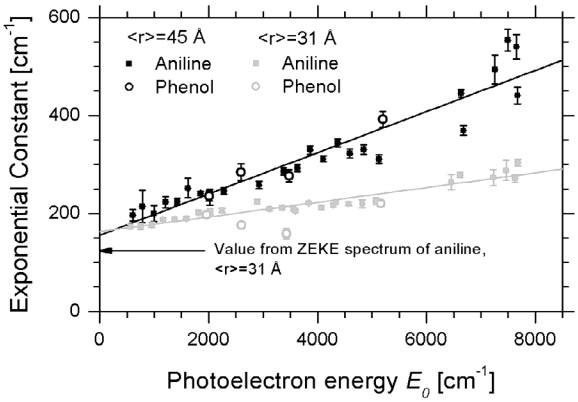

Figure 4.16: Variation of the exponential constant b of highest energy as function of the photoelectron kinetic energy E_0. Parameters are obtained by fitting the peak to expression 4.8. Photoelectron spectra are recorded by 1+1' REMPI of aniline and phenol in helium nanodroplets. The lines are linear fits to the aniline data points.

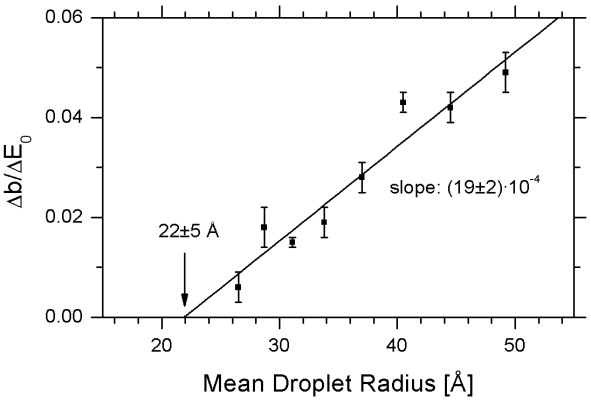

Figure 4.17: Slopes found from the linear fits of exponential constant b versus photoelectron kinetic energy E_0 obtained at fixed mean droplet size as illustrated in Figure 4.16.

The center of the peak, E_0 , was found to vary linearly with photon energy, having a slope of unity (not shown). The Gaussian width d did not change much with the mean droplet size and E_0, having values in the 100-120 cm^{-1} range for both molecules (not shown).

We will concentrate on the data for aniline as the data set for this molecule is the most complete. The exponential constant b is found to steadily increas with E_0 at fixed mean droplet size, see Figure 4.16. For droplets from a radius of <r> = 45 Å b increases up from $b \approx 200$ cm^{-1} at $E_0 \approx 700$ cm^{-1} to $b \approx 550$ cm^{-1} at $E_0 \approx 7\,000$ cm^{-1}, while for smaller droplet size <r> = 31 Å it increased only to $b \approx 300$ cm^{-1}. The variation of the exponential constant versus E_0 at each droplet size in the <r> = 27 - 50 Å range was fitted to a linear function. Extrapolated to zero photoelectron energy, we found an exponential constant $b \approx 160$ cm^{-1}, which is close to $b \approx 124$ cm^{-1} obtained from the ZEKE spectrum in Figure 4.14. The extracted slopes are plotted versus mean droplet radius in Figure 4.17. The data points in the figure can be readily fitted to linear function, the extrapolation of which to zero slope points to <r> = 22±5 Å.

The evolution of the exponential constant with mean droplet size at fixed value of E_0 is shown in Figure 4.18. The parameter increases with increasing droplet size. At high photoelectron kinetic energies the change in b is more pronounced: at $E_0 = 6\,600$ cm^{-1} it varies from $b \approx 220$ cm^{-1} for <r> = 27 Å to $b \approx 620$ cm^{-1} for <r> = 60 Å, while at $E_0 = 950$ cm^{-1} the variation is only in the range of ≈ 50 cm^{-1} and is pronounced only at <r> = 27 - 40 Å. In this range of droplet sizes, the data points can be well fitted to a linear function. The following extrapolations to the value of exponential constant found in ZEKE spectra of aniline show that the crossing points with the line of $b \approx 124$ cm^{-1} all fall within 4 Å from the previously found onset <r> = 22 Å. This value marks the droplet size when the shape of the ZEKE spectrum of aniline and the shape of the photoelectron peak are identical. The interpretation of the <r> ≈ 22 Å found with the two different approaches will be discussed below.

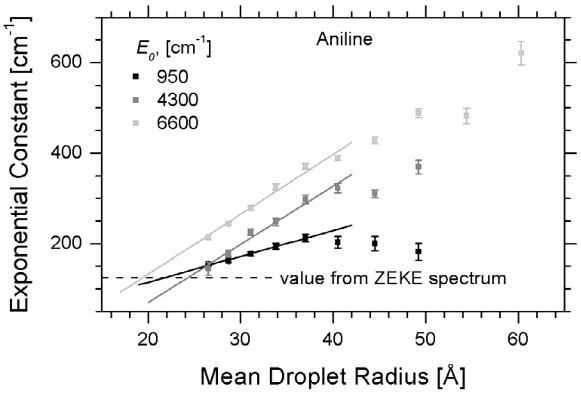

Figure 4.18: Change in the exponential constant as function of the mean droplet radius at three photoelectron energies E_0 indicated on the graph. The lines are linear fits to data points in the range of 25-41 Å.

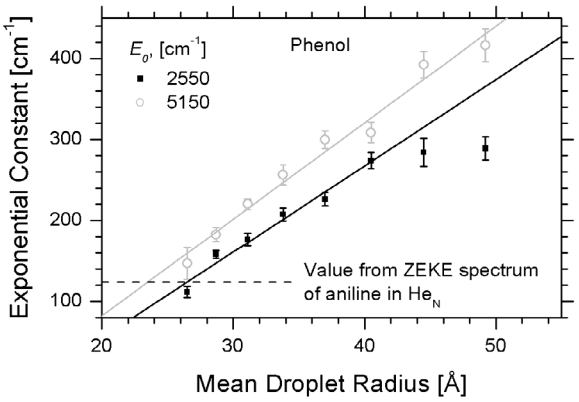

Figure 4.19: Change of the exponential constant as function of the mean droplet radius at two photoelectron energies E_0 indicated on the graph. The lines are linear fits to data points in the range of 25-41 Å for E_0=2 550 cm^{-1} and of 25-50 Å for E_0=5 150 cm^{-1}.

For checking the general character of the regular behavior of photoelectron peak shape found for aniline, two sets of measurements were performed for phenol, corresponding to E_0 = 5 150 cm^{-1} and E_0 = 2 550 cm^{-1} in the range of <r> = 27 - 50 Å of mean droplet size. The peak parameters in the photoelectron spectra of phenol in helium droplets demonstrated behavior that is similar to that in the aniline case, see Figure 4.19. There is a linear-like increase of the exponential constant b versus <r>: $\Delta b \approx 250$ cm^{-1} at E_0 = 5 150 cm^{-1} and $\Delta b \approx 150$ cm^{-1} at E_0 = 2 550 cm^{-1}, which corresponds well to the trends for the aniline in Figure 4.18. The extrapolation of linear fits of these two sets cross the $b \approx 124$ cm^{-1} obtained in the ZEKE spectrum of aniline within 5 Å from <r> ≈ 22 Å.

4.2.3.1 Discussion

The larger intensities in the lower energy part of the photoelectron peak, which are reflected by larger values of exponential constant b, may indicate droplet-induced kinetic energy loss of the photoelectrons during the escape process from the interior of the helium nanocluster. The probable nature of the relaxation may be the electron scattering off helium atoms. The found limit <r> ≈ 22 Å of the mean droplet size, where the shape of the aniline photoelectron peak ionization equals that of the corresponding ZEKE spectrum ("unperturbed" photoelectron peak shape), is in support of this hypothesis. The size effects on the shape of the photoelectron peak due to excitation of phonons, which are excited due to the helium rearrangement upon ionization, are unlikely. The reason is that the droplet radius of 22 Å is still large enough[32, 38, 39] for the nanocluster to possess the excitation spectrum of bulk liquid helium. On the other hand, given the neutral impurity radial distribution in the droplet with the maximum at $r_{imp}/R_{cluster} \approx 1/3$ [48], for a droplet with a radius of 22 Å the photoelectron will at least pass a distance of ≈15 Å through liquid helium. It is supposed that the droplet size effects due to collisional loss of photoelectron kinetic energy vanishes once the droplets radius approaches the limiting case, when the travelled distance is smaller than the mean free path of the electron in liquid helium. Taking into account the mean free path of electron in bulk liquid helium of ≈ 9 Å, see expression 4.15 below, this distance corresponds at least to two electron-helium collisions. In reality, one expects more collisions to happen due to pronounced side-scattering of the

electron in binary collisions with helium, so the travelled distance within the droplet should be larger than 15 Å. Furthermore, photoelectrons can travel in any other direction than the shortest to the surface, thus the range of travelled distance is between 15 and 29 Å. This should also increase the energy loss by collisions.

The contradiction between the limiting droplet sizes of <r> ≈ 22 Å found experimentally and the droplet size of <r> ≈ 12 Å that corresponds to a mean free path of ≈ 9 Å accepted above is not surprising. First, the limiting droplet size found depends on the ability to detect the energy loss of photoelectrons in our experimental setup. It is evident that an experiment will yield a larger droplet size, since the energy loss will be detectable starting from a certain threshold value. Second, it should be noted that the justification given above for the critical droplet size in the collisional loss of the electron kinetic energy depends on the actual mean free path and the nature of the collisional process. In this respect, the limiting droplet size found in our experiments would correspond to a mean free path of electron in a helium droplet of ≈ 29 Å. Therefore, we believe that the result found in our experiments on the reduction of the droplet size effects on the photoelectron peak broadening is in line with the hypothesis that the photoelectron peak broadening is due to the energy loss in electron-helium scattering and not due to the excitation of phonons. The remaining questions are the actual mean free path of the created electron in a helium droplet and the nature of the collisional process.

4.2.3.2 Monte-Carlo Simulation of the photoelectron energy loss by elastic binary collisions

We will present below a simulation of the loss in the kinetic energy of photoelectrons. Previous studies on the thermalization of hot quasi-free electrons indicated that the relaxation is mainly governed by elastic collisions between the electron and individual helium atoms[179, 180]. At first, it might not seem likely that elastic collisions can be responsible for an energy loss in the order of 100 cm^{-1} in view of the small amount of energy transferred in these encounters, the modest collisional cross section[181], and the limited size of the droplets. However, if one considers the presence of the ion and the fact that the electron scattering is to a large extent in the backward direction[181] it is not unfeasible to have an energy loss of this magnitude. In order to address this possibility more quantitatively, simulations were performed to estimate the resulting kinetic energy distribution of initially monoenergetic electrons escaping from nanodroplets.

The Monte-Carlo calculations were based on those in the previous study of molecular photodissociation in helium droplets carried out in our laboratory[82]. The use of Monte-Carlo method is required, since the individual photoionization events are characterized by a wide distribution of initial conditions. These conditions include most notably the droplet size and the 3D position of impurity inside the individual droplet. The size distribution of single-doped helium droplets is required, so the log-normal droplet size distribution was weighted by the pick-up probability that scales approximately as $N^{2/3}$[82]. The distribution of the initial position of the nascent electron inside a particular helium cluster of size N is taken to be isotropic and the same as the distribution of impurity molecule. The radial part of this distribution we describe with a Gaussian:

4.14
$$p(r/R) = \frac{1}{\sqrt{2\pi}w_r}\exp\left[-\frac{1}{2}\left(\frac{r/R - r_c}{w_r}\right)^2\right]$$

where R is the droplet radius as given by equation 1.3. The parameters r_c=0.48 and w_r=0.1 are the centre and the standard deviation of the distribution taken from modeling of CF_3I dissociation in He_N[82], both expressed as a fraction of the droplet radius R. The electrons are supposed to experience

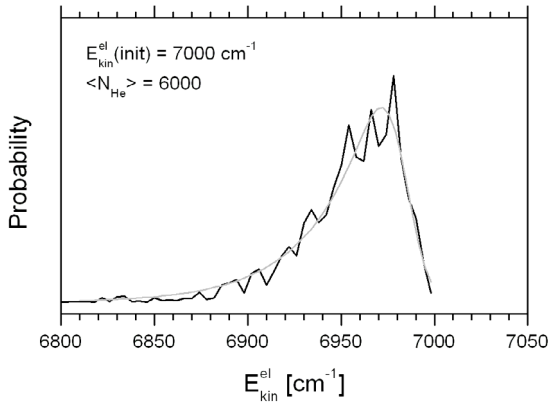

Figure 4.20: Simulated kinetic energy distribution of initially monoenergetic electrons with E_{kin}=7 000 cm^{-1} escaped from helium nanodroplets with <N_{He}> = 6 000. The gray line is the fit to expression 4.8.

elastic binary collisions with helium atoms with the differential cross-section[182] $d\sigma/d\Omega$, $d\Omega=\sin\theta d\theta d\varphi$. The randomly sampled angles θ and φ determine, via momentum and kinetic energy conservation laws, the loss of kinetic energy of the electron in the collision event. The traveled distance between collisions is fixed and is represented by the mean free path:

4.15 $$\lambda = \frac{1}{n_{bulk}\sigma} \approx 8.6 \text{ Å}$$

where σ = 5.3 Å^2 [182] is the integral cross-section taken at E_{kin}=5 eV, since it varies only slightly in the region 0-5 eV; n_{bulk}=0.022 Å^{-3} is the number density of bulk liquid helium. An individual trajectory calculation is terminated once the electron escapes into vacuum. In view of the small average number of collisions, which is of the order of 10-20, the electrons of energy ≈ 7 000 cm^{-1} never reach the translational temperature of 0.4K during the escape, when they may be considered as trapped. The result of 10^7 trajectories calculations is presented in Figure 4.20. The simulated kinetic energy distribution has an asymmetric shape with a FWHM ≈ 45 cm^{-1}. This is much narrower than the ZEKE spectra of aniline in helium droplets in Figure 4.14, and the shift of ≈ 30 cm^{-1} from the initial kinetic energy of 7 000 cm^{-1}. The peak profile can be fitted to expression 4.8 with the parameters listed in Table 22. The convolution of the ZEKE spectrum with the peak shape derived from the simulation, see the same table, shows that the broadening of the photoelectron kinetic energy distribution due to only elastic binary electron-helium collisions cannot reproduce the experimentally observed exponential constants.

A possible explanation of the discrepancies between the simulations and the experiment may be due to the underestimated mean free path. Partially it can originate from the assumption that the droplet's density equals to that of bulk liquid helium. However, Dalfovo[43] showed that there is an enhancement in the helium density by factor of 4 in the first solvation shell around the neutral impurity and by a factor of 1.5 in the second shell. This density increase in the very vicinity of the impurity might cause a "caging effect" by shortening the effective mean free path and thus "trapping" the nascent photoelectron for considerable time within the first two solvation shells due to the back-scattering. It is also possible that the assumption about binary electron-helium scattering is not valid and the electron interacts with more than one helium atom per collision. The consequence could result in a larger energy loss than in the binary collision. Further simulations, which will include the

influence of the ion field on the scattering cross-section, are required to clarify the nature of the loss of electron kinetic energy.

Table 22 Comparison of experimental and simulated photoelectron peak profiles

	Parameters derived from fitting of the photoelectron kinetic energy peaks to expression 4.8		
	E_0 [cm^{-1}]	d [cm^{-1}]	b [cm^{-1}]
simulations, initial E_{kin}=7 000 cm^{-1} <N> = 6 000	6 984±3	14±3	33±3
convolution of the simulated peak profile with that of the aniline ZEKE spectrum in He_N	27 481±1	101±1	128±1

4.2.4 The fate of aniline ion created in helium droplets

4.2.4.1 Ion ejection from helium cluster studied with velocity map imaging

To investigate the fate of the aniline ion created by 1+1 REMPI inside a helium droplet with <r> = 41 Å we have recorded velocity map ion images by detecting ions with mass corresponding to aniline, see Figure 4.21. The vertical streak in the image originates from the aniline molecules in the effusive beam coming from the doping chamber. To reduce the contribution of the effused feature the speed distribution was obtained only from the low part of the inverted image, see Figure 4.22. The resulting distribution can be readily fitted to Maxwell-Boltzmann distribution with T = 75±2 K which is shown in gray in the same figure. The use of droplets with the mean size <r> = 29 Å (<N_{He}> = 2150) yielded essentially the same result.

It is unlikely that the neutral aniline in the S_1 state is ejected during the relaxation of helium excitations. Even though the used 34 088 cm^{-1} excitation frequency is in the phonon wing, it is only 23 cm^{-1} above the ZPL level at 34 065 cm^{-1}. This small excess energy will be quickly dissipated, which will result in the evaporation of, at most, 5 He atoms. The ejection of vibrationally excited neutral aniline in the electronic T_1 triplet state, see section 4.1.2.2, is doubtful. Using equation 4.7 and assuming E_{ion}= 0, we get that at most ≈ 5 900 cm^{-1} energy could be released into the droplet during vibrational relaxation. This energy is the upper limit above which the ionization of free aniline is energetically impossible. The 5 900 cm^{-1} is equal to the evaporation of 1 180 He atoms, which is not enough to completely evaporate droplets with <r> = 41 Å (<N_{He}> ≈ 6 000) or <r> = 29 Å (<N_{He}> ≈ 2 200) used in the experiments.

A new process of ion ejection from helium clusters was recently discovered in the theoretical work of the group of Halberstadt[183]. They observed that during the relaxation of excited ionic Ne_n^+, n=4-6, in small N_{He}=100 helium clusters ejection of the ion from the cluster occurred. The individual helium atoms were ejected from the cluster during the relaxation process at kinetic energies up to several 10 cm^{-1}. The found speed distribution of ejected helium atoms consisted of two exponential (Boltzmann-type) distributions with the characteristic energies of 3-7 cm^{-1} and 28-45 cm^{-1}. Converting the effective temperature extracted from our experimental speed distribution to the average kinetic energy, we find the <E_{kin}> ≈ 50 cm^{-1}. This value correlates well to the energy of fast helium atoms in the modeling of Halberstadt. Thus, we speculate that the observed aniline ions might be ejected from the helium droplet with the flow of fast helium atoms during an explosion-like process.

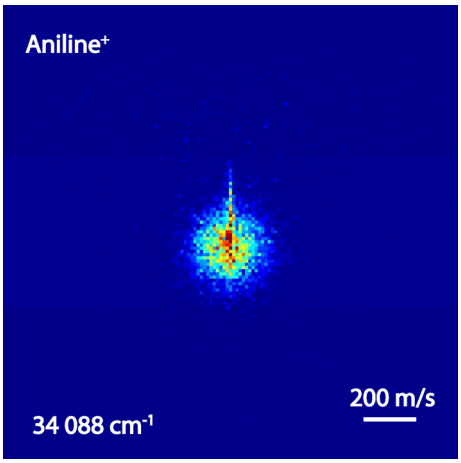

Figure 4.21 (color): Velocity map ion image recorded by 1+1 REMPI of aniline in helium droplets via the band origin of the $S_1 \leftarrow S_0$ transition. The photon frequency is 34 088 cm^{-1}. The image shows the central part of 140x140 pixels of the full frame consisting of 1000x1000 pixels. The image is normalized by the maximum number of counts per pixel. The vertical streak originates from the gas phase molecules effused from the doping chamber.

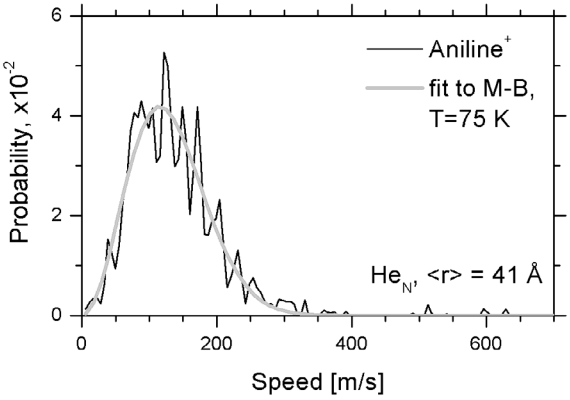

Figure 4.22: Speed distribution of the aniline ions ejected from helium droplets derived from Figure 4.21. The gray line is the fit to the Maxwell-Boltzmann distribution.

4.2.4.2 TOF mass-spectrum

Apart from being ejected from the droplet, the aniline ion may be solvated inside the helium nanodroplet. To verify this the TOF mass spectrum of aniline-doped droplets was recorded by 1+1 REMPI at parameters of the cluster source corresponding to the production of droplets with the $\langle N_{He} \rangle$ = 6 080, see Figure 4.23. It should be noted that the geometry of our ion imaging setup does not allow

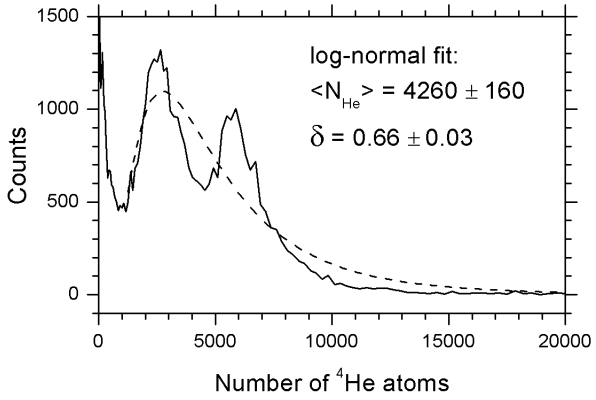

Figure 4.23: Time-of-flight mass spectrum recorded following 1+1 REMPI at 34 088 cm^{-1} of aniline in helium droplets with $\langle N_{He} \rangle$=6080 ($\langle r \rangle$= 41 Å). The fragment's mass is converted into the number of helium atoms. The dashed line is the fit of the mass spectrum to a log-normal distribution in expression 2.1.

the detection of masses heavier than ≈ $5 \cdot 10^4$ amu, thus the droplet distribution is detected only partially. In addition, little is known about the detection efficiency of the MCPs at such high masses. However, the obtained spectrum reveals the presence of heavy mass fragments that can be attributed to the helium nanodroplets containing the positive ion. The mass-spectrum consists of two prominent peaks, the positions of which change consistently with the variation of mean droplet sizes, so the non-uniform surface sensitivity of the MCP detector is likely not the reason of the observed structure. The fit of the overall mass spectrum, converted to the number of helium atoms in the fragment, to the log-normal distribution is shown by dashed line in Figure 4.23. The extracted parameters are in reasonable agreement with those found in other experiments[84].

4.3 Conclusion

The results on the photoexcitation and photoionization dynamics of helium droplets doped with aromatic molecules (aniline, phenol and toluene) studied with photoelectron spectroscopy can be summarized in two parts.

The first concerns the photoionization of embedded molecules. We have shown that the molecules inside helium droplets can be readily photoionized. The photoelectron spectra of embedded molecules resemble those in the gas phase. The influence of the helium droplet on the photoionization process is manifested as a lowering and broadening of the molecular ionization threshold. The lowering of the threshold can be ascribed to the polarization of the helium environment in the field of the created ion. It is around 800 cm^{-1} and can be readily described within the polarizable continuum model. The broadening is thought to stem from the excitation of helium environment due to the rearrangement of the solvation structure of the embedded molecule upon ionization. The observed relaxation of the kinetic energy of the photoelectrons is attributed to scattering off helium atoms during their passage into vacuum. The nature of the collisional process is, however, not clear. Monte-Carlo simulations of the escape process of electrons from a helium droplet, assuming elastic electron-helium collisions, were not able to reproducethe the kinetic energy loss found experimentally. The fate of the created molecular ion was also studied. It was found that the ion either remains solvated inside or is ejected from the droplet. The size distribution of helium droplets with a solvated molecular ion recorded experimentally is in a good agreement with the cluster size distribution predicted for our nanodroplet source. The kinetic energy distribution of the ejected ions corresponds well to the theoretical work of Bonhomeau *et al.*[183] on the ionization of small Ne clusters in helium droplets in which they found an explosion-like ejection of ions from the droplets.

The second part of our results concerns the dynamics related to the intermediate excited electronic state of embedded molecules. The excitation spectra of molecules inside helium droplets are shifted to higher frequencies with respect to the gas phase. The shift can be explained as the interplay between the solvation energies in the ground state and electronic excited state. A rovibration transition in the spectrum consists of a zero phonon line (ZPL), which relates to a pure electronic excitation of the molecule, and a phonon wing (PW), which relates to the simultaneous excitation of the helium environment[64]. The relative intensitiy between ZPL and PW in the spectra of embedded molecules depends on the molecule studied. The difference can be qualitatively explained within the configuration coordinate model describing the molecule-droplet interaction. Within this model, the pronounced phonon wings observed in the spectrum of aniline are attributed to the large change in molecular geometry upon electronic excitation as this results in a large rearrangement of the helium around the solvated aniline. In contrast, the excitation spectrum of toluene in helium droplets does not manifest pronounced phonon wings as the result of the very small geometry change upon electronic excitation. The observed variaton in the internsities of ZPL and PW with the fluence of laser light

supports the proposed explanation. Based on the line broadening of the ZPLs in the spectrum of embedded toluene we estimated the lower limit of the relaxation of vibrationally excited molecules to be of the order of 10 ps. Using photoelectron spectroscopy we found that the relaxation of vibrationally excited molecules in helium droplets is complete on the sub-nanosecond time scale. Inter-system crossing between the S_1 and the T_1 state of aniline, leading to the population of high vibrational levels in the T_1 state, is thought to be the cause of the observed abscence of low kinetic energy photoelectrons in the photoelectron spectra of aniline in helium droplets. Fast helium-induced vibrational relaxation in the T_1 state of aniline in droplets inhibits photoionization of these molecules. Comparison of gas phase and droplet photoelectron spectra of aniline recorded at different energies of the ioinization photon supports this explanation. These results clearly demonstrated that the photoionization of molecules in helium droplets via intermediate electronic excited states can be affected by helium-induced dynamics in these intermediate states.

Chapter 5 : Summary and Outlook

5.1 Summary

We studied the photoexcitation and photoionization dynamics of Na-doped and aromatic (aniline, phenol, toluene) molecule-doped helium nanodroplets with estimated mean sizes in the range of ≈ 2 000 - 20 000 atoms. The first system represented the case of surface-doped nanoclusters and processes taking place in the surface region of the droplets. The second system was an example of molecules embedded in the droplet's interior and processes occurring in the interior of nanodroplets.

For the first time the full electronic excitation spectrum of Na-He_N was measured by detecting the desorbed excited Na atoms and $NaHe_n$, n=1-4, exciplexes. The features observed in the spectrum correlated to transitions of free sodium atom, which were all broadened and shifted due to the perturbation by helium droplets. In order to assess the desorption dynamics of Na atoms and exciplexes the 3D speed and angular distributions of desorbed products were recorded using a velocity ion imaging setup. In addition, the internal energy states of desorbed species were probed with photoelectron imaging and ZEKE techniques. Relative abundances of products were obtained by time-of-flight mass spectra. The revealed photoexcitation dynamics were correlated to the perturbed excited state of Na atoms to which they were excited on the droplet's surface.

The key results can be summarized as follows.

Low excited states (3p, 4s, 3d and 4p) of Na-He_N

1. Excitation spectra. All excitation spectra of Na-He_N were shifted and broadened with respect to the corresponding atomic transitions. The spectra were semi-quantitatively reproduced within the pair-wise additive model of Na-He_N interaction of Stienkemeier et al.[69] using the density profiles of Barranco et al.[110, 116] and NaHe pair potentials of Pascale[106, 119]. The droplet size dependences of excitation spectra were qualitatively reproduced as well.

2. Exciplex formation. The exciplex formation observed in our experiments was strongly dependent on the excited state of sodium. It could be partially explained by the static model of Reho *et al.*[74]. The droplet size effects and velocity distributions of desorbed exciplexes observed in the experiment were difficult to interpret with the static model. They indicated that exciplexes might be formed "directly" via the pick-up of helium atoms from the droplets surface by desorbing excited Na.

3. Energy state of desorbed species. The photoelectron spectroscopy of products created after the excitation of Na-He_N revealed the presence of excited Na atoms not only in the state to which they were initially excited on the droplet's surface, but also in the lower states. The photoelectron peak intensities in the recorded spectra were semi-quantitatively reproduced by assuming that lower states

were populated by radiative decay of instantaneously desorbed excited bare sodium atoms. This way, the photoelectron peak intensities mainly reflected the interplay between the radiative decay and photoionization rates of desorbed excited atomic sodium. Good correspondence of the calculated and experimental peak intensities indicated that the droplet-induced effects in the relaxation of excited Na were rather weak.

4. Speed and angular distributions of desorbed species. The velocity distributions of the excited Na atoms desorbed from the helium droplets were qualitatively analogous to the instantaneous photodissociation of a diatomic molecule, where the helium droplet acted as the counterpart of infinite mass without the internal energy. This was supported by following observations: a) the mean kinetic energy of recoiled Na scaled linearly with the energy of the photolysis photon, and b) the angular distributions of desorbed Na correlated within the model, which was used to calculate the excitation spectra, to those in the Π←Σ and Σ←Σ photodissociative transitions of diatomics. The deviations of the observed behavior in Na-He_N photodissociation from the assumed properties were: a) the non-complete transfer of available kinetic energy to the recoiled excited Na atom, and b) broad kinetic energy and angular distributions. From the revealed discrepancies between the suggested model and the experiment, it followed that the helium droplet did not act as rigid counterpart of excited Na in the dissociation event and that the energy transfer from the excited sodium to the droplet played an important role.

Higher excited states of Na-He_N

After the 4p excitation band, the experimental results became more complex. In contrast to the low excited states of sodium, the excitation spectra of Na-He_N, which corresponded to excited states higher than 5s, were not clearly separated. The photoelectron spectra revealed the presence of Na in the states that could not be populated by radiative decay of free excited Na atoms. The ion imaging of desorbed fragments did not demonstrate simple velocity distributions of desorbed species: a) two speed components were often present in the speed distribution of desorbed species; b) the mean kinetic energies of recoiled Na did not always scale linearly with the excitation energy; c) the angular distributions of desorbed species were often isotropic. The models, which explained the observed features in the low excited states, were in general less successful in explaining the features in high excited states. This complex picture was thought to arise from the higher density and curve crossing of electronic excited states of Na that were perturbed by the helium droplet.

Photoionization of Na-He_N

The photoionization of Na-doped helium droplets studied with photoelectron and ZEKE spectroscopy revealed that the ionization threshold of Na-He_N was broadened and shifted to low energies compared to the free sodium atoms. The shift depended on the mean droplet size, while the width of the threshold did not. The shape and the shift of the ionization threshold were semi-quantitatively reproduced within the pair-wise additive model of Na-He_N and Na^+-He_N interaction. The time-of-flight mass spectrum recorded after the direct photoionization of Na-He_N showed the solvation of Na^+ in the droplet. The ion yield excitation spectrum recorded in the region of the ionization threshold of Na-He_N indicated that the sodium ion core might be solvated inside the droplet after the excitation of Na-He_N to high Rydberg states with principle quantum number $n \approx 100$. This way, the weakly bound to Na^+-He_N electron would continue to orbit outside the helium droplet. The measured life time of Na-He_N in these high Rydberg states was in line with theoretical predictions of Ancilotto et al.[142].

Photoionization of helium droplets doped with aromatic molecules

The photoelectron imaging revealed a number of important features in molecular photoionization inside helium nanodroplets. Firstly, the photoelectron spectra of molecules embedded in helium droplets resembled those in the gas phase, meaning moderate influence of the helium environment on the ionization process. The most remarkable modification was the red-shift of the ionization thresholds of molecules embedded in droplets compared to those in the gas phase. This shift could be readily described by polarization of the helium droplet in the field of the ion. Secondly, the broadening of the individual photoelectron peaks towards lower energies varied with the mean droplet size and the initial energy of the photoelectrons. These variations were compatible with the loss of the photoelectron kinetic energy by collisions with helium atoms during the electron's escape from the droplet. The Monte-Carlo calculations carried out to test the binary elastic scattering mechanism of photoelectron kinetic energy loss were not able to reproduce the observed broadening, showing systematically lower kinetic energy loss. This indicated that a more efficient relaxation mechanism of photoelectron energy relaxation might take place during their escape through the droplet. The fate of the created positive ion was also studied. It was found that the ion might stay solvated inside the droplet or might be ejected from the droplet during the local overheating of helium by energy released upon ion solvation in the droplet, which was in line with the theoretical predictions of Bonhommeau *et al.*[183].

5.2 Outlook

To extend this work, it would be interesting to study the photoexcitation and photoionization dynamics of other impurities located on the surface of helium droplets. We expect that the desorption of excited atoms from the surface of nanodroplet will depend on the mass of the impurity atom and its helium counterpart. In this respect, the experiments with other alkali atoms (Li, K, Rb, Cs) deposited on helium-4 and helium-3 droplets are of particular interest. The use of superfluid versus normal helium nanodroplets will shed light on the role of superfluidity in the energy relaxation of electronically excited atoms. There is an indication that heavy alkali atoms like Rb in the lowest excited state stay attached to the helium-4 droplets[184]. The exciplex formation can also depend on the helium isotope as was shown by Droppelmann et al.[75] for Rb-^{3}He and Rb-^{4}He cases.

A better understanding of desorption dynamics and exciplex formation disclosed in our experiments can be achieved in time-resolved experiments. The speed distributions of desorbed excited sodium and exciplexes indicate that the time scale of their detachment is within several picosecond. The current time resolution is limited by the duration of excitation and ionization laser pulses with typical FWHM ≈ 11 ns. We thus propose to carry out experiments by using ultra-short laser pulses from conventional femtosecond laser, which will require frequency mixing to produce the necessary frequency for excitation of Na-doped droplets, since the fundamental frequency of the conventional Ti:Sa laser lies in the 12 000 - 13 000 cm^{-1} range. The expected time resolution of the order of 100 fs is thought to be enough to ionize excited Na atoms and exciplexes when they are still close to the droplet. The shift of ionization threshold will thus indicate their position with respect to the droplet.

The extension of our studies to earth-alkali doped helium-3 and helium-4 droplets is of great interest, too. As was shown by Hernando et al.[185], the earth-alkali atoms can reside either on the surface of ^{4}He nanoclusters (Ca, Sr, Ba) or in the interior (Mg), while in ^{3}He droplets all earth-alkali are located inside. In the case of escape of excited atoms from the interior of superfluid and normal droplets a valuable information about translational motion of electronically excited species may be

obtained. The first experiments on Ba-doped ^{4}He droplets in our laboratory were successful and showed that excited Ba(6s6p $^1P_1$) atoms stay attached to the droplet and can be readily ionized. This opens up a new perspective to study ion-doped helium nanoclusters.

Our studies of photoionization of doped nanodroplets were focused on the kinetic energy of escaped photoelectrons. The angular distribution is another valuable source of information about the escape dynamics of photoelectrons. The extension of our experiments to systems, where the angular distribution of nascent photoelectrons from the impurity in the interior of droplets is well anisotropic, will provide information about the nature of kinetic energy relaxation of photoelectrons as they pass through the helium droplet. A good candidate for this may be silver-doped droplets in conjunction with direct one-photon ionization, which will avoid the complex dynamics in the intermediated states[104] in the case of two-photon ionization.

The complex dynamics of photoexcitation and photoionization of doped helium nanodroplets, which was revealed in the presented work, necessitates a high-level theoretical modeling for a better understanding of underlying mechanisms and the planning of future experiments. Particularly interesting is the origin of velocity distributions of desorbed excited sodium atoms. We have recently started a collaboration with the group of Barranco and their preliminary results are promising[186] and reproduce the experimental velocity distributions. A more realistic model than the pair-wise additive one is currently being developed by Ancilotto and Callegari[184] in order to calculate the excitation spectra of alkali-doped droplets. Their preliminary results on Na-He_N demonstrated very good correspondence with our experiments.

The experiments on photoelectron imaging clearly demonstrated that our capability to use high energy photons for ionization was significantly impaired by the background photoelectrons created by scattered UV light on the metal parts of the imaging setup. Therefore, the design of the current setup should be revised with the aim to reduce background photoelectrons and light scattering. The installation of an additional detection setup specially dedicated for ZEKE and MATI spectroscopy would be valuable in investigating the internal energy states of photoproducts.

List of Figures

List of Tables

References

1. J. Wilks, D.S.B., *An Introduction to Liquid Helium*. 2nd edition ed. 1987, Oxford: Clarendon Press.

2. L.Landau, *The theory of superfluidity of helium II.* Journal of Physics USSR, 1941. 5: p. 71-90.

3. L.Landau, *On the theory of superfluidity of helium II.* Journal of Physics USSR, 1947. 11: p. 91-92.

4. Cowley, R.A. and A.D.B. Woods, *Inelastic scattering of thermal neutrons from liquid helium.* Canadian Journal of Physics, 1971. 49(2): p. 177-200.

5. E.Andronikashvilli, *Direct observation of two kinds of motion in heium II.* Journal of Physics USSR, 1947. 10(3): p. 201-206.

6. Donnelly, R.J., *Quantized Vortices in Helium II*. Cambridge Studies in Low Temperature Physics, ed. P.V.E.M. A.M. Goldman, M. Springford. 1991, Cambridge: Cambridge University Press.

7. Allum, D.R., et al., *Breakdown of superfluidity in liquid He-4: An experimental test of Landau's theory.* Philosophical Transactions of the Royal Society of London Series A-Mathematical Physical and Engineering Sciences, 1977. 284(1320): p. 179-224.

8. Ellis, T. and P.V.E. McClintock, *The breakdown of superfluidity in liquid He-4: V. Measurement of the Landau critical velocity for roton creation.* Philosophical Transactions of the Royal Society of London Series A-Mathematical Physical and Engineering Sciences, 1985. 315(1532): p. 259-300.

9. McClintock, P.V.E., *Ions and the Landau critical velocity in He II.* Zeitschrift für Physik B Condensed Matter, 1995. 98(3): p. 429-434.

10. Joppien, M., R. Karnbach, and T. Moller, *Electronic excitations in liquid helium: The evolution from small clusters to large droplets.* Physical Review Letters, 1993. 71(16): p. 2654-2657.

11. Tabbert, B., H. Gunther, and G.Z. Putlitz, *Optical investigation of impurities in superfluid He-4.* Journal of Low Temperature Physics, 1997. 109(5-6): p. 653-707.

12. Kuper, C.G., *Theory of negative ions in liquid helium.* Physical Review, 1961. 122(4): p. 1007-1011.

13. Atkins, K.R., *Ions in liquid helium.* Physical Review, 1959. 116(6): p. 1339.

14. Whittle, E., D.A. Dows, and G.C. Pimentel, *Matrix isolation method for the experimental study of unstable species.* Journal of Chemical Physics, 1954. 22(11): p. 1943-1943.

15. Silvera, I.F., *Ultimate fate of a gas of atomic hydrogen in a liquid-helium chamber: Recombination and burial.* Physical Review B, 1984. 29(7): p. 3899-3904.

16. Fujisaki, A., et al., *Implantation of neutral atoms into liquid helium by laser sputtering.* Physical Review Letters, 1993. 71(7): p. 1039-1042.

17. Szalewicz, K., *Interplay between theory and experiment in investigations of molecules embedded in superfluid helium nanodroplets.* International Reviews in Physical Chemistry, 2008. 27(2): p. 273-316.

18. Stienkemeier, F. and K.K. Lehmann, *Spectroscopy and dynamics in helium nanodroplets.* Journal of Physics B-Atomic Molecular and Optical Physics, 2006. 39(8): p. R127-R166.

19. Barranco, M., et al., *Helium nanodroplets: An overview.* Journal of Low Temperature Physics, 2006. 142(1-2): p. 1-81.

20. Toennies, J.P. and A.F. Vilesov, *Superfluid helium droplets: A uniquely cold nanomatrix for molecules and molecular complexes.* Angewandte Chemie-International Edition, 2004. 43(20): p. 2622-2648.

21. Northby, J.A., *Experimental studies of helium droplets.* The Journal of Chemical Physics, 2001. 115(22): p. 10065-10077.

22. Dalfovo, F. and S. Stringari, *Helium nanodroplets and trapped Bose-Einstein condensates as prototypes of finite quantum fluids.* The Journal of Chemical Physics, 2001. 115(22): p. 10078-10089.

23. Callegari, C., et al., *Helium nanodroplet isolation rovibrational spectroscopy: Methods and recent results.* The Journal of Chemical Physics, 2001. 115(22): p. 10090-10110.

24. Ceperley, D.M. and E. Manousakis, *Path integral Monte Carlo applications to quantum fluids in confined geometries.* The Journal of Chemical Physics, 2001. 115(22): p. 10111-10118.

25. Stienkemeier, F. and A.F. Vilesov, *Electronic spectroscopy in He droplets.* The Journal of Chemical Physics, 2001. 115(22): p. 10119-10137.

26. Hartmann, M., et al., *Rotationally resolved spectroscopy of SF_6 in liquid helium clusters.* Physical Review Letters, 1995. 75(8): p. 1566-1569.

27. Scheidemann, A., et al., *Capture of foreign atoms by helium clusters.* Physica B, 1990. 165: p. 135-136.

28. Scheidemann, A., J.P. Toennies, and J.A. Northby, *Capture of neon atoms by ^{4}He clusters.* Physical Review Letters, 1990. 64(16): p. 1899-1902.

29. Lugovoj, E., J.P. Toennies, and A. Vilesov, *Manipulating and enhancing chemical reactions in helium droplets.* Journal of Chemical Physics, 2000. 112(19): p. 8217-8220.

30. Mozhayskiy, V., et al., *Use of helium nanodroplets for assembly, transport, and surface deposition of large molecular and atomic clusters.* Journal of Chemical Physics, 2007. 127(9): p. 094701.

31. Tiggesbaumker, J. and F. Stienkemeier, *Formation and properties of metal clusters isolated in helium droplets.* Physical Chemistry Chemical Physics, 2007. 9(34): p. 4748-4770.

32. Chin, S.A. and E. Krotscheck, *Systematics of pure and doped ^{4}He clusters.* Physical Review B, 1995. 52(14): p. 10405-10428.

33. Lewerenz, M., *Structure and energetics of small helium clusters: Quantum simulations using a recent perturbational pair potential.* Journal of Chemical Physics, 1997. 106(11): p. 4596-4603.

34. Guardiola, R., et al., *Magic numbers, excitation levels, and other properties of small neutral He-4 clusters (N <= 50).* Journal of Chemical Physics, 2006. 124(8): p. 084307.

35. Stringari, S. and J. Treiner, *Systematics of liquid helium clusters.* The Journal of Chemical Physics, 1987. 87(8): p. 5021-5027.

36. Harms, J., J.P. Toennies, and F. Dalfovo, *Density of superfluid helium droplets.* Physical Review B, 1998. 58(6): p. 3341-3350.

37. Brink, D.M. and S. Stringari, *Density of states and evaporation rate of helium clusters.* Zeitschrift Fur Physik D-Atoms Molecules and Clusters, 1990. 15(3): p. 257-263.

38. Krishna, M.V.R. and K.B. Whaley, *Microscopic studies of collective spectra of quantum liquid clusters.* The Journal of Chemical Physics, 1990. 93(1): p. 746-759.

39. Krotscheck, E. and R. Zillich, *Dynamics of He-4 droplets.* Journal of Chemical Physics, 2001. 115(22): p. 10161-10174.

40. Mudrich, M., et al., *Kilohertz laser ablation for doping helium nanodroplets.* Review of Scientific Instruments, 2007. 78(10): p. 103106.

41. Claas, P., S.O. Mende, and F. Stienkemeier, *Characterization of laser ablation as a means for doping helium nanodroplets.* Review of Scientific Instruments, 2003. 74(9): p. 4071-4076.

42. Ancilotto, F., P.B. Lerner, and M.W. Cole, *Physics of solvation.* Journal of Low Temperature Physics, 1995. 101(5-6): p. 1123-1146.

43. Dalfovo, F., *Atomic and molecular impurities in He-4 clusters.* Zeitschrift Für Physik D-Atoms Molecules and Clusters, 1994. 29(1): p. 61-66.

44. Ancilotto, F., et al., *The binding of alkali atoms to the surfaces of liquid helium and hydrogen.* Zeitschrift für Physik B-Condensed Matter, 1995. 98(3): p. 323-329.

45. Kwon, Y., et al., *Quantum solvation and molecular rotations in superfluid helium clusters.* Journal of Chemical Physics, 2000. 113(16): p. 6469-6501.

46. Feynman, R.P., *Atomic theory of the 2-fluid model of liquid helium.* Physical Review, 1954. 94(2): p. 262-277.

47. Toennies, J.P. and A.F. Vilesov, *Novel low-energy vibrational states of foreign particles in fluid ^{4}He clusters.* Chemical Physics Letters, 1995. 235(5-6): p. 596-603.

48. Lehmann, K.K., *Potential of a neutral impurity in a large ^{4}He cluster.* Molecular Physics, 1999. 97(5): p. 645-666.

49. Lehmann, K.K. and J.A. Northby, *Potential of an ionic impurity in a large ^{4}He cluster.* Molecular Physics, 1999. 97(5): p. 639-644.

50. Nauta, K. and R.E. Miller, *Formation of cyclic water hexamer in liquid helium: The smallest piece of ice.* Science, 2000. 287(5451): p. 293-295.

51. Nauta, K. and R.E. Miller, *Nonequilibrium self-assembly of long chains of polar molecules in superfluid helium.* Science, 1999. 283(5409): p. 1895-1897.

52. Nauta, K. and R.E. Miller, *Infrared spectroscopy and structures of Ar_n-HF in liquid helium nanodroplets.* Journal of Chemical Physics, 2001. 115(22): p. 10138-10145.

53. Grebenev, S., et al., *Evidence for superfluidity in para-hydrogen clusters inside helium-4 droplets at 0.15 Kelvin.* Science, 2000. 289(5484): p. 1532-1535.

54. Choi, M.Y., et al., *Infrared spectroscopy of helium nanodroplets: novel methods for physics and chemistry.* International Reviews in Physical Chemistry, 2006. 25(1-2): p. 15-75.

55. Stienkemeier, F. and A.F. Vilesov, *Electronic spectroscopy in He droplets.* Journal of Chemical Physics, 2001. 115(22): p. 10119-10137.

56. Goyal, S., D.L. Schutt, and G. Scoles, *Vibrational spectroscopy of sulfur-hexafluoride attached to helium clusters.* Physical Review Letters, 1992. 69(6): p. 933-936.

57. Goyal, S., D.L. Schutt, and G. Scoles, *Errata: Vibrational spectroscopy of sulfur-hexafluoride attached to helium clusters [Phys. Rev. Lett. 69, 933 (1992)].* Physical Review Letters, 1994. 73(18): p. 2512-2512.

58. Grebenev, S., J.P. Toennies, and A.F. Vilesov, *Superfluidity within a small helium-4 cluster: The microscopic Andronikashvili experiment.* Science, 1998. 279(5359): p. 2083-2086.

59. Andronikashvilli, E., *Direct observation of two kinds of motion in helium II.* Journal of Physcs USSR, 1946. 10(3): p. 201-206.

60. Miller, R.E., *Comparative studies of cluster dynamics in the gas and condensed phases.* Faraday Discussions, 2001. 118: p. 1-17.

61. Callegari, C., et al., *Superfluid hydrodynamic model for the enhanced moments of inertia of molecules in liquid ^{4}He.* Physical Review Letters, 1999. 83(24): p. 5058-5061.

62. Kwon, Y.K. and K.B. Whaley, *Atomic-scale quantum solvation structure in superfluid helium-4 clusters.* Physical Review Letters, 1999. 83(20): p. 4108-4111.

63. Callegari, C., et al., *First overtone helium nanodroplet isolation spectroscopy of molecules bearing the acetylenic CH chromophore.* Journal of Chemical Physics, 2000. 113(23): p. 10535-10550.

64. Hartmann, M., et al., *Direct spectroscopic observation of elementary excitations in superfluid He droplets.* Physical Review Letters, 1996. 76(24): p. 4560-4563.

65. Grebenev, S., et al., *Spectroscopy of molecules in helium droplets.* Physica B, 2000. 280(1-4): p. 65-72.

66. Bunermann, O., et al., *Spectroscopy of Cs attached to helium nanodroplets.* Journal of Chemical Physics, 2004. 121(18): p. 8880-8886.

67. Bruhl, F.R., R.A. Trasca, and W.E. Ernst, *Rb-He exciplex formation on helium nanodroplets.* Journal of Chemical Physics, 2001. 115(22): p. 10220-10224.

68. Callegari, C., et al., *Beam depletion spectroscopy of alkali atoms (Li, Na, K) attached to highly quantum clusters.* Journal of Physical Chemistry A, 1998. 102(1): p. 95-101.

69. Stienkemeier, F., et al., *Spectroscopy of alkali atoms (Li, Na, K) attached to large helium clusters.* Zeitschrift Für Physik D-Atoms Molecules and Clusters, 1996. 38(3): p. 253-263.

70. Bunermann, O., et al., *Unraveling the absorption spectra of alkali metal atoms attached to helium nanodroplets.* Journal of Physical Chemistry A, 2007. 111(49): p. 12684-12694.

71. Reho, J., et al., *Alkali-helium exciplex formation on the surface of helium nanodroplets. I. Dispersed emission spectroscopy.* Journal of Chemical Physics, 2000. 113(21): p. 9686-9693.

72. Reho, J., et al., *Spin-orbit effects in the formation of the Na-He excimer on the surface of He clusters.* Faraday Discussions, 1997: p. 161-174.

73. Schulz, C.P., P. Claas, and F. Stienkemeier, *Formation of K*He exciplexes on the surface of helium nanodroplets studied in real time.* Physical Review Letters, 2001. 8715(15): p. 4.

74. Reho, J., et al., *Alkali-helium exciplex formation on the surface of helium nanodroplets. II. A time-resolved study.* Journal of Chemical Physics, 2000. 113(21): p. 9694-9701.

75. Droppelmann, G., et al., *Formation times of RbHe exciplexes on the surface of superfluid versus normal fluid helium nanodroplets.* Physical Review Letters, 2004. 93(2): p. 023402.

76. Pacheco, A.B., et al., *Quantum dynamics of an excited alkali atom in a noble gas cluster: Lithium attached to a helium cluster.* The Journal of Chemical Physics, 2007. 127(24): p. 244504-21.

77. Takayanagi, T. and M. Shiga, *Theoretical study on photoexcitation dynamics of the K atom attached to helium clusters and the solvation structures of K*He$_n$ exciplexes.* Physical Chemistry Chemical Physics, 2004. 6(13): p. 3241-3247.

78. Polyakova, E., D. Stolyarov, and C. Wittig, *Multiple photon excitation and ionization of NO in and on helium droplets.* Journal of Chemical Physics, 2006. 124(21): p. 214308-11.

79. Przystawik, A., et al., *Photoelectron studies of neutral Ag_3 in helium droplets.* Journal of Chemical Physics, 2007. 126(18): p. 184306-5.

80. Przystawik, A., et al., *Spectroscopy of silver dimers in triplet states.* Journal of Physics B-Atomic Molecular and Optical Physics, 2006. 39(19): p. S1183-S1189.

81. Radcliffe, P., et al., *Excited-state relaxation of Ag_8 clusters embedded in helium droplets.* Physical Review Letters, 2004. 92(17): p. 173403-4.

82. Braun, A., *Photodissociation Studies of CH_3I and CF_3I in Fluid ^{4}Helium Nanodroplets*. 2004, Ecole Polytechnique Fédérale de Lausanne: Lausanne.

83. Buchenau, H., et al., *Mass-spectra and time-of-flight distributions of helium cluster beams.* Journal of Chemical Physics, 1990. 92(11): p. 6875-6889.

84. Lewerenz, M., B. Schilling, and J.P. Toennies, *A new scattering deflection method for determining and selecting the sizes of large liquid clusters of ^4He.* Chemical Physics Letters, 1993. 206(1-4): p. 381-387.

85. Knuth, E.L., *Size correlations for condensation clusters produced in free-jet expansions.* The Journal of Chemical Physics, 1997. 107(21): p. 9125-9132.

86. Lewerenz, M., B. Schilling, and J.P. Toennies, *Successive capture and coagulation of atoms and molecules to small clusters in large liquid helium clusters.* The Journal of Chemical Physics, 1995. 102(20): p. 8191-8207.

87. Tishchenko, O., E.S. Kryachko, and M.T. Nguyen, *Theoretical vibrational analysis of monohalogenated phenols.* Spectrochimica Acta Part A: Molecular and Biomolecular Spectroscopy, 2002. 58(9): p. 1951-1969.

88. Wojciechowski, P.M., et al., *Electronic structures, vibrational spectra, and revised assignment of aniline and its radical cation: Theoretical study.* The Journal of Chemical Physics, 2003. 118(24): p. 10900-10911.

89. Whiteside, P.T., A.K. King, and K.L. Reid, *Photoelectron spectroscopy of S_1 toluene: I. Photoionization propensities of selected vibrational levels in S_1 toluene.* Journal of Chemical Physics, 2005. 123(20): p. 6.

90. Eppink, A. and D.H. Parker, *Velocity map imaging of ions and electrons using electrostatic lenses: Application in photoelectron and photofragment ion imaging of molecular oxygen.* Review of Scientific Instruments, 1997. 68(9): p. 3477-3484.

91. Parker, D.H. and A. Eppink, *Photoelectron and photofragment velocity map imaging of state-selected molecular oxygen dissociation/ionization dynamics.* Journal of Chemical Physics, 1997. 107(7): p. 2357-2362.

92. Whitaker, B.J., *Imaging in molecular dynamics. Technology and applications. (A User's Guide)*, ed. B.J. Whitaker. 2003: Cambridge University Press.

93. Bor-Yu, C., et al., *Improved two-dimensional product imaging: The real-time ion-counting method.* Review of Scientific Instruments, 1998. 69(4): p. 1665-1670.

94. Zare, R.N., *Photoejection dynamics.* Molecular Photochemistry, 1972. 4(1): p. 1-37.

95. Michaelson, H.B., *Work function of elements and its periodicity.* Journal of Applied Physics, 1977. 48(11): p. 4729-4733.

96. Muller-Dethlefs, K., M. Sander, and E.W. Schlag, *Two-colour photoionization resonance spectroscopy of NO: Complete separation of rotational levels of NO^+ at the ionization threshold.* Chemical Physics Letters, 1984. 112(4): p. 291-294.

97. Schlag, E.W., *ZEKE Spectroscopy*. 1998: Cambridge University Press.

98. Hans A. Bethe, E.E.S., *Quantum Mechanics of One- and Two-Electron Atoms*. 1977, New York: Plenum Publishing Corporation.

99. Ralchenko, Y., Jou, F.-C., Kelleher, D.E., Kramida, A.E., Musgrove, A., Reader, J., Wiese, W.L., and Olsen, K. , *NIST Atomic Spectra Database (version 3.1.3), [Online]. Available: http://physics.nist.gov/asd3 [2007, December 10]*. 2007, National Institute of Standards and Technology, Gaithersburg, MD.

100. Gallagher, T.F., *Rydberg Atoms*. Cambridge Monographs on Atomic, Molecular, and Chemical Physics, ed. P.L.K. A. Dalgrano, F.H. Read, R.N. Zare. 1994, Cambridge: Cambridge University Press.

101. William, A.C., *Factors affecting lifetimes and resolution of Rydberg states observed in zero-electron-kinetic-energy spectroscopy.* The Journal of Chemical Physics, 1993. 98(6): p. 4520-4530.

102. Merkt, F., *Molecules in high Rydberg states.* Annual Review of Physical Chemistry, 1997. 48: p. 675-709.

103. Zhu, L. and P. Johnson, *Mass analyzed threshold ionization spectroscopy.* The Journal of Chemical Physics, 1991. 94(8): p. 5769-5771.

104. Loginov, E. and M. Drabbels, *Excited state dynamics of Ag atoms in helium nanodroplets.* Journal of Physical Chemistry A, 2007. 111(31): p. 7504-7515.

105. Enomoto, K., et al., *Emission spectra of alkali-metal (K,Na,Li)-He exciplexes in cold helium gas.* Physical Review A, 2004. 69(1): p. 012501-8.

106. Pascale, J., *Use of l-dependent pseudopotentials in the study of alkali-metal-atom-He systems. The adiabatic molecular potentials.* Physical Review A, 1983. 28(2): p. 632-644.

107. Soldan, P., E.P.F. Lee, and T.G. Wright, *Interatomic potentials for the Na^+-Rg complexes (Rg = He , Ne and Ar).* Molecular Physics, 1999. 97(1-2): p. 139-149.

108. Robert J. Le Roy, *LEVEL 8.0 A Computer Program for Solving the Radial Schrodinger Equation for Bound and Quasibound Levels*. 2007, University of Waterloo Chemical Physics Research Report CP-663 (2007); see http://leroy.uwaterloo.ca/programs.

109. Aymar, M., *Influence of core-polarization effects on photo-ionization cross-sections of ground level and excited nS levels of neutral sodium.* Journal of Physics B-Atomic Molecular and Optical Physics, 1978. 11(8): p. 1413-1423.

110. Stienkemeier, F., et al., *Surface location of sodium atoms attached to ^{3}He nanodroplets.* Physical Review B, 2004. 70(21): p. 214508-5.

111. Robert J. Le Roy and G.T. Kraemer, *BCONT 2.2 Computer Program for Calculating Absorption Coefficients, Emission Intensities or (Golden Rule) Predissociation Rates*. 2004, University of Waterloo Chemical Physics Research Report CP-650R (2004). The source code and manual for this program may be obtained from "Computer Programs" link at http://leroy.waterloo.ca.

112. Zare, R.N., *Angular Momentum*. 1988: Wiley-Interscience Publication.

113. Alexander, M.H., et al., *A collaborative theoretical and experimental study of the structure and electronic excitation spectrum of the BAr and BAr_2 complexes.* The Journal of Chemical Physics, 1997. 106(15): p. 6320-6331.

114. Pagaran, J., S. Fritzsche, and G. Gaigalas, *Maple procedures for the coupling of angular momenta. IX. Wigner D-functions and rotation matrices.* Computer Physics Communications, 2006. 174(8): p. 616-630.

115. Maplesoft^{TM}, *Maple*. 2005.

116. Barranco, M., *Personal communication.* 2007.

117. Hernando, A., *Personal communication*. 2008.

118. Patil, S.H., *Adiabatic potentials for alkali-inert gas systems in the ground state.* The Journal of Chemical Physics, 1991. 94(12): p. 8089-8095.

119. Pascale, J., *Personal communication.* 2007.

120. Geum, N. and G.H. Jeung, *Undulating potential curves of the Rydberg states of NaHe.* Chemical Physics Letters, 2001. 333(3-4): p. 314-318.

121. Jeung, G.-H., *Personal communication.* 2007.

122. Theodorakopoulos, G. and I.D. Petsalakis, *Potential-energy curves and radiative lifetimes of Rydberg states of NaHe.* Journal of Physics B-Atomic Molecular and Optical Physics, 1993. 26(23): p. 4367-4380.

123. Born, M. and R. Oppenheimer, *Quantum theory of molecules.* Annalen Der Physik, 1927. 84(20): p. 0457-0484.

124. Condon, E.U., *Nuclear motions associated with electron transitions in diatomic molecules.* Physical Review, 1928. 32(6): p. 0858-0872.

125. Herzberg, G., *Spectra of Diatomic Molecules*. Molecular Spectra and Molecular Structrure. Vol. I. 1950: Van Nostrand Reinhold Company.

126. Chen, K.-m. and E.S. Yeung, *Rovibronic two-photon transitions of symmetric top molecules.* The Journal of Chemical Physics, 1978. 69(1): p. 43-52.

127. Consalvo, D., et al., *High-resolution laser-induced fluorescence study of a cage molecule, 1,4-diazabicyclo[2,2,2]octane, DABCO.* Chemical Physics, 1993. 174(2): p. 267-276.

128. Janssen, M.H.M., et al., *Rotational alignment of the CD_3 fragment from the 266-nm photodissociation of CD_3I.* Journal of Physical Chemistry, 1991. 95(21): p. 8007-8013.

129. Demtroeder, W., *Laser Spectroscopy. Basic Concepts and Instrumentation.* Springer series in chemical physics. N5. 1988: Springer-Verlag.

130. Letokhov, V.S., V.I. Mishin, and A.A. Puretzky, *Selective photoionization of atoms by laser radiation and its applications.* Progress in Quantum Electronics, 1979. 5: p. 139-203.

131. Gallagher, T.F., S.A. Edelstein, and R.M. Hill, *Radiative lifetimes of excited p states of Na.* Physical Review A, 1976. 14(6): p. 2360-2362.

132. Eichenauer, D. and R.J. Leroy, *Monter Carlo simulations of structural properties and infrared spectra of SF_6-Ar_n clusters.* Journal of Chemical Physics, 1988. 88(5): p. 2898-2912.

133. Spelsberg, D., T. Lorenz, and W. Meyer, *Dynamic multipole polarizabilities and long range interaction coefficients for the systems H, Li, Na, K, He, H^-, H_2, Li_2, Na_2, and K_2.* Journal of Chemical Physics, 1993. 99(10): p. 7845-7858.

134. Cohen, J.S. and Schneide.B, *Ground and excited states of Ne_2 and Ne_2^+. I. Potential curves with and without spin-orbit coupling.* Journal of Chemical Physics, 1974. 61(8): p. 3230-3239.

135. Gallagher, T.F., S.A. Edelstein, and R.M. Hill, *Radiative lifetimes of S and D Rydberg levels of Na.* Physical Review A, 1975. 11(5): p. 1504-1506.

136. Aymar, M., *Personal communication*. 2007.

137. Aymar, M., E. Luc-Koenig, and F.C. Farnoux, *Theoretical investigation on photoionization from Rydberg states of lithium, sodium and potassium.* Journal of Physics B: Atomic and Molecular Physics, 1976. 9(8): p. 1279-1291.

138. Miculis, K. and W. Meyer, *Phototransition of Na($3p_{3/2}$) into high Rydberg states and the ionization continuum.* Journal of Physics B-Atomic Molecular And Optical Physics, 2005. 38(13): p. 2097-2108.

139. Amin, N., et al., *Measurement of the 4d-photoionization cross section via two-photon and two-step excitation in sodium.* Journal of Quantitative Spectroscopy & Radiative Transfer, 2006. 102(2): p. 269-276.

140. Beterov, I.M. and I.I. Ryabtsev, *Studies of single- and two-photon ionization of the 4s excited states of the sodium atoms.* Optics and Spectroscopy, 1993. 75(3): p. 313-316.

141. Smith, A.V., et al., *Absolute photoionization cross-section measurements of the excited 4D and 5S states of sodium.* Physical Review A, 1980. 22(2): p. 577-581.

142. Ancilotto, F., et al., *Squeezing a helium nanodroplet with a Rydberg electron.* Journal of Physical Chemistry A, 2007. 111(49): p. 12695-12701.

143. Yeretzian, C., et al., *Breakdown of the Born-Oppenheimer approximation in ZEKE states of Ag_2.* Chemical Physics Letters, 1995. 239(1-3): p. 61-66.

144. Jortner, J., *Cluster size effects.* Zeitschrift Für Physik D-Atoms Molecules and Clusters, 1992. 24(3): p. 247-275.

145. Rossi, M., et al., *Alkali and alkali-earth ions in ^{4}He systems.* Physical Review B, 2004. 69(21): p. 212510-4.

146. Golov, A. and S. Sekatskii, *Rydberg branch of electronic excitations of helium clusters.* Physica B, 1994. 194-196: p. 555-556.

147. Golov, A. and S. Sekatskii, *A new type of excimer atom: electron+ionized helium cluster.* Zeitschrift Für Physik D-Atoms Molecules and Clusters, 1993. 27(4): p. 349-355.

148. Woolf, M.A. and G.W. Rayfield, *Energy of Negative Ions in Liquid Helium by Photoelectric Injection.* Physical Review Letters, 1965. 15(6): p. 235.

149. Levine, R.D. and R.B. Bernstein, *Molecular Reaction Dynamics and Chemical Reactivity*. 1987, Oxford: Oxford University Press.

150. Lehmann, K.K., *Microcanonical thermodynamic properties of helium nanodroplets.* Journal of Chemical Physics, 2003. 119(6): p. 3336-3342.

151. Ashfold, M.N.R. and J.D. Howe, *Multiphoton spectroscopy of molecular species.* Annual Review of Physical Chemistry, 1994. 45: p. 57-82.

152. Brand, J.C.D., D.R. Williams, and T.J. Cook, *Vibrational analysis of first ultraviolet band system of aniline.* Journal of Molecular Spectroscopy, 1966. 20(4): p. 359-380.

153. Roth, W., et al., *Reassignment of ground and first excited state vibrations in phenol.* Chemical Physics, 2000. 252(1-2): p. 247-256.

154. Hickman, C.G., J.R. Gascooke, and W.D. Lawrance, *The S_1-S_0 ($^1B_2$-$^1A_1$) transition of jet-cooled toluene: Excitation and dispersed fluorescence spectra, fluorescence lifetimes, and intramolecular vibrational energy redistribution.* Journal of Chemical Physics, 1996. 104(13): p. 4887-4901.

155. Boatwright, A., et al., *A systematic shift in the electronic spectra of substituted benzene molecules trapped in helium nanodroplets.* Journal of Chemical Physics, 2005. 123(2): p. 021102-3.

156. Krasnokutski, S., G. Rouille, and F. Huisken, *Electronic spectroscopy of anthracene molecules trapped in helium nanodroplets.* Chemical Physics Letters, 2005. 406(4-6): p. 386-392.

157. Lehnig, R., et al., *Fine structure of the (S_1←S_0) band origins of phthalocyanine molecules in helium droplets.* Journal of Chemical Physics, 2004. 121(19): p. 9396-9405.

158. Hartmann, M., et al., *Hole-burning studies of the splitting in the ground and excited vibronic states of tetracene in helium droplets.* Journal of Physical Chemistry A, 2001. 105(26): p. 6369-6377.

159. Hartmann, M., et al., *The phonon wings in the (S_1←S_0) spectra of tetracene, pentacene, porphin and phthalocyanine in liquid helium droplets.* Physical Chemistry Chemical Physics, 2002. 4(20): p. 4839-4844.

160. Brand, J.C., D.R. Williams, and T.J. Cook, *Aniline - planar or nonplanar?* Journal of Molecular Spectroscopy, 1966. 20(2): p. 193-195.

161. Larsen, N.W., *Microwave spectra of the six mono-^{13}C-substituted phenols and of some monodeuterated species of phenol. Complete substitution structure and absolute dipole moment.* Journal of Molecular Structure, 1979. 51(2): p. 175-190.

162. Schumm, S., et al., *A CASSCF study of the S_0 and S_1 states of phenol.* Chemical Physics Letters, 1996. 263(1-2): p. 126-132.

163. Borst, D.R. and D.W. Pratt, *Toluene: Structure, dynamics, and barrier to methyl group rotation in its electronically excited state. A route to IVR.* Journal of Chemical Physics, 2000. 113(9): p. 3658-3669.

164. East, A.L.L., et al., *Toluene internal-rotation: Measurement and simulation of the high-resolution S_1-S_0 fluorescence excitation spectrum at 0.5 K.* Journal of Chemical Physics, 2000. 112(1): p. 167-175.

165. Keil, T.H., *Shapes of impurity absorption bands in solids.* Physical Review, 1965. 140(2A): p. A601-A617.

166. Meek, J.T., et al., *The laser photoelectron spectrum of gas phase aniline.* The Journal of Chemical Physics, 1985. 82(4): p. 1741-1749.

167. de Groot, M. and W.J. Buma, *A time-dependent density functional study of vibrationally resolved excitation, emission, and ionization spectra of the S_1 state of phenol.* Chemical Physics Letters, 2006. 420(4-6): p. 459-464.

168. Song, X., et al., *Zero kinetic energy photoelectron spectra of jet-cooled aniline.* The Journal of Chemical Physics, 1993. 99(5): p. 3224-3233.

169. Reiser, G., et al., *A new approach to vibrational spectroscopy of ion clusters: the "zero kinetic energy (ZEKE)" photoelectron spectrum of the phenol-water complex.* Chemical Physics Letters, 1991. 181(1): p. 1-4.

170. Meek, J.T., S.R. Long, and J.P. Reilly, *Observation of polyatomic ion vibrational state distribution by laser photoelectron spectroscopy.* Journal of Physical Chemistry, 1982. 86(15): p. 2809-2811.

171. Lehnig, R. and A. Slenczka, *Emission spectra of free base phthalocyanine in superfluid helium droplets.* Journal of Chemical Physics, 2003. 118(18): p. 8256-8260.

172. Lehnig, R. and A. Slenczka, *Spectroscopic investigation of the solvation of organic molecules in superfluid helium droplets.* Journal of Chemical Physics, 2005. 122(24): p. 9.

173. Peterka, D.S., et al., *Photoionization dynamics in pure helium droplets.* Journal of Physical Chemistry A, 2007. 111(31): p. 7449-7459.

174. Peterka, D.S., et al., *Photoelectron imaging of helium droplets.* Physical Review Letters, 2003. 91(4): p. 043401-4.

175. A. Tramer, C.J., F.Lahmani, *Energy Dissipation in Molecular Systems*. 2005: Springer.

176. Gonzalez-Lafont, A., et al., *Excited states and electronic spectra of monosubstituted benzenes. An AM1 study.* Spectrochimica Acta Part A-Molecular and Biomolecular Spectroscopy, 1988. 44(12): p. 1427-1434.

177. Kim, B., C.P. Schick, and P.M. Weber, *Time-delayed two-color photoelectron spectra of aniline, 2-aminopyridine and 3-aminopyridine: Snapshots of the nonadiabatic curve crossings.* Journal of Chemical Physics, 1995. 103(16): p. 6903-6913.

178. Frisch, M.J., et al., *Gaussian 03 Revision B.05*. 2003, Gaussian, Inc.: Pittsburgh PA.

179. Onn, D.G. and M. Silver, *Injection and thermalization of hot electrons in solid, liquid, and gaseous helium at low temperatures.* Physical Review A, 1971. 3(5): p. 1773-1779.

180. Onn, D.G. and M. Silver, *Attenuation and lifetime of hot electrons injected into liquid helium.* Physical Review, 1969. 183(1): p. 295-307.

181. Williams, J.F., *A phaseshift analysis of experimental angular distributions of electrons elastically scattered from He, Ne and Ar over the range 0.5 to 20 eV.* Journal of Physics B-Atomic Molecular and Optical Physics, 1979. 12(2): p. 265-282.

182. Saha, H.P., *Accurate ab initio calculation on the low-energy elastic scattering of electrons from helium.* Physical Review A, 1989. 40(6): p. 2976-2990.

183. Bonhommeau, D., M. Lewerenz, and N. Halberstadt, *Fragmentation of ionized doped helium nanodroplets: Theoretical evidence for a dopant ejection mechanism.* The Journal of Chemical Physics, 2008. 128(5): p. 054302-17.

184. Callegari, C. and F. Ancilotto, *Personal communication*. 2008.

185. Hernando, A., et al., *The structure and energetics of ^{3}He and ^{4}He nanodroplets doped with alkaline earth atoms.* Journal of Physical Chemistry A, 2007. 111(31): p. 7303-7308.

186. Hernando, A. and M. Barranco, *Personal communication*. 2008.

Curriculum Vitae

2003-2008 Ecole Polytechnique Fédérale de Lausanne
Ph.D. in physical chemistry, advisor: Dr. Marcel Drabbels
"Photoexcitation and Photoionization Dynamics of Doped Liquid Helium-4 Nanodroplets"

2001-2003 Master degree in applied physics and mathematics, Moscow Institute of Physics and Technology.
Diploma work in nonlinear optics with Dr. A. Erokhin it the Laboratory of Non-linear Optics and Light Scattering at the Institute of Physics of Russian Academy of Sciences, Moscow
"Investigation of Laser Pulse Compression by Stimulated Brillouin Scattering in Frequency and Time Domains"

1997-2001 Bachelor degree in applied physics and mathematics, Moscow Institute of Physics and Technology

Acknowledgments

I would like to express my sincere gratitude to people who helped me all along my thesis work.

Dr. Marcel Drabbels, my advisor, for accepting me as a graduate student in the helium droplet project and guiding me during the thesis preparation, for prompt assistance, the sharing of scientific experience and for amount of time to read and correct this manuscript.

Prof. Tom Rizzo for accepting me in the LCPM group and giving the opportunity to work with the excellent collaborators in very well equipped laboratories.

Dr. Andreas Braun, for his help and guidance in introducing me to the technical design and UHV techniques.

Dr. Oleg Boiarkine, for assistance in the lab.

The members of the mechanical workshop, especially André Fattet and Jean-Luc Passard for rapid and high-quality work and assistance in mechanical design.

Gabriel Roch from the electronic workshop for his technical assistance.

Marianne Dang, our kind secretary in the LCPM for caring for administrative matters and beyond.

Prof. Rainer Beck, Dr. Mikhail Polianski, Dr. Richard Bossart, Dr. Plinio Maroni, Dr. Anthi Kamariotis, Dr. Sébastien Mercier, Dr. Thanh Tung Dang, Dr. Pavel Maksyutenko, Dr. Marco Sacchi, Dr. Régis Bisson, Dr. Jaime Stearns, Dr. Annette Svendsen, Amanz Ruf, Bruce Yoder, Caroline Seaiby, George Papadopoulos, Natalia Nagornova, Ulrich Lorenz, Monia Guidi, Maxim Grechko, Pradip Chakraborty, Li Chen, past and present members of the LCPM, for friendly atmosphere and discussions.

My friends and family for their love and support.